

Copyright © 1984, by the author(s).
All rights reserved.

Permission to make digital or hard copies of all or part of this work for personal or classroom use is granted without fee provided that copies are not made or distributed for profit or commercial advantage and that copies bear this notice and the full citation on the first page. To copy otherwise, to republish, to post on servers or to redistribute to lists, requires prior specific permission.

ANALYSIS OF BACKSCATTERED ELECTRON
SIGNALS FOR X-RAY MASK INSPECTION

by

M. G. Rosenfield

Memorandum No. UCB/ERL M84/16

30 January 1984

ELECTRONICS RESEARCH LABORATORY

College of Engineering
University of California, Berkeley
94720

**ANALYSIS OF BACKSCATTERED ELECTRON SIGNALS
FOR X-RAY MASK INSPECTION**

Copyright © 1984

by

Michael G. Rosenfield

ANALYSIS OF BACKSCATTERED ELECTRON SIGNALS FOR X-RAY MASK INSPECTION

Michael G. Rosenfield

Department of Electrical Engineering and Computer Sciences
and The Electronics Research Laboratory
University of California
Berkeley, California 94720



Research Advisor

ABSTRACT

The use of an electron-beam lithography system for the inspection of x-ray masks requires an in-depth understanding of the electron scattering properties of the defects. Mask imperfections can be detected by a comparison of the backscattered electron signal from the mask with the design data used by the electron-beam system to write the mask.

A new Monte Carlo computer program has been developed to simulate the backscattered electron signal from three independent, infinitely long, variable width, variable edge-slope, gold lines on a silicon substrate. The program is based on the continuous slowing down approximation, Bethe energy loss equation, and screened Rutherford collision cross-section. Excellent agreement with experimental results has allowed the program to be used to investigate the effects of different collection angle ranges and structure geometries on the backscattered electron signal. The relationships of the inspecting beam size and beam voltage with the quality of the signal are also investigated. Universal curves of the backscatter coefficient versus material thickness, normalized to the Gruen and Bethe ranges, have been obtained.

Different types of backscattered electron detectors are analyzed, from a practical viewpoint, for use in an electron-beam inspection system and it is observed that currently available, high speed, diode detectors are most favorable. The effects of shot noise, the fundamental limitation to reliable high speed inspection, are studied for various structures. It is found that shot noise will not be a fundamental limitation to electron-beam inspection if the

comparator thresholds, used to determine the presence or absence of masking material, are placed correctly.

After gaining fundamental insight into the backscattered electron signal characteristics, the systems aspects of using electron-beam techniques for mask inspection are then discussed. A mask inspection algorithm is demonstrated using a vector scan electron-beam system and a complete mask inspection system is proposed. Finally, electron-beam scanning techniques for inspection are discussed and it is observed that the proposed inspection system will allow inspection throughput comparable to existing optical techniques at 2-4 times the resolution.

ACKNOWLEDGEMENT

There have been many people over the past several years who have made contributions, either directly or indirectly, to the completion of this research. I would first like to thank and express my sincere appreciation to my Research Advisor, Professor Andy Neureuther, for his guidance, support, and friendship which made this work possible. His patience and editorial skills are also greatly appreciated.

I also wish to thank Professor Bill Oldham for his advice and comments throughout this research. Thanks are also to be extended to Professors Dennis Hess and Ted Van Duzer. Much of the artwork in this thesis was made possible by the expert drafting of Tom King.

The research which went into this thesis was a bit different than most in that it was a collaborative effort with people at the IBM T.J. Watson Research Center in Yorktown Heights, New York. I would like to thank Alan Wilson for giving me the chance to work at IBM and also for his encouragement and many helpful suggestions. There are many other individuals at IBM who have made contributions and I would like to show my appreciation. I am indebted to G.R. Viswanathan (Visu) for his advice and help throughout all phases of this research. I also would like to thank Hank Voelker for his expert technical assistance in many of the experiments using the vector scan electron-beam system. I also wish to thank Walter Molzen for his patience and help in the post-processing of data for the electron-beam systems. The helpful advice from John Warlaumont and Dieter Kern is also greatly appreciated. I am also grateful to Bob Scott and Joe Conte for their technical skills. I would also like to thank Raul Acosta and Juan Maldonado for their contributions. Thanks are also to be extended to Juan LaFuente and Arthur Kern for their aid in using the vector scan computer software. I would also like to thank Warren Grobman, Mike Hatzakis, Bob Simpson, Oliver Wells, Haskell Reich, Jim Rosenberg, and Norman Bobroff for their contributions. The administrative help and pleasantness of Maryann Shaw and Karen Hack are also greatly appreciated. I am also grateful to Grant Willson of IBM Research in San Jose for helping to expedite this research. Finally, I would like to thank Jurij Paraszczak and Bob Flavin for their advice and help and also for being my very good friends over the past several years.

I also wish to thank my colleagues at Berkeley, especially those in the SAMPLE group, for their contributions. I am indebted to Sharad Nandgaonakar for the countless times he helped with difficult problems on the computer. I would also like to thank John Reynolds, Ken Lee, Gino Addiego, Paul Carey, Charlie Giancarlo, Scott Schafer, Keith Bentley, Claudia Liska, Tom Berger, Wendy Fong, Wing Leung, and Grace Mah for making life in Berkeley that much more interesting.

I am also grateful to Dave Kyser of Signetics and Y.C. Lin of Texas Instruments for their help while I was writing the Monte Carlo program for this research.

I would now like to turn my attention to those people who made contributions to this thesis by being my closest friends and giving me the strength to continue. I would like to thank Dave Catalano for his friendship over the last 12 years or so and for the use of his couch on those days when I had to travel down to San Jose. I would also like to thank Francois Henley for many stimulating conversations, some of which even concerned electrical engineering. I would also like to thank a group of friends, in addition to Maf, whom I've known since high school. I would like to thank Bill Tella (Waldo), Steve Lancellotta (Lance), Marty Politelli, Bob Heon, John Roch (Boom-Boom), and John and Patty Thompson for making my visits home to Rhode Island that much more enjoyable.

I would also like to thank Jeff and Patty Voigt for their friendship and for the many good times we have had in New York, Philadelphia, Vermont, Rhode Island, Connecticut, and California. I would also like to thank Lad Ricker for his friendship and information on nuclear power. I also wish to thank Mark Socinski for his friendship and illegible letters. I would also like to thank Heather Stengel for her friendship and hospitality. Finally, I would like to thank Kat deCaracena for her faith in me over the years and for being one of my best friends.

I would now like to thank my parents, David and Lois Rosenfield, and sister, Elaine, for their love, support, and faith in me. Without them, it would have been impossible. Finally, I would also like to thank my relatives for their kindness over the years.

This work was a collaborative study supported in part by the X-Ray Lithography group at the IBM Thomas J. Watson Research Center and the National Science Foundation under grant ECS-8106234.

Dedicated to

my parents, sister, friends, and family.

Table of Contents

| | |
|--|-----|
| Abstract | 1 |
| Acknowledgement | i |
| Dedication | iii |
| Table of Contents | iv |
| Chapter 1: Introduction | 1 |
| Chapter 2: Fabrication of Inspection Test Patterns | 5 |
| 2.1. Introduction | 5 |
| 2.2. Design | 6 |
| 2.3. Programmed Defects | 6 |
| 2.4. Fabrication Process | 6 |
| Chapter 3: Monte Carlo Simulation Program | 14 |
| 3.1. Introduction | 14 |
| 3.2. The Monte Carlo Program | 15 |
| 3.3. Comparison of Simulation to Experiment | 20 |
| 3.4. Summary | 41 |
| Chapter 4: Simulation of Backscattered Electron Signals for X-ray Mask Inspection | 47 |
| 4.1. Introduction | 47 |
| 4.2. Optimization of Experimental Detector Placement | 48 |
| 4.3. A Study of the Effects of Beam Size and Angle Collection Range | 51 |
| 4.3.1. Δ SNR | 58 |
| 4.3.2. Backscattered Electron Signal Fwhm | 65 |
| 4.3.3. Threshold (DC Level) | 74 |
| 4.4. Absorber Thickness Studies | 83 |
| 4.5. Effects of Scanning Near the Edges of a Structure | 92 |
| 4.6. Extension to Three Dimensional Simulation | 96 |
| 4.7. Summary | 100 |
| Chapter 5: Backscattered Electron Detectors and SNR | 104 |

| | |
|---|------------|
| 5.1. Introduction | 104 |
| 5.2. Backscattered Electron Detectors | 105 |
| 5.3. Shot Noise SNR Studies | 107 |
| 5.3.1. Calculating Shot Noise SNR | 107 |
| 5.3.2. SNR Requirements for X-ray Mask Inspection | 116 |
| 5.3.3. A SNR Comparison of Gold and Chrome Masking Material | 127 |
| 5.4. Relationship of Δ SNR to SNR | 129 |
| 5.5. Summary | 132 |
| Chapter 6: Mask Inspection Using an Electron-Beam System | 134 |
| 6.1. Introduction | 134 |
| 6.2. Optical and Electron-Beam Inspection | 134 |
| 6.2.1. Optical Inspection Techniques | 134 |
| 6.2.2. Electron-Beam Inspection Techniques | 136 |
| 6.3. Inspect Mask or a Copy of the Mask? | 138 |
| 6.4. Demonstrating Mask Inspection Using a Vector Scan Electron-Beam System | 139 |
| 6.5. A Mask Inspection System Using a Vector Scan Electron-Beam System | 145 |
| 6.6. Mask Inspection Experiments | 152 |
| 6.7. Software and Hardware Requirements | 163 |
| 6.7.1. Software Requirements | 163 |
| 6.7.2. Hardware Requirements | 164 |
| 6.8. Inspection Scanning Techniques | 165 |
| 6.9. Summary | 173 |
| Chapter 7: Conclusion | 175 |
| Appendix A: The Monte Carlo Simulation Program | 181 |
| A.1. Introduction | 181 |
| A.2. Program Operation | 181 |
| References | 191 |

CHAPTER 1

INTRODUCTION

A rapid and automated inspection system is a necessity for the detection of defects in x-ray and optical lithography masks. As masks become more complex and critical feature sizes shrink below one micron, the limits of optical inspection systems become apparent. Presently, it is impossible to reliably detect submicron defects in submicron mask patterns with commercial inspection systems. However, the use of an electron-beam lithography system, with its high resolution and overlay capabilities will make it possible to inspect submicron mask patterns for defects. Mask inspection is a natural extension of an electron-beam system since the data used to write the mask can be used to inspect it as well. Electron-beam techniques have been suggested and/or applied to mask inspection by several groups [1-6]. However, there has not been, to date, any fundamental work characterizing the backscattered electron signal properties from structures encountered during x-ray mask inspection.

This thesis will be concerned with the many different aspects which must be considered in using an electron-beam lithography system for x-ray mask inspection. Conceptually, the idea of using an electron-beam system to perform the mask inspection function is simple. Mask defects can be detected by a comparison of the backscattered electron signal from the mask with the design data used by the electron-beam system to write the mask. However, the design and implementation of a practical electron-beam mask inspection system requires the design and fabrication of test patterns, a complete analysis and understanding of the backscattered electron signal from different defect structures, a high speed backscattered electron detector, an algorithm to detect discrepancies between the backscattered electron signal and design data, electronics to perform the inspection function, and software to run the entire system.

The basic approach of this research has been to gain an understanding of the factors involved in implementing a practical electron-beam mask inspection system. The research has been broken up into several distinct phases. First, test patterns were designed on an IBM computer aided design (CAD) system to simulate the various types of defects which would be

encountered on an x-ray mask: indentations, protrusions, isolated holes, isolated pieces of masking material, bridge structures, and arrayed lines and spaces. A vector scan electron-beam lithography system [7] was used to pattern these shapes with designed minimum feature sizes ranging from 0.25 to 1.50 μm . Typically, x-ray masks are constructed of gold absorber patterns on a thin, 2-5 μm , low atomic number substrate [8-12]. Thus, the test patterns were fabricated as gold on silicon structures to simulate an x-ray mask or copy of an x-ray mask.

The presence or absence of masking material must be detected in some way. Low energy (< 50 eV) secondary electrons, generated near the surface by the inelastic scattering of primary and backscattered electrons with loosely bound outer electrons, are often used to form images in scanning electron microscopes (SEM's) [13-15]. Secondary electrons yield topographical information since they are generated near the surface of the structure. High energy backscattered electrons have also been used in SEM's [16-18] and are widely accepted for use in electron-beam lithography systems for detection of registration marks [19-21]. Backscattered electrons are produced by the elastic scattering of the incident electrons with the nuclei of the target material or with the electron clouds surrounding the nuclei. The energy of backscattered electrons can range almost up to the incident beam energy and also yield information about the material make-up of the target structure.

Backscattered electrons are desirable for registration in electron-beam systems since they allow for the detection of registration marks through resist or other process related planarizing coatings [19-21]. Backscattered electrons are also favored in lithography systems for a very practical reason - backscattered electron detectors are simple to install inside the electron-beam chamber and do not require large (kV range) bias voltages. These high voltages create electric fields which can negatively influence the electron-beam as it is writing a pattern. As far as x-ray mask inspection is concerned, backscattered electrons are also favored because of the larger signal difference between high and low atomic number materials as compared to secondary electrons [22]. For these reasons backscattered electron signals have been chosen to be used in the mask inspection system studies described in this thesis.

An in depth understanding of the backscattered electron signal from the various structures encountered during x-ray mask inspection is therefore necessary in order to achieve the best possible signal for comparison to design data. This has been accomplished in the second phase of the research. This phase involved a study of the various characteristics of the backscattered electron signal. A new Monte Carlo simulation program [19,23] was written to study the effects of gold thickness, electron-beam size, electron-beam voltage, and backscattered electron collection range (or detector placement) on the quality of the signal from different structures. Good agreement with experimental backscattered electron signals gave confidence in using the Monte Carlo program for the studies outlined in this thesis.

The third phase of this research involved developing an algorithm which would enable the backscattered electron signal from the mask pattern to be compared with the design data. A technique, similar to the method described by Simpson and Davis [4], was demonstrated on an IBM vector scan electron-beam system [6,7]. In this experiment, the inspection was accomplished by scanning the electron-beam over all areas where there was gold. During this scan, the backscattered electron signal should have always remained high. If the signal went low, a clear defect or hole in the gold had been detected. A similar method was used to detect opaque defects (gold in designed clear areas). From this study and further experiments, a mask inspection system for implementation on a vector scan electron-beam system has been designed.

Chapter 2 will discuss the design and fabrication of the test structures used in the backscattered electron signal studies as well as in the mask inspection studies. Submicron gold on silicon structures were fabricated using a simple single layer resist process, a vector scan electron-beam lithography system [7], and electroplating.

Chapter 3 deals with the Monte Carlo simulation program written to gain an understanding of the scattering properties from a variety of two dimensional structures. Simulated backscattered electron signals show good agreement with experiment demonstrating that the simulation program will be a very useful tool in the analysis of backscattered electron signals for mask inspection.

Chapters 4 and 5 are Monte Carlo studies of the backscattered electron signal from different structures. In Chapter 4, Monte Carlo analysis is used to optimize the placement of the backscattered electron detector used in the experimental studies. The effects of incident electron-beam size and different take-off angle ranges on the signal are also discussed in a quantitative manner. The required gold thicknesses and effects of scanning near the edge of a shape as a function of beam voltage are investigated. Results are presented in the form of universal curves with distance units normalized to the range of the incident electrons in the material. Finally, a simple calculation technique is outlined to predict the signal levels from simple three dimensional defect structures.

Chapter 5 discusses the detector requirements in an electron-beam inspection system and investigates the fundamental shot noise limitations to high speed inspection. It is seen that shot noise will not fundamentally limit the speed of inspection for most electron-beam systems if the comparator threshold used for determining the presence or absence of masking material is set correctly for the minimum sized clear and opaque defects.

Chapter 6 begins with an overview of present optical and electron-beam mask inspection systems. A method of mask inspection using a vector scan electron-beam system will be demonstrated. An algorithm to perform the inspection function using an electron beam system will be discussed and hardware and software requirements are listed. Finally, different scanning techniques are investigated in order to speed up the inspection process. The main body of the thesis ends with Chapter 7, which is a conclusion.

Appendix A contains a short description of the operation of the Monte Carlo program and input and output examples.

CHAPTER 2

2. FABRICATION OF INSPECTION TEST PATTERNS

2.1. Introduction

It is important in the development of an electron-beam system for mask inspection to investigate the characteristics of the backscattered electron signal. This can be accomplished with experimental studies as well as with Monte Carlo simulation techniques. Computer simulation, if accurate, is the preferred approach since the parameters of interest are well known and easily adjusted. Thus, test patterns were designed and fabricated to experimentally verify the simulated results from the Monte Carlo simulation program developed for this research. Another important use for the test patterns was to investigate different mask inspection algorithms for the comparison of the backscattered electron signal to design data. In other words, it was desired to fabricate a group of patterns whose sole purpose was to be used for the studies outlined in this thesis.

The test patterns were fabricated as gold on silicon structures because the large atomic number difference, or material contrast, between gold and silicon allows the presence or absence of gold to be easily detected with backscattered electrons. Backscattered electrons are preferred since the change in secondary electron yield with increasing atomic number is much smaller than the backscattered electron yield [14,24]. As we shall see, high speed inspection requires a significant difference between high (presence of masking material) and low (absence of masking material) signal levels for adequate signal to noise characteristics. Also, gold on silicon is somewhat similar to the materials used in x-ray mask fabrication and is easy to process. As will be discussed in Chapter 6, it may be desirable to inspect a copy of the x-ray mask made using x-ray lithography. The logical choice for such a copy would be gold on silicon.

2.2. Design

Inspection test patterns were designed to simulate the various types of defects which are likely to be found on a mask. These patterns, shown in Figure 2.1, include isolated and arrayed lines and contact squares, protrusions, indentations, and bridge structures. The negative, or inverse, images of these shapes were also designed so that both clear and opaque defects could be investigated. These patterns were designed on an IBM CAD system with minimum feature sizes ranging from 0.25 to 1.50 μm .

2.3. Programmed Defects

Since inspection will consist of a comparison of design data to the backscattered electron signal, pseudo or programmed defects can be introduced by changing the design data. The programmed defect concept is illustrated in Figure 2.2 [6]. The original CAD design is fabricated as a gold on silicon structure. Then the original design is altered in the CAD system so that several features are modified. When this modified design is used for inspection, programmed defects should be detected wherever the original design was changed. Thus, the precise locations of the programmed defects are known before testing the inspection system. Also, since a wide range of minimum feature sizes and structure types were fabricated on the test patterns, the size and type of defects can be programmed. The use of programmed defects eliminates the need to rely on random process related defects in the testing of a mask inspection system.

2.4. Fabrication Process

The techniques used in fabricating the test patterns are relatively simple. A [100] silicon wafer coated with 0.01 μm chrome and 0.03 μm gold plating base was used as the starting material. A thin 0.65 μm layer of PMMA 2010 (10 percent in chlorobenzene) was spun on and the wafer was then baked at 160 °C for 30 minutes. The wafer was then exposed with a dose of 100 $\mu\text{C}/\text{cm}^2$ using an IBM vector scan electron-beam lithography system [7]. All pattern data was proximity corrected using internal IBM proximity correction computer programs.

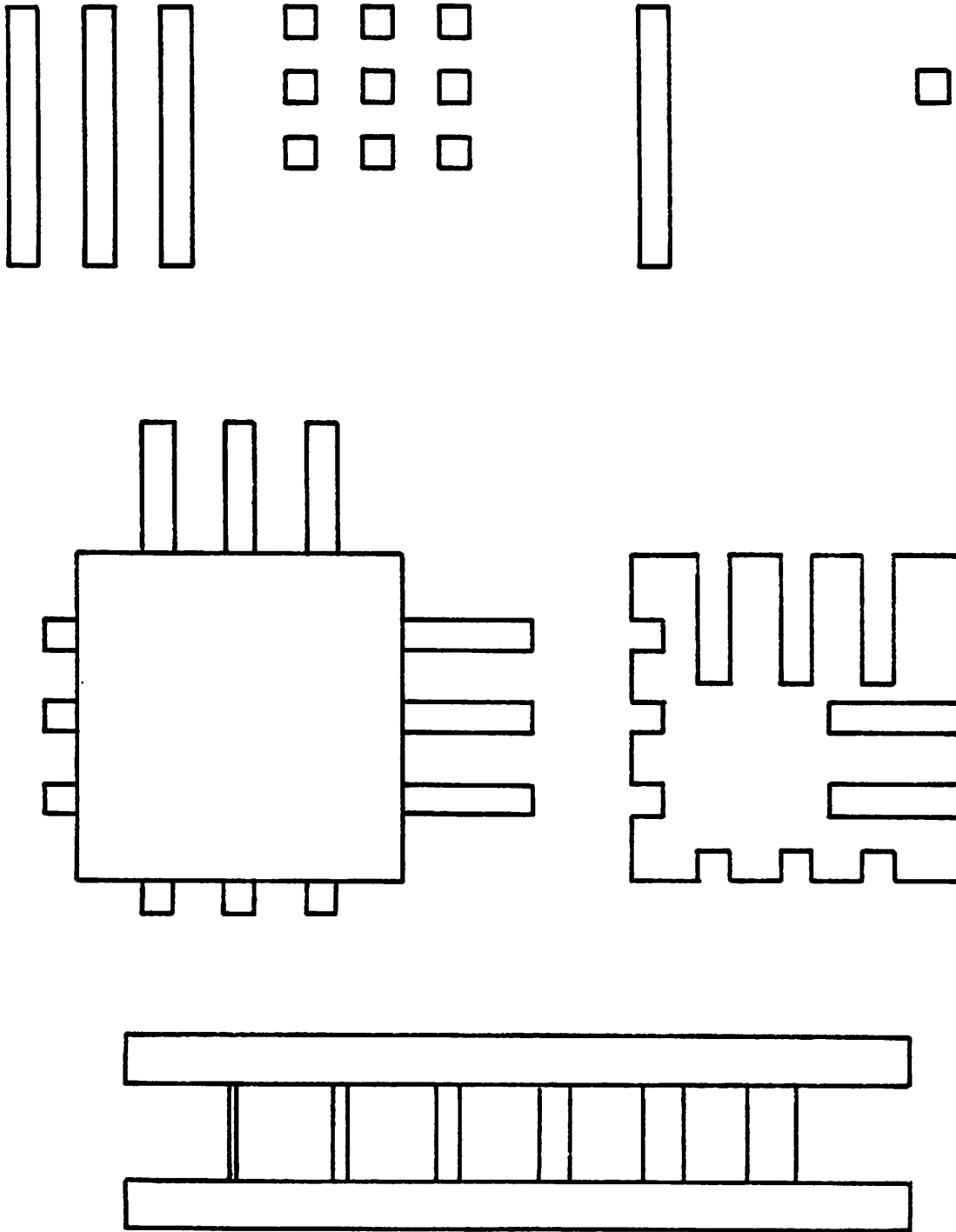


Figure 2.1. Mask inspection test patterns.

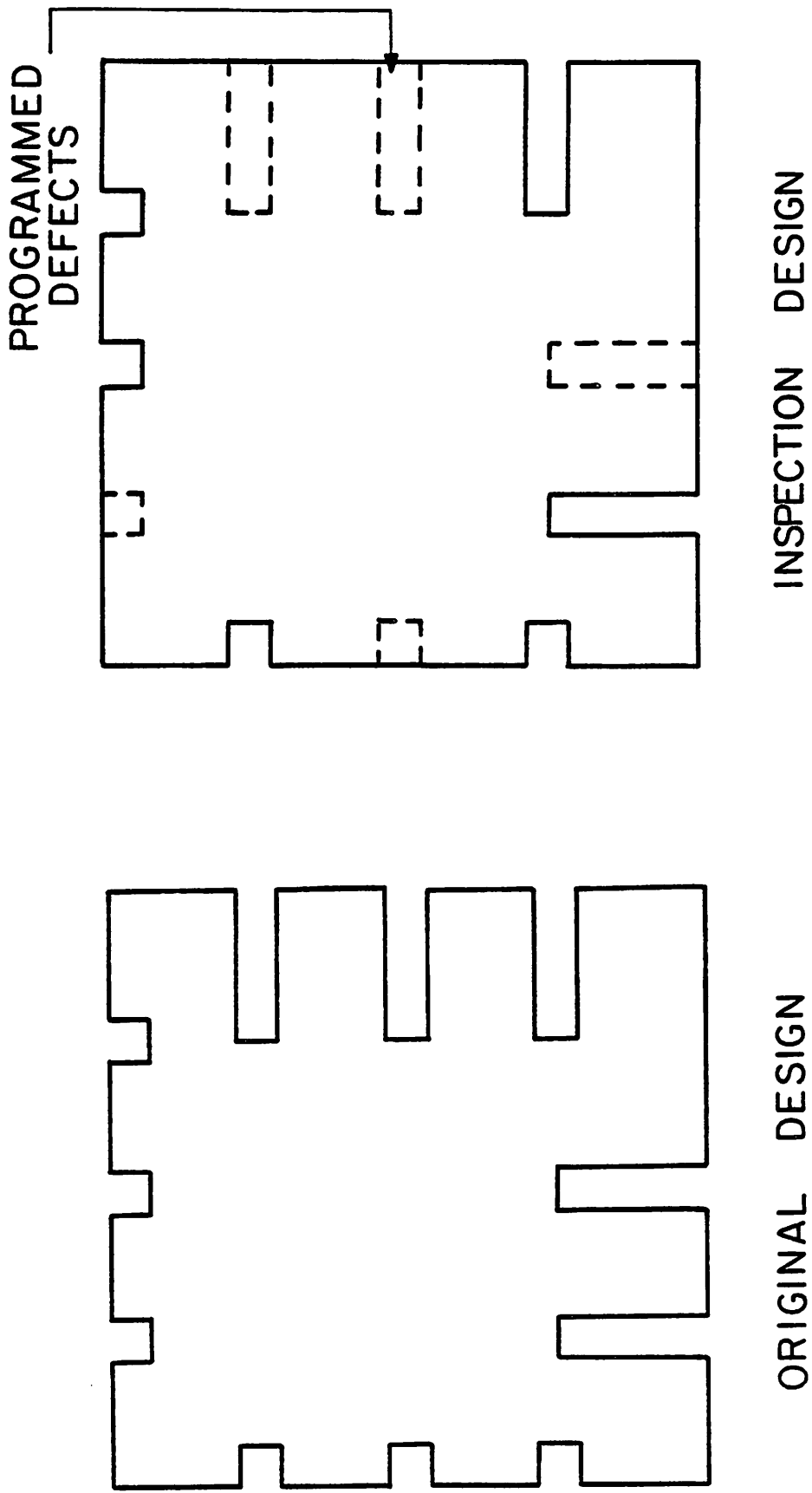


Figure 2.2. The concept of programmed defects.

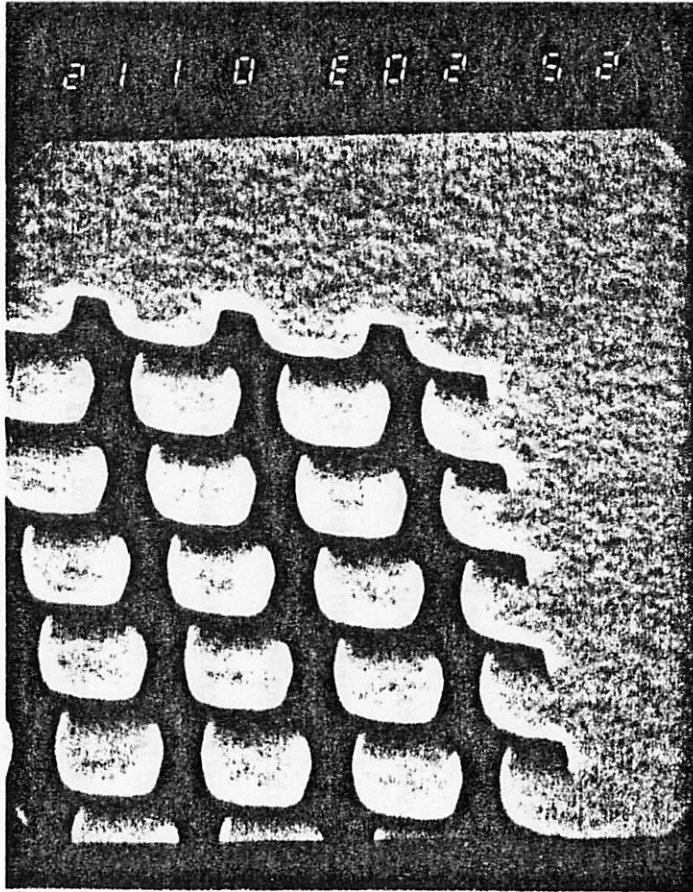
Development was performed in a 1:2 MIBK:IPA solution and monitored using an exposure wedge [25]. The developed patterns were etched for several minutes in an oxygen plasma (50 W, 0.1 torr oxygen) to remove debris at the plating base surface. The wafer was then electroplated in a standard commercially available electroplating solution and the resist was stripped. A short ion milling removed the plating base leaving the gold on silicon structures.

Figures 2.3-2.5 are SEM micrographs of some of the fabricated patterns. Note the square contacts and very straight submicron lines fabricated using the electron-beam lithography system. Sidewalls are fairly vertical and various gold thicknesses, ranging from 0.11 to 0.55 μm were fabricated.

It was found, using the single layer resist technique outlined above, that the actual pattern dimensions were approximately 0.25 to 0.30 μm larger than the designed pattern dimensions. In other words, there was about 0.25 to 0.30 μm of process bias because of the over development required to fabricate vertical sidewalls [26]. Thus, the smallest isolated gold structures had minimum dimensions of about 0.50 μm (Figure 2.4) because of the bias. However, the bias also caused the fabrication of very small (on the order of 0.1 μm) holes in the gold film (Figure 2.5).

Process bias can be significantly reduced by the use of multi-layer resist techniques [27-29] in which imaging is done in a very thin 0.2-0.4 μm top layer of resist. A trilevel scheme of PMMA/polysiloxane/AZ1350J was developed to fabricate smaller features [30]. The process consisted of exposing the thin top layer of PMMA, reactive ion etching the siloxane with a CF_4 plasma, and then reactive ion etching through the AZ1350J with O_2 . Figure 2.6 shows some submicron resist patterns obtained with this process. The sizes of the structures were the same as the designed feature sizes. The reticulated material in the micrographs is the siloxane after the O_2 etch. The structures fabricated using the the simple single layer PMMA process were found to be adequate for the studies conducted for this research. However, if gold structures with much greater than a 1:1 height to width aspect ratio are desired, a multilevel resist scheme such as the one outlined in this chapter is essential for reproducible results.

Figure 2.3. SEM micrographs of some of the gold on silicon test structures. Note the vertical sidewalls. Gold thickness is $0.46 \mu\text{m}$.



1 μm

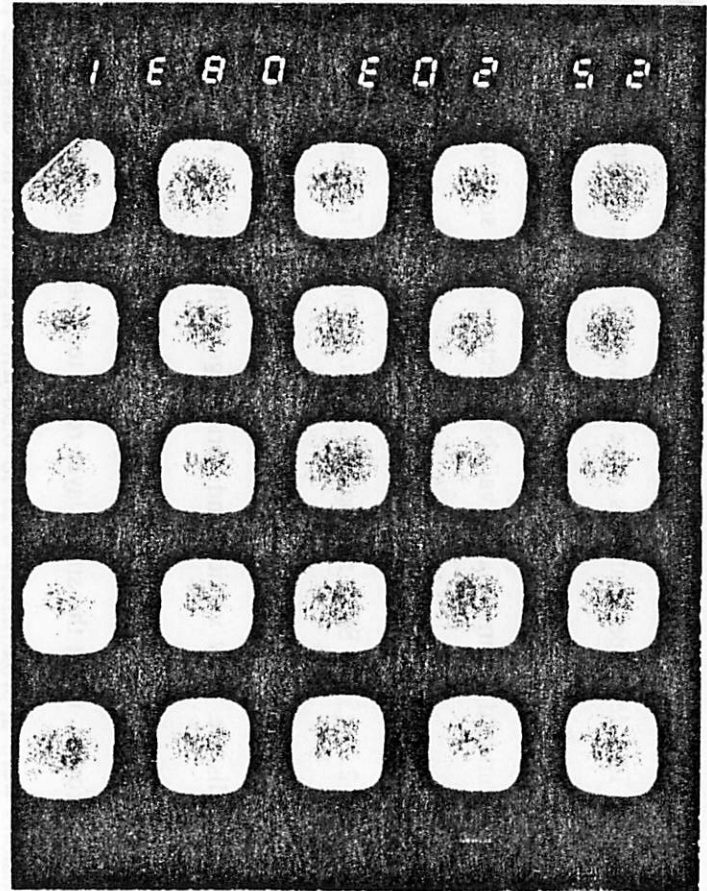
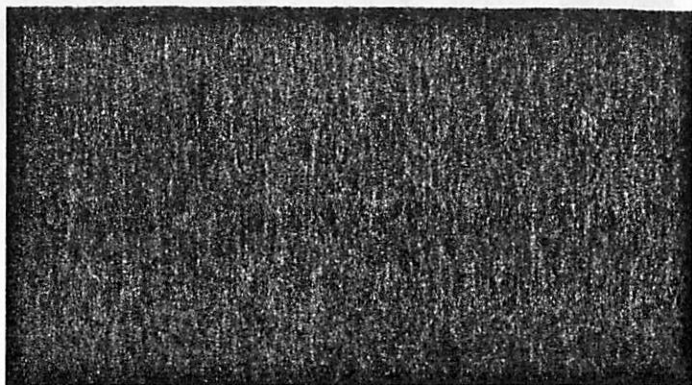
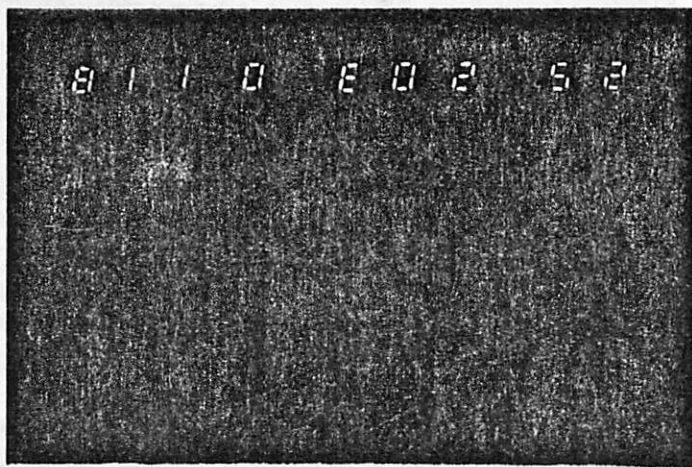


Figure 2.4. SEM micrographs of some of the gold on silicon test structures. The gold line in the bottom micrograph is about $0.5\ \mu\text{m}$ wide. Gold thickness is $0.46\ \mu\text{m}$.



1 μm

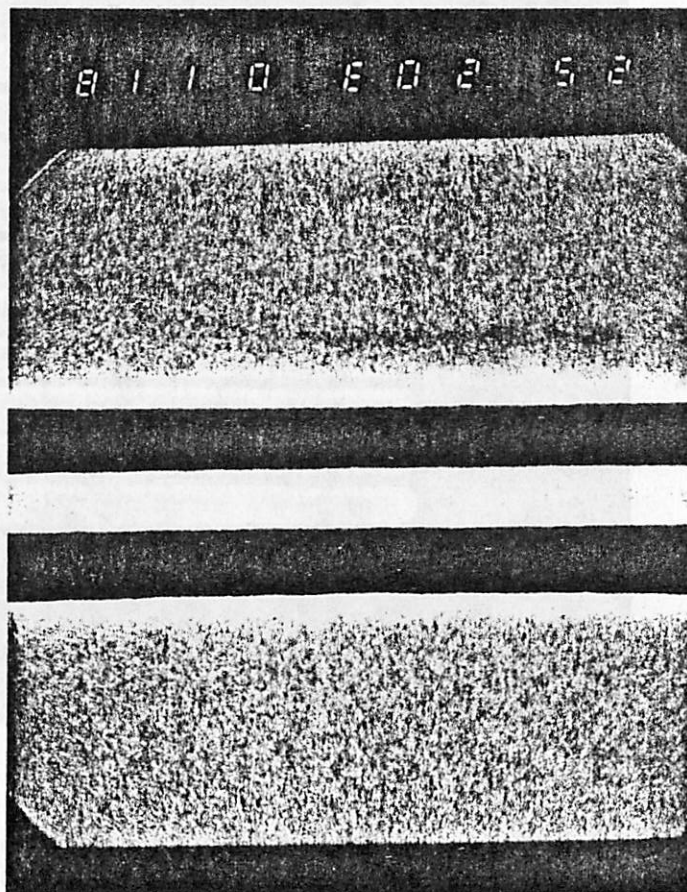
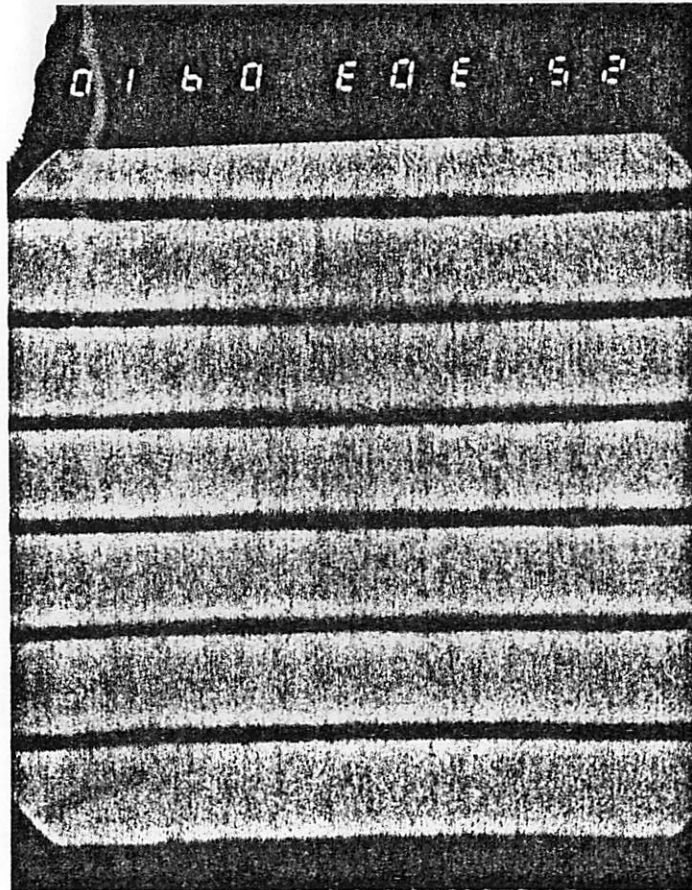
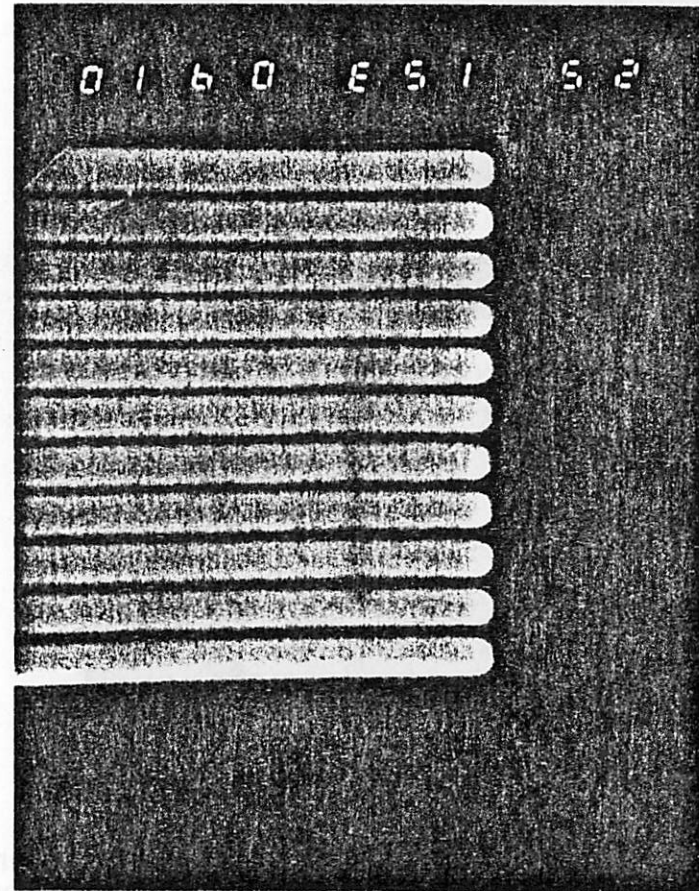


Figure 2.5. SEM micrographs of some of the gold on silicon test structures. The gaps between the gold lines are less than $0.1 \mu\text{m}$ wide. Gold thickness is $0.46 \mu\text{m}$.

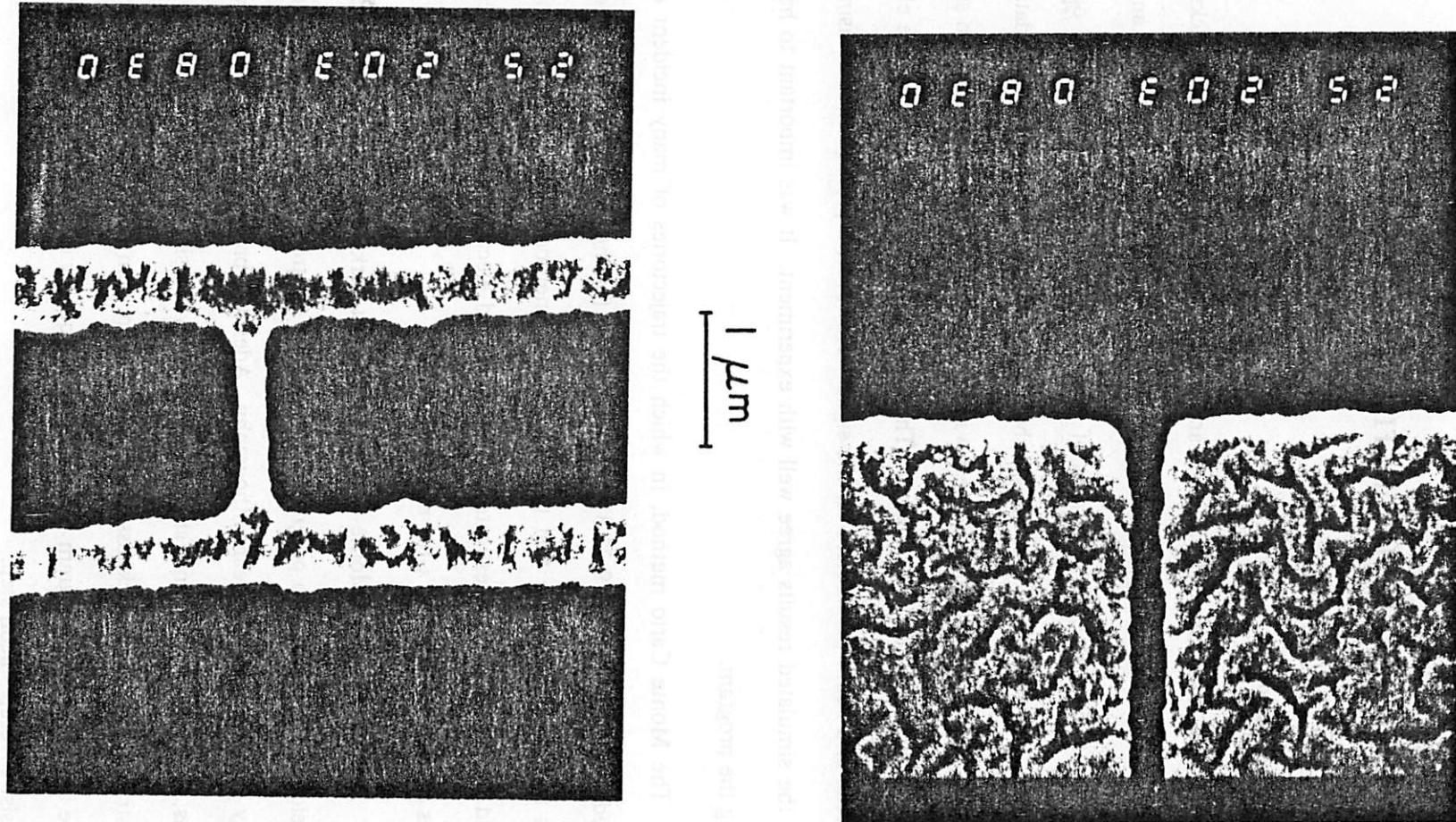


1 μm



1 μm

Figure 2.6. SEM micrographs of resist structures fabricated with a trilevel technique. Minimum dimensions are about $0.25\ \mu\text{m}$. Resist thickness is about $0.7\ \mu\text{m}$.



CHAPTER 3

3. MONTE CARLO SIMULATION PROGRAM

3.1. Introduction

A mask inspection system using an electron-beam system will use a backscattered electron signal to determine the presence or absence of masking material. Thus, an in-depth understanding of the scattering properties of the defects is necessary in order to optimize the backscattered electron signal which will be compared to the mask design data. Early in this research, it was decided that the best way to study the backscattered electron signal would be to use an accurate simulation program. Thus, it would be easy to examine the effects of different material and beam parameters on the signal. However, a prerequisite for using simulation was that the simulated results agree well with experiment. It was important to have confidence in using the program.

The Monte Carlo method, in which the trajectories of many incident electrons are followed through a target [19,23,31-41], was chosen for the simulation technique. The main reasons for this choice were that the Monte Carlo method is fairly well documented and that it could be modified to investigate the backscattered electron signal from the complicated structures encountered during x-ray mask inspection.

A short history of Monte Carlo simulation at Berkeley seems to be in order. Adesida [31] developed a Monte Carlo program to investigate electron scattering and the reduction of proximity effects in electron-beam lithography. Adesida's program simulated the backscattered electrons, transmitted electrons, and absorbed energy density in a planar layer of PMMA resist on substrates of variable thicknesses and composition. Lin [19] used parts of Adesida's program to write a Monte Carlo program to investigate the quality of electron-beam alignment signals from a resist covered silicon step.

Stephani and others not at Berkeley have also used Monte Carlo techniques to study the registration signals from simple structures [33,34]. Hembree et al [34] have used a Monte Carlo program to look at submicron linewidth measurement in the SEM and George and Robinson have used the method to investigate contrast in the SEM [35]. However, the inspection of x-ray masks requires an understanding of the backscattered electron signal from submicron structures which exhibit material as well as the topographical contrast seen in registration marks. Moreover, it is necessary to understand the relationship of incident electron-beam size, incident beam energy, collection angle range, gold thickness, and defect type to the quality of the backscattered electron signal.

3.2. The Monte Carlo Program

A new Monte Carlo computer program has been developed to simulate the backscattered electron signal from a variety of two-dimensional gold on silicon structures expected to be encountered during x-ray mask inspection. The program uses the standard continuous slowing down approximation with the screened Rutherford collision cross-section and Bethe energy loss equation [19,23]. The program, written in Fortran 77, uses some of the techniques introduced by Lin [19,41] to keep track of the electron as it scatters into different areas of the target structure. Whereas Lin's program calculated the backscattered electron signal from an infinitely long long resist covered silicon step, this new program is used to simulate the backscattered electron signal from three independent, infinitely long, variable width, variable edge slope, gold lines on a silicon substrate. Through appropriate placement of the three gold on silicon lines, the backscattered electron signal from different types of defects typically found on x-ray masks or mask copies can be simulated. Although gold on silicon was primarily simulated, other combinations such as PMMA on gold or chrome on silicon can be specified. Appendix A contains a more detailed description of the operation of the program as well as input and output examples.

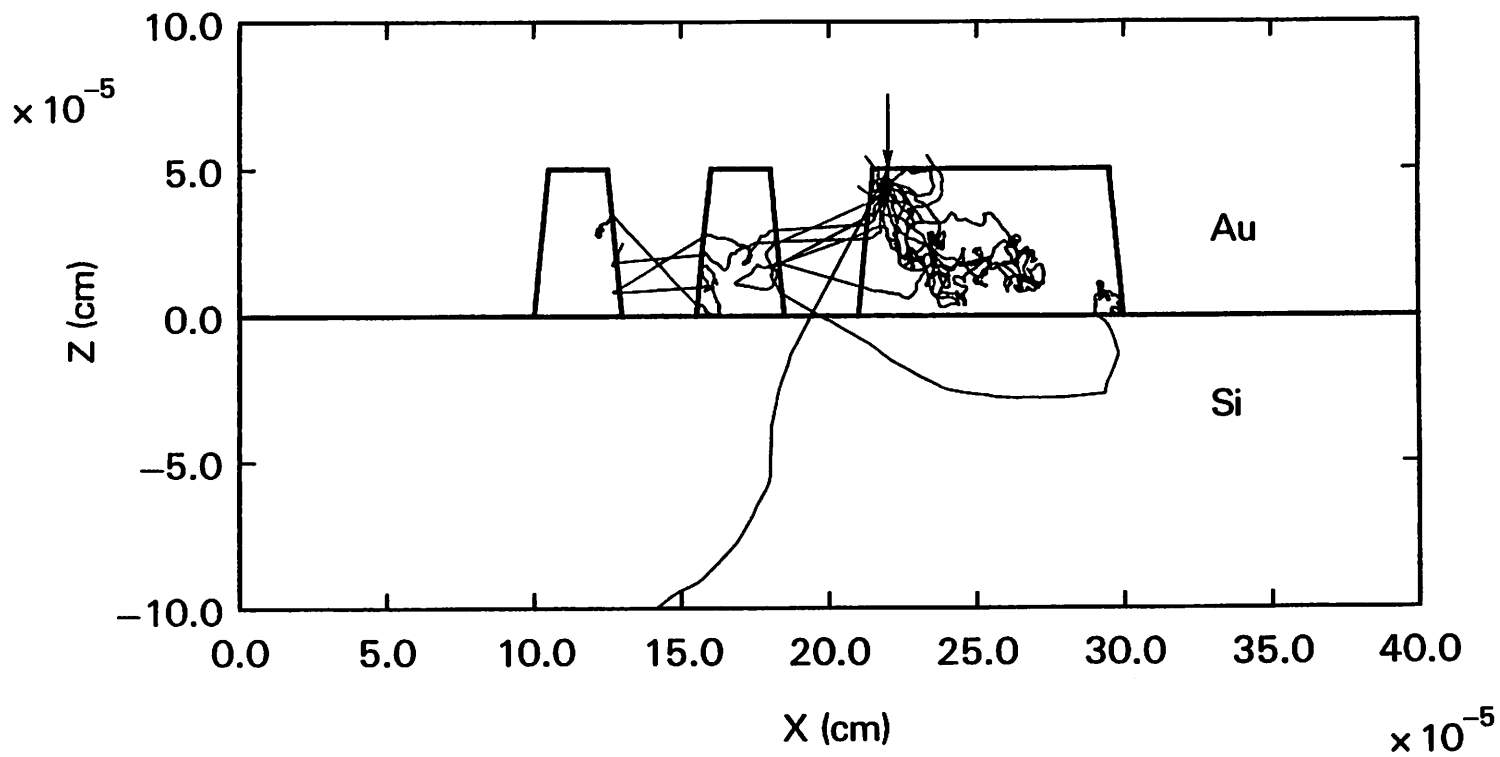
As is well known, the Monte Carlo technique involves tracking many electrons incident from a zero width δ -function electron-beam as they scatter through the target. An example

which illustrates the program's capabilities is shown in Figure 3.1, a plot of 15 electron trajectories projected onto the x-z plane. The target is composed of two $0.25 \mu\text{m}$ full width at half-maximum (fwhm) gold steps and a $0.85 \mu\text{m}$ fwhm gold step separated by $0.3 \mu\text{m}$. The four backscattered electrons in this example can clearly be seen. The energy, take-off angle, azimuthal angle, and position of each backscattered electron is stored and the resulting total energy and number distribution of backscattered electrons are output for the take-off angle, azimuthal angle, and backscatter energy [19, see Appendix A].

A backscattered electron signal for a given structure is calculated by first simulating the δ -function signal. This is done by stepping the position of the incident beam in small ($.0125$ -. $05 \mu\text{m}$) steps over the structure. This process is illustrated in Figure 3.2. Figure 3.2a shows the Gaussian beam shape used in most of the simulations and also a rectangular beam shape whose use will be discussed later in this chapter. Figure 3.2b shows the δ -function electron-beam stepped over the target and also the convolution of the δ -function beam with the Gaussian beam shape. This simulates the actual finite sized electron-beam scanning over a target. Note how symmetry of the structure necessitates only one half of the signal being calculated. The advantage of this approach is that the δ -function response can be convolved with a variety of beam sizes and shapes. For the experiments to be described here, a Gaussian beam shape was assumed. To save computer time, symmetry was used whenever possible. For the simulations in this paper, 5000-10000 electrons per incident δ -function electron-beam were used. The calculations were mostly performed on an IBM 3081 computer. The required CPU time is approximately 1 minute per 1000 trajectories for a 25 kV incident beam voltage.

The δ -function signal for a given target consists of typically twenty to thirty output files of the type shown in Appendix A. Thus, a tremendous amount of data describes the signal from even a simple structure. A graph of the backscattered electron signal from a structure is made by first adding up the electrons or electron energy which strike the backscattered electron detector. This partial δ -function signal must then be convolved with a given beam shape and the output must be put into a format suitable for plotting. The process of adding up the electrons

Figure 3.1. An example of the Monte Carlo program's capabilities.

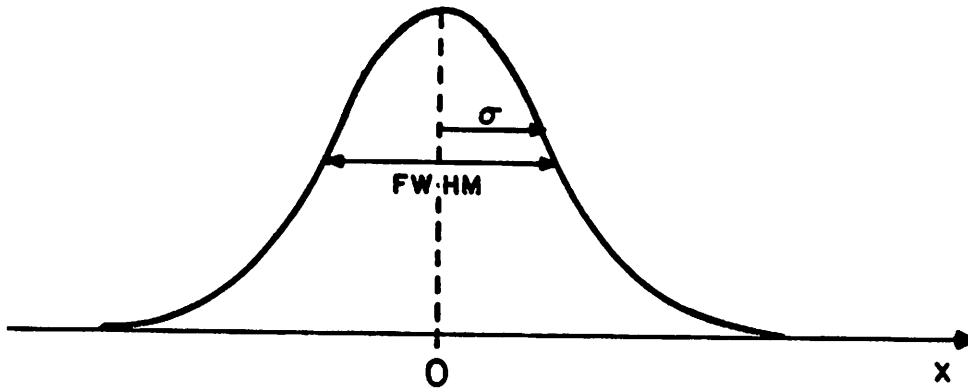


MONTE CARLO SIMULATION OF ELECTRON TRAJECTORIES

Au thickness = .50 μm , beam energy = 25 kV

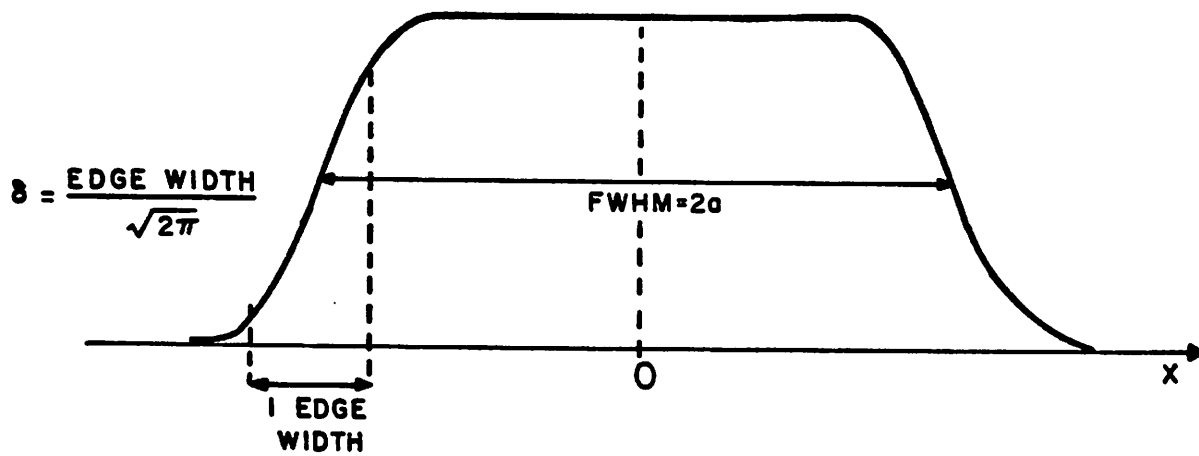
15 incident electrons at $x = 2.20 \mu\text{m}$

GAUSSIAN ROUND BEAM



$$F(x) = Ke^{-x^2/2\sigma^2}$$

RECTANGULAR SHAPED BEAM



$$f(x) = K \left\{ \operatorname{erf}[(a-x)/\sqrt{2\delta}] + \operatorname{erf}[(a+x)/\sqrt{2\delta}] \right\}$$

Figure 3.2a. Beam shapes used in the simulations.

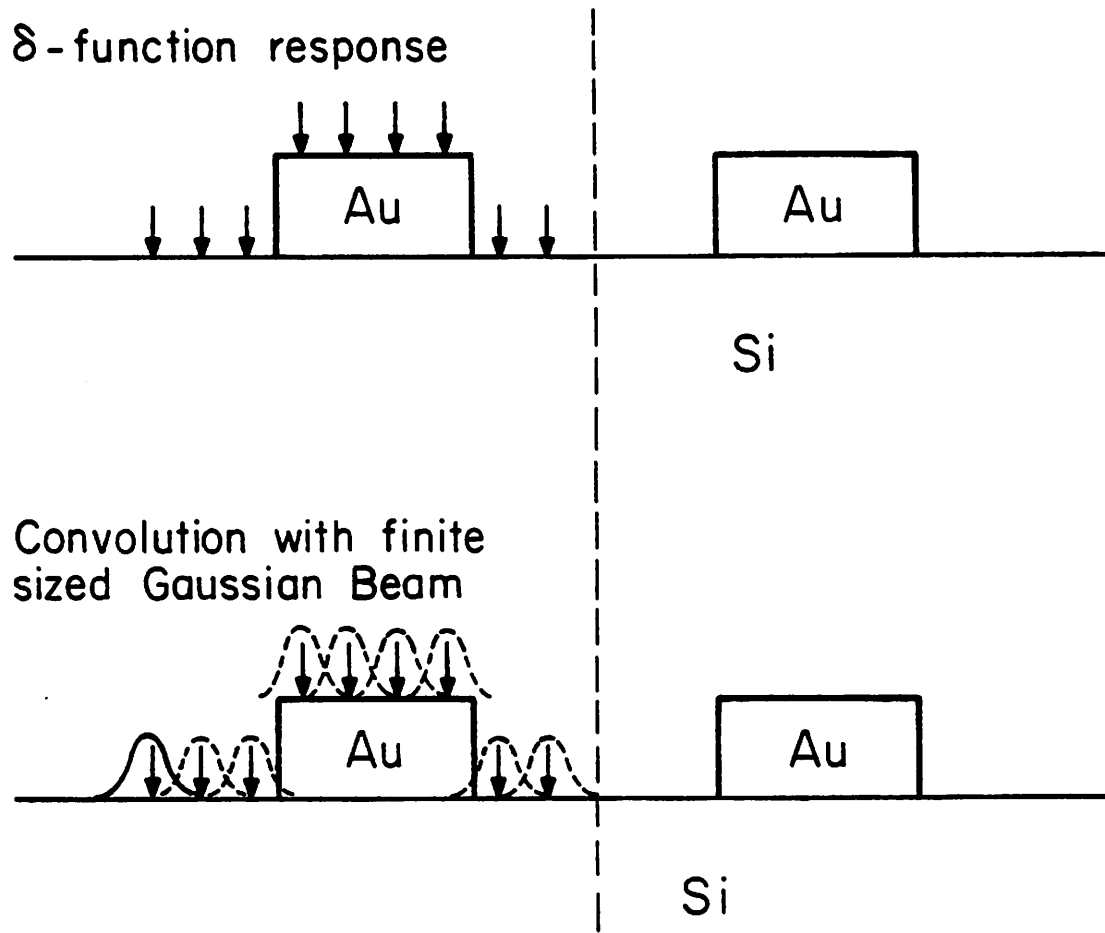


Figure 3.2b. The process of simulating a backscattered electron signal. First calculate the δ -function response. Then convolve with the desired beam shape. Typically, the beam size will be much larger than the spacing between δ -function electron-beams.

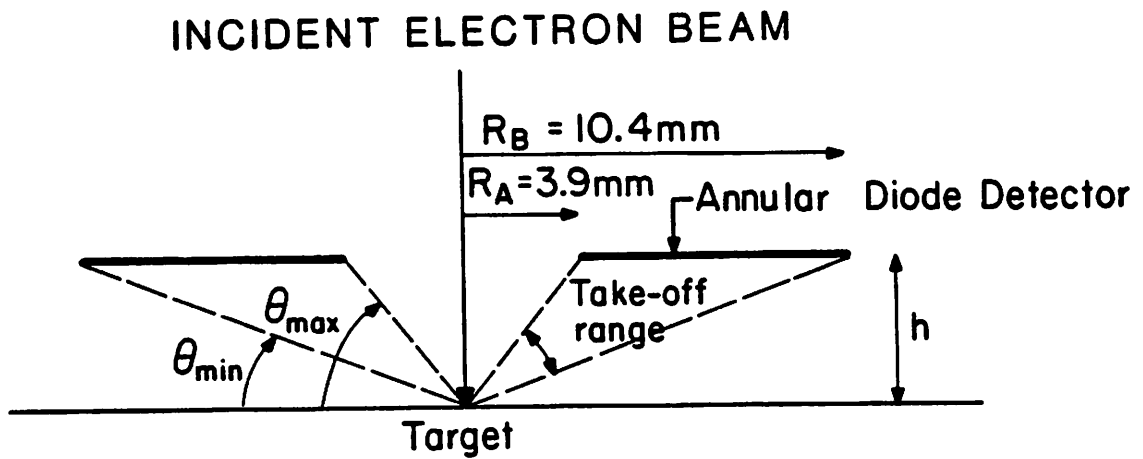
striking the detector is too time consuming to be done by hand. It is for this reason, and also to have the option of processing the data in different ways, that the output file of the Monte Carlo program can be read in as an input file to an external post-processing program. This post-processor can read in the files describing the δ -function signal, selectively pick out the desired information, and put the processed signal into plotting format. Another post-processor was written to take a given δ -function signal, convolve it with different beam sizes and/or shapes, quantitatively analyze the resultant backscattered electron signals, and put the results in plotting format. These external post-processors consist of Fortran 77 programs linked by EXECs in IBM's CMS operating system. The reason for developing these post-processors was to automate the analysis as much as possible in order to be able to investigate the many different parameters which affect the backscattered electron signal.

3.3. Comparison of Simulation to Experiment

It is important in the development of any simulation program to show that there is good agreement with experimental results. In this study, backscattered electron signals were experimentally measured using an annular silicon diode detector (GW Electronics Type 113), Figure 3.3, in an IBM vector scan electron-beam machine [7]. Gold on silicon structures, whose fabrication was outlined in Chapter 2, were used in the experiments to represent typical mask defects. The take-off angle ranges used in the experiments were measured to be approximately 35-62.5 and 55-75 degrees as measured from the plane of the wafer. This corresponds to the detector being at heights of 7.4 and 15 mm, respectively, above the wafer (Figure 3.3). A beam current of 1.5 nA and a SEM scan rate of 10 msec/line were used in all the experiments. The gain and contrast settings of the diode amplifier were kept the same throughout the experiments by using the pattern of Figure 3.4a at 25 kV and 35-62.5 degrees as a reference.

Two types of simulated signals were calculated: (1) The energy signal was evaluated by adding up the total backscattered energy into the desired take-off angle range and then normalizing this quantity to the total input energy for a 25 kV electron beam. (2) The number signal

BACKSCATTERED ELECTRON DETECTOR



Experimental h

7.4 mm

15 mm

Take-off range

35-62.5°

55-75°

Figure 3.3. The backscattered electron detector used in the experiments.

was calculated by simply adding up the electrons which scatter into the desired take-off angle range and normalizing to the total number of incident electrons. A Gaussian beam fwhm of $0.2 \mu\text{m}$ was used in all the simulations. A SEM analysis of the experimental gold on silicon structures showed approximately vertical sidewalls; therefore, 90 degrees gold sidewalls were used in all the simulations.

Figure 3.4 shows the experimental and simulated backscattered electron signals from different structures for the two experimental take-off angle ranges. Figure 3.4a shows the signals from two $0.7 \mu\text{m}$ holes in gold separated by a $0.7 \mu\text{m}$ gold step and Figure 3b shows the signals from an isolated $0.55 \mu\text{m}$ gold on silicon step. Figure 3.4c is a comparison for two $0.85 \mu\text{m}$ gold on silicon steps separated by a $0.5 \mu\text{m}$ space and Figure 3.4d shows the signals from a $0.25 \mu\text{m}$ hole in a gold film. The gold thickness is approximately $0.46 \mu\text{m}$ and the beam voltage is 25 kV for these cases. Figure 3.4e shows the signals from two $0.6 \mu\text{m}$ holes in a $0.2 \mu\text{m}$ thick gold film separated by a $0.6 \mu\text{m}$ step at 25 kV. Figure 3.4f is the same as Figure 3.4c except that the beam voltage has been reduced to 15 kV.

Good qualitative agreement between simulation and experiment was obtained for the two take-off angle ranges, different gold thicknesses, and different beam voltages. For example, the simulation correctly predicts that the low signal levels in Figures 3.4a and 3.4d are smaller than the low levels in Figures 3.4b and 3.4c. This is because most of the electrons are being trapped under the gold when the beam passes over the holes. The simulation also correctly predicts that the signals are reduced at the higher take-off angle range.

Signal contrast was used to quantitatively compare simulation and experiment. The contrast is defined as:

$$C = \frac{S_{\max} - S_{\min}}{S_{\max} + S_{\min}} \quad (3.1)$$

Note that it is independent of the diode amplifier gain and DC level setting. Figure 3.5 gives a comparison of experimental and simulated contrasts for the various structures. The energy and number signal contrasts are listed for the simulations. As can be seen, the agreement between

Figure 3.4a.

Comparison of experimental and simulated backscattered electron signals. Gold thickness is about 0.46 μm . Two 0.7 μm holes in gold separated by a 0.7 μm gold step.

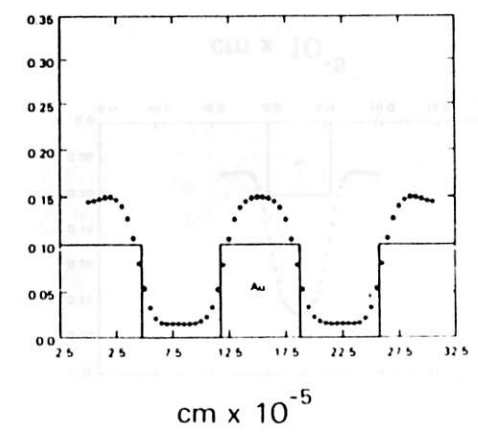
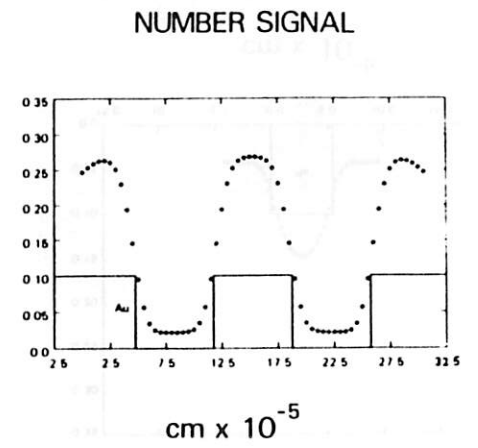
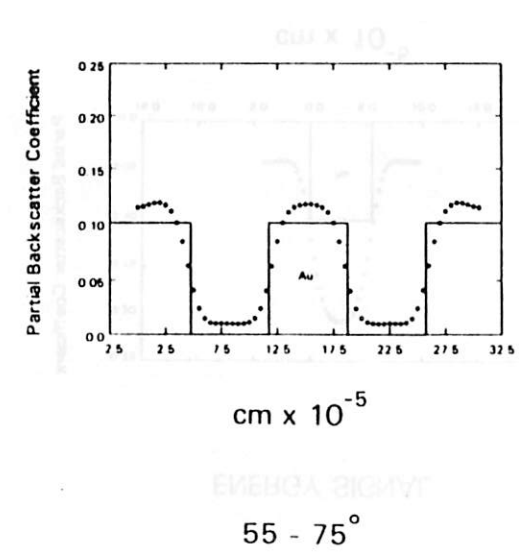
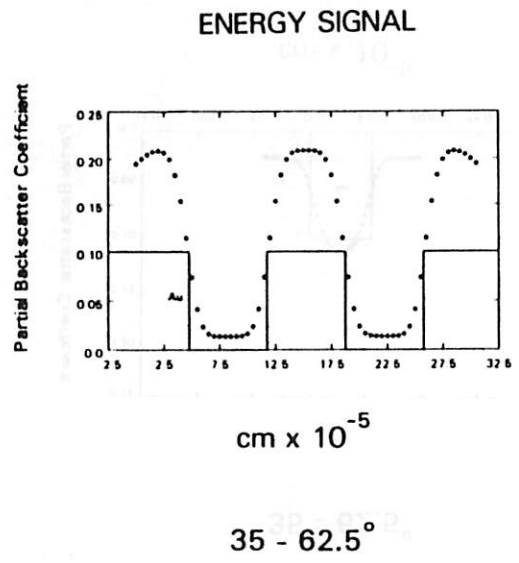
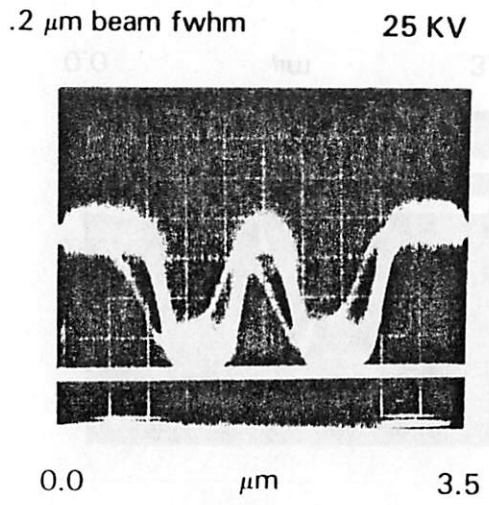
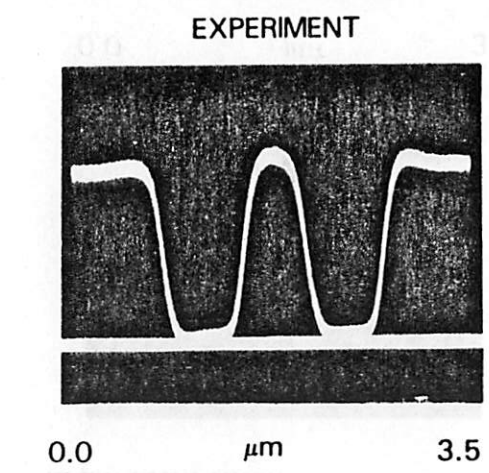


Figure 3.4b. Comparison of experimental and simulated backscattered electron signals. Gold thickness is about 0.46 μm . Beam voltage is 25 kV. A 0.55 μm gold step on silicon.

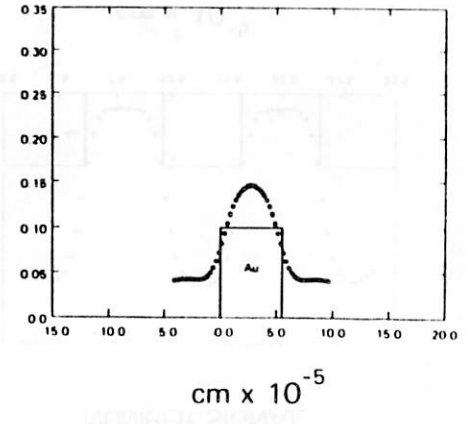
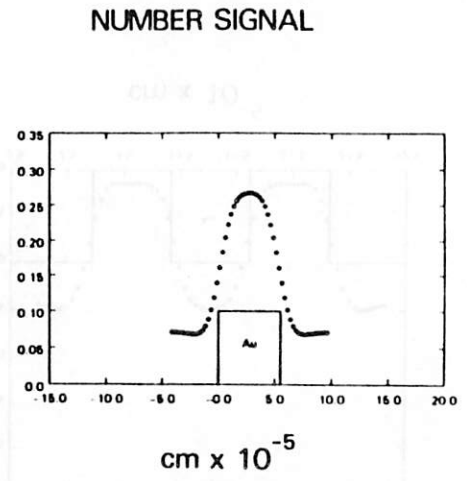
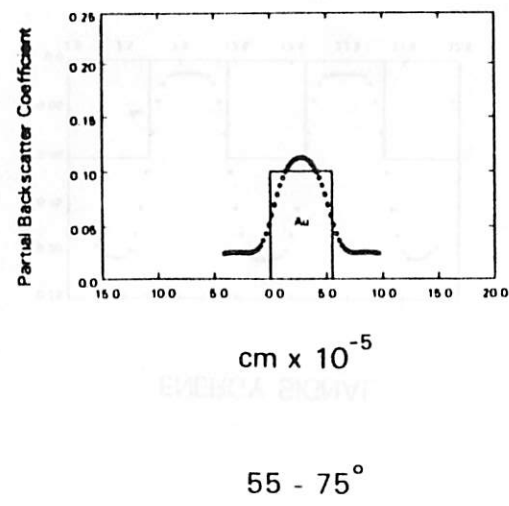
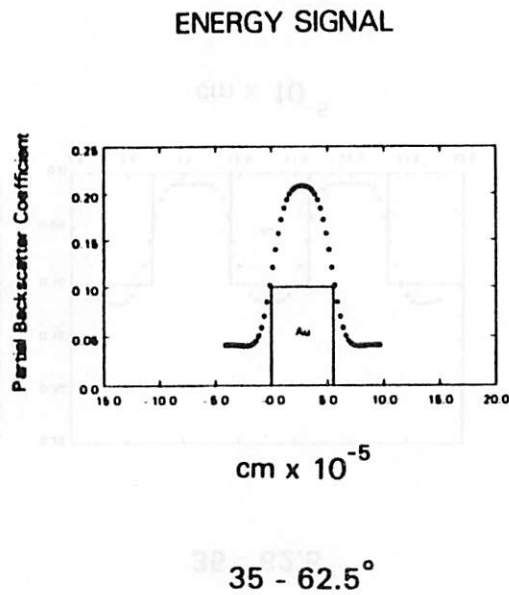
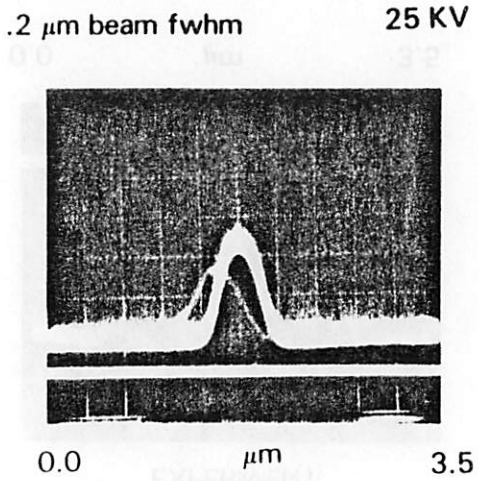
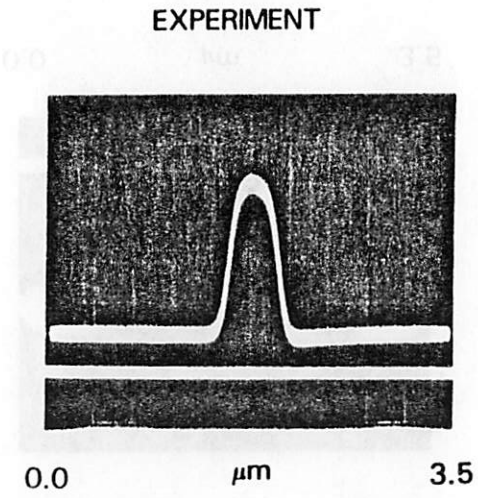
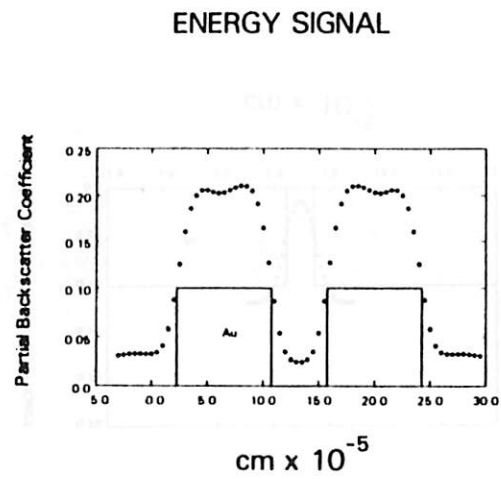
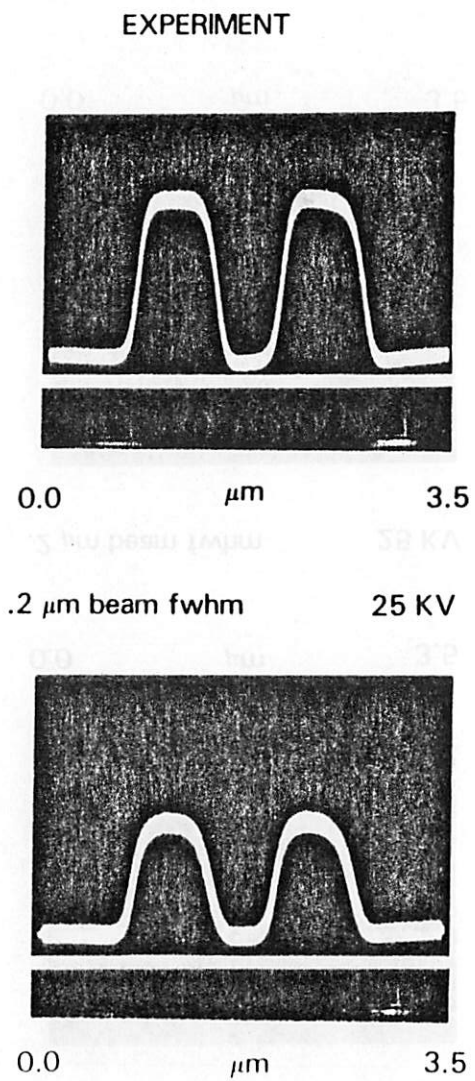
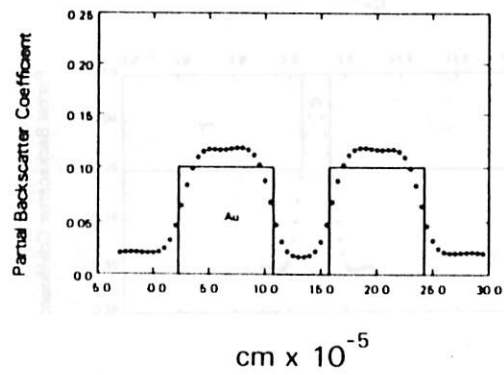


Figure 3.4c. Comparison of experimental and simulated backscattered electron signals. Gold thickness is about $0.46 \mu\text{m}$. Beam voltage is 25 kV. Two $0.85 \mu\text{m}$ gold steps on silicon separated by a $0.5 \mu\text{m}$ space.



$35 - 62.5^\circ$



$55 - 75^\circ$

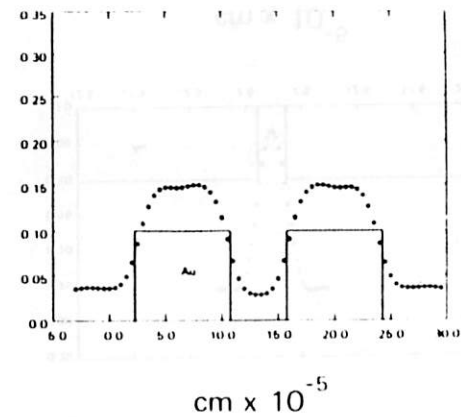
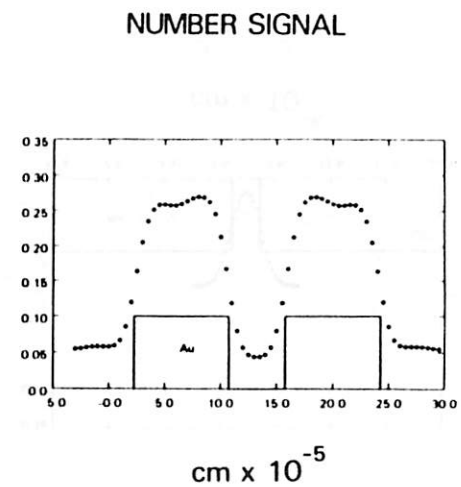
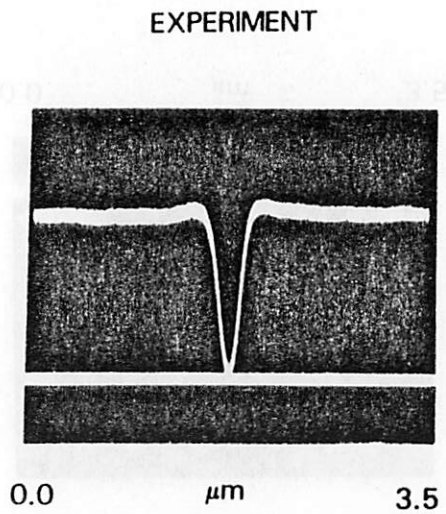
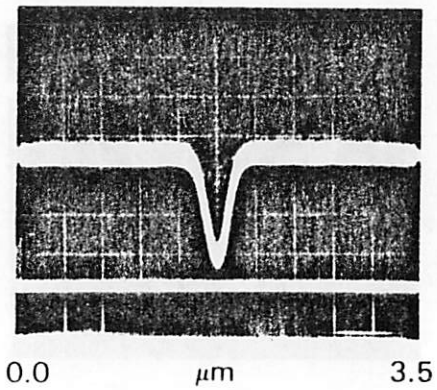


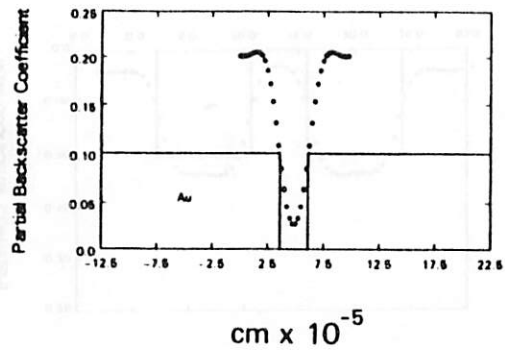
Figure 3.4d. Comparison of experimental and simulated backscattered electron signals. Gold thickness is about 0.46 μm . Beam thickness is 25 kV. A 0.25 μm hole in a gold film.



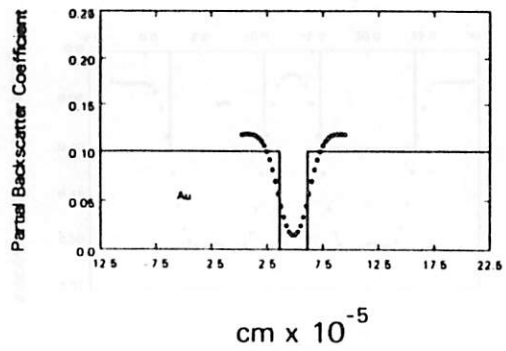
.2 μm beam fwhm 25 KV



ENERGY SIGNAL



35 - 62.5 $^{\circ}$



55 - 75 $^{\circ}$

NUMBER SIGNAL

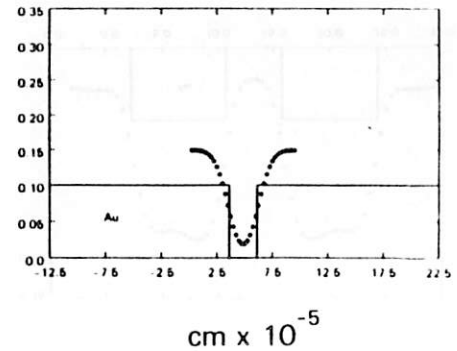
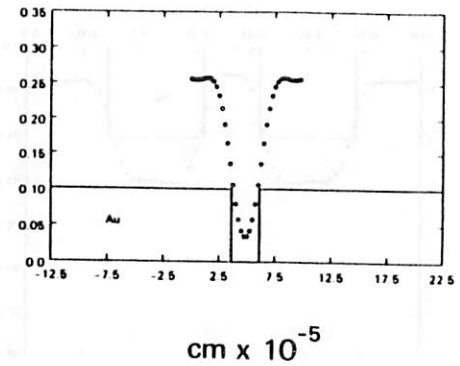


Figure 3.4e. Comparison of experimental and simulated backscattered electron signals. Gold thickness is about $0.2 \mu\text{m}$. Beam voltage is 25 kV. Two $0.6 \mu\text{m}$ holes in gold separated by a $0.6 \mu\text{m}$ gold step.

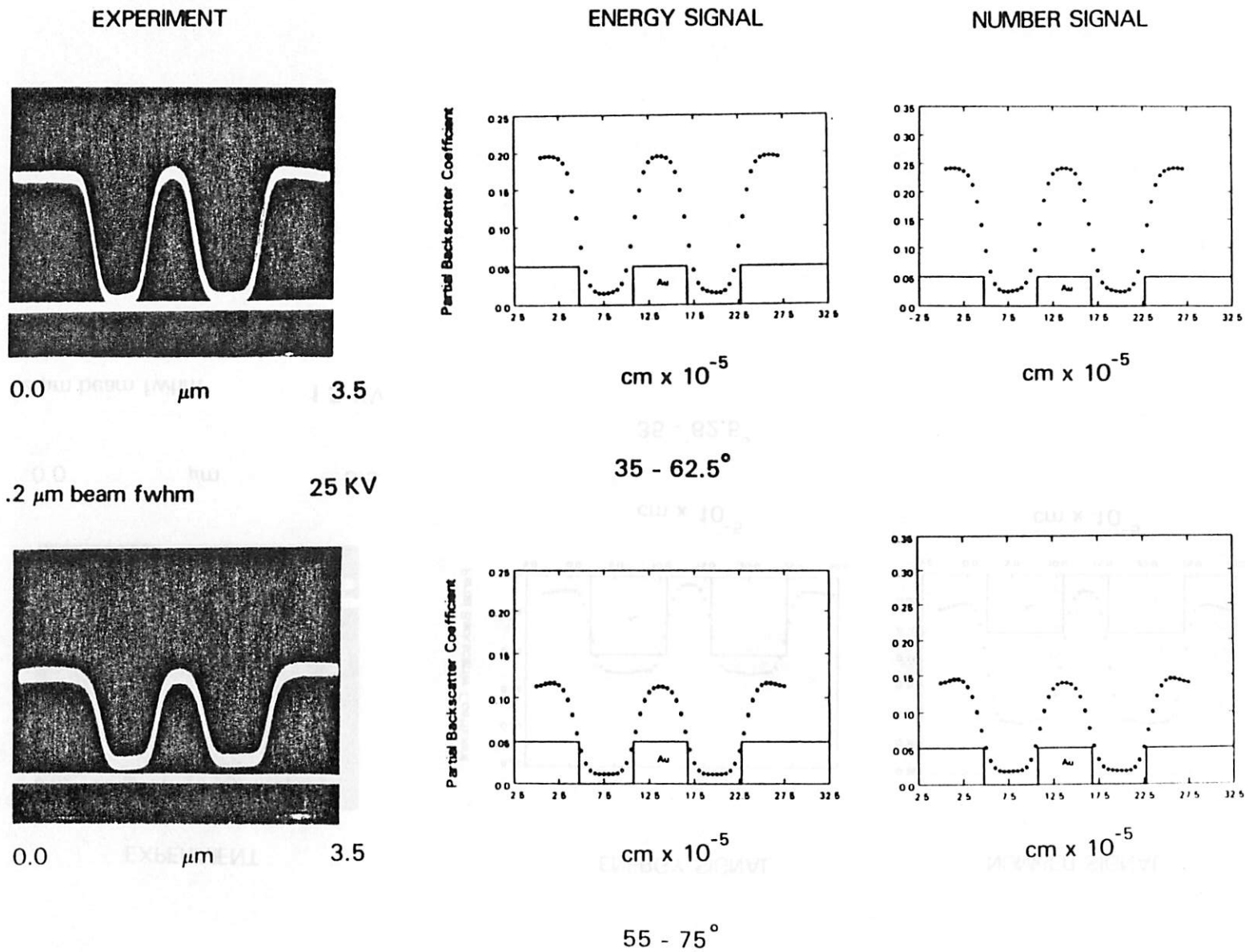
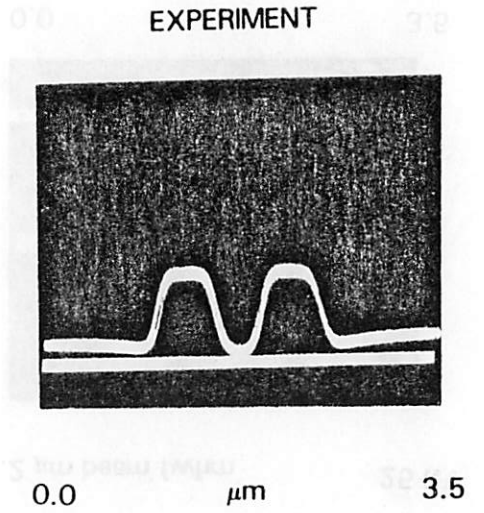


Figure 3.4f. Comparison of experimental and simulated backscattered electron signals. Same as Figure 3.4c except that the beam voltage is 15 kV.



.2 μm beam fwhm **15 KV**

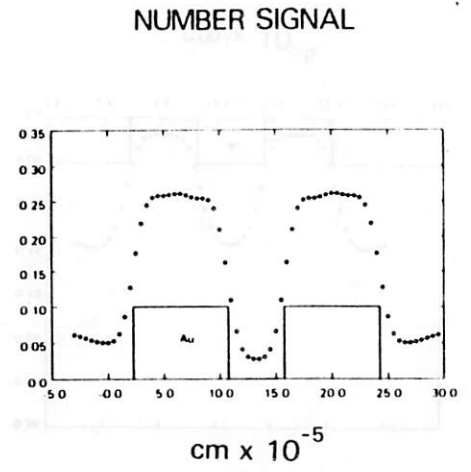
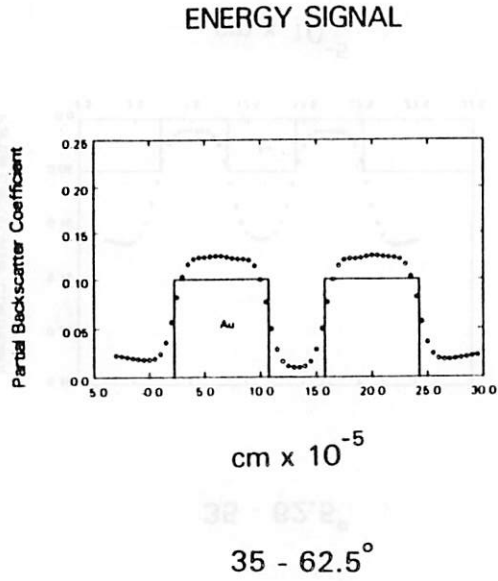


Figure 3.5. A comparison of experimental and simulated contrasts for the structures of Figure 3.4.

| STRUCTURE | CONTRAST EXPERIMENT | | SIMULATION | | | |
|---|---------------------|--------|------------|--------|----------|--------|
| | 32-62.5° | 55-75° | Number | | Energy | |
| | | | 35-62.5° | 55-75° | 35-62.5° | 55-75° |
| .7 μm holes in Au, .7 μm step | .92 | .84 | .86 | .79 | .88 | .86 |
| .85 μm Au steps, .5 μm space | .81 | .73 | .71 | .67 | .78 | .75 |
| .55 μm Au step | .71 | .60 | .58 | .54 | .67 | .63 |
| .25 μm hole in Au | .87 | .66 | .76 | .77 | .77 | .77 |
| .6 μm hole in Au, .6 μm step (.2 μm Au) | .89 | .77 | .82 | .76 | .85 | .81 |
| .85 μm Au steps, .5 μm space, 15 kV | .83 | -- | .79 | -- | .85 | -- |

BEAM ENERGY = 25 KV Au THICKNESS = .46 μm

experiment and number contrast is good in some cases; but, is low when the structure is an isolated gold step on silicon. This is because the diode detector's initial amplification is proportional to electron energy. The backscattered electron energy distribution for gold has a maximum near 9/10 of the incident beam energy while that for silicon has a maximum at about 7/10 of the incident energy [19]. Thus, the backscattered electrons from gold tend to have higher energies and create more diode current than those from silicon. For small holes in the gold, this difference in backscattered electron energies is not as important since so few electrons escape from underneath the gold.

The simulated energy signal properly takes the backscattered electron energies into account and the resultant simulated contrasts show better agreement with experiment, especially for gold steps on silicon. This is especially true for the 15 kV case of Figure 3.4f. The energy signal correctly predicts the reduction in high signal level because of the lower energy electrons. Note that even for the simulated energy signal, the agreement is not as good for the 0.25 μm hole in gold. This is because for this size of structure, the measurement is very sensitive to factors which are not accurately known such as beam size, focus, and the slope of the gold sidewalls.

While being useful for comparisons of simulation and experiment, contrast is not a good measure of the quality of the backscattered electron signal. This is because contrast does not contain any information about the signal to noise ratio, SNR, of the signal. It is well known that for high speed inspection of masks with an electron-beam, a high SNR ratio is desirable to guard against false defect detection and the missing of defects [2,4]. Assuming a shot noise limited signal, the most noise will be found in the maximum part of the signal and this noise is proportional to the square root of the maximum signal [19]. A parameter, ΔSNR which gives information about the SNR quality of the signal for alignment has been introduced by Lin [19]. For defect detection, it is more appropriate to normalize to the energy ΔSNR between 0.5 μm thick gold on silicon and bulk silicon. The ΔSNR can be written:

$$\Delta SNR = \frac{\frac{S_{\max} - S_{\min}}{\sqrt{S_{\max}}}}{\frac{S_{\max-Au} - S_{\max-Si}}{\sqrt{S_{\max-Au}}}} \quad (3.2)$$

Note that this parameter is in terms of the energy signal levels and that the normalizing signals from the gold and silicon are total signals covering the entire 90 degrees take-off angle range.

A direct comparison of ΔSNR 's between experiment and simulation is not practical since the diode amplifier gain is unknown. However, the ΔSNR ratio for the two different take-off angle ranges can be compared. Figure 3.6 is a comparison of the experimental and simulated ΔSNR ratios for the 35-62.5 and 55-75 degrees ranges. The simulated energy and number signals, predicting a higher quality signal for the 35-62.5 degrees range, are in very close agreement with experiment. Thus, the Monte Carlo simulation program will be a very accurate and useful tool in determining the optimum take-off angle collection range for a given backscattered electron detector.

Agreement between simulation and experiment was investigated in several other ways to gain even more confidence in using the Monte Carlo program. Figure 3.7 is a plot of the simulated and experimental [42] total number backscatter coefficient, η_B , versus atomic number. It can be seen that the present Monte Carlo program agrees well with experiment as well as with the simulation results from Lin's program [19].

The Bethe range, R_B , is defined as the total path distance of an electron in a given material [43]. It can be calculated analytically by a direct integration of Bethe's energy loss equation for an electron in a solid [43,44] or simply by adding up all of the path lengths in an electron's Monte Carlo calculated trajectory [19,31,45]. Figure 3.8 compares the Bethe ranges calculated using other Monte Carlo programs and analytical techniques [19,31,45,46,46a]. Again, the agreement is very good.

Large gold on silicon pad structures on the test wafers described in Chapter 2 were used to determine whether the change in backscatter coefficient with varying gold thickness could be correctly predicted. A 25 kV electron-beam and a backscattered electron collection angle range

$$\frac{\Delta\text{SNR (35-62.5}^\circ)}{\Delta\text{SNR (55-75.0}^\circ)}$$

| STRUCTURE | EXPERIMENT | SIMULATION | |
|--|------------|------------|--------|
| | | Number | Energy |
| .7 μm holes in Au, .7 μm step | 1.23 | 1.39 | 1.34 |
| .85 μm Au steps, .5 μm space | 1.25 | 1.39 | 1.35 |
| .55 μm Au step | 1.34 | 1.42 | 1.41 |
| .25 μm hole in Au | 1.34 | 1.30 | 1.30 |
| .6 μm hole in Au, .6 μm step (.2 μm Au) | 1.27 | 1.37 | 1.34 |

BEAM ENERGY = 25 KV Au THICKNESS = .46 μm

Figure 3.6. A comparison of experimental and simulated ΔSNR ratios for the 35-62.5 and 55-75 degrees take-off ranges.

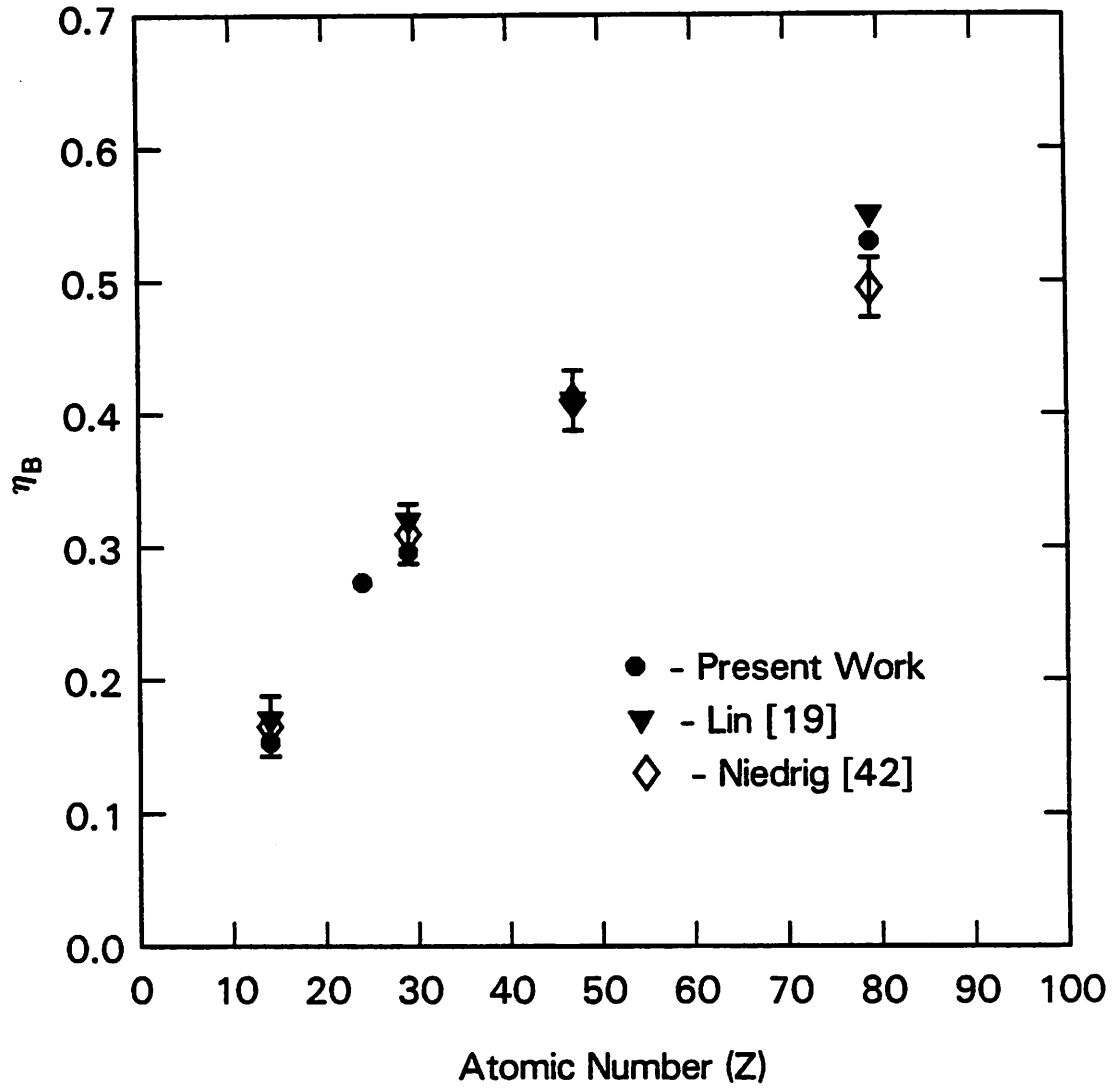


Figure 3.7. A plot of the simulated and experimental [42] total number backscatter coefficient versus atomic number.

| Calculated Bethe Ranges | | | | | |
|--------------------------------|----------------------------------|--|------------------------------|----------------------|-------------------------|
| Material | Beam Voltage (kV) | R_B (μm) | | | |
| | | Present Work | Parikh and Kyser [45] | Hawryluk [46] | Wolf et al [46a] |
| Au | 10 | 0.40 | 0.42 | — | 0.40 |
| Au | 20 | 1.20 | — | 1.10 | 1.16 |
| Au | 25 | 1.73 | 1.68 | — | — |
| Au | 30 | 2.34 | — | — | 2.24 |
| Si | 10 | 1.51 | 1.58 | 1.52 | — |
| Si | 20 | 5.07 | 5.00 | 5.08 | — |
| Si | 30 | 10.40 | 10.00 | — | — |
| PMMA | 5 | 0.63 | — | 0.65 | — |
| PMMA | 10 | 2.12 | — | 2.18 | — |
| PMMA | 20 | 7.32 | — | 7.55 | — |

Figure 3.8. Comparison of Bethe ranges calculated using different Monte Carlo programs and analytical techniques.

of 35-62.5 degrees were used in the experiments. Figure 3.9 is a plot of simulated energy signal and experimental contrasts versus gold thickness. Again, we see good agreement between simulation and experiment.

Much of the material to be presented in Chapters 4 and 5 is concerned with the effects of the electron-beam fwhm on various backscattered electron signal characteristics. Thus, it is important to verify that the Monte Carlo program and convolution routines will correctly track the change in signal as the beam size changes. A 0.55 μm wide gold on silicon step and a 0.40 μm wide hole in gold on silicon were used in the experiments. The gold thickness was 0.46 μm and the beam energy was 25 kV. The backscattered electron detector was used in the 35-62.5 degrees take-off angle collection position. An incident beam current of 1.5 nA was used and the beam size was changed by defocusing. The beam was defocused by increasing the current in the final lens of the vector scan electron-beam system. The resulting backscattered electron signal was photographed on an oscilloscope. The horizontal or distance axis of the scope trace was calibrated by either moving the laser interferometer controlled stage [47] a specified distance or by measuring the period of accurate grating structures fabricated on the test wafer.

The experimental contrast, 10-90 percent rise distance, and threshold of the signal were measured from the scope tracings. Note that when measuring the 10-90 percent rise distances, the 10 and 90 percent points were measured, for the step, from the bulk silicon and peak gold levels, respectively. For the hole, the reference levels were the bulk gold and minimum signal. The threshold was defined as the middle of the two levels used in describing the signal's 10-90 percent rise distance and was normalized to the peak signal level at the focused condition. The same levels were used in determining the position to measure the signal fwhm.

Once this data was collected, some method had to be found to compare it with simulation. It was decided to match the experimental and simulated 10-90 percent rise distances for a given structure and then investigate the agreement for the signal fwhm, contrast, and threshold as the beam size was changed. Good agreement would imply that the simulation program was

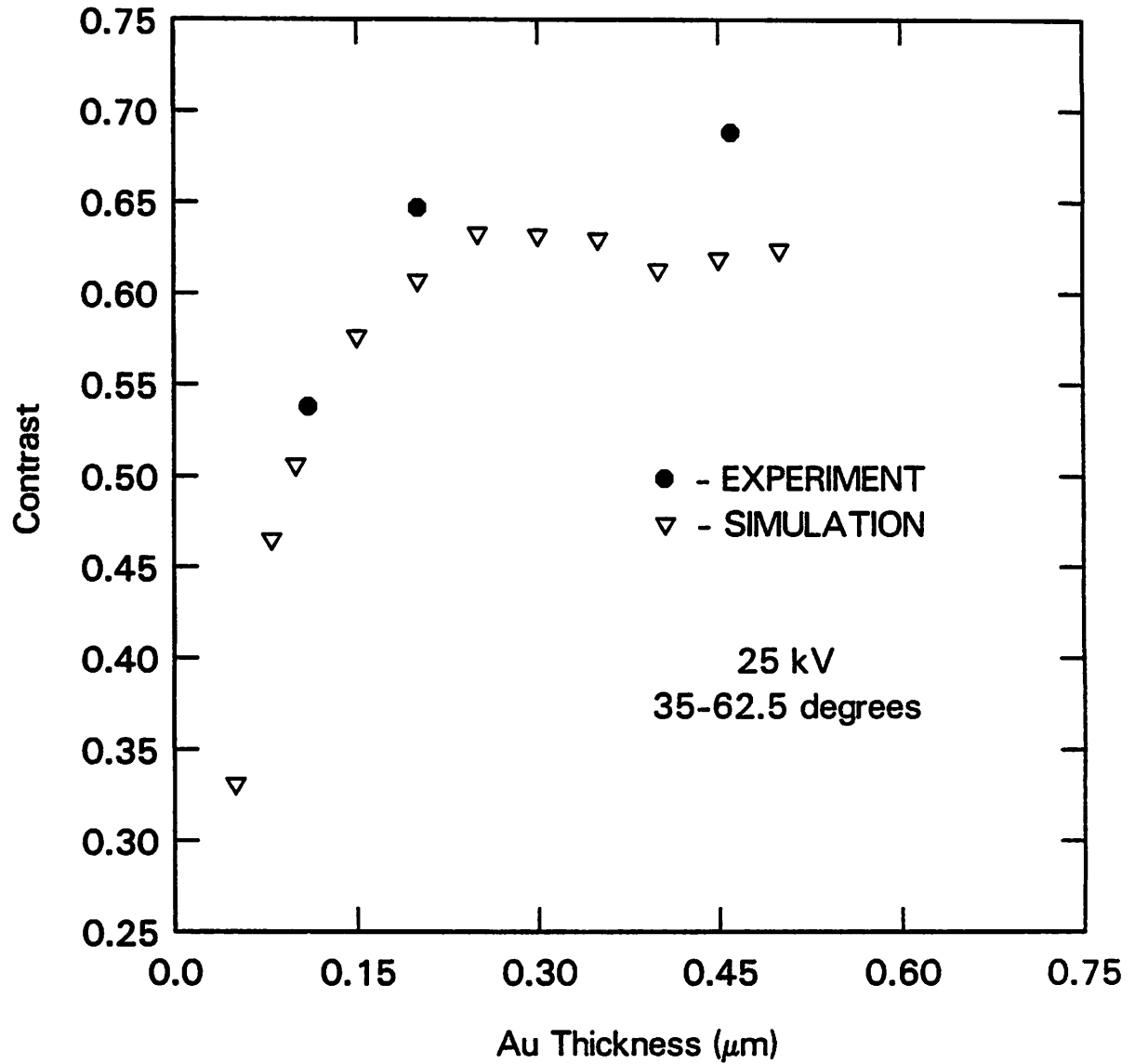


Figure 3.9. A plot of simulated and experimental contrasts versus gold thickness. The energy signal was used in the simulations.

correctly predicting the change in signal characteristics with increasing beam size. We decided to match the simulated and experimental rise distances since the size of the electron-beam did not linearly scale with the defocus settings. Also, the rise distance is a very sensitive function of the beam's fwhm; but, is relatively insensitive, compared to other signal characteristics, to small changes in the structure's linewidth. During the experiments there was some misalignment of the electron-beam in the vector scan system causing unsymmetrical signals as the beam was defocused. Thus, the experimental 10-90 percent rise distances were measured by averaging the rise distances of the left and right sides of the signal.

The experimental and simulated results for the $0.55\ \mu\text{m}$ step and $0.40\ \mu\text{m}$ hole are shown in Figures 3.10 and 3.11. A Gaussian beam shape was assumed in the simulations. For both structures, the simulated signal fwhm does not rise as quickly with increasing beam fwhm as the experimental signal fwhm does. However, there is a good reason for these discrepancies.

Figure 3.12 shows what happens as the beam is defocused in the vector scan electron-beam system [48]. When the beam is focused, the electron-beam can be thought of as the convolution of a Gaussian with a point - i.e a Gaussian. However, when the beam is defocused, the final electron-beam shape can be described by the convolution of a Gaussian with a disk. In two dimensions, this is essentially a rectangular shaped electron-beam which can be described as the sum of two error functions [49]. Rectangular shaped beams are currently used in several high throughput electron-beam systems [50,51].

A program was written to convolute the δ -function backscattered electron signal with a rectangular beam shape [49,52]. The size of the beam is specified by the fwhm and a parameter known as the edge slope or 10-90 percent rise distance. By making the edge slope equal to the edge slope of a Gaussian beam, the rectangular beam will resemble a Gaussian. If the edge slope is reduced, then the beam becomes more rectangular in shape.

The simulated beam fwhm was varied from 0.10 to $1.0\ \mu\text{m}$ with the beam shape arbitrarily changing from a Gaussian at near focus conditions to rectangular at defocused conditions. The resulting agreement with experiment is shown for the two structures in Figures

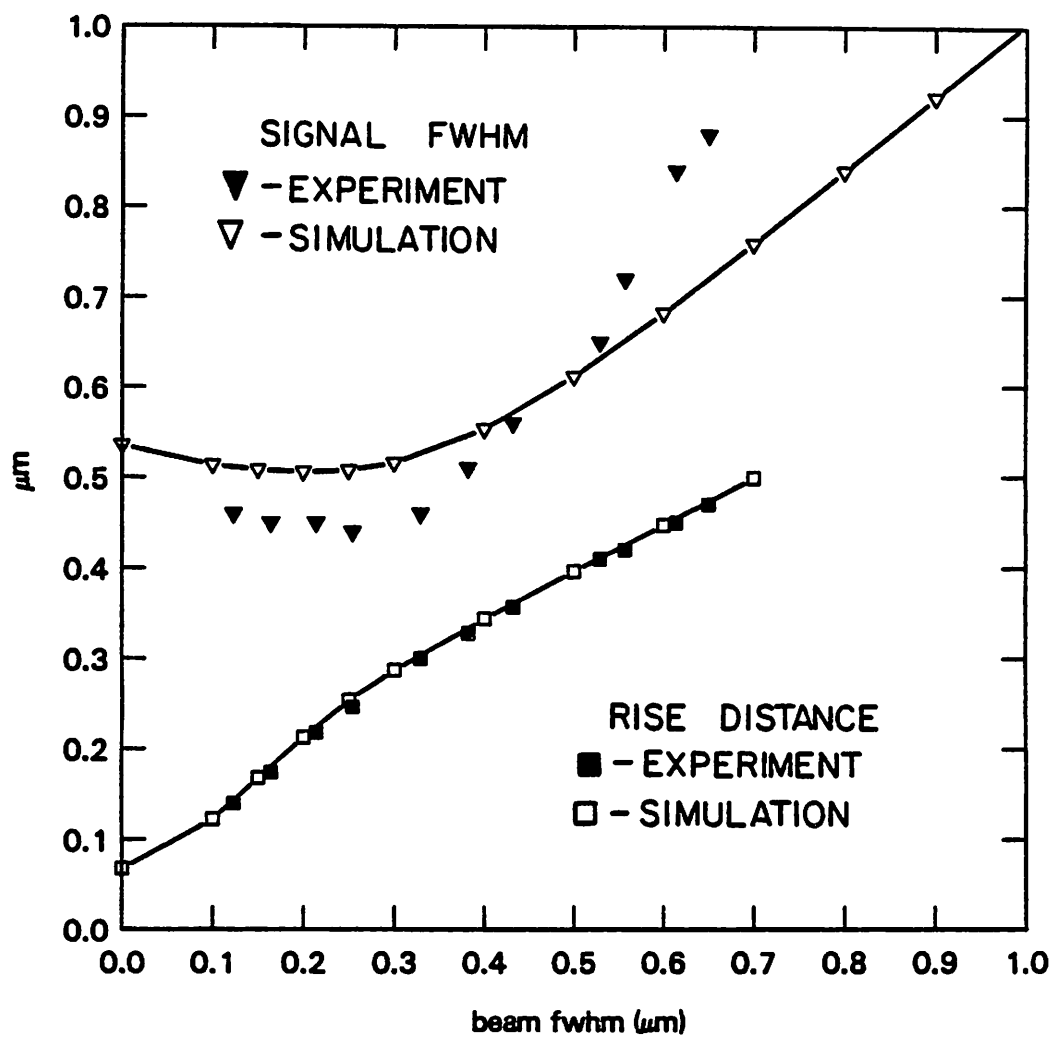


Figure 3.10. A plot of the simulated and experimental signal fwhm and rise distance versus beam fwhm assuming a Gaussian beam shape for the $0.55 \mu\text{m}$ step structure.

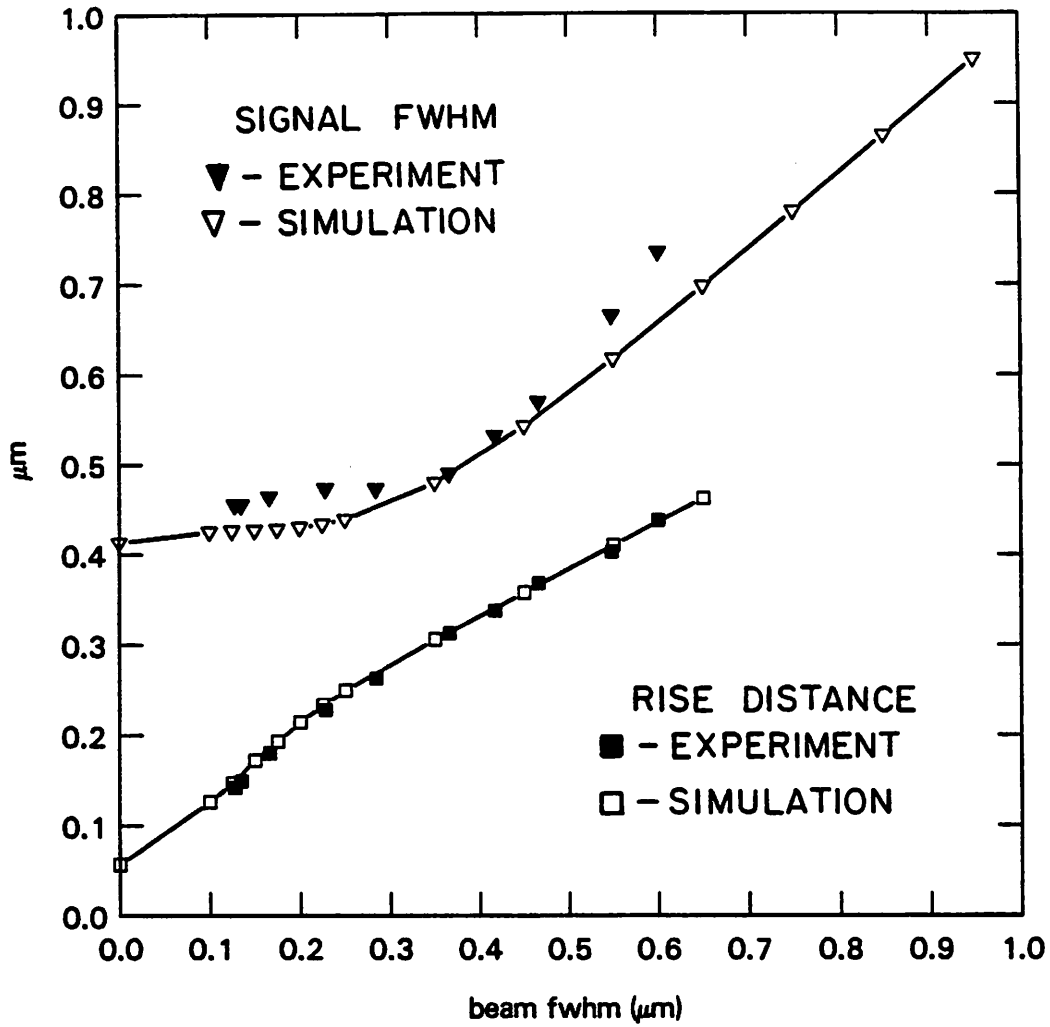


Figure 3.11. A plot of the simulated and experimental signal fwhm and rise distance versus beam fwhm assuming a Gaussian beam shape for the $0.4 \mu\text{m}$ hole structure.

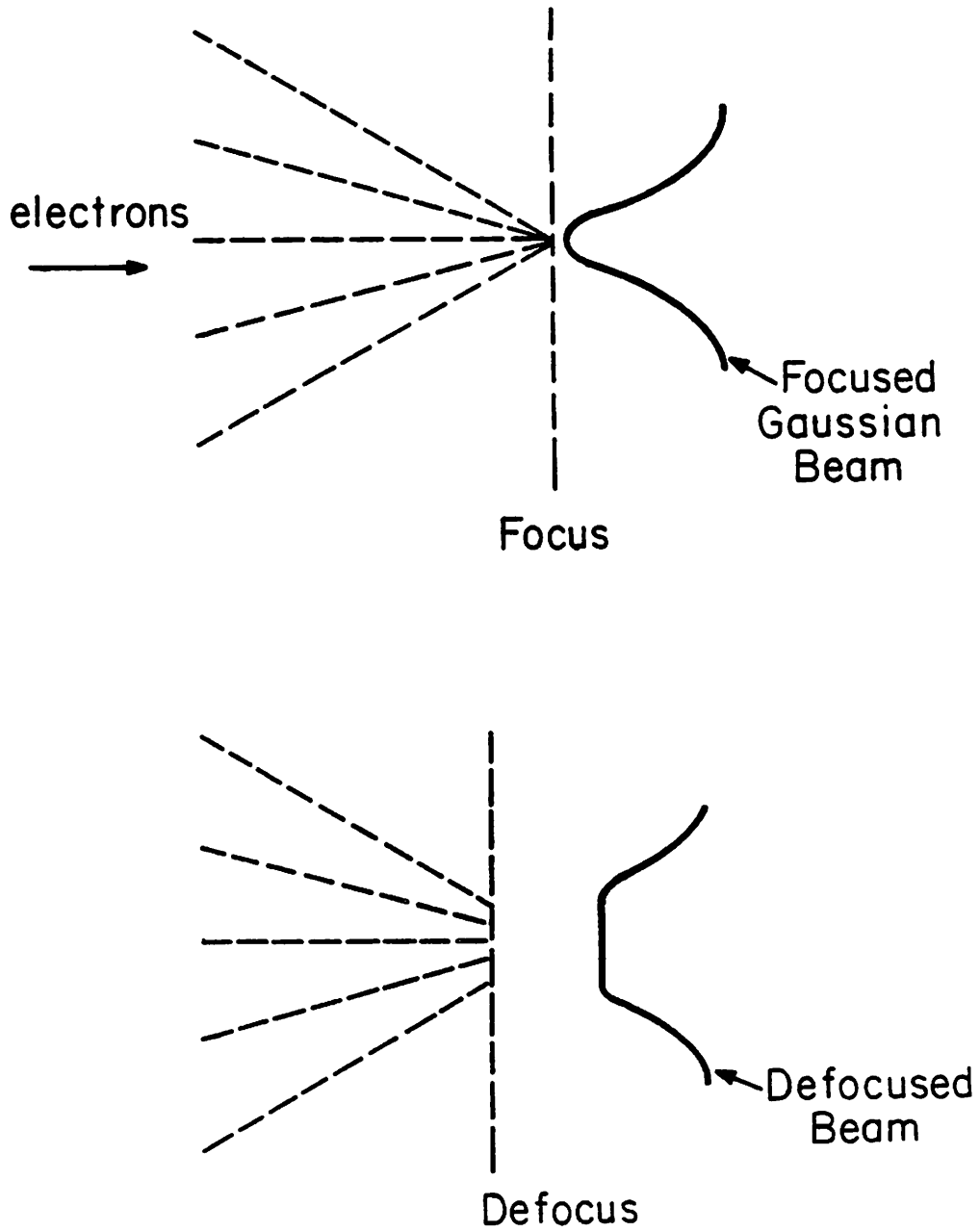


Figure 3.12. An illustration of what happens when the electron-beam is defocused.

3.13-3.16. The agreement between the experimental and simulated signal fwhm for the step structure, shown in Figure 3.13, is still not perfect; but, shows considerable improvement over that of Figure 3.10. The agreement for the hole structure signal fwhm, Figure 3.14, is relatively good and shows improvement over that of Figure 3.11. It should be noted that the experiments for the step and hole were done on different days with possibly different lens current settings. Figures 3.15 and 3.16 show the experimental and simulated contrasts and normalized thresholds. As can be seen the agreement is quite good, even for the step structure.

Keeping in mind that as the beam is defocused, the actual beam shape is unknown, the agreement between simulation and experiment is quite good for the two complementary structures. Note that the simulation was sensitive enough to determine that the defocused electron-beam had deviated from having a strictly Gaussian beam shape. Another way in which the beam size could have been changed, without defocusing, would have been to increase or decrease the beam current. However, the backscattered electron detector pre-amplifier and amplifier saturated at about 4-5 nA of beam current. Thus, it was impossible to observe a large change in beam size without saturating the detector.

The actual beam size of a given electron-beam system can be determined by scanning the focused beam over a mark and matching the resulting signal rise distance to the simulated rise distance for the same structure. Focused beams with currents of 0.75, 1.5, and 3.0 nA were scanned across the 0.55 μm step and the measured rise distances were matched with the simulated rise distances shown in Figure 3.10. The calculated beam sizes for the three currents were 0.086, 0.12, and 0.15 μm , respectively.

3.4. Summary

A new Monte Carlo program has been developed to simulate the backscattered electron signal from complicated submicron structures encountered during x-ray mask inspection. The program uses the standard continuous slowing down approximation, screened Rutherford collision cross-section, and the Bethe energy loss equation. The simulated energy signals from

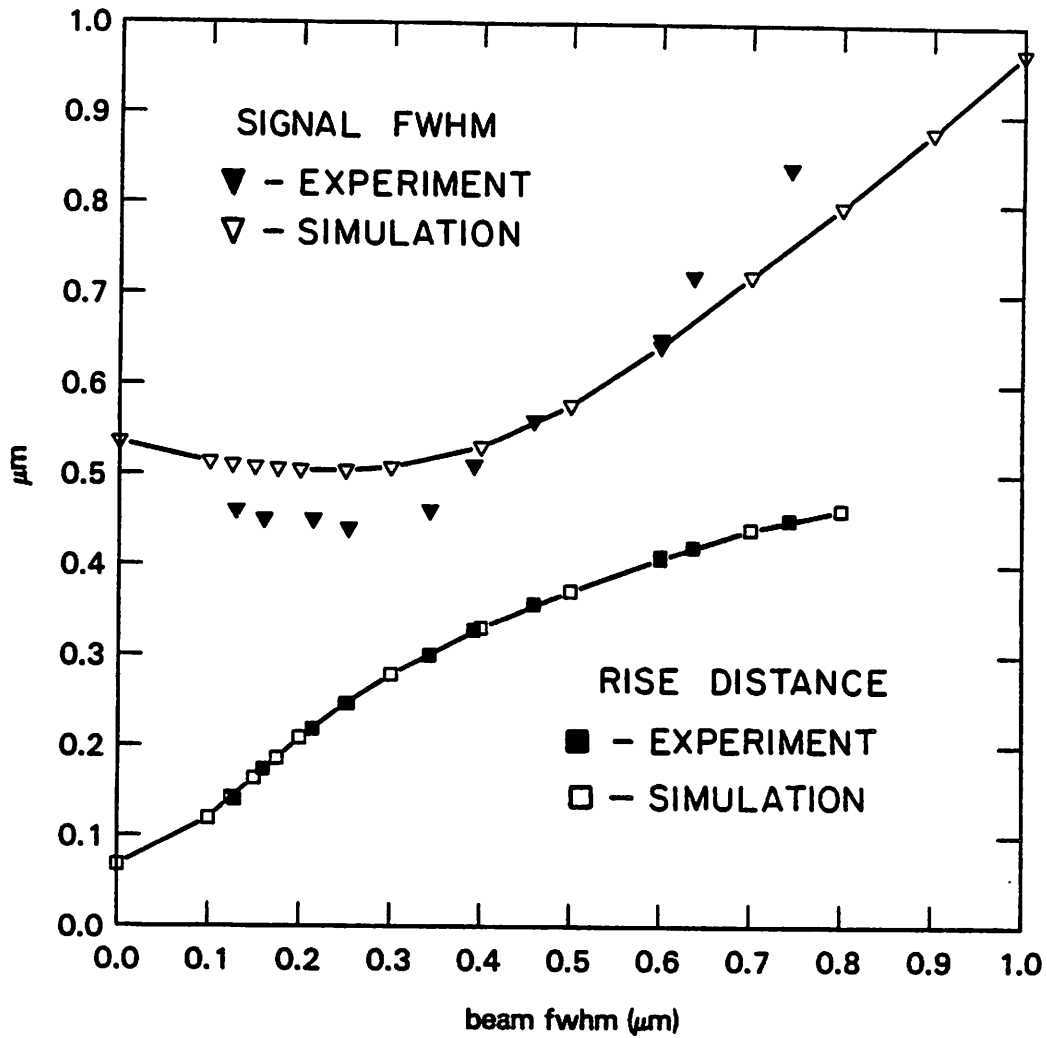


Figure 3.13. A plot of the simulated and experimental signal fwhm and rise distance versus beam fwhm assuming a variable beam shape for the $0.55 \mu\text{m}$ step structure.

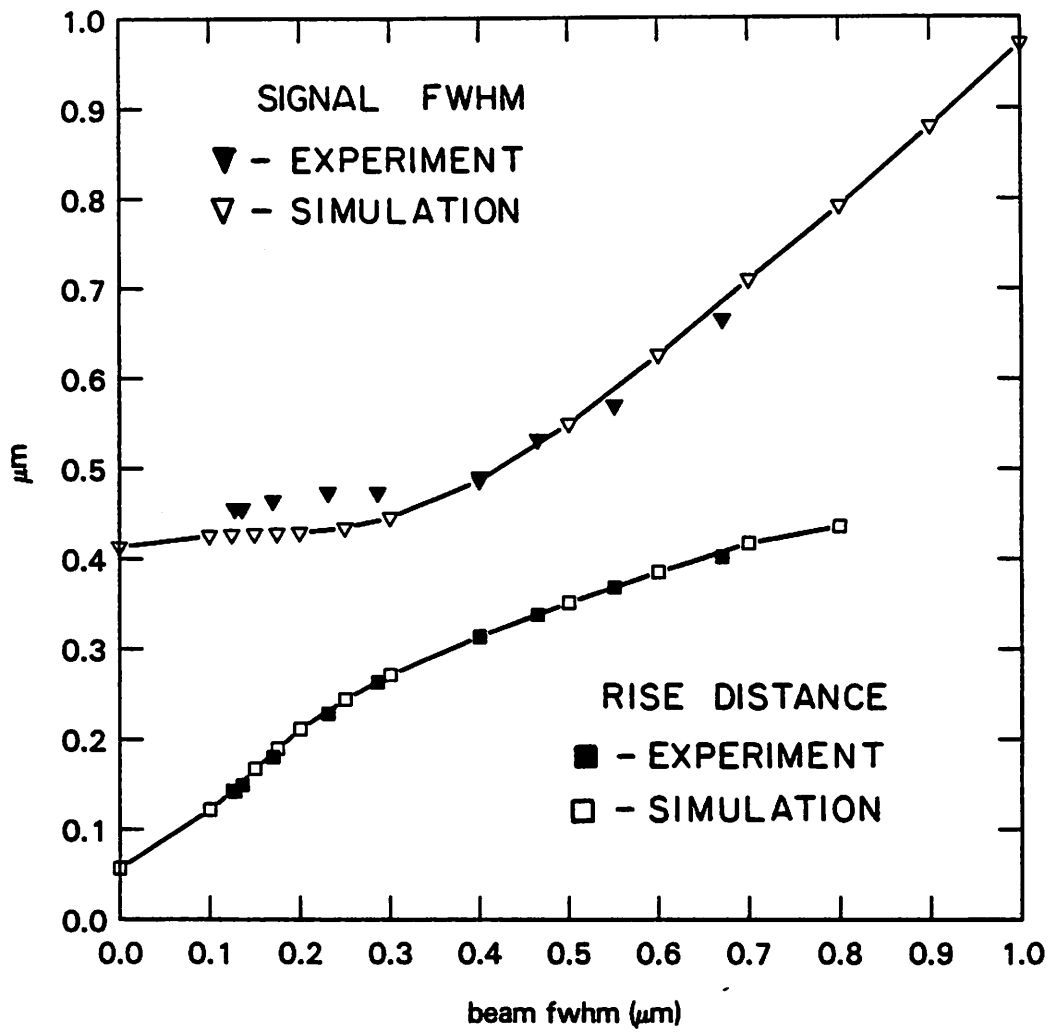


Figure 3.14. A plot of the simulated and experimental signal fwhm and rise distance versus beam fwhm assuming a variable beam shape for the 0.4 μm hole structure.

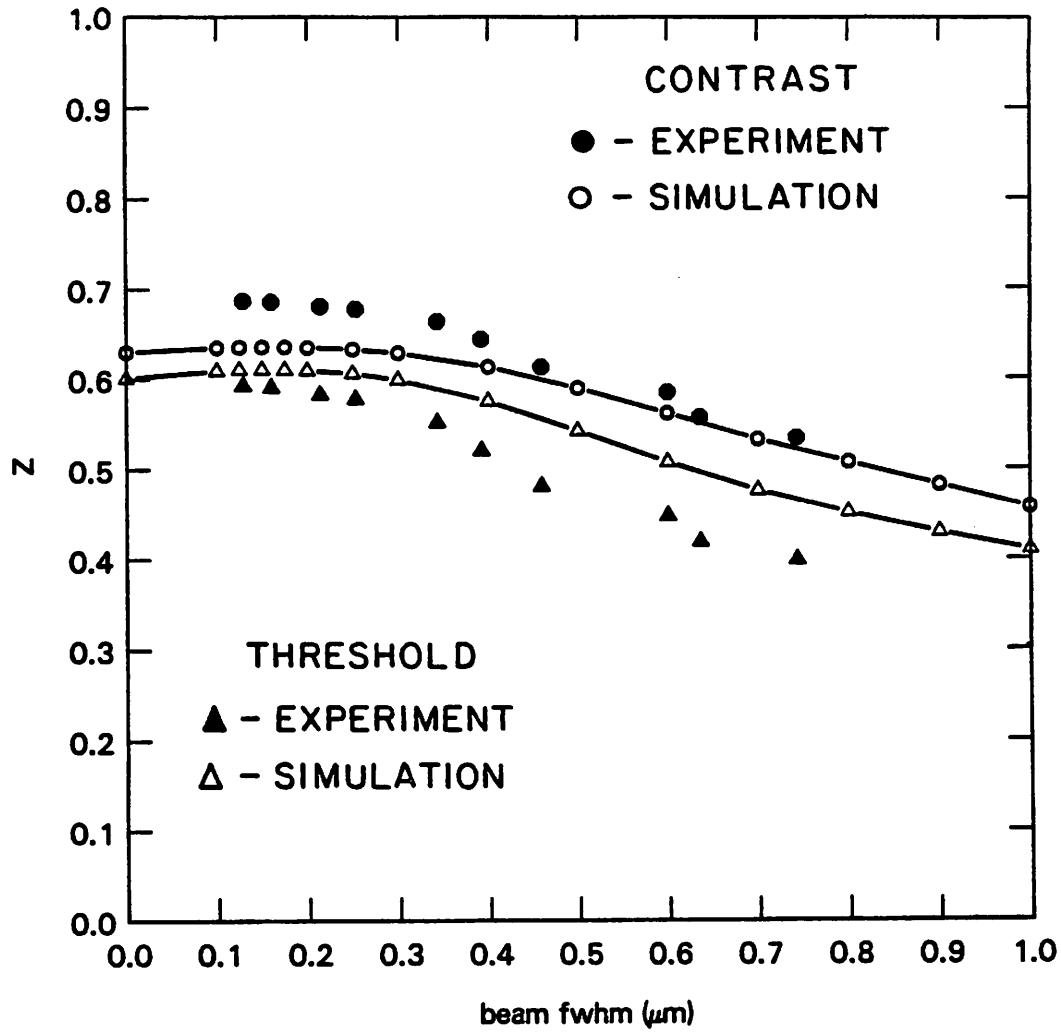


Figure 3.15. A plot of the simulated and experimental contrast and threshold versus beam fwhm assuming a variable beam shape for the $0.55 \mu\text{m}$ step structure. The threshold is normalized to the threshold at the focused condition.

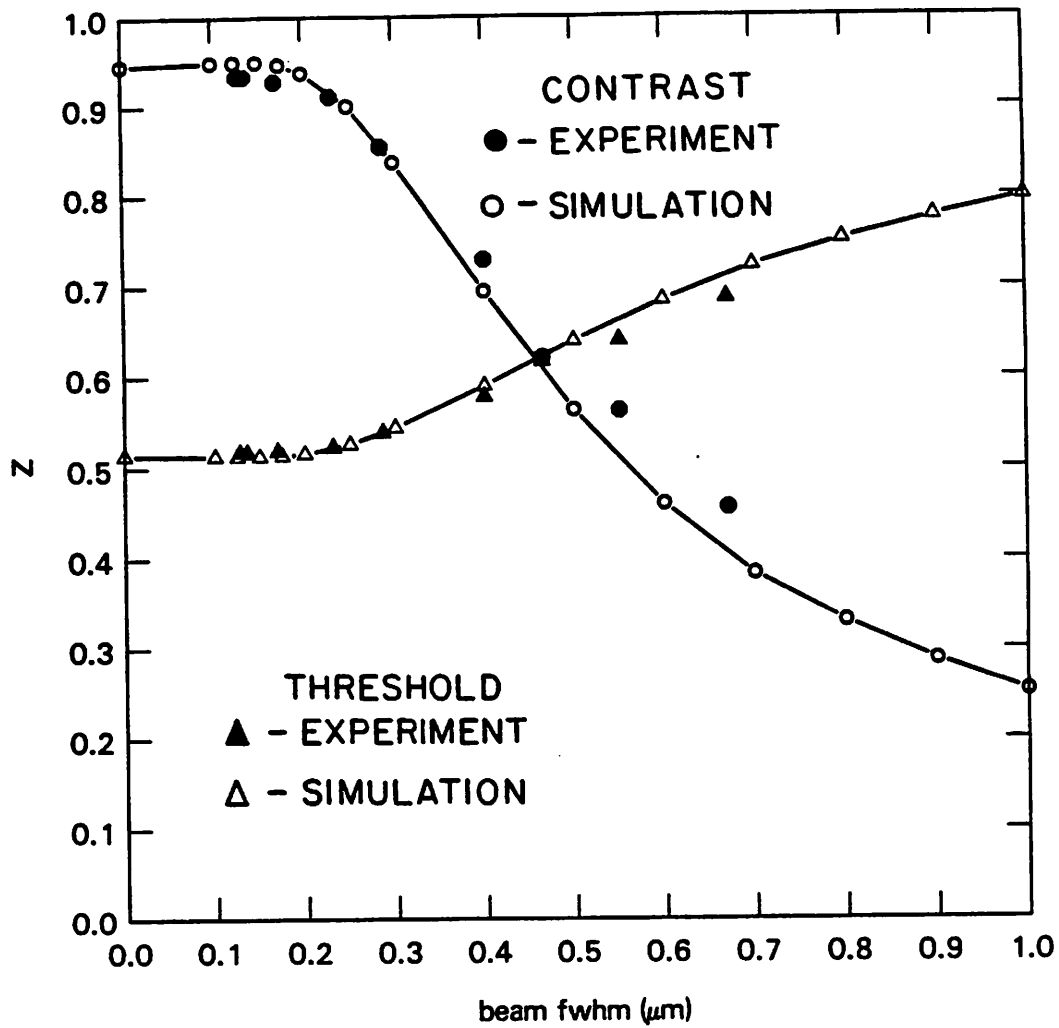


Figure 3.16. A plot of the simulated and experimental contrast and threshold versus beam fwhm assuming a variable beam shape for the $0.4 \mu\text{m}$ hole structure. The threshold is normalized to the threshold at the focused condition.

different submicron gold on silicon structures agree well with experimental backscattered electron signals for different take-off angle ranges, beam voltages, and gold thicknesses. The program has been shown to correctly predict the change in signal characteristics as the incident electron-beam size is changed. Thus, we have confidence in using the Monte Carlo program to investigate various aspects of defect detection and signal quality in x-ray mask inspection - the subject of the next two chapters.

CHAPTER 4

4. SIMULATION OF BACKSCATTERED ELECTRON SIGNALS FOR X-RAY MASK INSPECTION

4.1. Introduction

The Monte Carlo program, outlined in Chapter 3, has been shown to give results which agree well with experimental backscattered electron signals. In this chapter, we will use the simulation program to investigate important parameters which affect the characteristics and quality of the backscattered electron signal. The usefulness of the program will be demonstrated by using simulation to optimize the placement of the solid state diode detector used in the experiments of Chapter 3. The signal quality from this detector in its optimum position will then be characterized.

The effects of beam size at three different angle collection ranges will then be investigated. The required gold thickness for the maximum signal will be determined for various beam energies. Required chrome thicknesses will also be determined and we will see that the required thicknesses can be related, in a universal fashion, to the Gruen and Bethe ranges [43] of the electrons in the scattering material. It will be observed that the backscattered electron signal will drop off if the beam is scanned near the edge of the gold. A universal curve using the Gruen range will be presented to determine at what point inside a gold structure, the electron-beam will see essentially bulk gold. Effects of collection angle range will also be considered. Finally, a simple technique for calculating signal levels for two and three dimensional structures will be presented.

4.2. Optimization of the Experimental Detector Placement

The optimum placement of the annular diode detector used in the experiments of Chapter 3 will now be considered [53]. The Monte Carlo program was used to determine the optimum placement of this detector to achieve the best signal from a wide range of structures.

Histograms of the partial energy backscatter coefficient versus take-off angle for 0.5 μm gold on silicon, bulk silicon, and the center of a 0.25 μm gold step on silicon are shown in Figure 4.1. The material contrast between the gold and silicon can clearly be seen. The distribution of backscattered electrons changes from a cosine distribution ($\cos\theta\sin\theta$) for the 0.5 μm thick gold to a distribution weighted towards the lower angles for the small gold step. On the other hand, a small hole in a gold film will essentially look like bulk gold (i.e. a cosine distribution) except in the immediate vicinity of the hole. The backscattered electron signals from most defects will range from the signal from a small gold step to the signal from a small hole in a gold film. Thus, it is instructive to examine the take-off angle distribution from these two types of defects in order to optimize the placement of the detector.

The simulated energy signals for a 0.25 μm gold step and 0.25 μm hole in a gold film at 25 kV and 0.5 μm gold thickness are shown in Figure 4.2. A minimum detectable defect size of 0.25 μm and beam fwhm of 0.20 μm was assumed when optimizing the placement of the detector. Vertical sidewalls were used in all simulations. Three different take-off angle ranges corresponding to different detector heights above the wafer surface are shown to illustrate the change in signal as the collection range changes. It can be seen from Figure 4.2 that the 15-35 degrees range gives the maximum ΔSNR of the three ranges shown for the gold step. This is expected after examining the take-off angle distributions of Figure 4.1. However, since the angle distribution from a small hole in a gold film is almost a cosine distribution, it is clear why the 15-35 degrees signal for the 0.25 μm hole has such a poor ΔSNR .

A trade-off is needed so that the signals from the small step and small hole will be maximized. The 30-57.5 degrees take-off angle range, corresponding to a detector height of 6.1 mm above the wafer, is a good compromise as can be seen from Figure 4.2. A more detailed

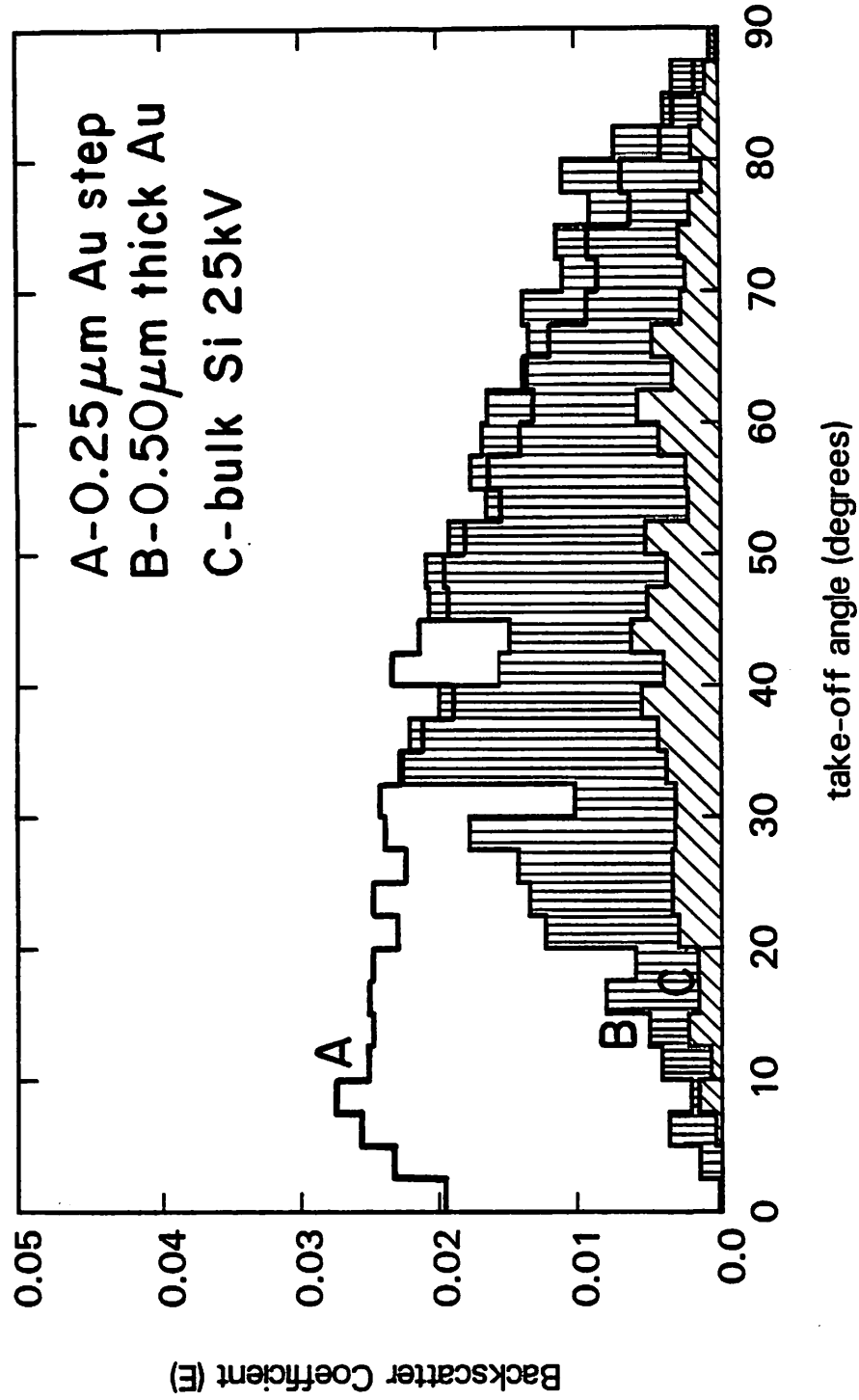


Figure 4.1. Histograms of the partial energy backscatter coefficient versus take-off angle for 0.5 μm thick bulk gold on silicon, bulk silicon, and for a δ -function electron-beam incident at the center of a 0.25 μm gold step on silicon.

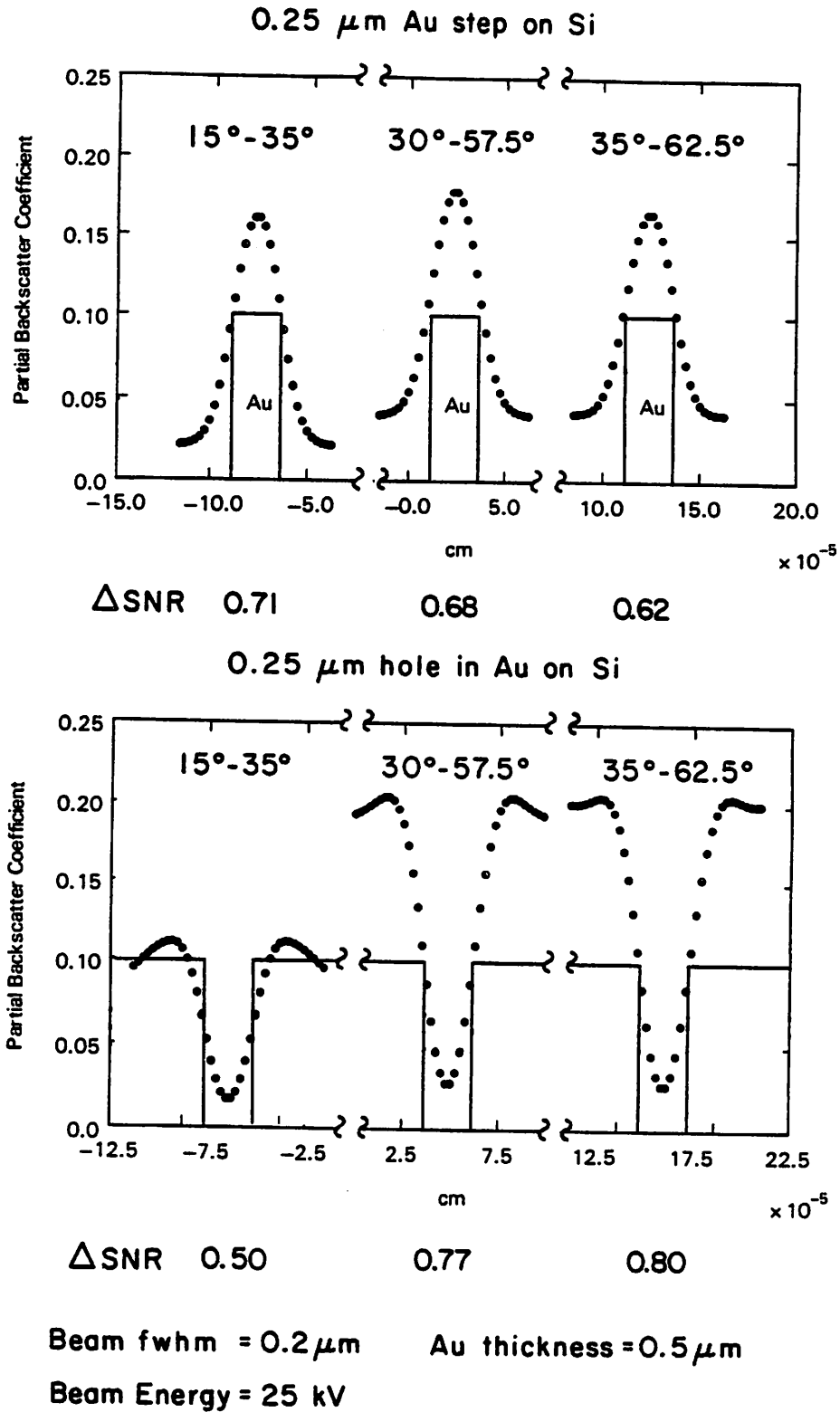


Figure 4.2. The simulated energy signals for a 0.25 μm gold step and a 0.25 μm hole in a gold film for three different take-off angle ranges.

analysis of Δ SNR's for 25-50, 30-57.5, and 35-62.5 degrees ranges for these structures as well as the various structures simulated in Figure 3.4 showed that the 30-57.5 degrees range gives better signals than the other ranges. It should be mentioned that this optimum range is different than the optimum range (0-30 degrees) calculated for the detection of registration signals [19,32,41]. This is expected since gold on silicon structures exhibit material as well as topographical contrast while registration marks have mostly topographical contrast.

At the optimum detector height, it was found that small gold steps show the worst Δ SNR while holes in a gold film show the best. A plot of the Δ SNR for various defect types is shown in Figure 4.3 for the optimum take-off range determined earlier. It can be seen that holes in the gold film and similar structures have much higher Δ SNR than steps and similar structures. Note that the 0.4 μ m hole has a better Δ SNR than the 0.25 μ m hole. This is because the overlap of the 0.2 μ m beam on the gold raises the low part of the signal from the 0.25 μ m hole. The information in Figure 4.3 coupled with the information in Figure 4.1 seem to suggest that it would be advantageous to use different detector arrangements to detect different defects. A low angle detector would be favored for steps while a middle angle range detector would be favored for holes in a gold film.

4.3. A Study of the Effects of Beam Size and Angle Collection Range

As was shown in section 4.2, we can gain much information about the scattering properties of various defects by examining the limiting cases of an isolated gold on silicon step and an isolated hole in gold on silicon. We are interested primarily in submicron structures since it is the minimum detectable defect size which will influence the design of the mask inspection system [4]. From a practical viewpoint, an electron-beam system with a 0.25 μ m fwhm beam will have much more difficulty detecting a 0.125 μ m defect than in detecting a 1.0 or 2.0 μ m defect. In this section, the effects of Gaussian beam size (fwhm) and angle collection range on the backscattered electron signal from the following structures will be discussed: 0.125, 0.25, and 0.55 μ m fwhm gold on silicon steps with vertical sidewalls; a step structure with a 0.10 μ m top

ΔSNR FOR DIFFERENT STRUCTURES

BEAM ENERGY = 25 KV .46-.5 μM AU
BEAM fwhm = .2 μm

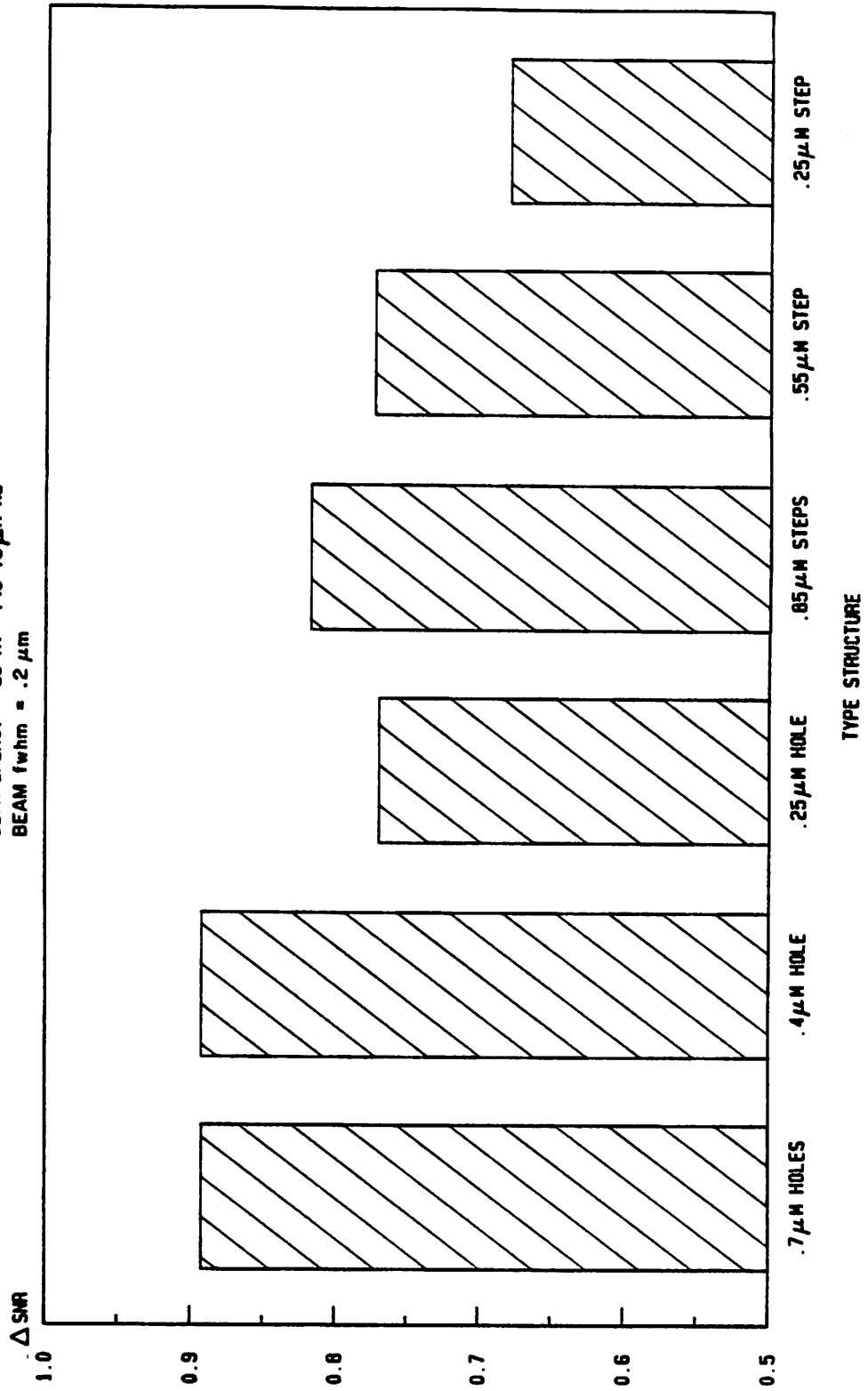


Figure 4.3. A plot of the Δ SNR for various types of defects for the 30-57.5 degrees optimum take-off angle range.

dimension and a $0.25 \mu\text{m}$ bottom dimension; 0.125 , 0.25 , $0.40 \mu\text{m}$ holes in gold on silicon; and a hole structure with a $0.25 \mu\text{m}$ opening at the top and a $0.10 \mu\text{m}$ opening at the bottom. The gold thickness is $0.50 \mu\text{m}$ and the beam energy is 25 kV . The effects of beam voltage on the required absorber thickness will be discussed later. The angle ranges of 10 - 40 , 30 - 60 , and 50 - 80 degrees will be studied. The 0 - 10 and 80 - 90 degrees angle ranges were neglected since electrons scattered into these ranges will be extremely difficult to detect inside an electron-beam chamber. All backscattered electron signals were calculated as the energy signal which was shown to give good agreement with experiment.

The effects of beam size and angle collection range will be studied by looking at the backscattered electron signal fwhm, threshold, and ΔSNR . The threshold is defined as the midpoint between the changing signal of interest for a given structure and the bulk signal level of the material surrounding the structure. For example, the threshold for a hole in a gold film would be the midpoint between the level for the bulk gold surrounding the defect and the minimum signal level caused by the hole. Conversely, the threshold for a step or line is the midpoint between the signal for bulk silicon and the high signal generated by the gold step.

It is important to first show why the signal contrast, very useful for comparisons of simulation to experiment, is not a useful indication of signal quality for backscattered electron signals. Figures 4.4a and 4.4b show contrast versus beam fwhm at the three different angle ranges for the $0.25 \mu\text{m}$ gold on silicon step and $0.25 \mu\text{m}$ hole in gold on silicon. Figures 4.5a and 4.5b are similar graphs for the ΔSNR signal characteristic. As can be seen, the contrast shows the difference in signal quality for the step structure for different angle ranges; however, the contrast would lead one to believe that the signal quality from the hole is relatively independent of angle collection range. Figure 4.2 shows that this is clearly not the case. The problem with using contrast is that because so few electrons escape from the bottom of a small hole structure, the minimum signal is relatively independent of the geometry of the hole and changes with different angle collection ranges in a similar manner to the maximum signal. Thus, even though the high signal level, and consequently, the difference between high and low levels,

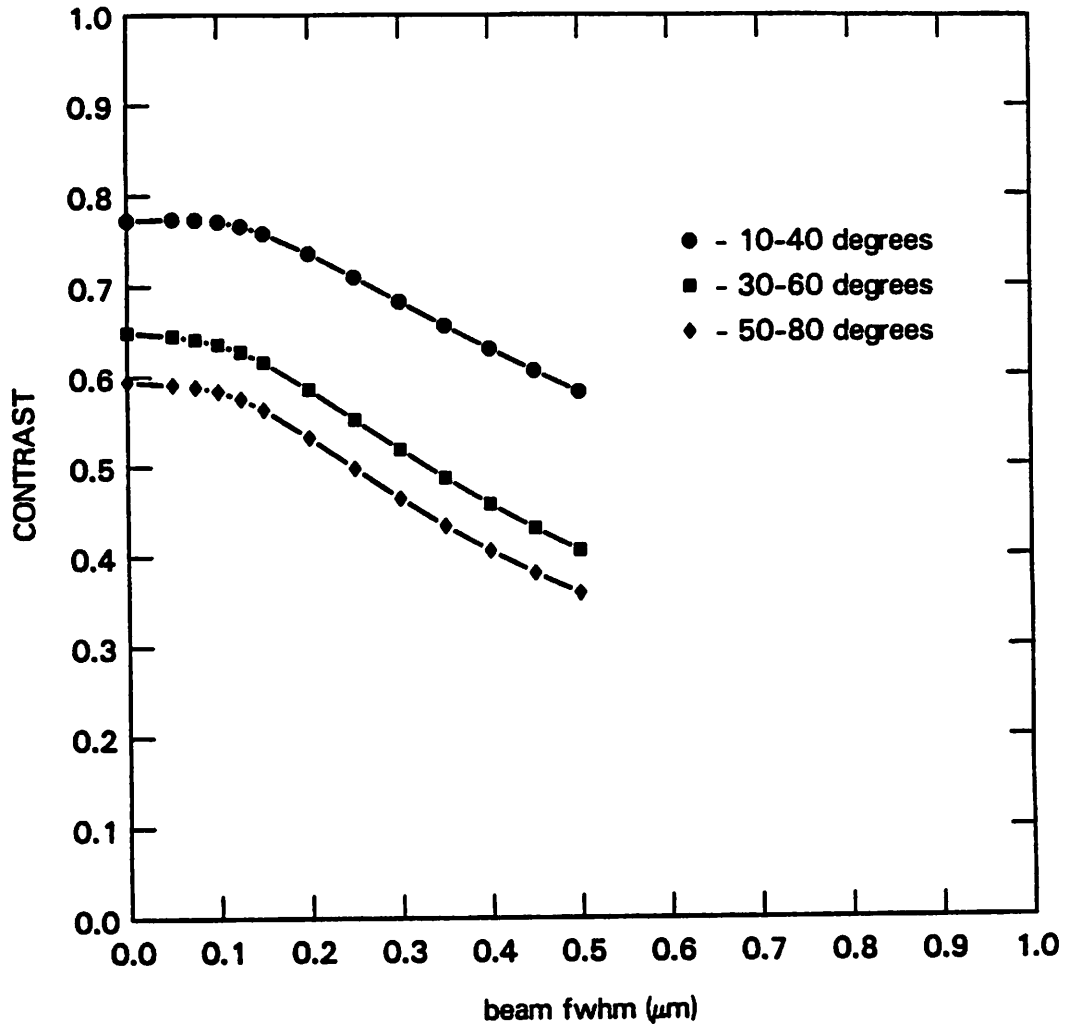


Figure 4.4a. A plot of contrast versus beam fwhm for the $0.25 \mu\text{m}$ step at 25 kV beam voltage.

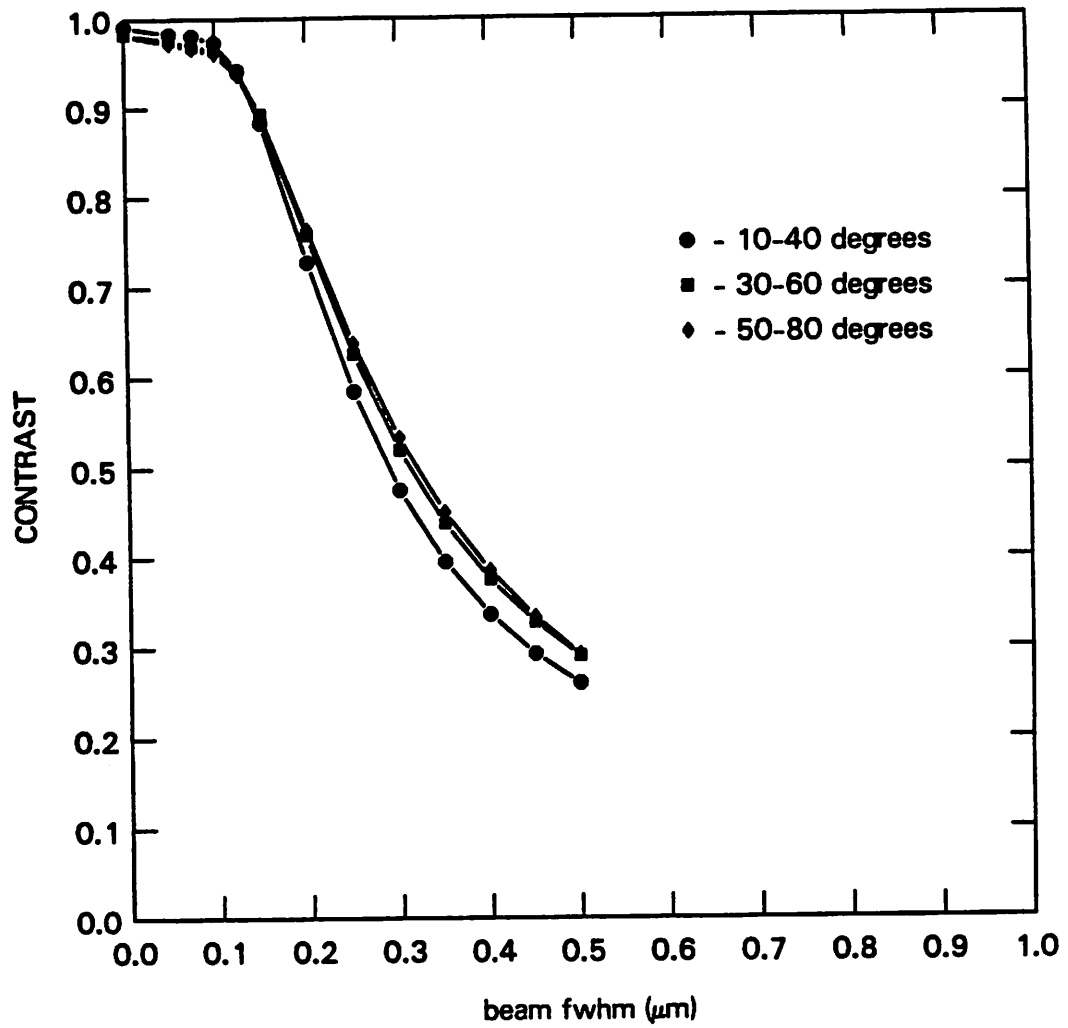


Figure 4.4b. A plot of contrast versus beam fwhm for the $0.25 \mu\text{m}$ hole at 25 kV beam voltage.

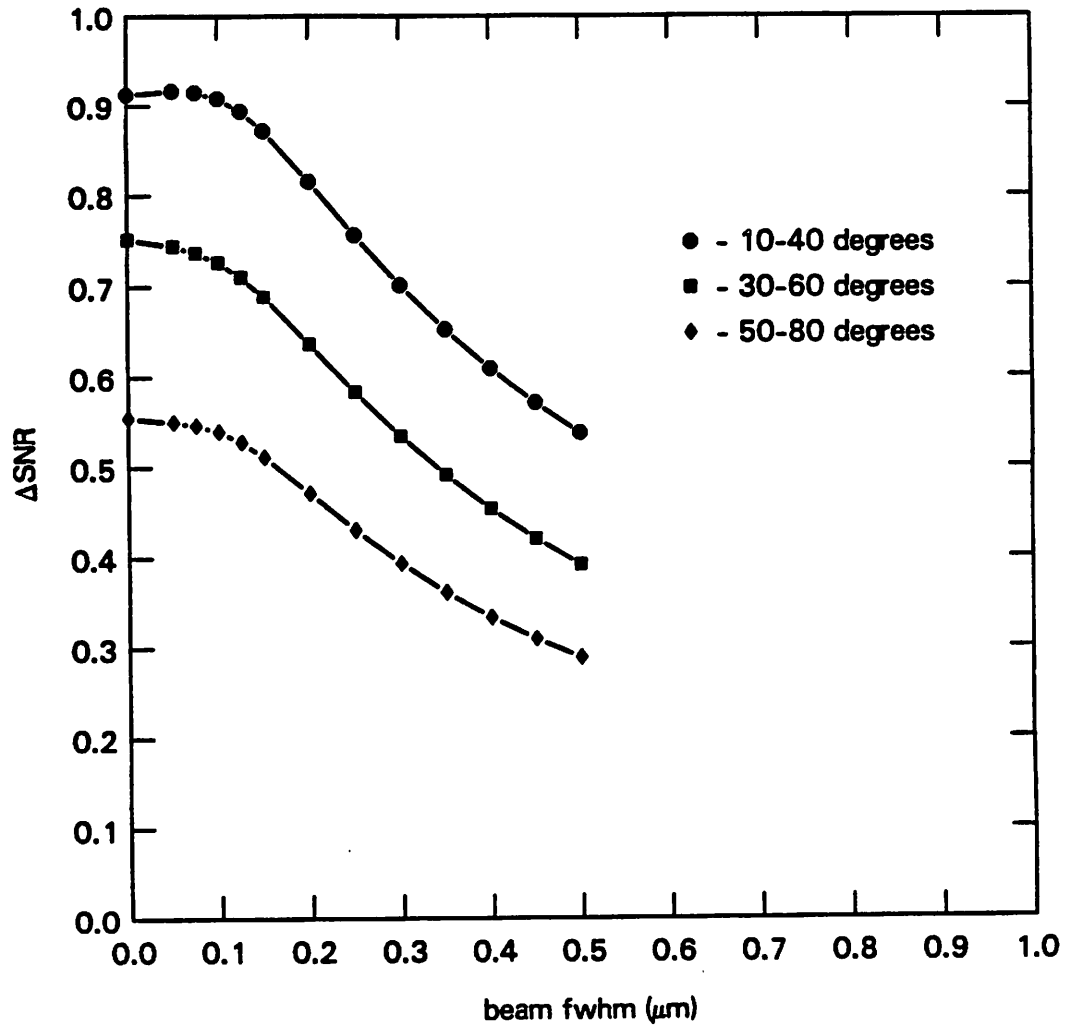


Figure 4.5a. A plot of ΔSNR versus beam fwhm for the $0.25 \mu\text{m}$ step at 25 kV beam voltage.

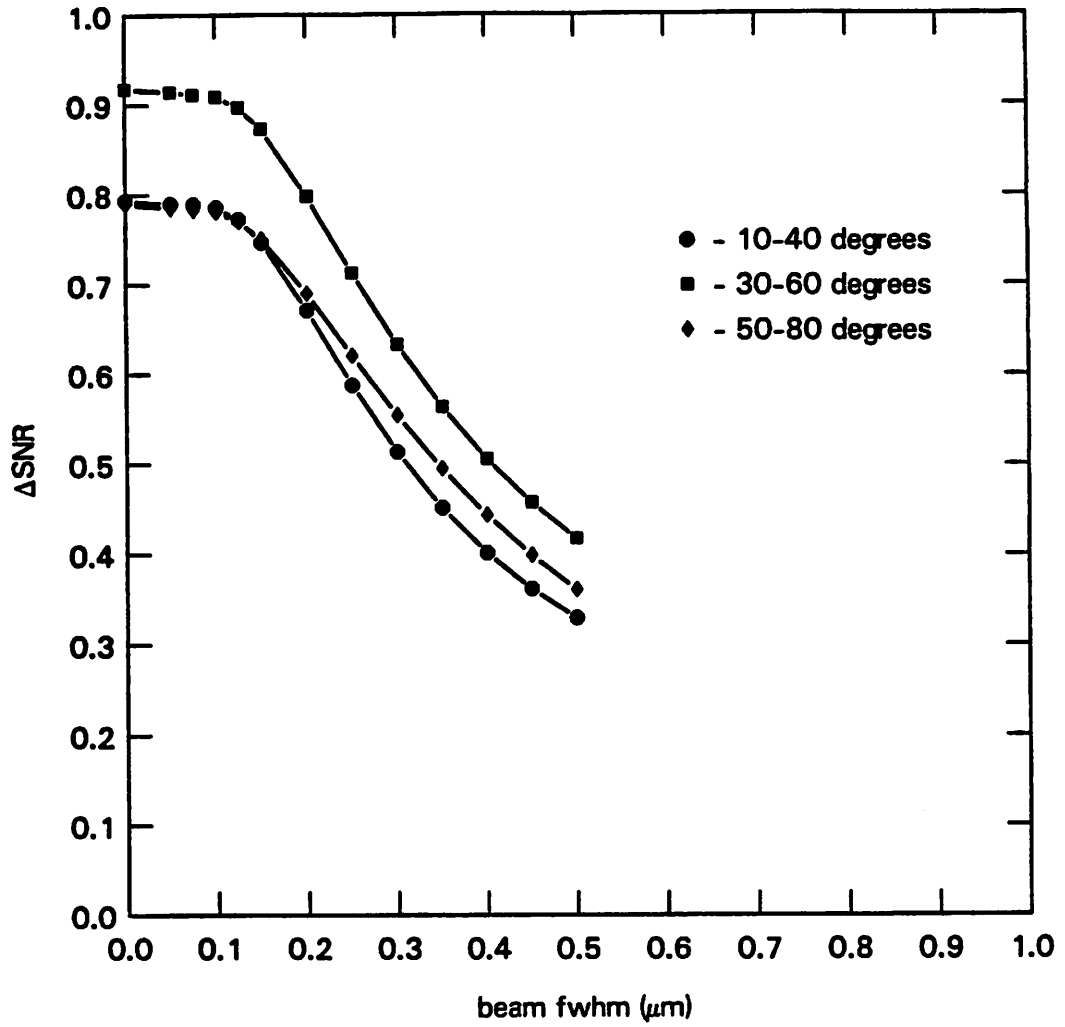


Figure 4.5b. A plot of ΔSNR versus beam fwhm for the $0.25 \mu\text{m}$ hole at 25 kV beam voltage.

show large changes with different angle collection ranges, the contrast remains high for holes. As was discussed in the previous section and will be shown in Chapter 5, the difference between the gold and silicon signal levels is an important factor in determining the noise quality of the signal. Therefore, it is the Δ SNR graph of Figure 4.5b which correctly shows the effects of angle collection range on the noise quality of the signal. Note that the contrast curves for the $0.25 \mu\text{m}$ step do show the effects of changing the angle collection range. This is because a step structure's signal levels change differently with different angle collection ranges. Thus, the Δ SNR will be used as one measure of signal quality in this chapter.

4.3.1. Δ SNR

The effects of beam size and angle collection range on the noise quality of the backscattered electron signal are shown in Figures 4.5a-h, Δ SNR versus beam size for the different structures simulated. The first observation which can be made is that for submicron step structures, the lower angle range gives the best signal. This is because many electrons exit from the sides of the step at low take-off angles. However, the 30-60 degrees range appears to be best for the holes. This is what was shown in section 4.2 and implies that if a single detector is used for mask inspection, some type of tradeoff in placement will be required. Note that the 10-40 and 50-80 degrees ranges are almost identical for the hole structures. This agrees with the observation made in section 4.2 that holes look like bulk gold except in the immediate vicinity of the defect. Thus, the optimum detector placement for clear defects will be the same as for bulk gold. The fundamental shot noise limitations of the backscattered electron signals will be discussed in Chapter 5.

As far as the effects of beam size are concerned, a degradation in Δ SNR starts when the beam size becomes at least four-tenths of the structure fwhm. For the steps, a 25 percent loss of Δ SNR occurs when the (beam fwhm)/(structure fwhm) ratio is about 1.2. Similar results are seen for the holes with a 25 percent reduction in Δ SNR being observed at a ratio of about 1.1.

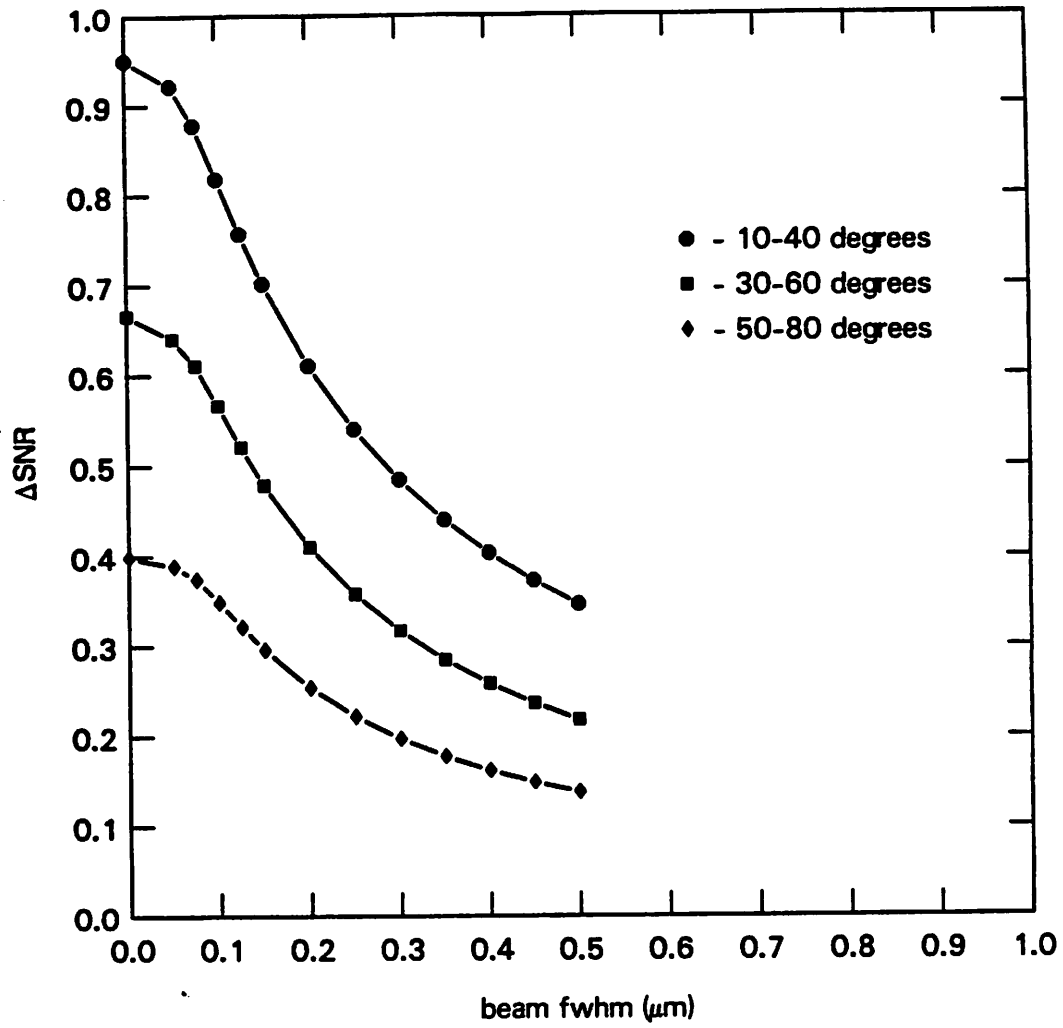


Figure 4.5c. A plot of ΔSNR versus beam fwhm for the $0.125 \mu\text{m}$ step at 25 kV beam voltage.

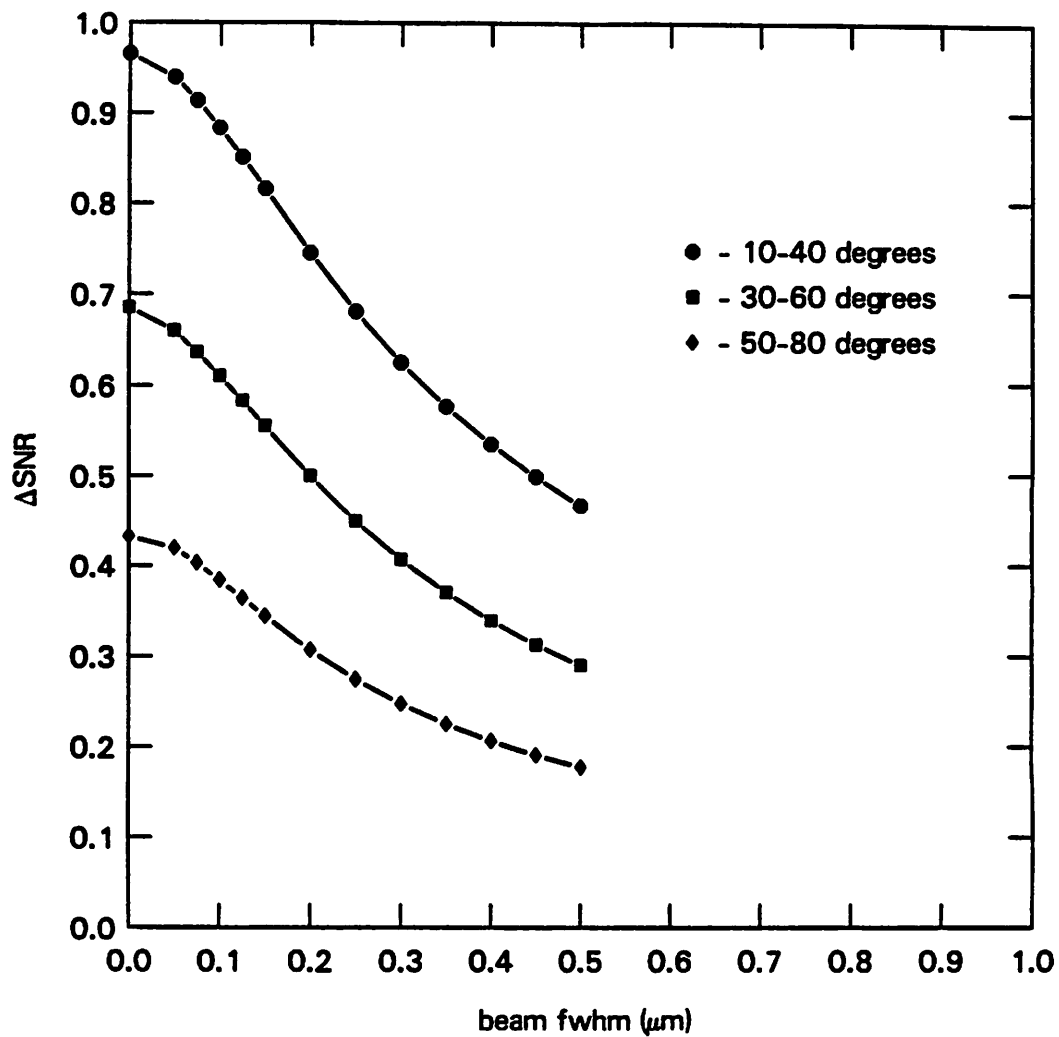


Figure 4.5d. A plot of ΔSNR versus beam fwhm for the angled step at 25 kV beam voltage. The top dimension is $0.1 \mu\text{m}$ and the bottom dimension is $0.25 \mu\text{m}$.

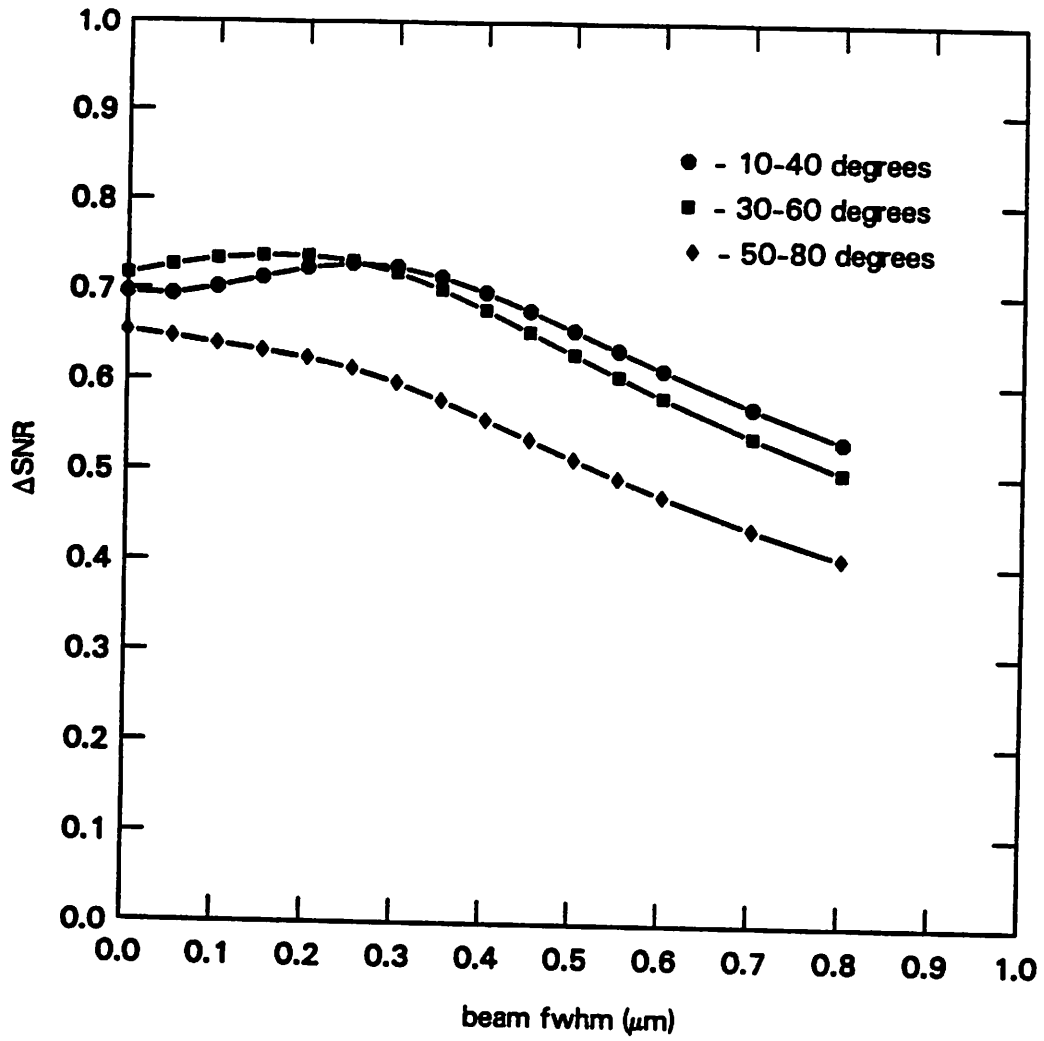


Figure 4.5e. A plot of ΔSNR versus beam fwhm for the $0.55 \mu\text{m}$ step at 25 kV beam voltage.

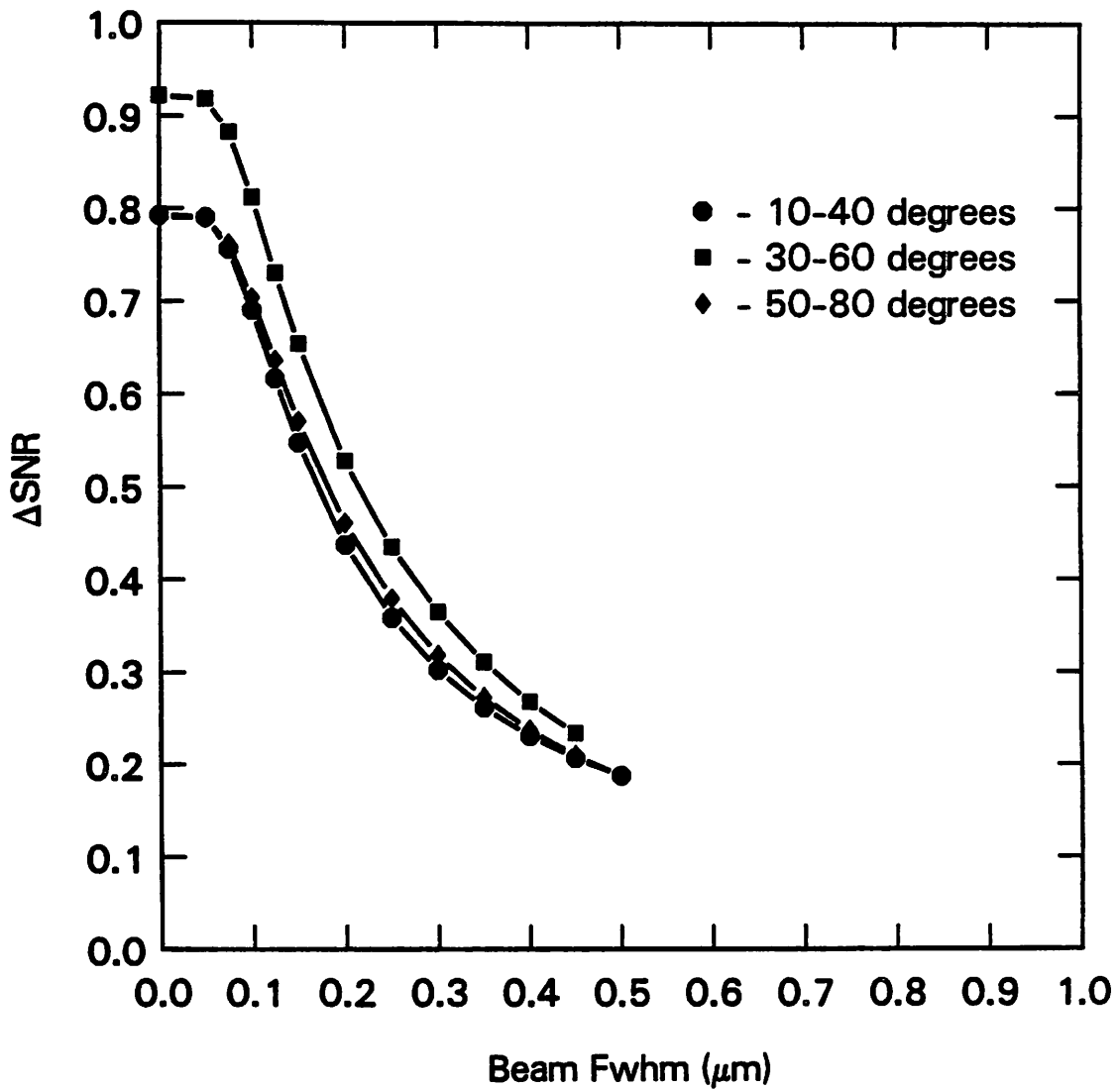


Figure 4.5f. A plot of ΔSNR versus beam fwhm for the $0.125 \mu\text{m}$ hole at 25 kV beam voltage.

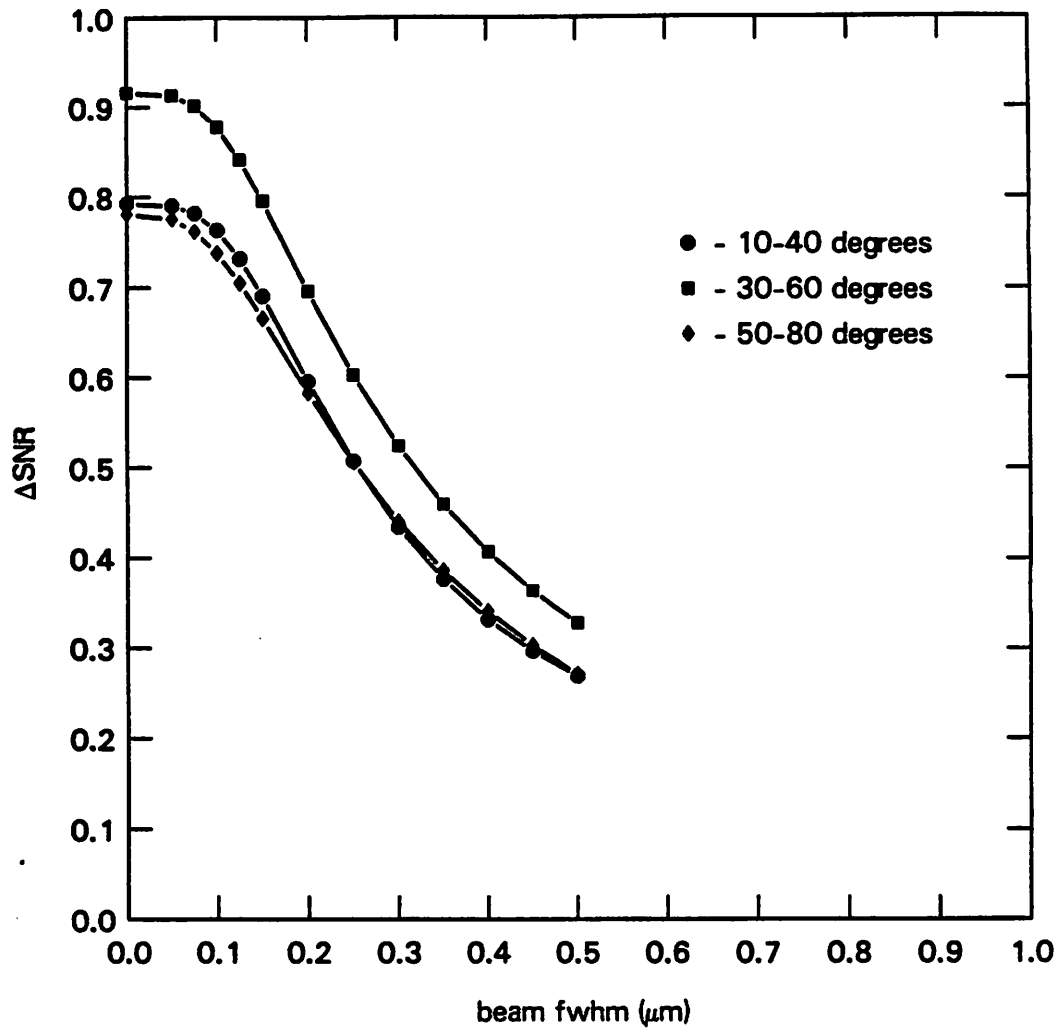


Figure 4.5g. A plot of ΔSNR versus beam fwhm for the angled hole at 25 kV beam voltage. The top dimension is $0.25 \mu\text{m}$ and the bottom dimension is $0.1 \mu\text{m}$

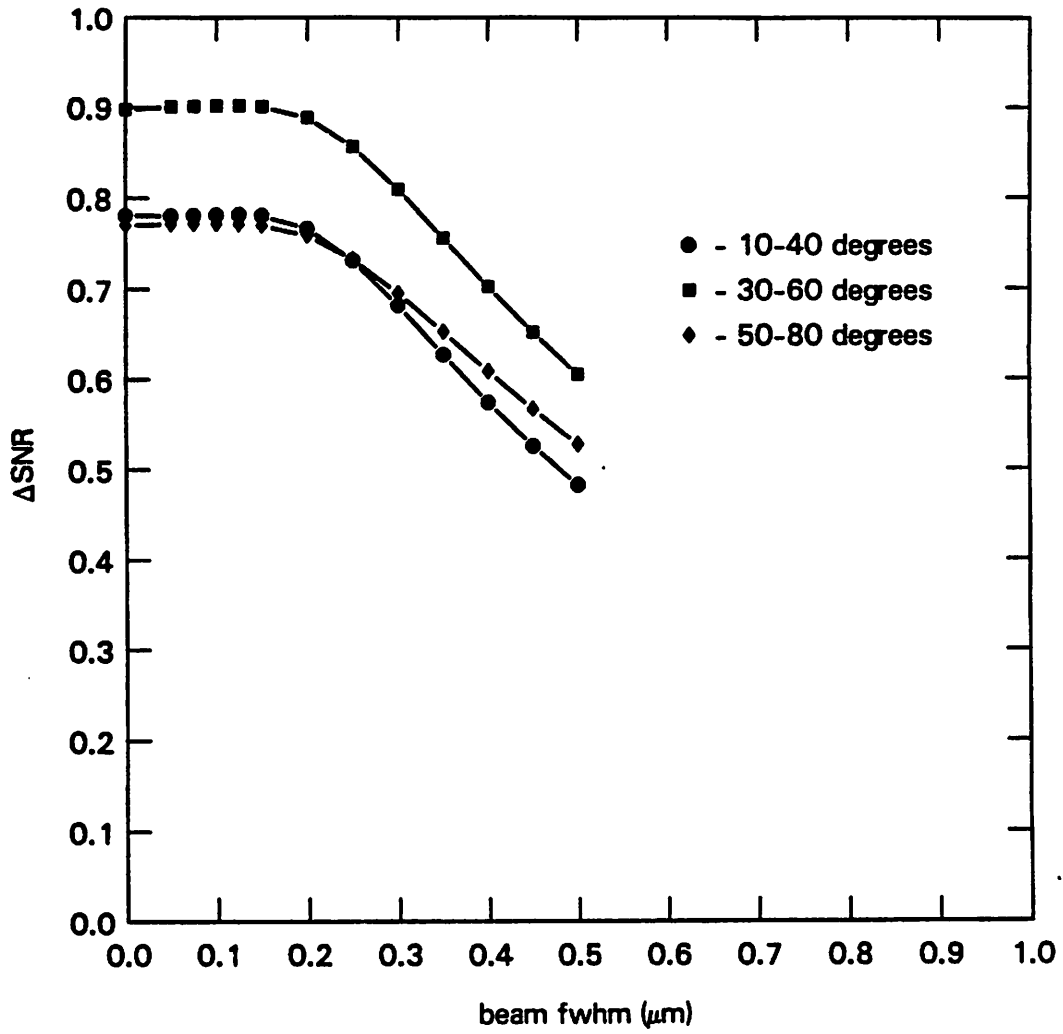


Figure 4.5h. A plot of ΔSNR versus beam fwhm for the $0.4 \mu\text{m}$ hole at 25 kV beam voltage.

4.3.2. Backscattered Electron Signal Fwhm

The effects of beam size and angle collection range on the fwhm of the backscattered electron signals are shown in Figures 4.6a-h. As would be expected, the lower angle range tends to give a signal fwhm which is closer to the actual fwhm of the structure. This becomes more apparent as the structure size increases. For the smaller structures, 0.25 μm and below, the angle collection range does not appear to have a significant influence on the signal fwhm. For the larger structures, in which the two sides of the structure are isolated (as far as the electrons are concerned), the higher angle range gives a smaller signal fwhm than the lower ranges. This is because the electrons scattering near the edge are concentrated in the lower angle ranges; therefore, the signal rises more slowly if only higher angles are collected. Generally, and especially for the middle angle ranges, the signal fwhm from steps are slightly smaller than the step fwhm and signals from holes are slightly larger than the hole fwhm. This, of course, pertains to beam sizes which do not significantly affect the signal fwhm. The discrepancy of signal fwhm and structure fwhm has implications when using an electron-beam system or SEM for linewidth measurement [3,54].

Generally, the signal fwhm is fairly constant for small beam sizes and then begins to increase steadily when the incident beam size becomes larger than about 0.4-0.5 of the structure fwhm. In other words, there are two distinct regions of the signal fwhm versus beam fwhm curves. The first is the level area of the curve in which material and scattering properties dominate and the other is the rising area of the curve in which the beam size dominates. For steps, a signal fwhm 50 percent larger than the structure fwhm occurs for a (beam fwhm)/(structure fwhm) ratio of about 1.3-1.4. For holes, a 50 percent increase is seen for a ratio of about 1.1-1.2. This has implications in mask inspection if the desired minimum detectable defect size is smaller than the probing electron-beam. Depending on the threshold setting of the comparator used to digitize the signal, the detected size of the defect could be considerably larger than the actual size.

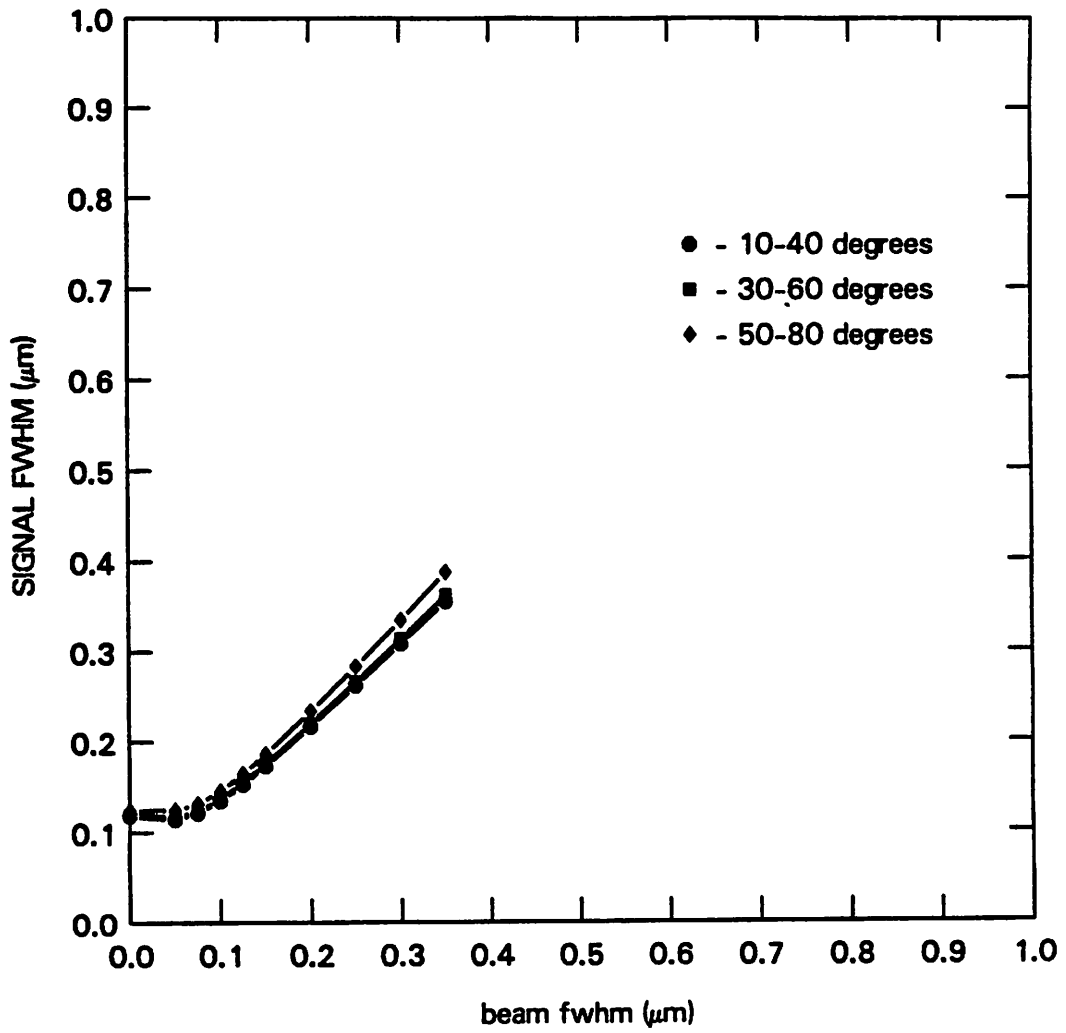


Figure 4.6a. A plot of signal fwhm versus beam fwhm for the 0.125 μm step at 25 kV beam voltage.

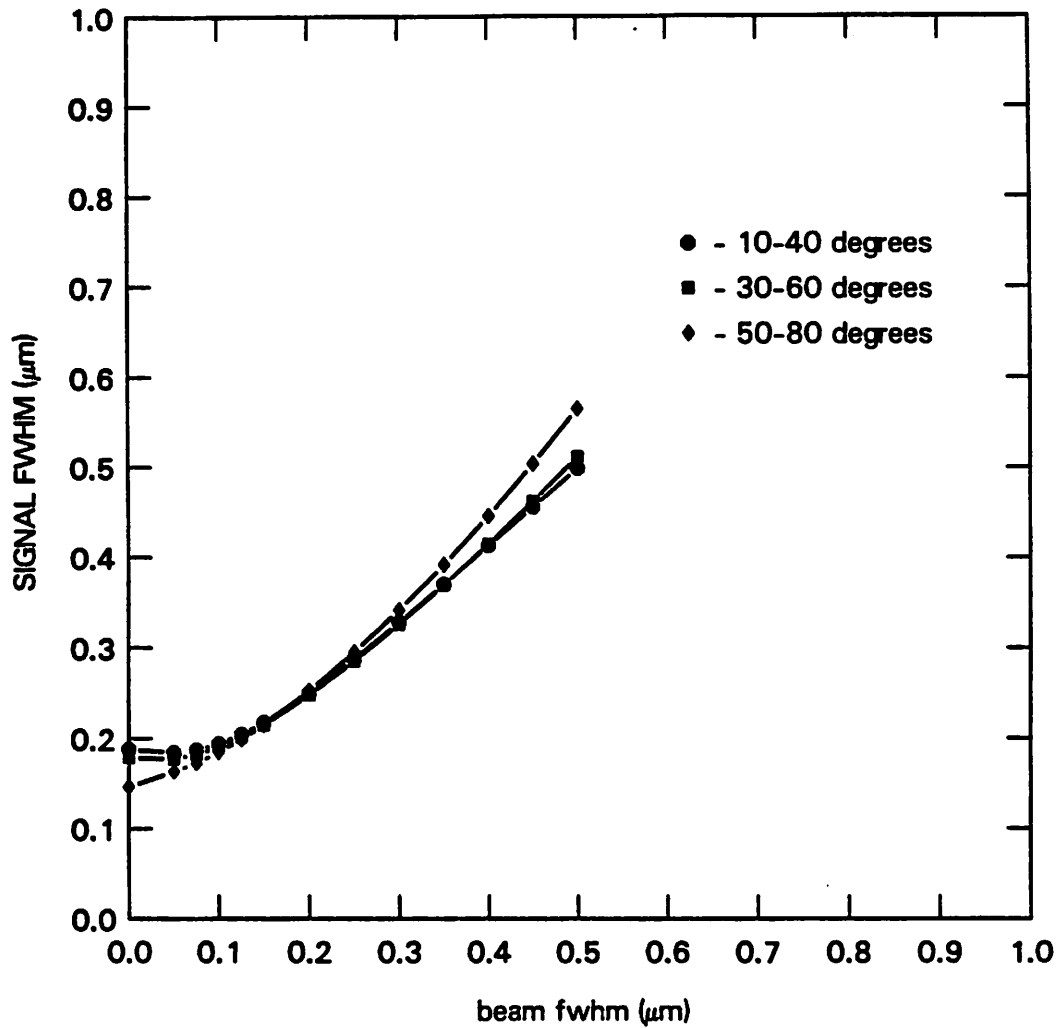


Figure 4.6b. A plot of signal fwhm versus beam fwhm for the angled step at 25 kV beam voltage. The top dimension is $0.1 \mu\text{m}$ and the bottom dimension is $0.25 \mu\text{m}$.

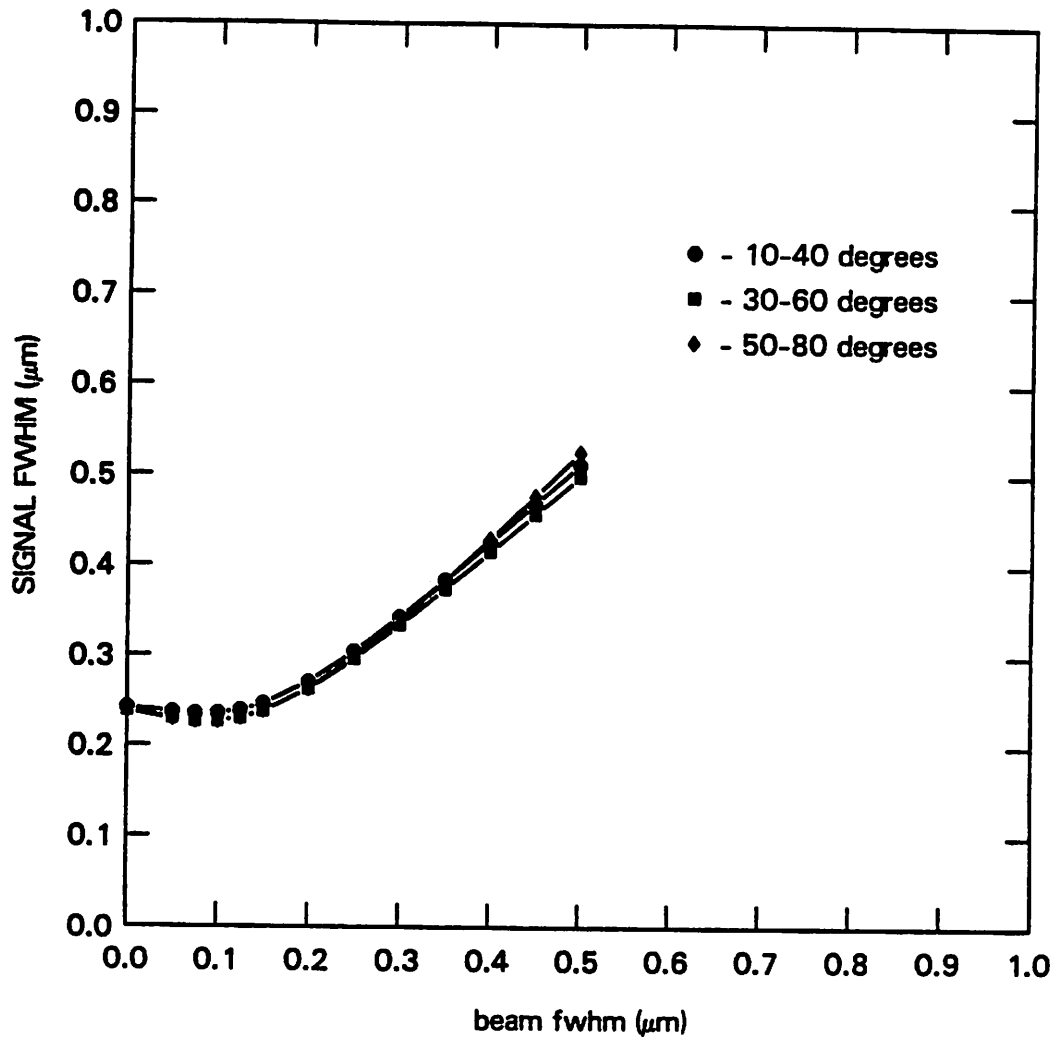


Figure 4.6c. A plot of signal fwhm versus beam fwhm for the 0.25 μm step at 25 kV beam voltage.

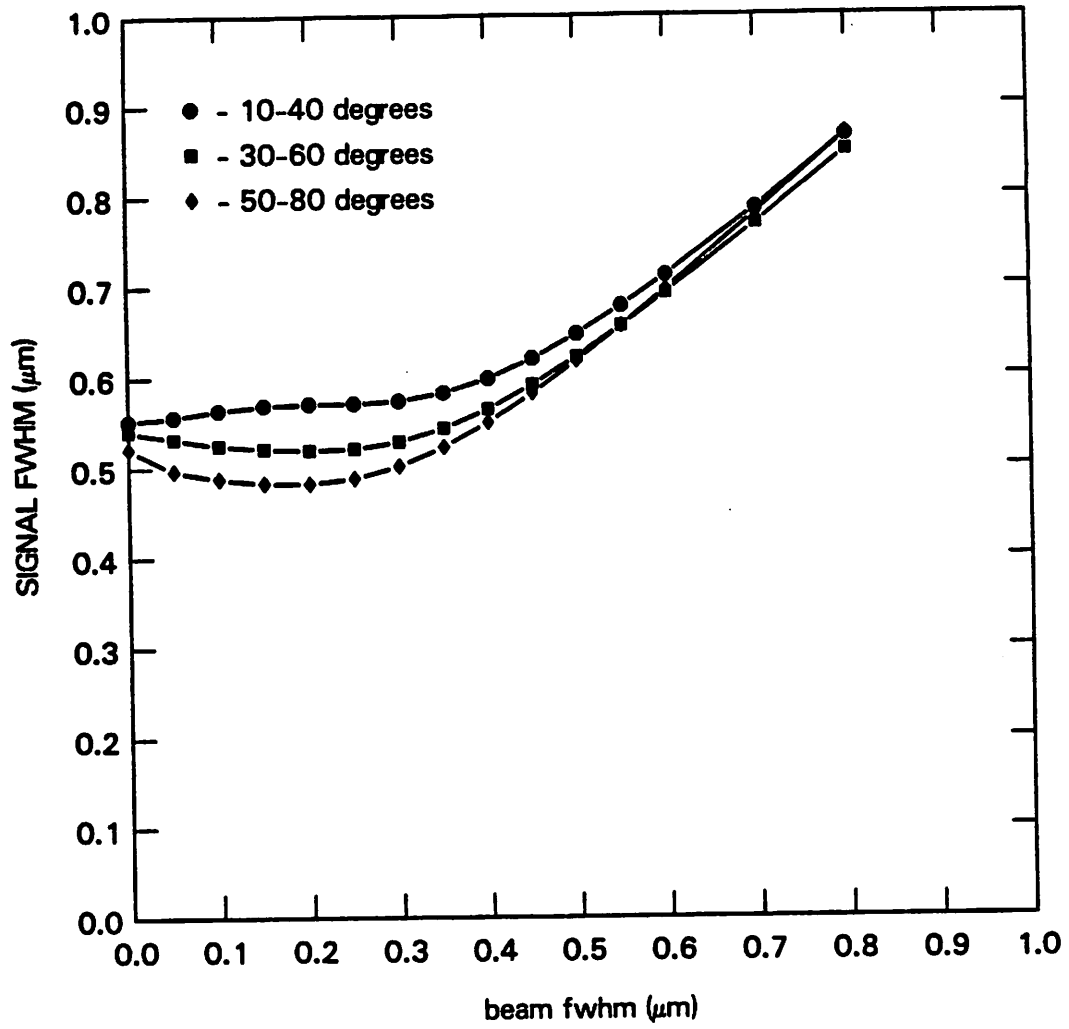


Figure 4.6d. A plot of signal fwhm versus beam fwhm for the 0.55 μm step at 25 kV beam voltage.

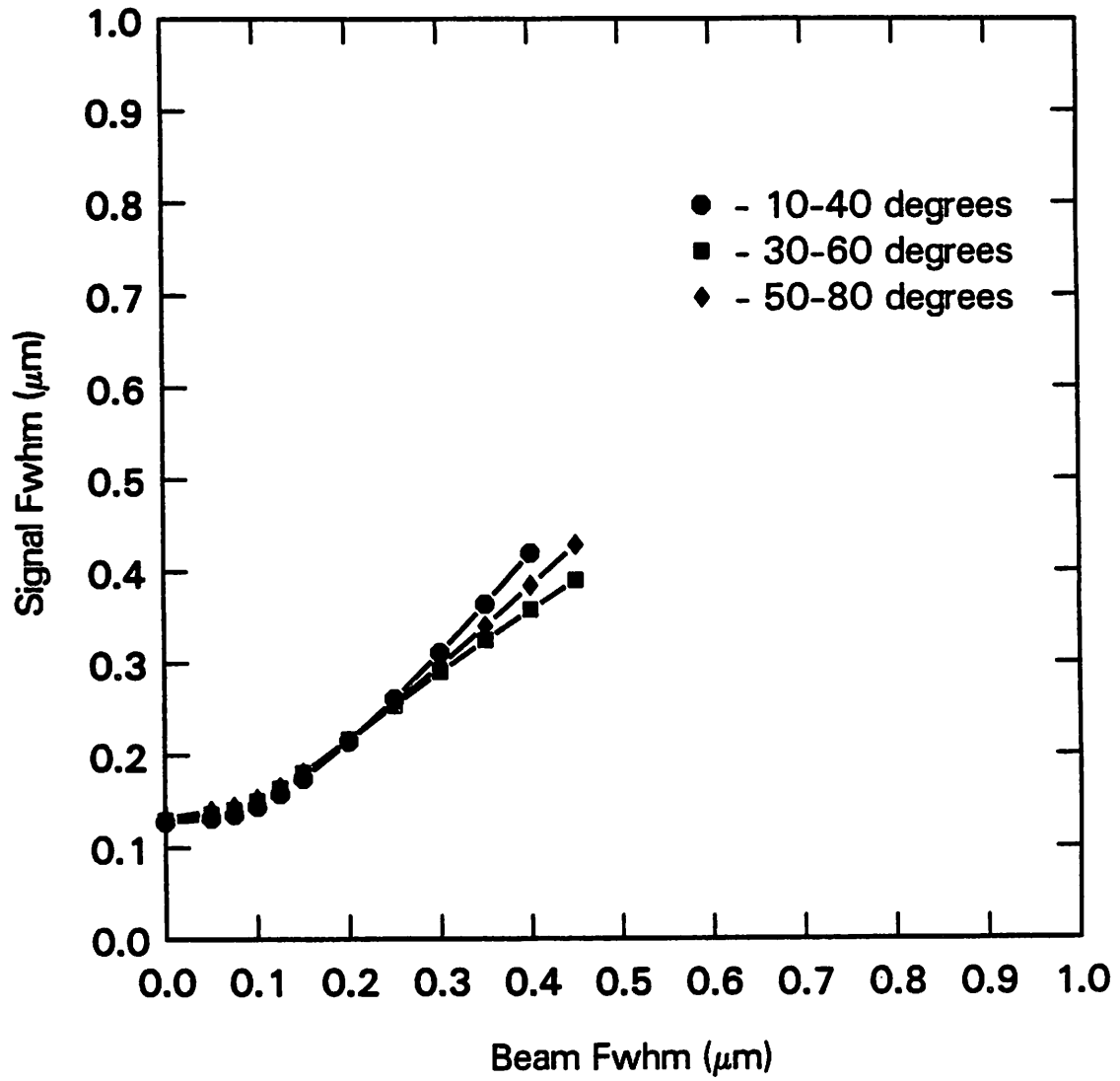


Figure 4.6e. A plot of signal fwhm versus beam fwhm for the 0.125 μm hole at 25 kV beam voltage.

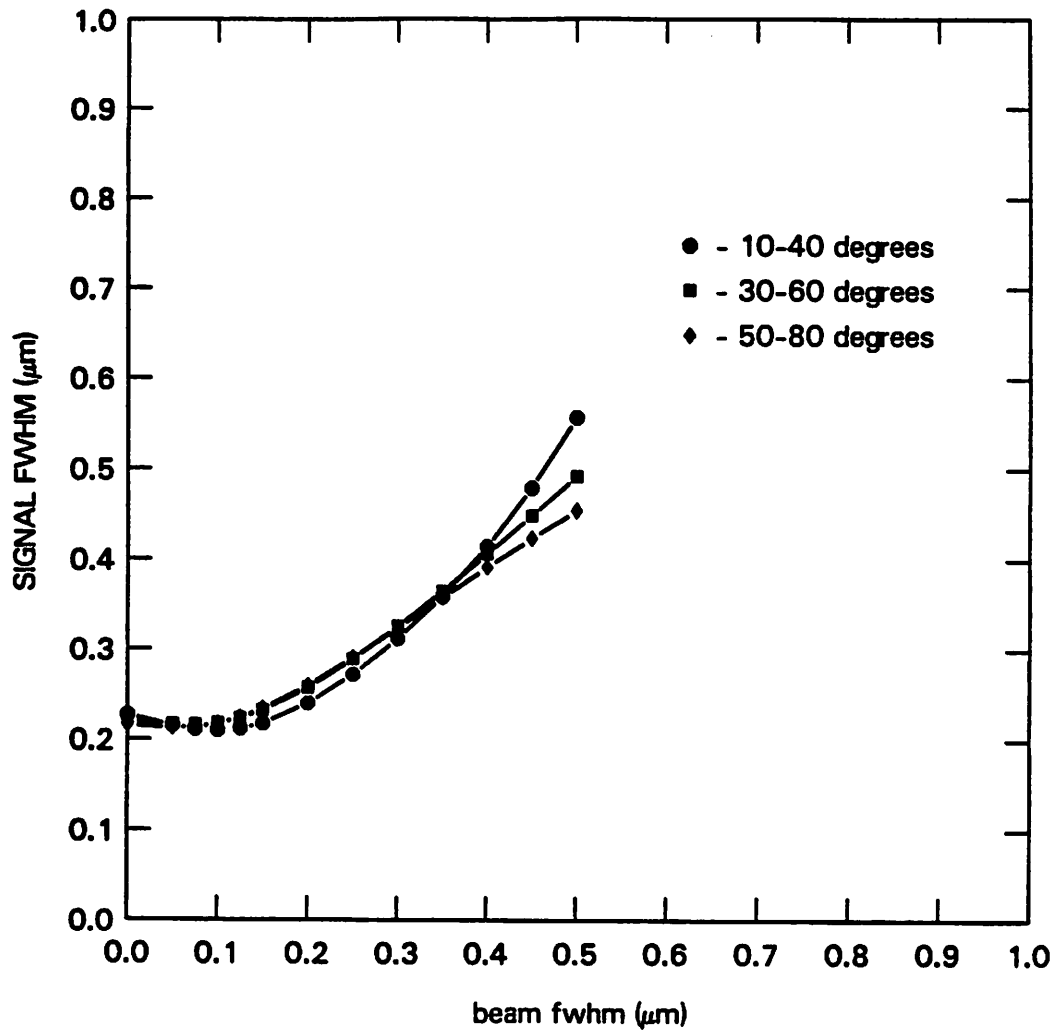


Figure 4.6f. A plot of signal fwhm versus beam fwhm for the angled hole at 25 kV beam voltage. The top dimension is $0.25 \mu\text{m}$ and the bottom dimension is $0.1 \mu\text{m}$

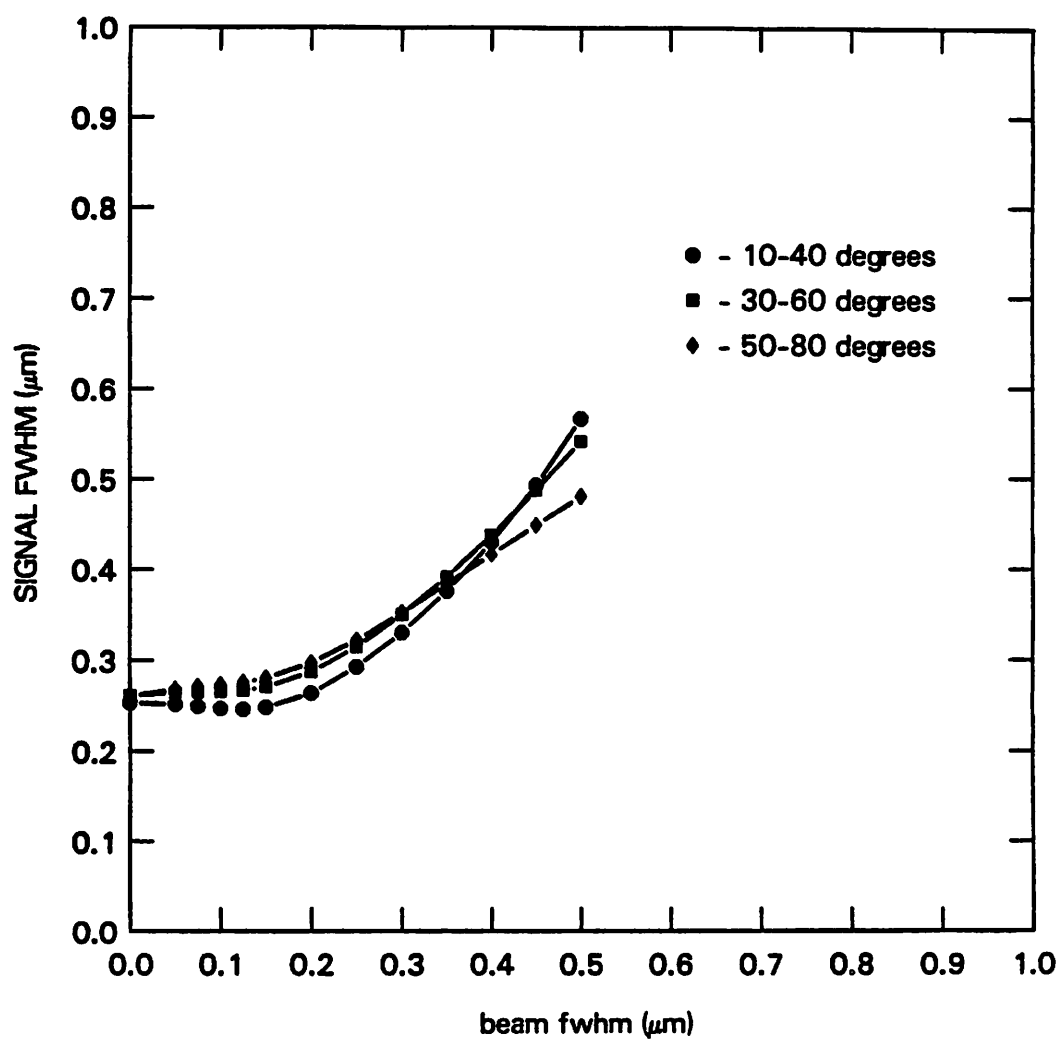


Figure 4.6g. A plot of signal fwhm versus beam fwhm for the $0.25 \mu\text{m}$ hole at 25 kV beam voltage.

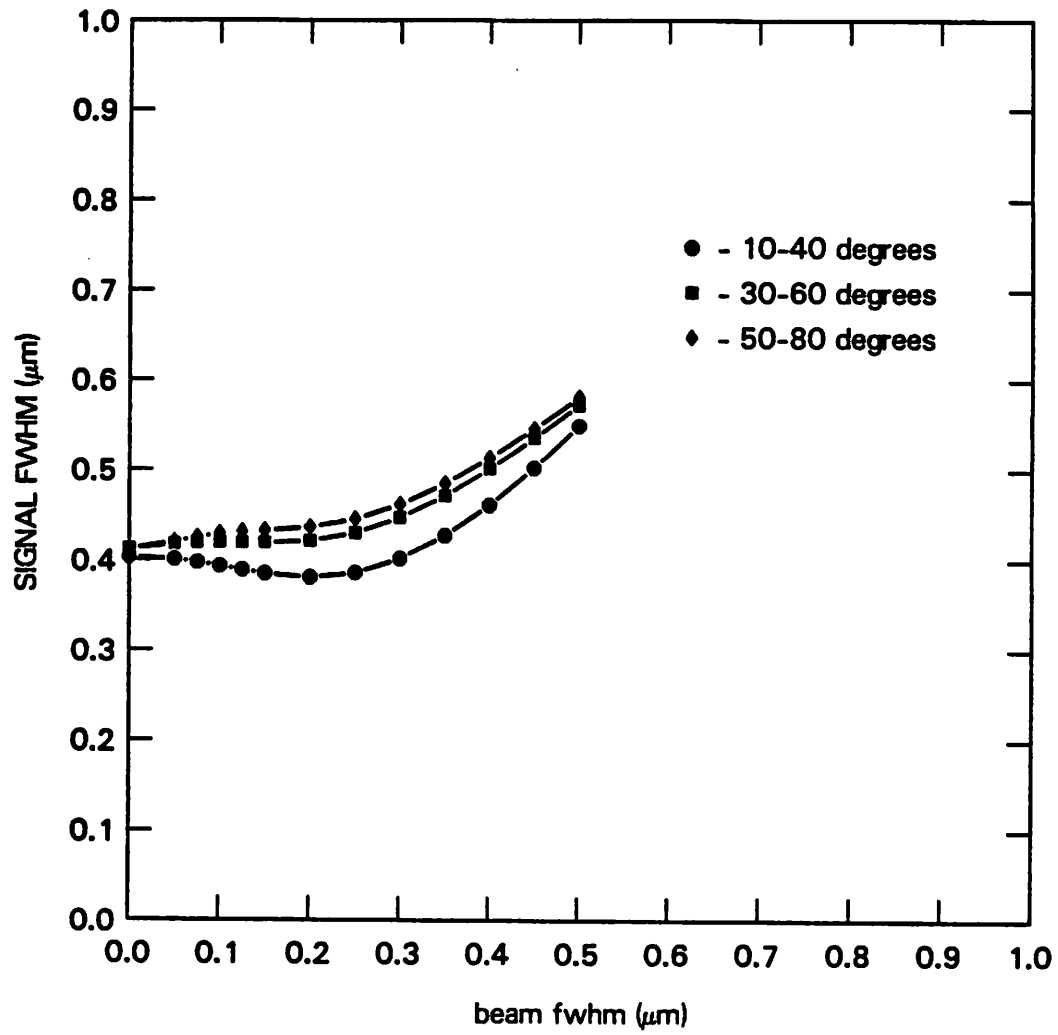


Figure 4.6h. A plot of signal fwhm versus beam fwhm for the 0.4 μm hole at 25 kV beam voltage.

4.3.3. Threshold (DC Level)

The threshold, or midpoint between high and low signal levels, will change with increasing beam size. For small steps, the high signal level will drop towards the silicon level as the beam size becomes larger than the structure. In other words, the presence of the structure has less of an effect on the scanning beam. A similar process occurs for holes in a gold film with the minimum signal level rising towards the gold signal level as the beam size increases. Graphs of threshold versus beam fwhm are shown in Figures 4.7a-4.7h. The units for the threshold are in terms of the partial energy signal.

As would be expected for holes, the 10-40 and 50-80 degrees angle collection ranges have essentially the same thresholds. The 30-60 degrees range gives higher thresholds since the high signal level is larger (see Figures 4.2, 4.5b, and 4.5f-h). For the 0.25 μm and smaller step structures, the lower angle ranges give higher thresholds. As the structure size increases (Figure 4.7d, the 0.55 μm step), the 30-60 degrees range gives a higher threshold since the maximum signal level is generated from an area which, to the electrons, almost resembles bulk gold.

It can be seen by examining Figure 4.7 that for a given beam size, there is a difference in threshold or DC level between steps and holes. The threshold of a signal is a complex function of the beam size, beam voltage, structure size, and detector configuration. The DC level difference is important since in most cases a comparator threshold will have to be set so that the mask inspection system can electronically determine the presence or absence of masking material. As will be seen in Chapter 5, the placement of the comparator threshold, in relation to the high and low signal levels, will greatly influence the SNR characteristics of the backscattered electron signal.

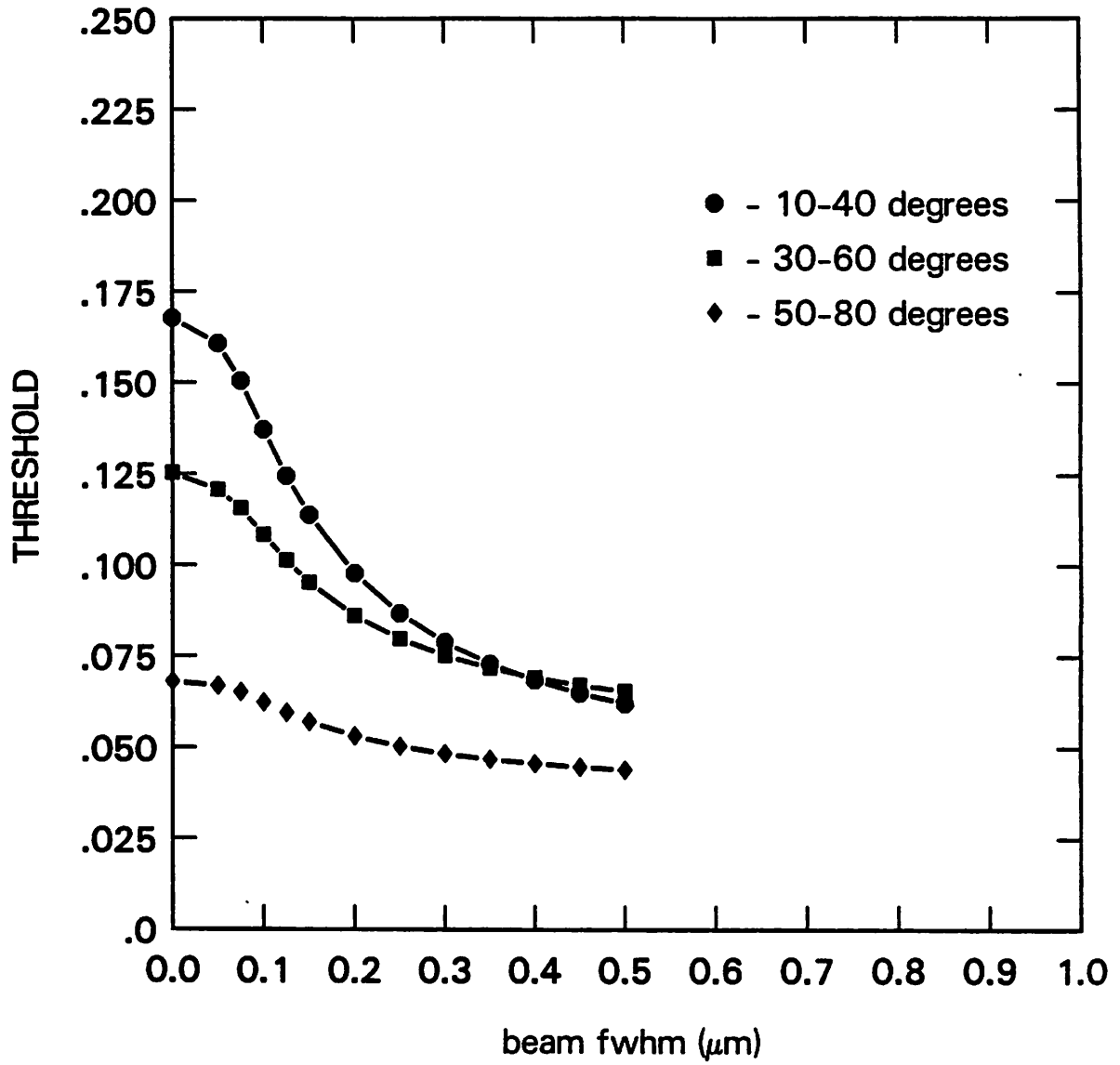


Figure 4.7a. A plot of threshold versus beam fwhm for the $0.125 \mu\text{m}$ step at 25 kV beam voltage.

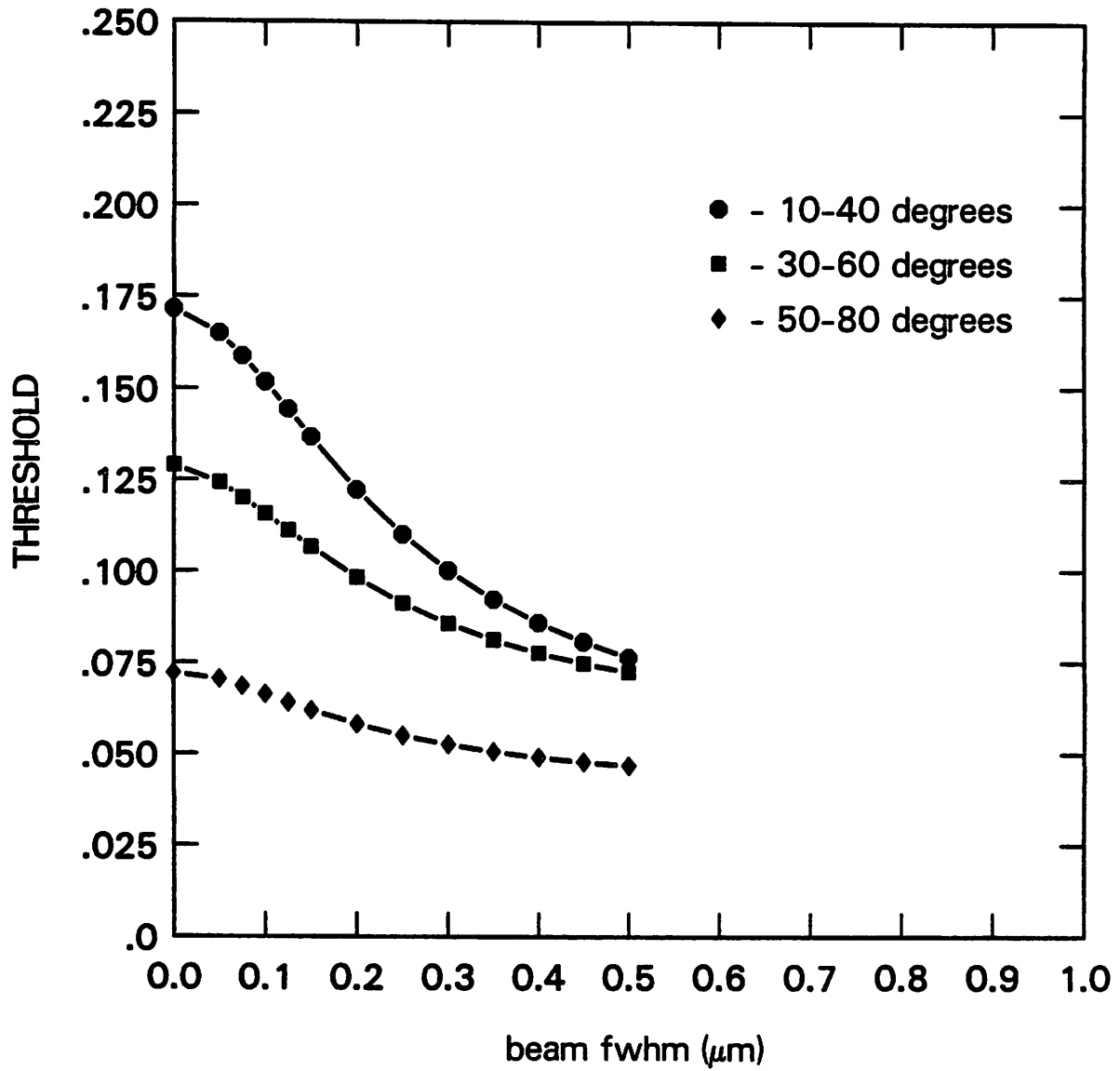


Figure 4.7b. A plot of threshold versus beam fwhm for the angled step at 25 kV beam voltage. The top dimension is $0.1 \mu\text{m}$ and the bottom dimension is $0.25 \mu\text{m}$.

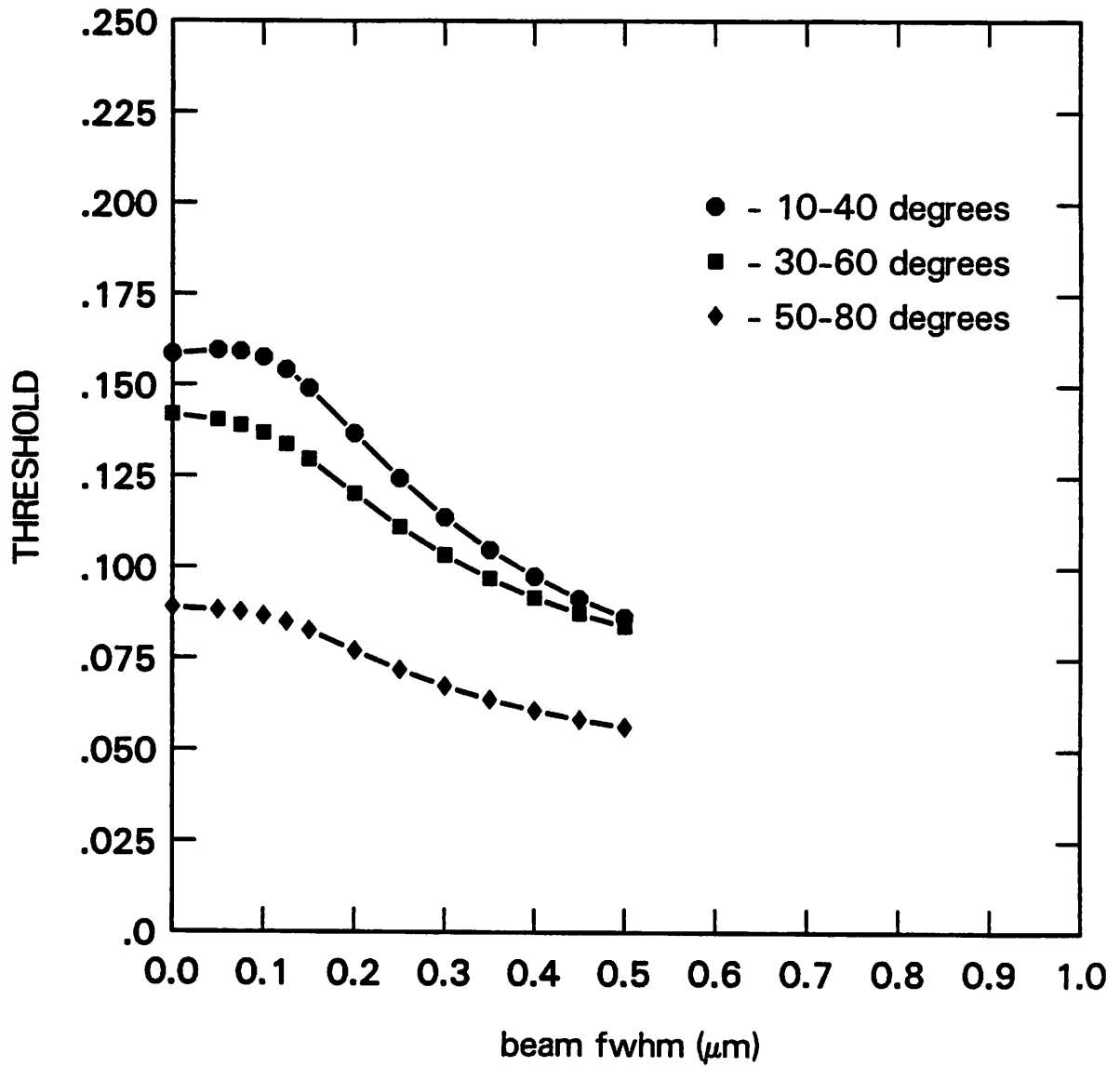


Figure 4.7c. A plot of threshold versus beam fwhm for the 0.25 μm step at 25 kV beam voltage.

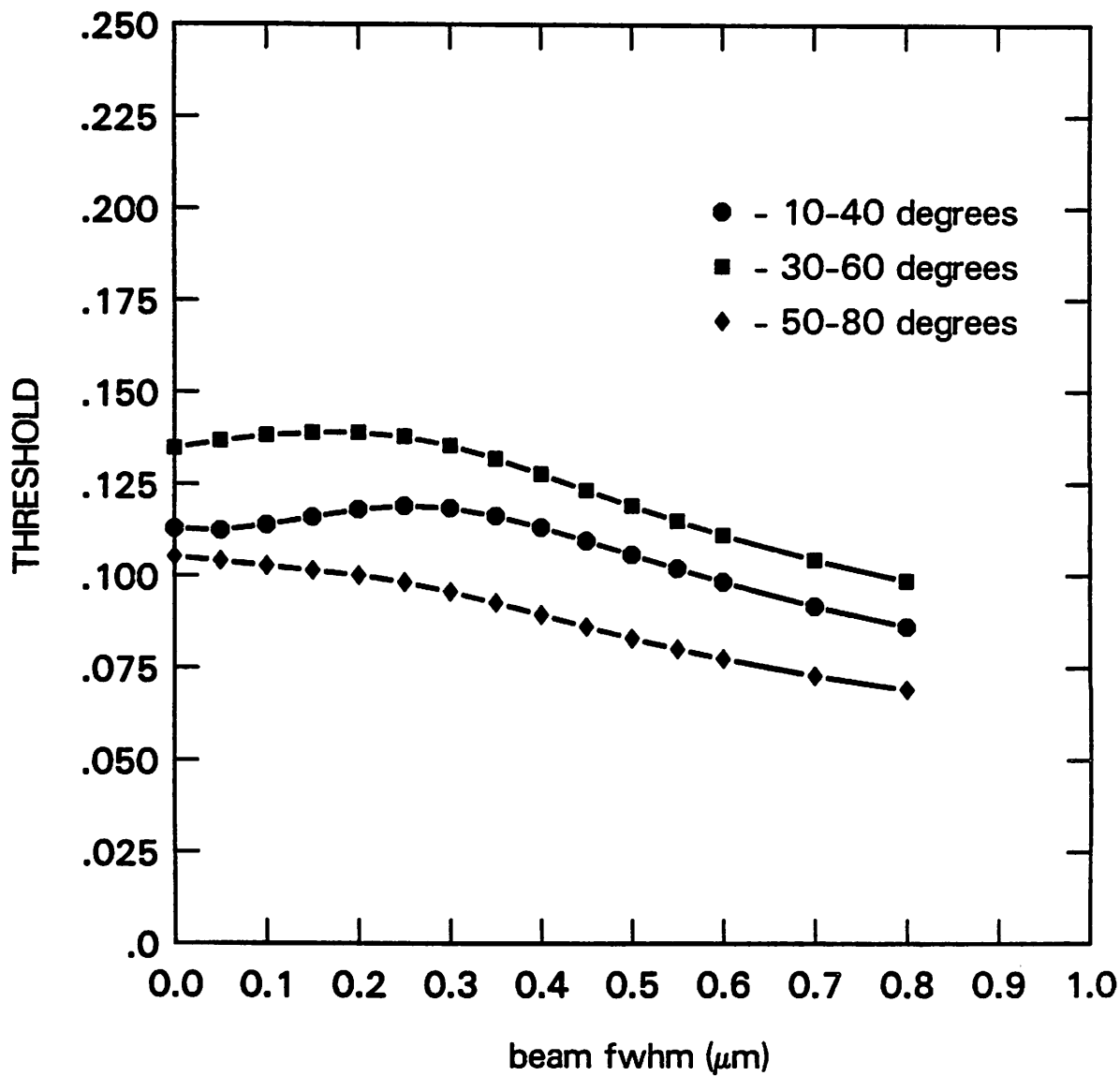


Figure 4.7d. A plot of threshold versus beam fwhm for the $0.55 \mu\text{m}$ step at 25 kV beam voltage.

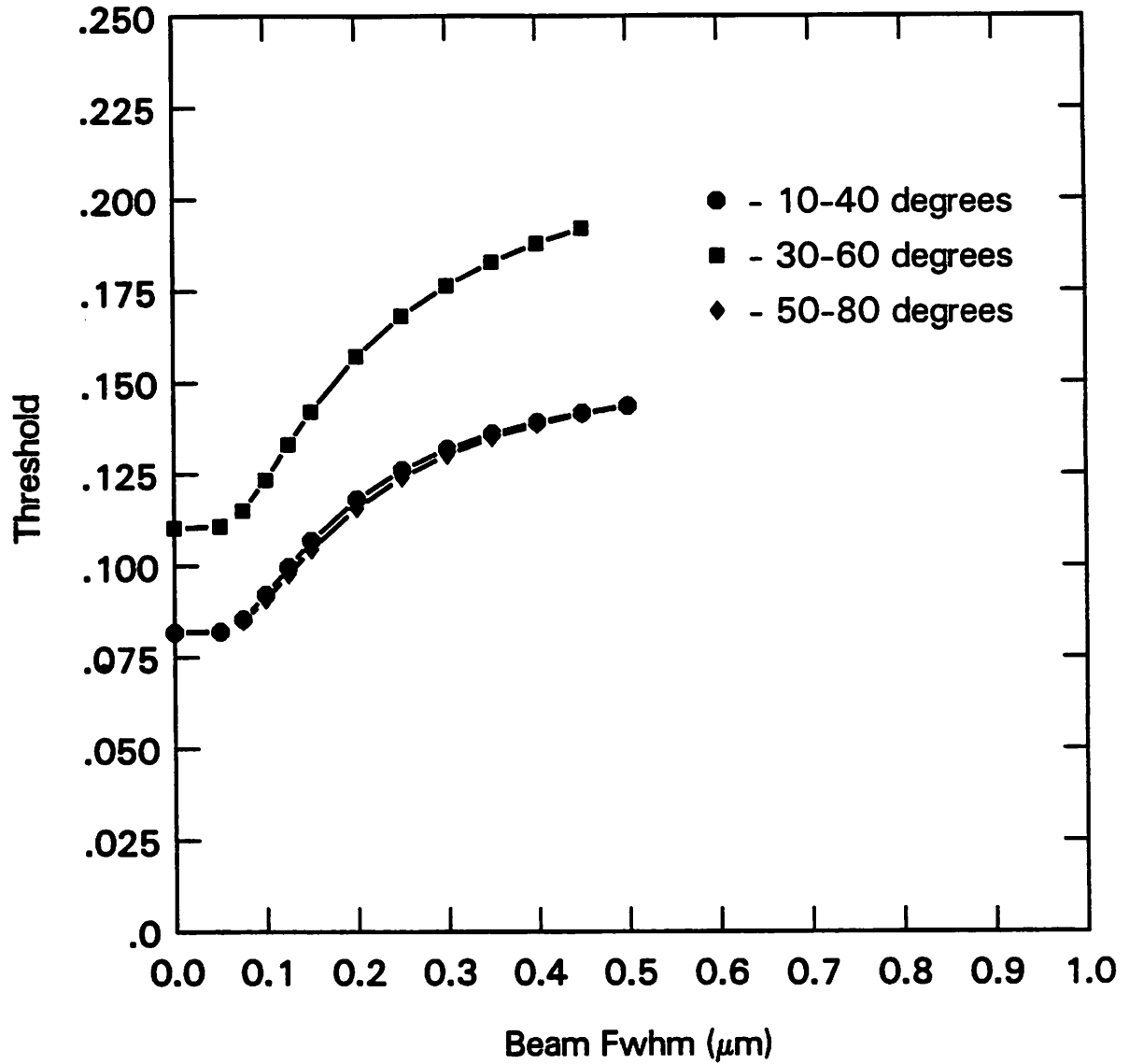


Figure 4.7e. A plot of threshold versus beam fwhm for the $0.125 \mu\text{m}$ hole at 25 kV beam voltage.

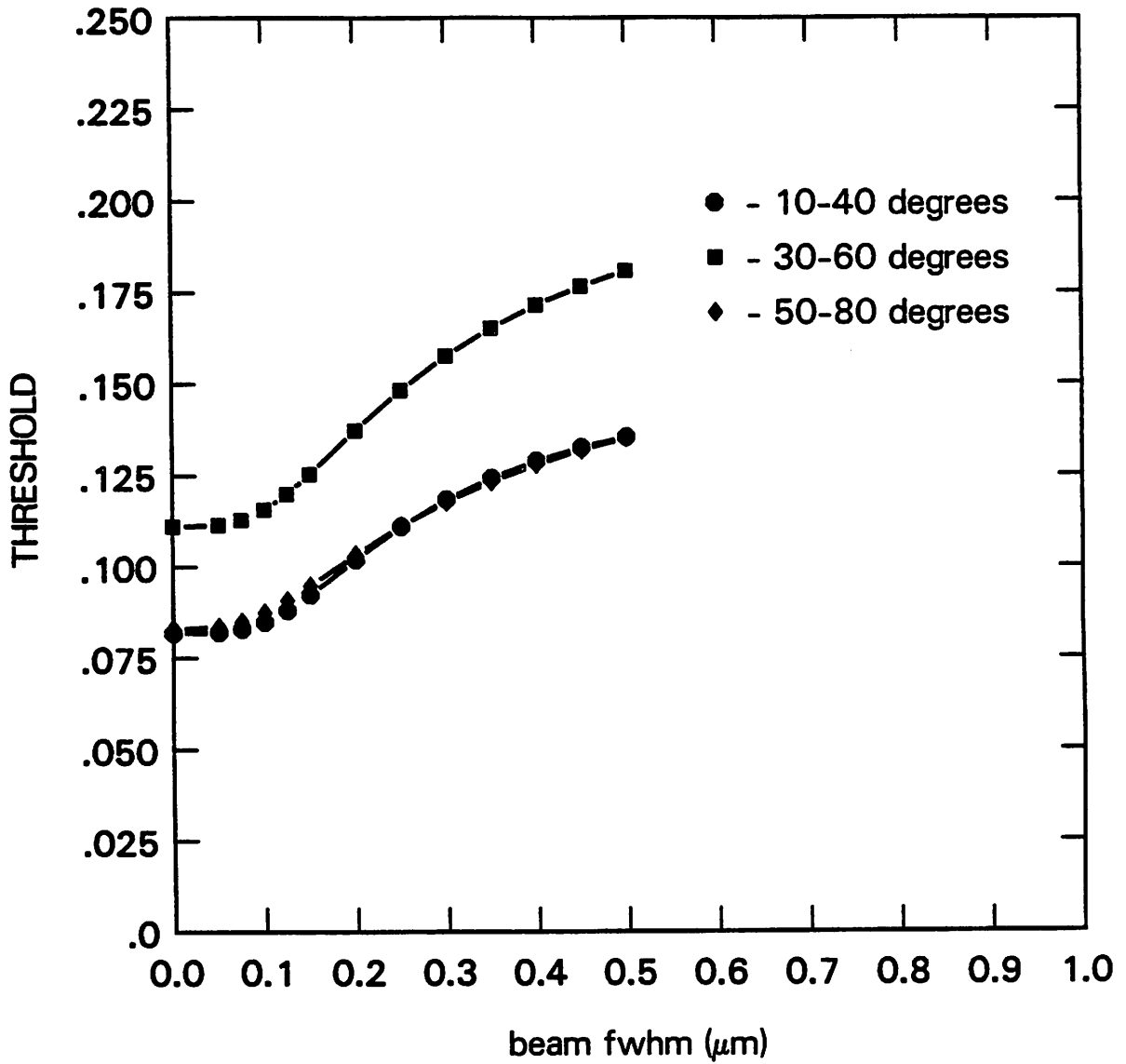


Figure 4.7f. A plot of threshold versus beam fwhm for the angled hole at 25 kV beam voltage. The top dimension is $0.25 \mu\text{m}$ and the bottom dimension is $0.1 \mu\text{m}$

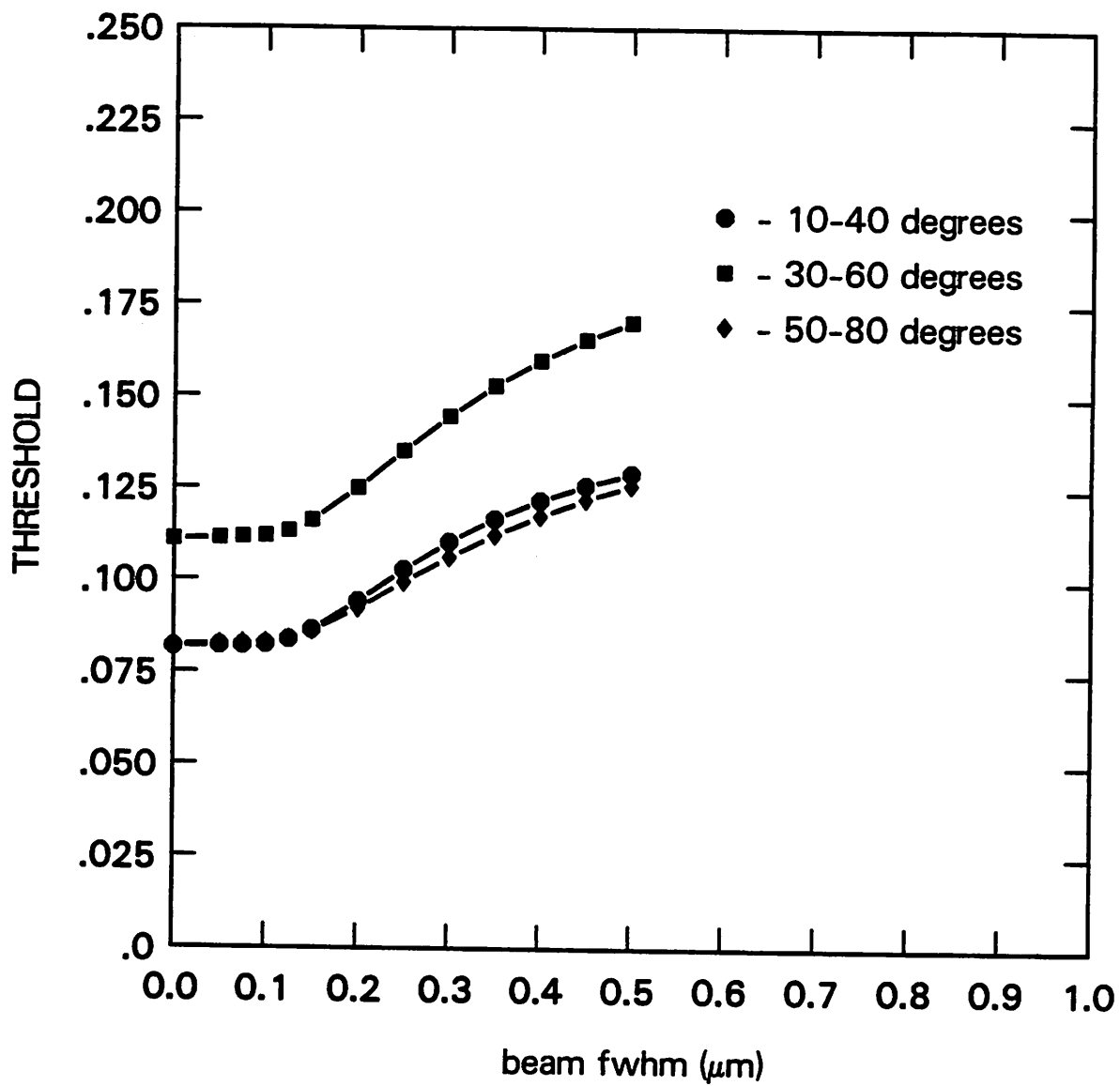


Figure 4.7g. A plot of threshold versus beam fwhm for the 0.25 μm hole at 25 kV beam voltage.

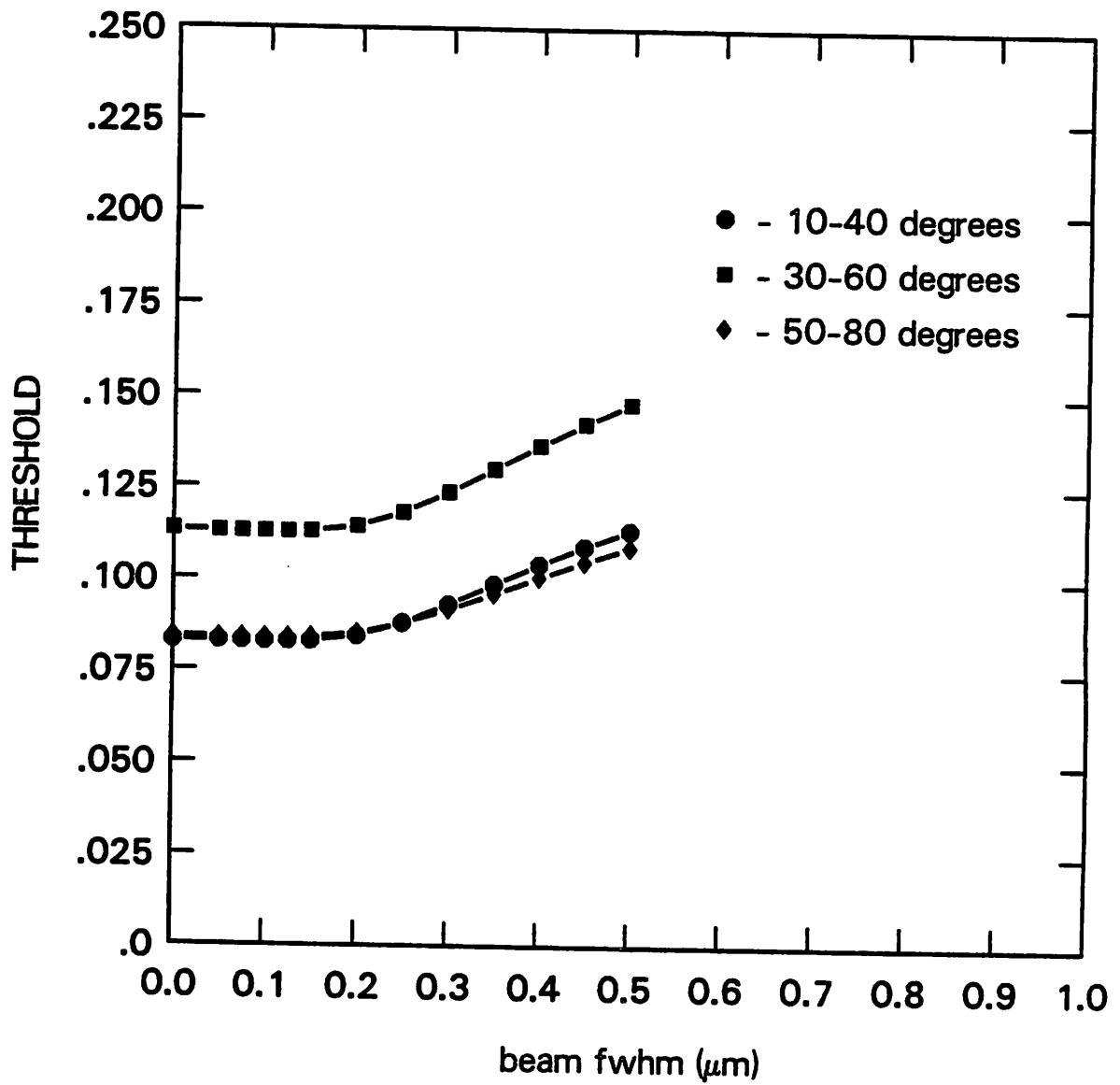


Figure 4.7h. A plot of threshold versus beam fwhm for the 0.4 μm hole at 25 kV beam voltage.

4.4. Absorber Thickness Studies

The previous section was concerned with the effects of beam size and angle collection range on structures with a fixed 0.50 μm gold thickness and with a fixed incident 25 kV electron-beam energy. To repeat the work of the previous section for every combination of defect type, gold thickness, and beam energy would clearly be impossible. Therefore, we will look at infinite films on silicon to gain an understanding of the film thickness requirements for maximum signal levels in mask inspection. Gold on silicon as well as chrome on silicon films will be considered. The simulations were done by calculating the number and energy backscatter coefficients for a single δ -function electron-beam incident on different thicknesses of gold and chrome on silicon.

One of the goals of this study was to see if some simple rules of thumb could be developed for absorber thickness requirements. In his study on alignment signals, Lin [19], introduced a quantity, Z , which was the step depth of the silicon alignment mark normalized to the Bethe range of the electrons in silicon. By normalizing to the Bethe range, Lin obtained universal curves describing the alignment signal characteristics for beam energies ranging from 5-30 kV [19].

A similar technique was used in this study by plotting the backscatter coefficient versus film thickness normalized to the Bethe range, R_B and also the Gruen range [43]:

$$R_G = \frac{.04E_0^{1.75}}{\rho} \quad (4.1)$$

where E_0 is the incident beam energy in kV, ρ is the density in g/cm^3 , and R_G is in μm . Note that many authors use 0.046 instead of 0.04 in their expression for the Gruen range. The expression containing 0.046 was Gruen's original expression for electron energy dissipation in air [43]. In any case, it is only a constant and will not have an effect on the results obtained in this study. Values for R_G and R_B for gold, chrome, and silicon at different beam energies are listed in Figure 4.8. It is important to remember that R_B is calculated using the Monte Carlo program while the Gruen range expression originally was derived from experimental

| Gruen and Bethe Ranges | | | | | | |
|-------------------------------|----------------------------|----------------------------|----------------------------|----------------------------|----------------------------|----------------------------|
| Beam Voltage (kV) | Au | | Cr | | Si | |
| | R_G (μm) | R_B (μm) | R_G (μm) | R_B (μm) | R_G (μm) | R_B (μm) |
| 10 | 0.12 | 0.40 | 0.31 | 0.60 | 0.97 | 1.44 |
| 20 | 0.39 | 1.19 | 1.05 | 1.97 | 3.24 | 4.84 |
| 25 | 0.58 | 1.50 | 1.56 | 2.91 | 4.80 | 7.50 |
| 30 | 0.80 | 2.32 | 2.14 | 4.01 | 6.60 | 9.97 |

Figure 4.8. Gruen and Bethe ranges for gold, chrome, and silicon at different beam voltages.

observations.

Figure 4.9a is a plot of the total number backscatter coefficient, η_B , versus gold thickness normalized to the Bethe range of electrons in gold. Figure 4.9b is a similar curve for the total energy backscatter coefficient, η_E . Figures 4.10a and 4.10b are similar to Figures 4.9a and 4.9b except the gold thickness is normalized to the Gruen range. A range of beam voltages from 10 to 30 kV is shown and it can be seen that a universal relationship is obtained by normalizing the gold thickness to R_B or R_G . It can be seen from these curves that η_B reaches 90 percent of its maximum at a gold thickness of approximately $0.15 R_B$ or $0.37 R_G$. The more important, from a simulation and practical viewpoint, η_E reaches 90 percent of its peak at about $0.13 R_B$ or $0.33 R_G$. The thickness requirements for η_E are slightly lower than those for η_B since η_B weights all electrons the same, even though those backscattered electrons scattered from deep in the gold will have a very low energy. These electrons will not contribute a significant amount to the signal since most backscattered electron detectors are energy sensitive. Universal curves from partial angle ranges (10-40 and 30-60 degrees) were found to give similar results as those shown in Figures 4.9 and 4.10. This is expected since there is no surface topography to influence the electron scattering.

As was previously mentioned, R_B must be calculated using the Monte Carlo program or else by interpolation on a universal curve [43]. The Gruen range can be calculated by anyone possessing a periodic table. It is because of this ease of calculation that R_G will be used when normalization is required for all of the proceeding discussion. The universal quality of the curves of Figure 4.10 is very interesting since the values for η_B and η_E were calculated using the Monte Carlo program while the normalization factor was calculated using an unrelated independent equation.

Universal curves for chrome films on silicon are shown in Figures 4.11a and 4.11b. There is more scatter in the curves; but, the results are essentially the same as for gold. The increased scatter may be due to different materials having slightly different exponents in the R_G expression at different beam voltages [43]. However, a good rule of thumb is that to obtain

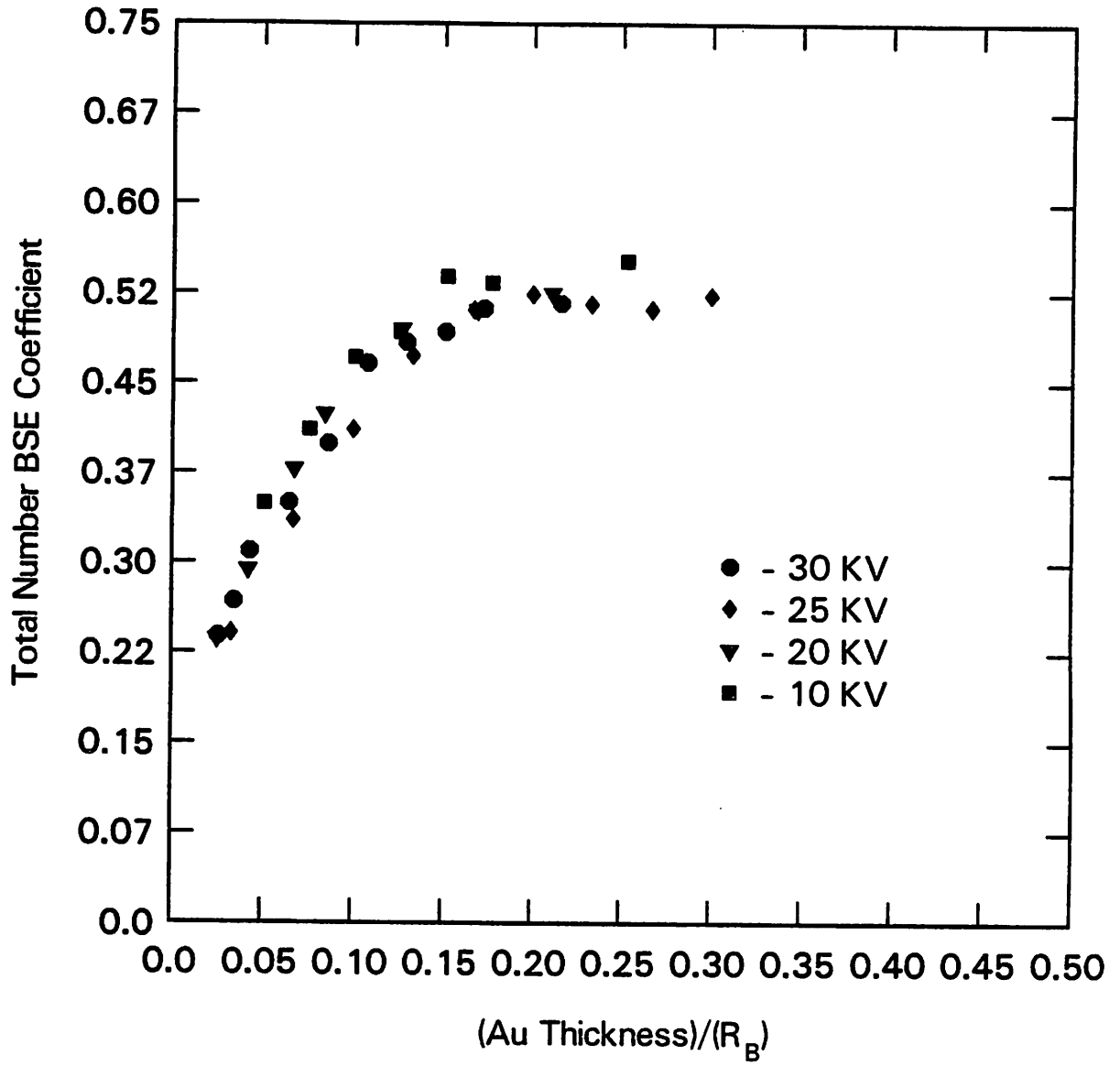


Figure 4.9a. A universal plot of η_B versus gold thickness normalized to R_B for different beam voltages. The substrate material is silicon.

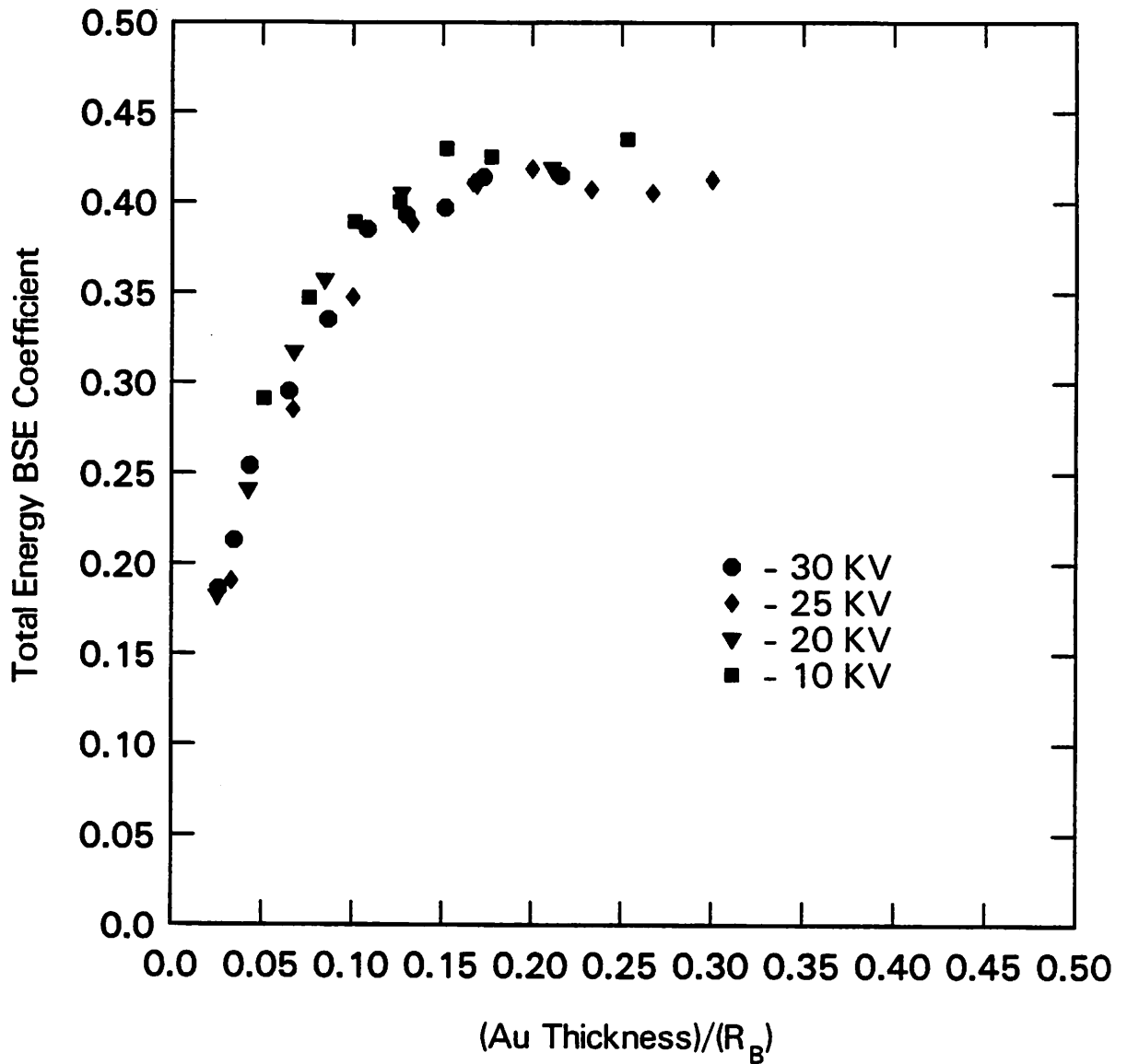


Figure 4.9b. A universal plot of η_E versus gold thickness normalized to R_B for different beam voltages. The substrate material is silicon.

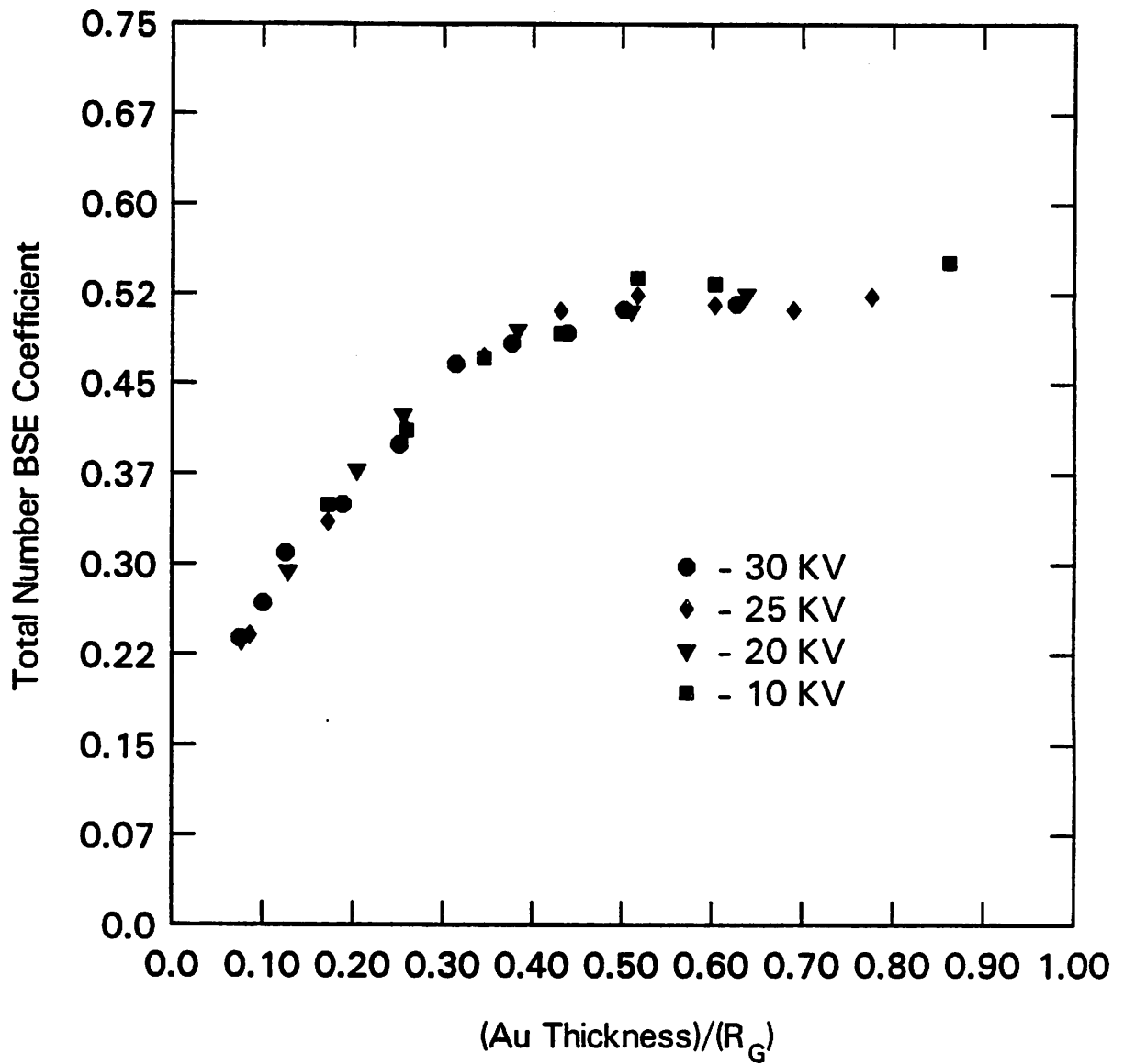


Figure 4.10a. A universal plot of η_B versus gold thickness normalized to R_G for different beam voltages. The substrate material is silicon.

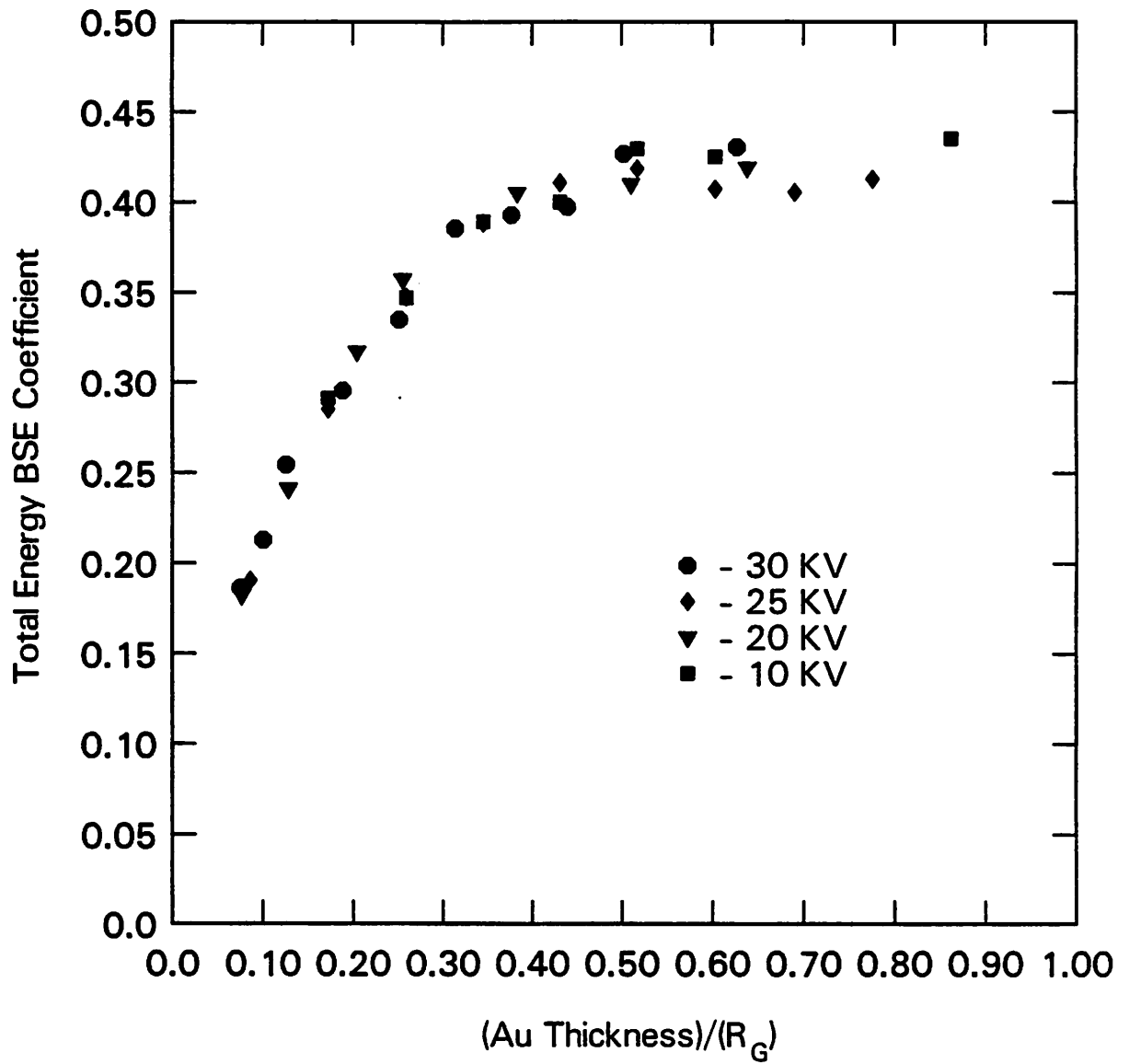


Figure 4.10b. A universal plot of η_E versus gold thickness normalized to R_G for different beam voltages. The substrate material is silicon.

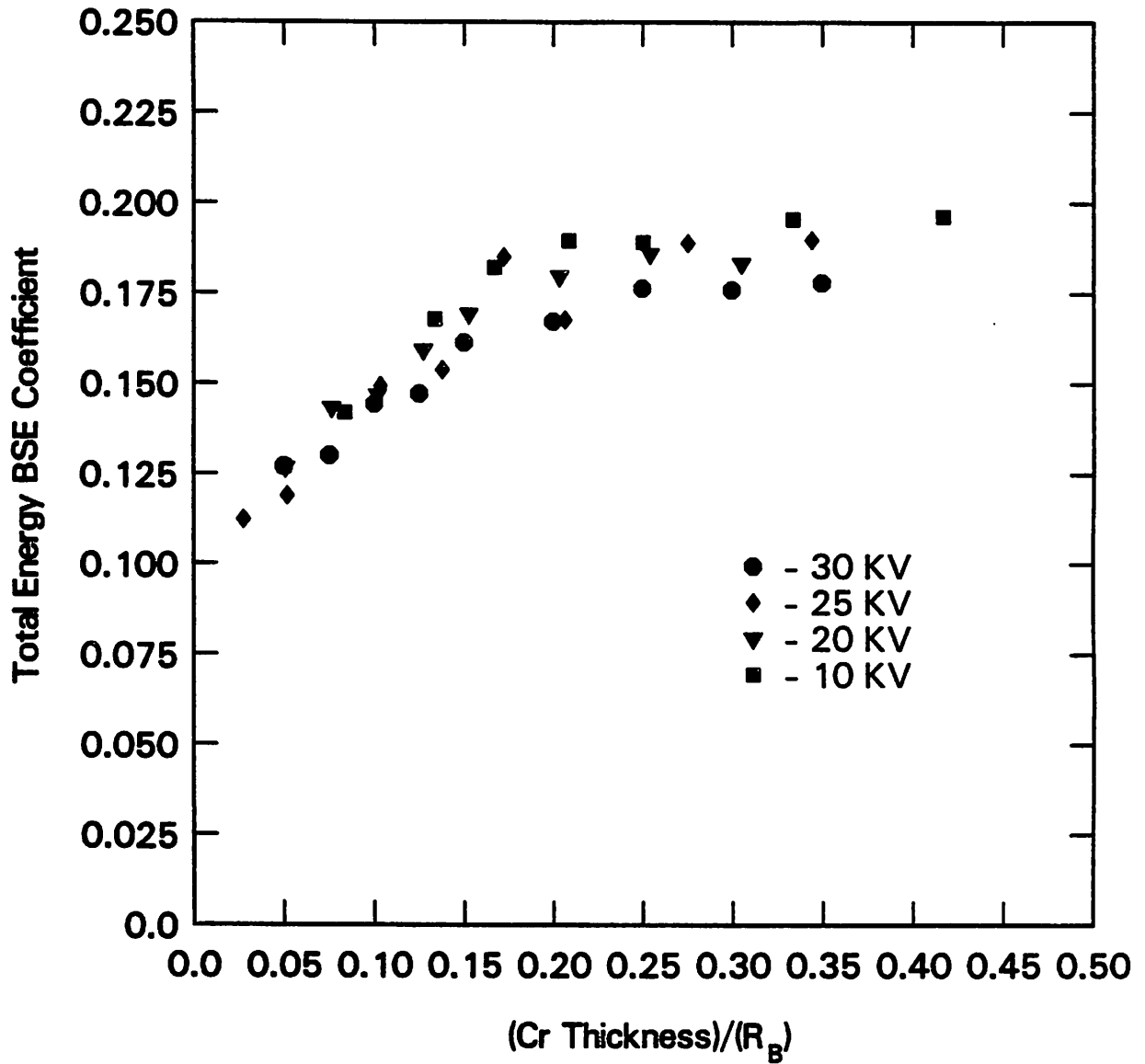


Figure 4.11a. A universal plot of η_E versus chrome thickness normalized to R_B for different beam voltages. The substrate material is silicon.

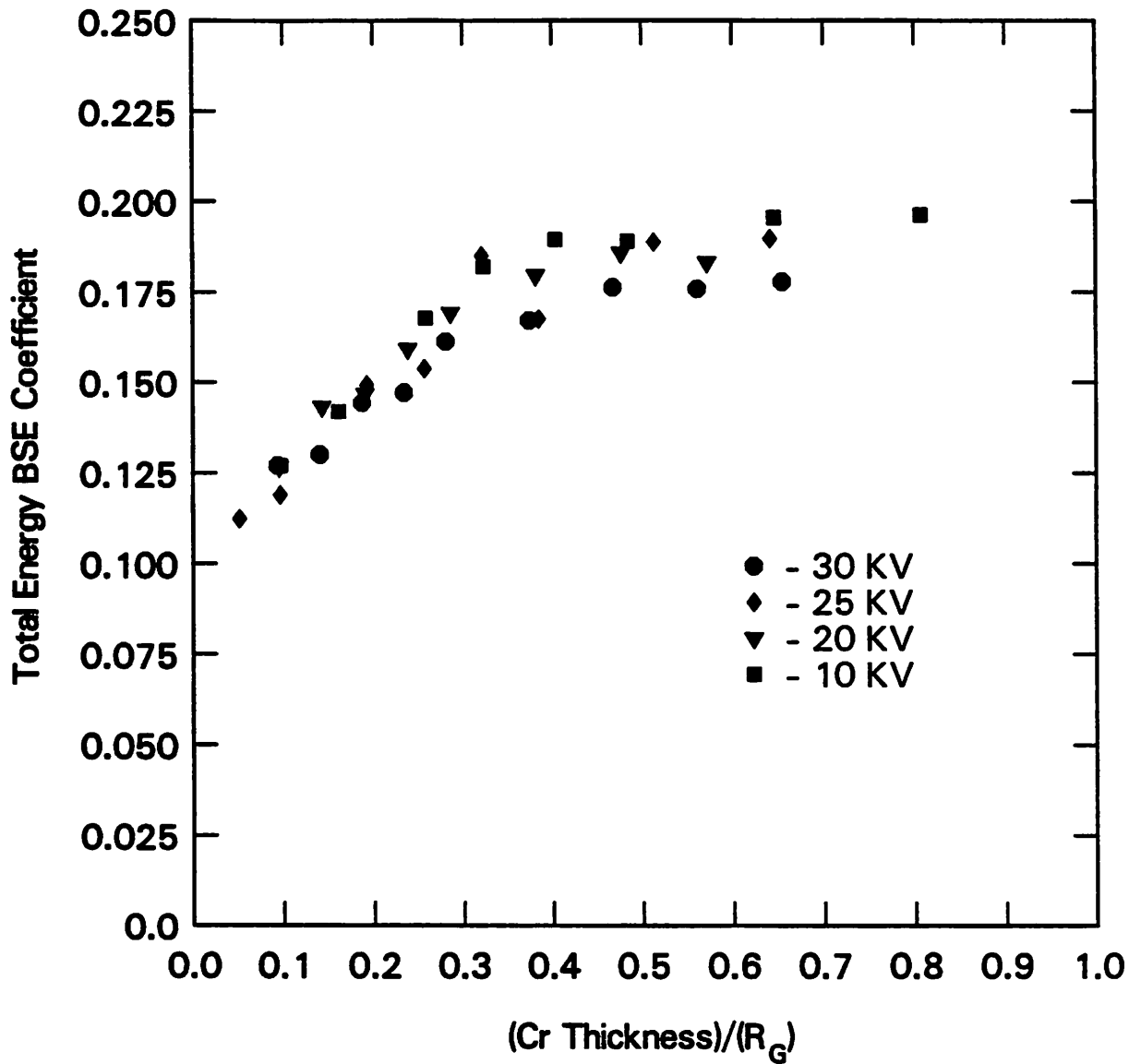


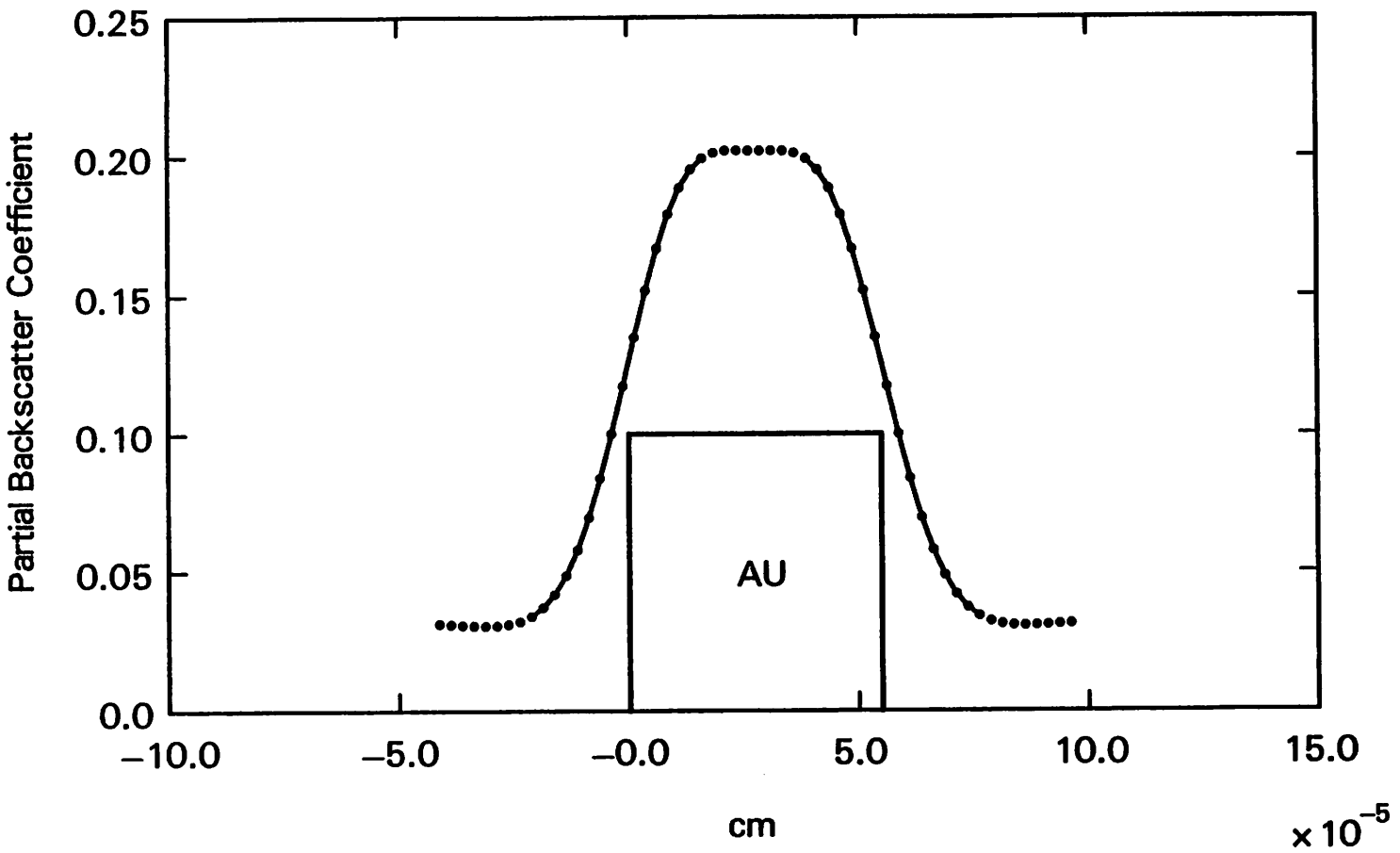
Figure 4.11b. A universal plot of η_E versus gold thickness normalized to R_G for different beam voltages. The substrate material is silicon.

more than 90 percent of the available signal, a film thickness greater than $0.33 R_G$ is required. For a 25 kV electron-beam, a gold thickness of about $0.2 \mu\text{m}$ would be required.

4.5. Effects of Scanning Near the Edges of a Structure

We have seen, in section 4.2, the increased scattering into lower take-off angles for sub-micron step structures and have observed the effects of different angle collection ranges in section 4.3. A practical problem, as far as inspection is concerned, caused by these scattering effects is that the backscattered electron signal does not instantly rise to a maximum signal as soon as the beam begins scanning over a step or into a hole. This is a function of electron scattering and the incident beam size and is true even for very small fwhm electron-beams or the δ -function signal. The electron-beam must be somewhat inside the structure before the signal reaches a maximum (or minimum). How far inside the structure will depend on the angle collection range, the beam size, and the beam voltage. This effect is most important if one is adopting a mask inspection scheme [4,6] in which the inside or positive areas of a mask are scanned for clear defects and the outside or negative areas are scanned for opaque defects. A dead zone or non-inspection area is left around all shapes to allow for registration error. The problem is that if the dead zone region is small, it is possible that the backscattered electron signal level could drop when the beam scans near the edge of a gold structure. A complementary occurrence takes place when the beam is scanning on silicon in the vicinity of a gold structure. In this case, the signal rises because of overlap of the beam onto the gold. These changes in signal levels, depending on the comparator threshold settings, could cause false defects to be detected.

The effect is illustrated in Figures 4.12a-4.12c, showing the backscattered electron energy signal for a $0.55 \mu\text{m}$ gold step on silicon. The beam fwhm is $0.25 \mu\text{m}$, the beam energy is 25 kV, and the gold thickness is $0.46 \mu\text{m}$. The signal can be seen to drop off 0.1 - $0.2 \mu\text{m}$ inside the step for the 30-60 and 50-80 degrees angle ranges. This reduced signal is what would be detected if the electron-beam was scanning near the edges of that shape.



PARTIAL ENERGY SIGNAL - 10.0-40.0 DEGREES
 0.55 μm Au step on Si, beam fwhm = 0.25 μm
 Au thickness = .46 μm , beam energy = 25 kV

Figure 4.12a. A simulated backscattered electron signal to show the fall off of the signal near the structure's edge.

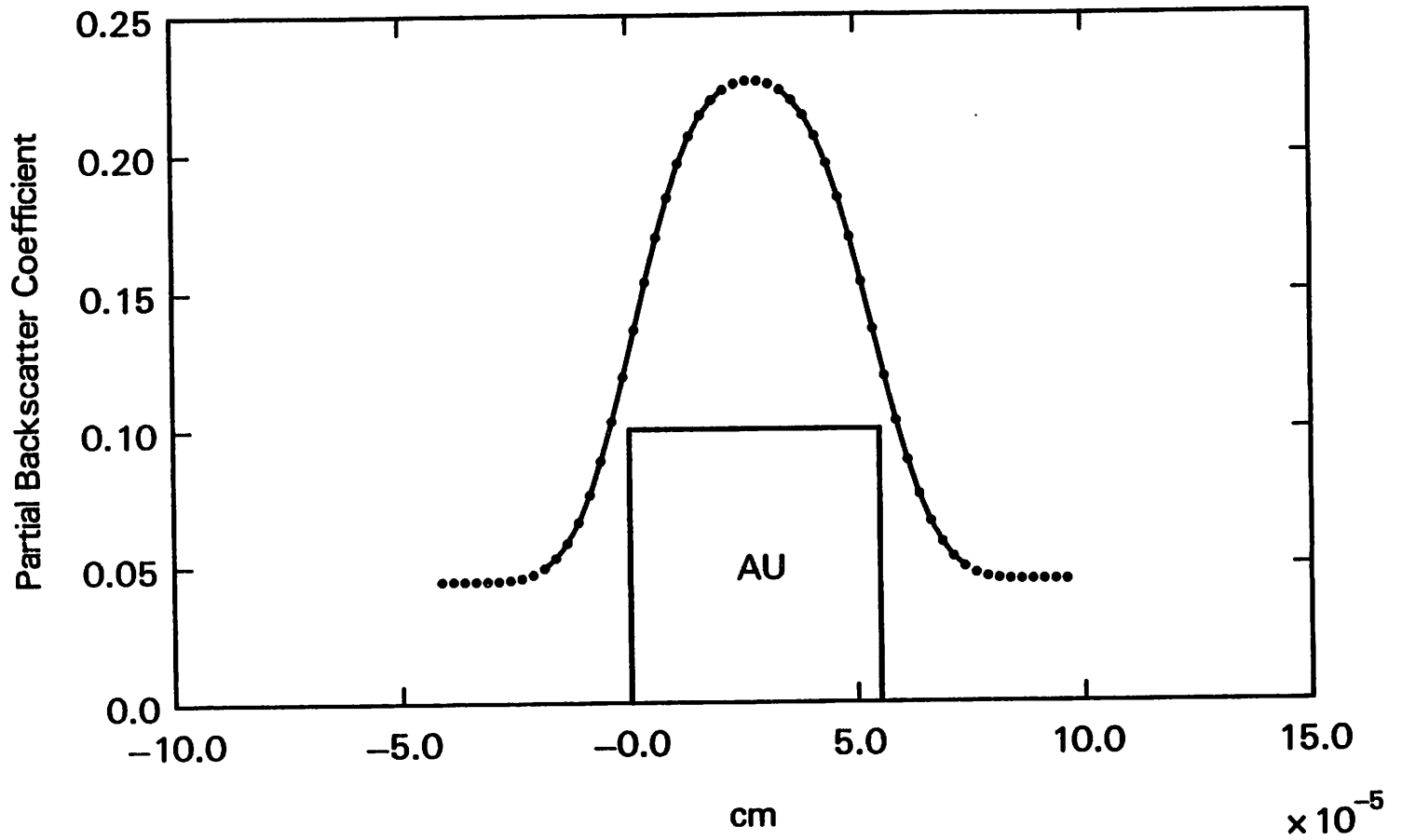
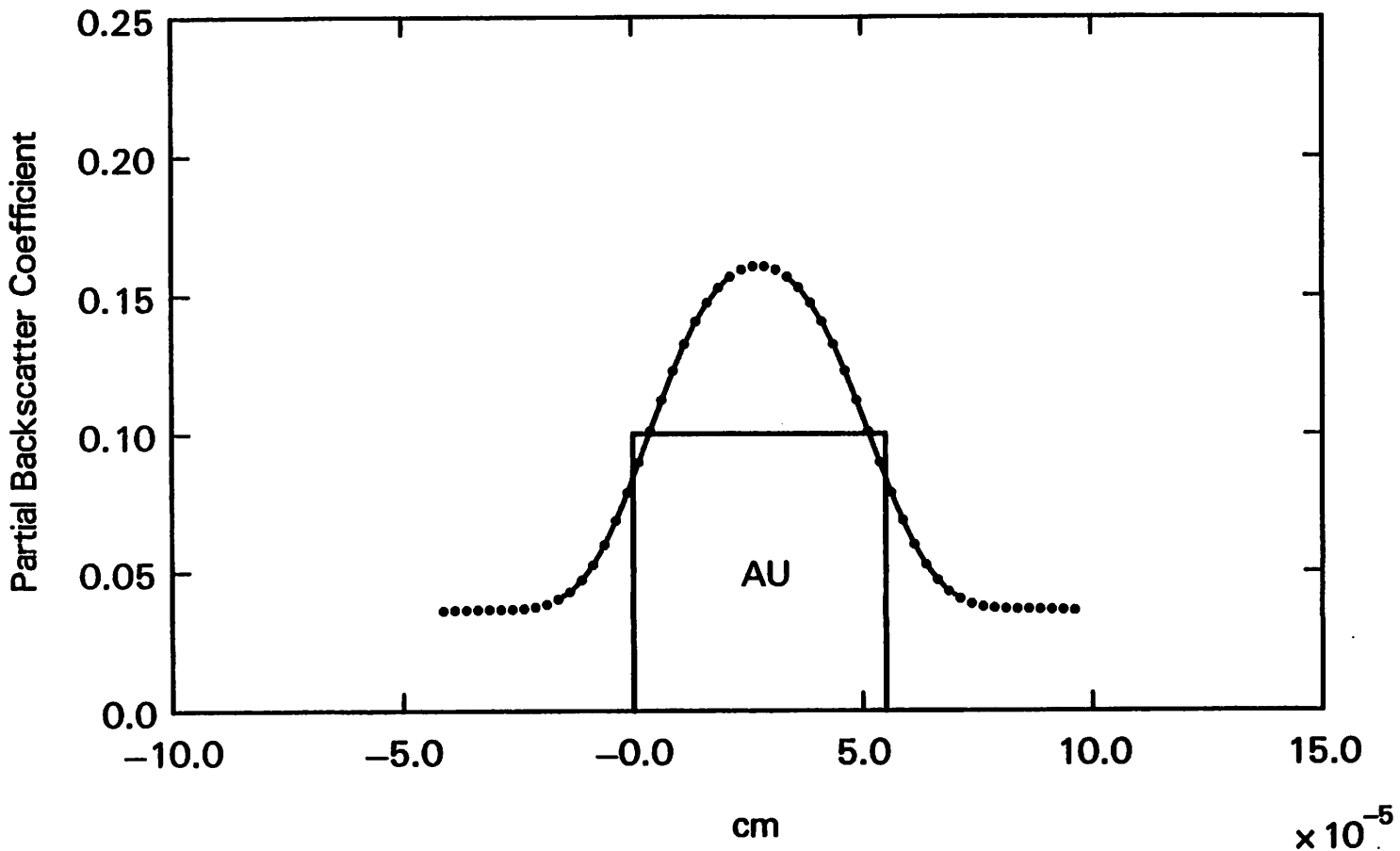


Figure 4.12b. A simulated backscattered electron signal to show the fall off of the signal near the structure's edge.

PARTIAL ENERGY SIGNAL - 30.0-60.0 DEGREES
 0.55 μm Au step on Si, beam fwhm = 0.25 μm
 Au thickness = .46 μm , beam energy = 25 kV



PARTIAL ENERGY SIGNAL - 50.0-80.0 DEGREES
 0.55 μm Au step on Si, beam fwhm = 0.25 μm
 Au thickness = .46 μm , beam energy = 25 kV

Figure 4.12c. A simulated backscattered electron signal to show the fall off of the signal near the structure's edge.

A simulation experiment was conducted to further investigate the effect of the signal level dropping near the edges of gold shapes. The partial energy backscatter coefficient was plotted versus half the step linewidth (or distance from the δ -function beam to the shape edge) normalized to the Gruen range. The results for the three angle ranges and 10 and 25 kV beam energies are shown in Figure 4.13. A sharp drop in signal occurs for the 50-80 degrees range starting about $0.33 R_G$ from the edge. For the 30-60 degrees range, the signal begins to drop off about $0.2 R_G$ from the edge. The signal actually increases if the lower angle range is used. A possible compromise would be to collect backscattered electrons in the 20-50 degrees angle range. In this case, there would only be a 6 percent loss of signal from bulk materials and a significant increase in the signal level near the edges of steps.

4.6. Extension to Three Dimensional Simulation

In its present form, the Monte Carlo program simulates the two dimensional backscattered electron signal from two dimensional structure. However, it is possible to predict the maximum and minimum signal levels from submicron three dimensional structures using a simple technique.

First, assume that the three dimensional defects, small holes in a gold film and small pieces of gold on silicon, are relatively circular. To calculate the minimum signal level from a hole in a gold film, simply calculate the fraction of the beam, when positioned at the center of the structure, which overlaps onto the surrounding gold film. To obtain the minimum signal level, this fraction can then be multiplied by the partial energy backscatter coefficient, $\eta_E(\theta)$ for bulk gold at the desired beam energy, gold thickness, and angle collection range. This simple calculation is based on the knowledge that almost all of the electrons which enter the small hole will be trapped under the gold and will not backscatter. This simple method for calculating the signal levels can also be applied to two dimensional structures as well.

It is slightly more difficult to calculate the maximum signal level for a three dimensional circular piece of gold on silicon. The maximum signal level can be calculated by determining

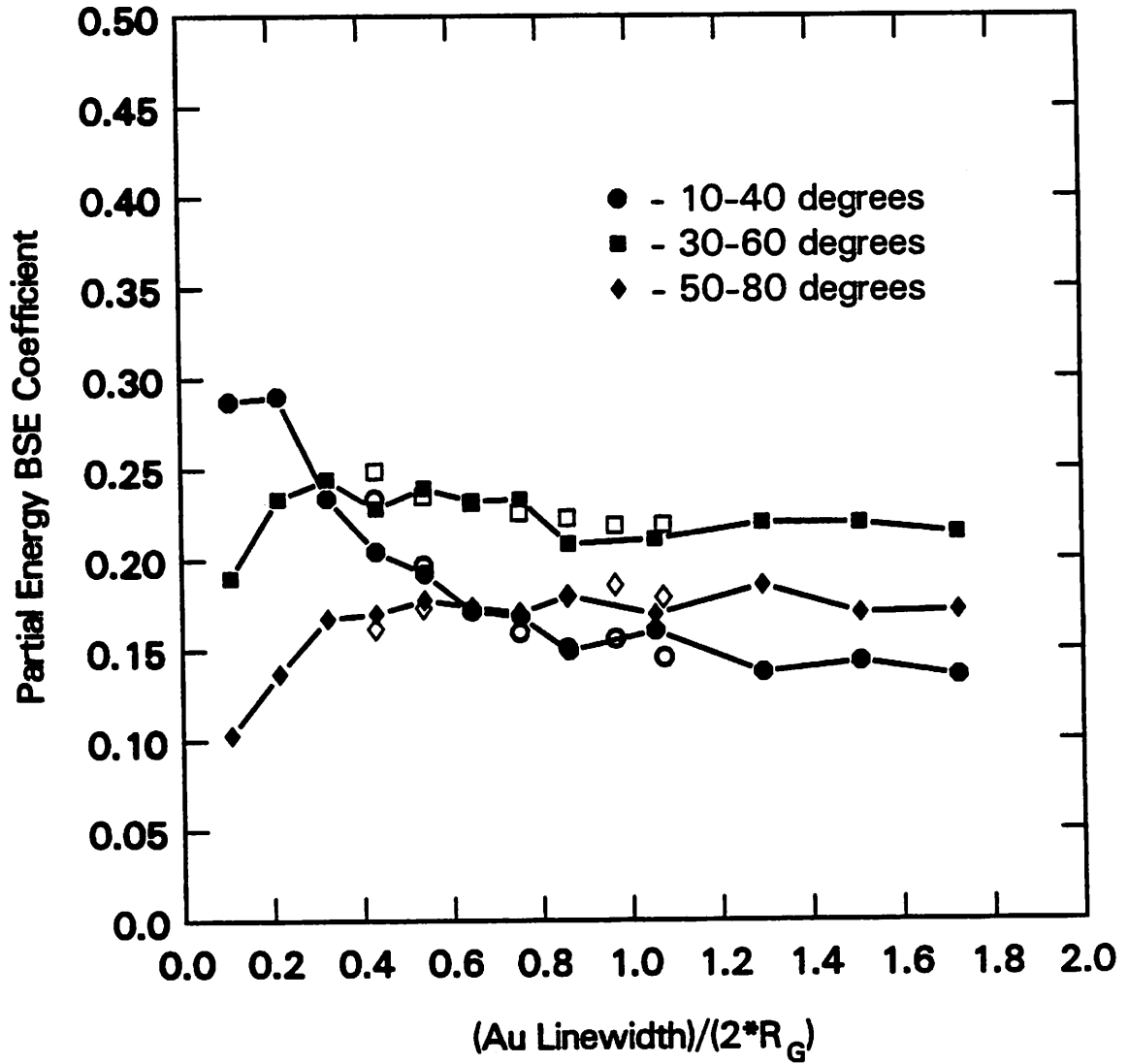


Figure 4.13. A plot of η_E versus normalized gold linewidth to illustrate the effect of scanning near a structure's edge. The δ -function beam is incident at the center of a gold step on silicon. The gold thickness is $0.5 \mu\text{m}$. The dark symbols are for a 25 kV beam voltage and the open symbols are for a 10 kV beam voltage.

the fraction of the beam, positioned at the center of the structure, which covers the gold and the corresponding fraction which covers the silicon. To obtain $\eta_E(\theta)$, multiply the fraction of the beam over silicon by $\eta_{E-Si}(\theta)$ and add to that result the fraction of the beam over gold multiplied by $\eta_E(\theta)$ for a δ -function electron-beam at the center of the structure. $\eta_E(\theta)$ for bulk gold cannot be used since $\eta_E(\theta)$ for the three dimensional structure can be much larger due to the increased scattering of the electrons from the sides. At this point in time, it is not possible to use the Monte Carlo program to directly calculate $\eta_E(\theta)$ for a δ -function beam at the center of a three dimensional structure. However, it is reasonable to assume that if a two dimensional step (i.e. a line) increases $\eta_E(\theta)$ by a certain amount over the value for bulk gold, then a three dimensional structure will increase the bulk value of $\eta_E(\theta)$ by twice that amount. Consider 1000 electrons incident at the center of a small two-dimensional gold on silicon step. Assume 500 of the electrons scatter from the top of the step and 75 electrons scatter from each of the two sides of the structure. By symmetry, it follows that if the infinitely long step is cut into a three dimensional structure, then 150 more electrons out of the incident 1000 would scatter from the two newly created sides.

In their paper on mask inspection, Simpson and Davis [4] present a somewhat similar method for calculating the $S_{\max}-S_{\min}$ signal of a rectangular shaped electron-beam incident on defects of various sizes. Their calculations graph the changing percentage of the $S_{\max}-S_{\min}$ signal versus (defect diameter)/(spot size). In their analysis, they do not consider the electron scattering and assume the reduction in signal levels with increasing beam size is caused strictly by a smaller portion of the beam being incident on the defect. This is true, however, the 100 percent signal difference listed in their graph will not be the same for all structures. For example, a hole in a gold film will have a different $S_{\max}-S_{\min}$ signal than a gold step on silicon.

Figure 4.14 is a graph of the fraction of a Gaussian beam which falls over the gold versus the ratio of (beam fwhm)/(defect fwhm) for holes in gold on silicon. This graph can also be used to calculate the fraction of the beam falling into the hole or onto a three dimensional gold step on silicon. The calculations which produced this graph assume the beam is centered on

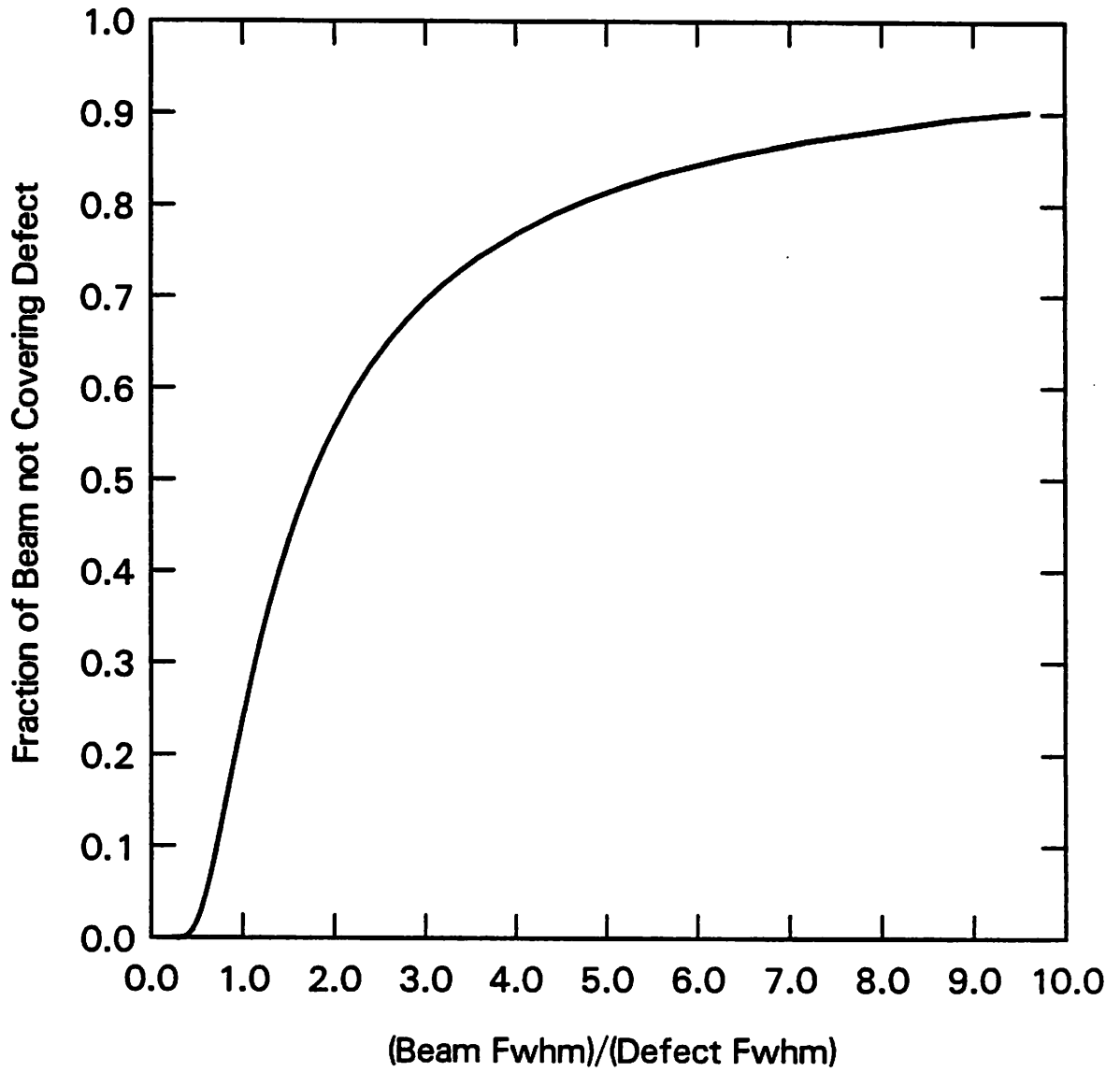


Figure 4.14. A curve to aid in using the simple analytical technique to determine signal levels.

the structure and that the defects are circular.

The technique outlined above was tested with the two dimensional $0.25 \mu\text{m}$ step and hole structures at 25 kV. As can be seen from Figure 4.15, the simple calculations agree rather well with the Monte Carlo results obtained by the standard method outlined in Chapter 3. There are some discrepancies for the hole structure at the $0.1 \mu\text{m}$ beam fwhm. This is because most of the beam is falling into the hole and; therefore, the backscattered electrons from the hole, which are usually insignificant, are the dominant part of the very small signal level.

It can be seen from this simple analysis that the results for the two dimensional hole case will be similar to the results for the three dimensional circular hole. This is because electrons which enter the hole, in either case, will usually not backscatter. Thus, the results in this chapter and in Chapter 5 for hole structures will be valid for the three dimensional case as well.

As far as steps are concerned, the effect of a three dimensional structure will be to increase the maximum signal level due to increased scattering at the edges of the structure. Thus, the results in this chapter and in Chapter 5 for step structures can be considered worst case results; therefore, conclusions drawn from these studies will be valid.

It is understood that as the size of the hole structure increases, the assumption of zero contribution from the portion of the beam over the silicon becomes invalid. However, the size of the hole at this point (defect size greater than about $1.0 \mu\text{m}$) will be much larger than the minimum detectable defect sizes important in x-ray mask inspection. As we will note in later chapters, it is the smallest defect which will influence the inspection system parameters.

4.7. Summary

In this chapter, the Monte Carlo program has been used to investigate the effect of material, detector, and beam parameters on the backscattered electron signal quality. The placement of the diode detector used for the experiments in Chapter 3 was optimized by conducting a series of simulation experiments. It was shown that the middle backscattered electron take-off angle collection range gives the best results for submicron hole and step structures.

| 0.25 μm hole | | | | |
|-----------------------------------|--------------------------|---------------------------|--------------------------|---------------------------|
| Beam Fwhm (μm) | 10-40° | | 30-60° | |
| | Calculated S_{\min} | Monte Carlo S_{\min} | Calculated S_{\min} | Monte Carlo S_{\min} |
| 0.10 | 0.0005 | 0.0022 | 0.0007 | 0.0040 |
| 0.20 | 0.0229 | 0.0257 | 0.0310 | 0.0302 |
| 0.50 | 0.0905 | 0.0955 | 0.1222 | 0.1207 |
| 0.25 μm step | | | | |
| Beam Fwhm (μm) | 10-40° | | 30-60° | |
| | Calculated S_{\max} | Monte Carlo S_{\max} | Calculated S_{\max} | Monte Carlo S_{\max} |
| 0.10 | 0.289 | 0.279 | 0.233 | 0.224 |
| 0.20 | 0.254 | 0.237 | 0.208 | 0.191 |
| 0.50 | 0.149 | 0.137 | 0.131 | 0.118 |

Figure 4.15. Comparison of the simple calculation and Monte Carlo techniques for determining signal levels. All levels are in units of η_E .

The effects of Gaussian beam size on the backscattered electron signal was also investigated. It was found that signal contrast gives misleading results as far as the noise quality of the backscattered electron signal is concerned. The Δ SNR parameter, introduced in Chapter 3, gives a more realistic representation of the degradation in signal noise quality with increasing beam size and changing angle collection range. A degradation in Δ SNR starts when the beam size becomes at least four-tenths of the structure fwhm. For steps, a 25 percent loss of Δ SNR occurs when the (beam fwhm)/(structure fwhm) ratio is about 1.2. Similar results are seen for holes with a 25 percent reduction in Δ SNR being observed at a ratio of about 1.1.

It was observed that the graph of signal fwhm versus beam fwhm has two distinct regions for various structures. There is a flat region for beam sizes up to about 0.5 of the structure fwhm and a region for larger beam sizes in which the signal fwhm rises steadily with the beam fwhm. For steps, a signal fwhm 50 percent larger than the structure fwhm occurs for a (beam fwhm)/(structure fwhm) ratio of about 1.3-1.4. For holes, a 50 percent increase is seen for a ratio of about 1.1-1.2. It was also found that the thresholds or DC levels of the signals from step and hole structures are different and behave in different manners as the beam size is increased. For steps, the threshold drops towards the silicon signal level as the beam size increases. For holes, the threshold rises toward the gold signal level. The effect of beam size on the preceding signal characteristics was illustrated through a series of signal characteristic versus beam fwhm curves for different take-off angle collection ranges and various submicron gold on silicon structures.

Universal curves for various beam energies showed that to collect 90 percent of the available backscattered electron signal, the scattering material should be about $0.13 R_B$ or $0.33 R_G$ thick. It is desirable to use the Gruen range, R_G since it is easily calculated using a simple analytical expression. The universal relationship of the backscatter coefficients to material thickness normalized to R_G is interesting because the backscatter coefficients are calculated using the Monte Carlo program while R_G is calculated using an empirically derived equation. Similar universal curves were introduced to illustrate the effect of scanning the electron-beam

near the edges of shapes. As the beam scans near the shape edges, it is possible that the back-scattered electron signal can fall off. If low take-off angle electrons are collected, an increase in signal is observed. For a 30-60 degrees angle collection range, the signal begins to drop off at about $0.2 R_G$ from the edge while for a 50-80 degrees range, the signal begins to drop off at about $0.33 R_G$ from the edge. This decrease in signal level is important since it can cause the signal to fall below the comparator threshold used for determining the presence or absence of masking material. Collecting backscattered electrons in the 20-50 degrees range should reduce the drop in signal near a step edge with only a 6 percent loss in signal from bulk materials.

Finally, a simple technique of calculating signal levels for two and three dimensional structures was introduced. The method is based on knowing the fraction of the beam which is incident on the structure along with knowledge of the scattering properties of that structure.

CHAPTER 5

5. BACKSCATTERED ELECTRON DETECTORS AND SNR

5.1. Introduction

There are several different types of detector and amplifier combinations which can be used for generating the backscattered electron signal. These include scintillator-photomultiplier, silicon diode, and channel plate detectors. The first part of this chapter will discuss the available detector options and look at the practical issues one is confronted with when installing a detector system in an electron-beam lithography system.

The fundamental limitation of a mask inspection system which uses a backscattered electron signal for defect detection will be the shot noise in the signal. A noisy signal can cause the detection of false defects (false alarms) and the missing of real defects. The shot noise comes from the statistical fluctuations of the number of electrons incident on the backscattered electron detector [19,55]. This portion of the signal path between the sample and the detector is frequently called the noise bottleneck since the number of signal carrying electrons is at a minimum [19,56-58]. It has been shown that the limiting shot noise signal to noise ratio (SNR) of a signal is the SNR calculated at the noise bottleneck [19,55]. In the second part of this chapter, we will examine how the limiting SNR can be calculated for structures encountered during x-ray mask inspection. The influence of various parameters, such as threshold setting and beam size, on the SNR from small defect structures will be examined and the fundamental shot noise limitations to electron-beam mask inspection will be discussed. The relationship of the Δ SNR signal characteristic to the actual SNR will also be investigated.

5.2. Backscattered Electron Detectors

There are three types of backscattered electron detectors which are of practical use in an electron-beam system. In a scintillator-photomultiplier detector [42,59-71], backscattered or accelerated secondary electrons strike a scintillation material. Photons are generated and transferred by a light pipe to the photocathode of a high gain photomultiplier tube. In a silicon diode detector [55,72-74], energetic electrons produce an electron-hole pair for every 3.6 eV of energy. This current is then conventionally amplified. These detectors have initial amplification gains which are energy dependent. We have seen this in Chapter 3 for the case of the diode detector. A third type of detector is the channel plate electron multiplier [75]. It consists of an array of micro channel tubes connected axially to form a disk. Each microchannel is internally coated with a semi-insulating layer of high secondary electron yield. The gain of the channel plate depends upon the channel length to diameter ratio and the channel bias voltage [75].

Most references for electron detectors are concerned with the use of these detectors in SEM's. However, electron-beam lithography systems have their own set of restrictions as far as detectors are concerned. Typically, there will be very little space for the detector in the chamber of an electron-beam system because of the requirements of an extremely accurate deflection system and precise knowledge of the table position (requiring an x,y laser interferometer). Also, depending on the operating field size of the system, there is a minimum width for the hole in the detector which the beam passes through. The detector must be constructed of non-magnetic materials so that the beam deflection is not affected and any detector bias voltages must be shielded from the electron-beam. Once the detector is in place, the signal must be transferred out of the chamber and to external amplifiers. Ports for this purpose are restricted since room is required to load and unload the wafers or masks. More room is required for the laser interferometer for the sample stage. The minimum distance of the detector above the sample may also be restricted if the system is capable of using different sample holders which position the mask or wafer at different distances from the pole piece of the

electron gun. These practical limitations in an electron-beam system are quite important and will limit the choice of detectors which can be used to collect the backscattered electrons.

If one examines the references for scintillator detectors [59-71], the conclusion would probably be reached that a P-47 scintillator detector would theoretically allow high speed (about 10 Mhz) inspection and large angle collection ranges. However, the P-47 detector is limited in practice for several reasons. The P-47 scintillation material degrades with exposure to high energy electrons [59,62]. This degradation may not be important in an SEM with electron-beam currents below 10^{-9} amps; but will become a problem in electron-beam lithography systems using beam currents in the 10^{-6} to 10^{-8} amp range. Also, once photons are generated in the scintillation material, they must travel to the photomultiplier tube (PMT) for amplification. It is not desirable to locate the PMT's inside the chamber so long light pipes are required to get the photons out of the chamber and into the PMT. Consequently, some of the signal will be lost. It is desirable to collect electrons scattered into all azimuthal angles so that the backscattered electron signal will be symmetrical. This requires a 4 quadrant or annular detector, which, in turn requires 4 light pipes. For minimum loss of photons, it is obvious that the light pipes should be straight. However, this will be difficult to accomplish in many systems because of the lack of space inside the chamber and the limited availability of ports to the outside. Thus, the light pipes must be curved, leading to more signal loss, or else some type of fiber optic scheme [76] must be used. In any case, the scintillator detector system looks promising on paper; but, will be difficult to implement in a practical electron-beam system.

The channel plate detector, on the other hand, is relatively compact [75] and is easily installed in an electron-beam system's chamber. However, a complicated biasing scheme is required [75] in which the collection plate bias must be periodically recharged. This is fine for SEM or registration scans; but, this recharge delay would limit the throughput of a mask inspection system. Also, as discussed earlier, the gain of the channel plate detector is not a function of the incident electron energy. Thus, the detected signal difference between gold and silicon will be reduced somewhat from that of an energy sensitive detector. As we shall see,

the difference in signal levels between gold and silicon is directly related to the SNR of the signal.

The silicon diode detector, especially in an annular form, is easy to fabricate and simple to install in an electron-beam system. Annular diodes which operate at 5-10 Mhz bandwidths and collect electrons backscattered into the 30-60 degrees range are currently available [55] and present no practical problems when installed in an electron-beam system. The diode should be reverse biased to reduce the bandwidth limiting capacitance and there must be some type of circuitry which compensates for variations in the DC output level due to leakage current variations. The diode can also be broken up into several sections and each section amplified independently to reduce capacitance. The angle range of collected electrons is somewhat reduced by an annular detector since the diode area (and thus capacitance) increases dramatically if it is desired to collect low as well as middle range backscattered electrons. A more efficient method of collecting electrons would be to construct a multi-channel diode detector placed at a 45 degree angle to the sample surface. Thus, there is a trade-off between angle collection range and the size and speed of the diode which is beyond the scope of this chapter.

Thus, for inspection speeds up to approximately 10 Mhz, an annular silicon diode detector appears to be most promising. Annular diode detectors are currently available and easily installed. Inspection bandwidths much greater than 10 Mhz will require smaller diode areas and more efficient geometries.

5.3. Shot Noise SNR Studies

5.3.1. Calculating Shot Noise SNR

Lin [19], following a derivation by Davis [21], obtained the following expression for the SNR of a shot noise limited signal:

$$SNR_i = (\gamma\eta_B I_B / 2e\Delta f)^{1/2} = (\gamma\eta_B n_0 / 2\Delta f\tau)^{1/2} \quad (5.1)$$

where γ is the ratio of the number of backscattered electrons intercepted by the detector to the total number of backscattered electrons, η_B is the total number backscatter coefficient, e is the electronic charge, I_B is the primary beam current in amps, Δf is the bandwidth of the system, n_0 is the number of electrons incident on a pixel element, and τ is the time the beam stays on each pixel. The shot noise has been shown to be a Poisson distribution which can be described by a Gaussian [4,19,55]. The quantity, $\gamma\eta_B$ is just the partial number backscatter coefficient for a given angle collection range. Also, not all the electrons which are backscattered into the detector will be counted. Some electrons will backscatter from the diode detector and others will not have enough energy to penetrate into the depletion region and create electron-hole pairs. Since the backscatter coefficient for silicon is approximately 0.15 for normal incidence, the calculations in this chapter will assume a conservative twenty percent loss of electrons backscattering from the diode. Note that the backscatter coefficient increases for electrons striking a sample at oblique angles [42]. Equation 5.1 becomes:

$$\frac{S}{\sigma} = SNR_i = (0.8\eta_B(\theta)I_B/2e\Delta f)^{1/2} \quad (5.2)$$

where $\eta_B(\theta)$ is the partial number backscatter coefficient.

Equation 5.2 gives the SNR of an isolated signal referenced to a zero level (Figure 5.1). For example, consider a 10 Mhz bandwidth, 20 nA beam current, and a collection range of 30-60 degrees. Using the Monte Carlo program to calculate $\eta_B(\theta)$, SNR_i comes out to be 37. The same conditions for silicon give a SNR_i of about 20. However, these numbers are extremely misleading if applied to mask inspection where the signal of interest is the difference between the gold and silicon levels. Somewhere in between these two levels, a comparator threshold must be set so that the electronics can determine the presence or absence of masking material (i.e. digitize the analog backscattered electron signal). The signals and threshold important for mask inspection are shown in Figure 5.2. The Gaussian describing the noise around the gold signal is larger than that around the the silicon signal because of the larger number of electrons backscattered from gold. Although Figure 5.2 is labeled for gold and silicon, it applies to any

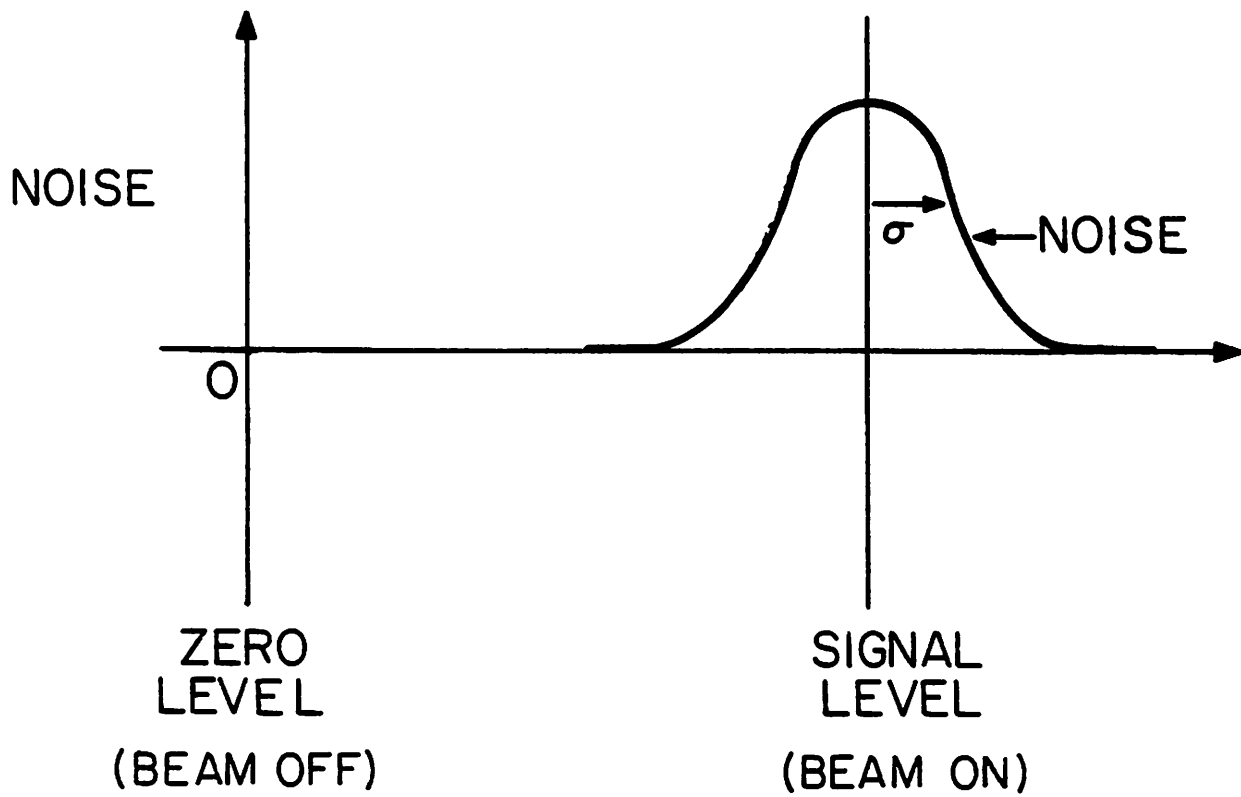


Figure 5.1. An illustration of *SNR*.

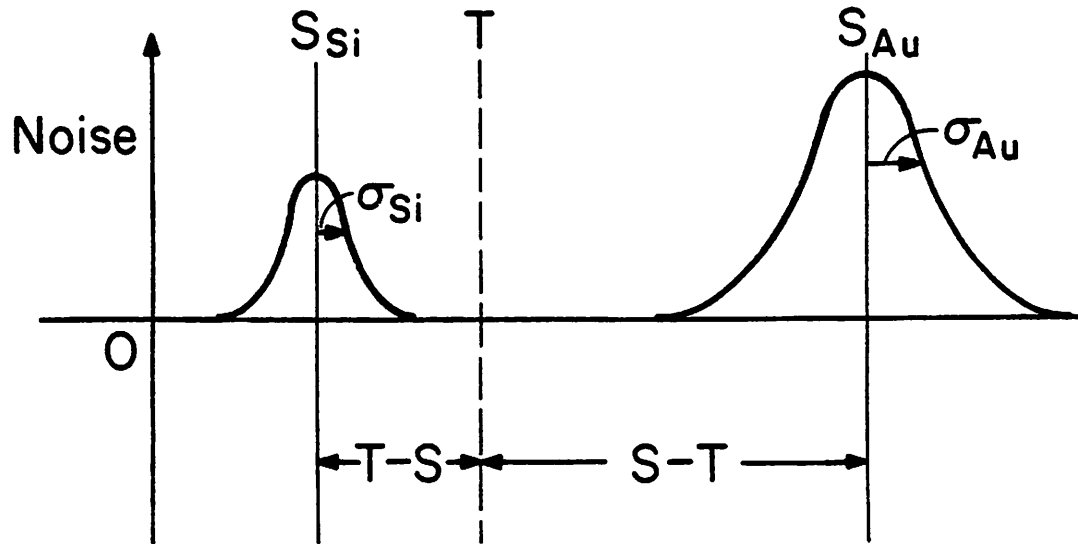


Figure 5.2. The important levels for determining the SNR for x-ray mask inspection back-scattered electron signals.

two materials.

As can be seen in Figure 5.2, the SNR of interest is not the isolated signal to noise ratio, SNR_i ; but, the SNR of the signal described by the signal level of interest and the comparator threshold. Thus, we are interested in:

$$\frac{S - T}{\sigma} \quad (5.3)$$

where T is the comparator threshold level. Using equation 5.2, we obtain:

$$\frac{S - T}{\sigma} = SNR_i \times \frac{(S - T)}{S} \quad (5.4)$$

Equation 5.4 is the SNR of interest since it is concerned with the level of the signal above or below the threshold and not with the meaningless zero level.

A first order calculation would assume that the ratio of the gold and silicon signal levels would be equal to the ratio of their respective number backscatter coefficients (approximately 3.5). However, a diode or energy sensitive detector's gain is proportional to the energy of the incident electrons. Thus, the actual ratio of gold and silicon signal levels can be described by:

$$\frac{S_{Au}}{S_{Si}} = \frac{I_{out_{Au}}}{I_{out_{Si}}} = \frac{G_{Au}(E)\gamma\eta_{B_{Au}}I_B}{G_{Si}(E)\gamma\eta_{B_{Si}}I_B} = \frac{G_{Au}(E)\eta_{B_{Au}}}{G_{Si}(E)\eta_{B_{Si}}} \quad (5.5)$$

where $G_{Au}(E)$ and $G_{Si}(E)$ are the energy dependent gains of the detector for gold and silicon respectively. $I_{out_{Au}}$ and $I_{out_{Si}}$ are the detector output currents from the backscattered electrons from gold and silicon respectively. It is easily seen that the Monte Carlo program can be used to evaluate equation 5.5 since:

$$\frac{G_{Au}(E)\eta_{B_{Au}}}{G_{Si}(E)\eta_{B_{Si}}} = \frac{\eta_E(\theta)_{Au}}{\eta_E(\theta)_{Si}} \quad (5.6)$$

where $\eta_E(\theta)_{Au}$ and $\eta_E(\theta)_{Si}$ are the partial energy backscatter coefficients for gold and silicon for a given angle collection range. The effective $\frac{S_{Au}}{S_{Si}}$ for bulk gold and bulk silicon, collecting

all electrons, at 25 kV calculated using the Monte Carlo program and equation 5.6 is 4.4, a 27 percent increase over the ratio of the number backscatter coefficients.

As an example, assume that the threshold is set midway between the bulk gold and silicon signal levels as shown in Figure 5.3. For a 30-60 degrees collection range, the SNR_i for gold is 37 and the SNR_i for silicon is 20 for a 25 kV incident electron beam. Using 5.4, the inspection SNR comes about to be 14.4 for the gold and 34.4 for the silicon. We see an increase in the effective SNR for silicon since the difference in signal levels between the threshold and silicon is greater than the difference in signal levels between the silicon and zero. For similar reasons, the effective SNR for gold drops from the isolated value. It can be seen that the SNR for gold can be increased at the expense of the SNR for silicon by moving the threshold closer to the silicon level.

In summary, the shot noise limited SNR for a given backscattered electron signal can be calculated in the following manner: First, the isolated SNR can be determined using equation 5.2. Knowing the ratio $\frac{S_{Au}}{S_{Si}}$ from Monte Carlo analysis, and the location of the threshold setting, the effective inspection SNR can be calculated using equation 5.4.

As was stated in the introduction to this chapter, the SNR is important in mask inspection since its value determines how reliable the inspection results will be. From Figure 5.2 it can be seen that if the electron-beam is scanning over a gold area, it is possible for the random noise fluctuations to trip the comparator threshold. A similar event can occur when the beam is scanning over silicon. The probability of these false alarms occurring is given, using a Gaussian noise distribution, as [77]:

$$P_e = \frac{1}{\sqrt{2\pi}} \int_{\frac{S-T}{\sigma}}^{\infty} e^{-\frac{\lambda^2}{2}} d\lambda \quad (5.7)$$

where P_e is the probability of an error occurring. Values of P_e for different SNR's are shown in Figure 5.4 [77]. Note that P_e is an indication of the probability of a false alarm or the

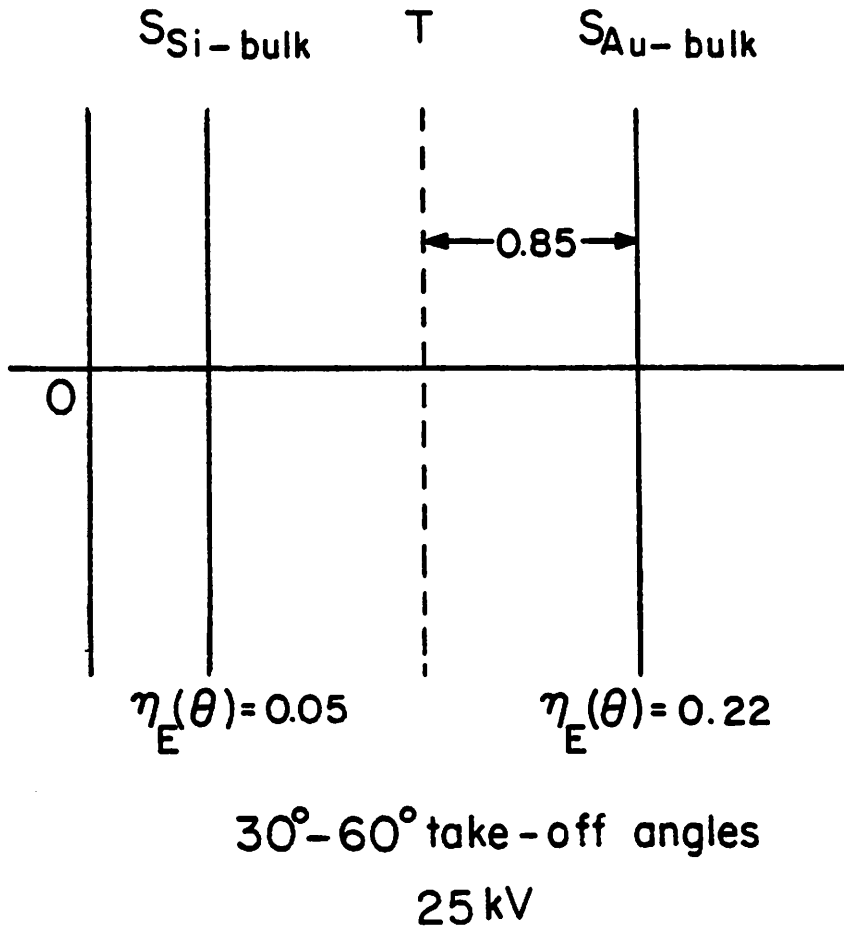


Figure 5.3. The signal levels of interest for calculating the SNR for bulk gold and silicon at 25 kV beam voltage.

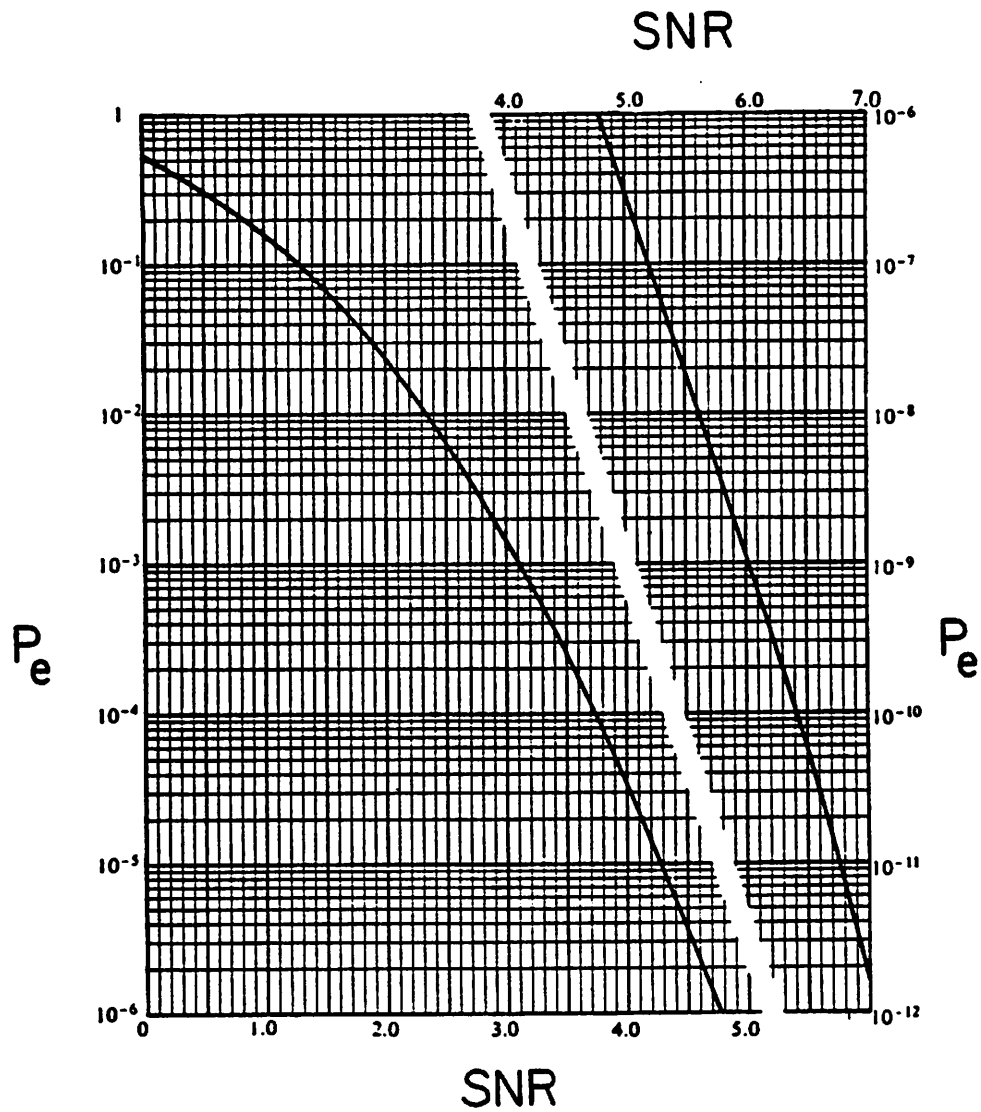


Figure 5.4. The probability of error versus SNR using equation 5.7 [77].

probability of missing an actual defect. The total probability of error can be written [4]:

$$P_e = P_d P_{ed} + P_{nd} P_{end} \quad (5.8)$$

where P_d is the probability of having a defect, P_{ed} is the probability of missing that defect, P_{nd} is the probability of not having a defect, and P_{end} is the probability of a false alarm. Since $P_d + P_{nd}$ must equal 1, $P_e = P_{ed} = P_{end}$ if the threshold is set so that the SNR's for both levels are equal. The number of false alarms and missed defects can be calculated by multiplying P_{ed} and P_{end} by the number of defect locations and number of inspection locations, respectively. It can be seen that by adjusting the location of the threshold, the probabilities of error for detecting different defects can be changed. A study of the required SNR's for mask inspection will be undertaken in section 5.3.2.

The threshold location, T_{opt} , at which the SNR's for both levels are equal is not at the midpoint of the signal; but can be calculated fairly easily. For a gold on silicon structure, equation 5.4 gives:

$$SNR_{Au} = \left(\frac{S_{Au} - T}{S_{Au}} \right) SNR_{i_{Au}} \quad (5.9a)$$

$$SNR_{Si} = \left(\frac{T - S_{Si}}{S_{Si}} \right) SNR_{i_{Si}} \quad (5.9b)$$

Equating 5.9a and 5.9b yields:

$$T_{opt} = \frac{\frac{SNR_{i_{Au}}}{S_{Au}} + \frac{SNR_{i_{Si}}}{S_{Si}}}{\frac{SNR_{i_{Au}}}{S_{Au}} + \frac{SNR_{i_{Si}}}{S_{Si}}} \quad (5.10)$$

For the 30-60 degrees and 25 kV case for bulk gold and silicon, the optimum threshold, T_{opt} , is calculated from equation 5.10 to be 0.1 in $\eta_E(\theta)$ units. $\eta_E(\theta)$ from gold is about 0.22 and $\eta_E(\theta)$ from silicon is about 0.05 for this angle range. The resulting SNR calculated from either equations 5.9a or 5.9b is 20.2. The T_{opt} is significantly closer to the silicon level than to the

gold level. T_{opt} , as calculated from equation 5.10, is independent of the ratio, $I_B/\Delta f$. It is a function of the number backscatter coefficient for the high and low levels as well as the magnitudes of those levels. These are in turn dependent on collector geometry, structure type and size, beam size, and beam voltage.

5.3.2. SNR Requirements for X-Ray Mask Inspection

To insure error-free inspection of a mask, a certain SNR quality is required for the back-scattered electron signal. This required SNR will depend on the number of inspection locations on the mask, the number of defect locations, and also the number of false alarms which can be tolerated. Let us consider a typical x-ray mask which would be used for a step-and-repeat x-ray lithography system. Assume a 2.5 cm by 2.5 cm mask area and 0.5 μm minimum feature sizes. This mask would most likely be written using 4-8 electron-beam scans per minimum feature size. On an IBM vector scan electron-beam machine [7,78], a 1.024 mm field size would be used with $(16384)^2$ addressable beam locations. Thus, it would require 625 fields or 1.678×10^{11} beam locations to cover the entire mask with 100 percent coverage. For false alarm free inspection over the entire mask, it can be seen from Figure 5.4 that a SNR of about 7 is required. This SNR requirement can be reduced if the inspection scheme allows for a certain number of false alarms which are checked in a re-inspection of all defect locations [4]. The SNR requirement can also be reduced if the effective number of inspection locations are reduced. Fewer pixels translates into lower SNR requirements. Various scanning techniques such as these will be discussed in Chapter 6. For now we shall concentrate on the complete inspection of a 2.5 cm \times 2.5 cm mask requiring a SNR of 7.

The minimum detectable defect size will influence the settings of the comparator threshold levels of the mask inspection system. If the system is set up to reliably detect this minimum sized defect, it follows that larger defects will be detected with even greater certainty. The optimum thresholds and SNR's will now be calculated for 0.125 and 0.25 μm steps and holes for a 25 kV beam voltage and 0.5 μm thick gold on silicon. Results for a 10 kV beam

voltage and 0.25 μm defects will also be listed. For step structures, the level for bulk silicon was used as the low level and for hole structures, the bulk gold signal level was used for the high level. This is identical to the way the levels were chosen for the calculations of Chapter 4. Recall that at the optimum threshold level, the SNR for both signal levels are equal. Thus, the SNR calculated at T_{opt} will determine the number of false alarms during the inspection. For example, when scanning for opaque defects, the electron-beam will be scanning over silicon. If T_{opt} is being used for the minimum sized defect, the SNR calculated for that signal can be used to calculate the number of false alarms while the beam is scanning over silicon. The threshold level can be increased from T_{opt} for steps and reduced for holes to reduce the false alarm rate. This will increase the chances of missing a defect by lowering the SNR of the defect signal. However, there will be much fewer defect locations than inspection locations.

The bulk signal levels (partial energy backscatter coefficients) and the SNR_i values calculated using equation 5.2 for 0.5 μm thick gold and bulk silicon at 10 and 25 kV are shown in Figure 5.5 for the 10-40, 30-60, and 50-80 degrees angle collection ranges. The 10-40 and 50-80 degrees values are the same since a bulk sample's backscatter distribution can be described by a cosine function [see Figure 4.1, 19,42]. Since a Monte Carlo program has statistical variations in its output, the η_E values were calculated by averaging the results from the 10-40 and 50-80 degrees angle ranges. The SNR_i values are left in terms of $(I_B/\Delta f)^{1/2}$ where I_B is the beam current in nA and Δf is the bandwidth in Mhz.

The SNR characteristics of the 0.125 and 0.25 μm structures as well as bulk gold and silicon were studied using the Monte Carlo program and equations 5.2-5.6 and 5.10. Figure 5.6 shows the partial number and energy backscatter coefficients for the signals of interest (maximum signal for steps and minimum signal for holes) and the optimum thresholds for the three different angle ranges. Figure 5.6a shows the results for the 0.125 μm structures for 0.1 and 0.25 μm Gaussian electron-beam fwhms. Figure 5.6b shows the results for the 0.25 μm structures at 25 kV for 0.2 and 0.5 μm beam sizes. Figure 5.6c shows some results for the 0.25 μm structures at 10 kV. Figure 5.7a lists the SNR values for the 0.125 μm structures at the

| 25 kV Incident Beam Energy | | | | |
|----------------------------|---------------|-------|------------------------------------|-------|
| Angle Range | η_E | | $SNR_i / (I_B / \Delta f)^{1/2} *$ | |
| | Au | Si | Au | Si |
| 10-40° | 0.163 | 0.036 | 22.51 | 11.70 |
| 30-60° | 0.220 | 0.050 | 26.22 | 14.21 |
| 50-80° | 0.163 | 0.036 | 22.51 | 11.70 |
| 00-90° | 0.426 | 0.096 | 36.40 | 19.56 |
| 10 kV Incident Beam Energy | | | | |
| Angle Range | η_E^{**} | | $SNR_i / (I_B / \Delta f)^{1/2} *$ | |
| | Au | Si | Au | Si |
| 10-40° | 0.063 | 0.018 | 22.42 | 13.25 |
| 30-60° | 0.087 | 0.024 | 26.22 | 15.60 |
| 50-80° | 0.063 | 0.018 | 22.42 | 13.25 |
| 00-90° | 0.168 | 0.045 | 36.50 | 21.34 |

* I_B is in nA, Δf is in Mhz

** normalized to 25 kV incident beam energy

Figure 5.5. Partial energy backscatter coefficients and isolated SNRs for bulk gold and silicon at 25 and 10 kV.

| 25 kV Incident Beam Energy | | | | | | |
|----------------------------|------------------------|-------------------|-----------|-------------------------|-------------------|-----------|
| 0.125 μm hole | | | | | | |
| Angle Range | 0.1 μm fwhm | | | 0.25 μm fwhm | | |
| | $\eta_{B_{\min}}$ | $\eta_{E_{\min}}$ | T_{opt} | $\eta_{B_{\min}}$ | $\eta_{E_{\min}}$ | T_{opt} |
| 10-40° | 0.027 | 0.022 | 0.060 | 0.110 | 0.090 | 0.121 |
| 30-60° | 0.034 | 0.027 | 0.077 | 0.145 | 0.117 | 0.160 |
| 50-80° | 0.025 | 0.019 | 0.059 | 0.109 | 0.085 | 0.120 |
| 0.125 μm step | | | | | | |
| Angle Range | 0.1 μm fwhm | | | 0.25 μm fwhm | | |
| | $\eta_{B_{\max}}$ | $\eta_{E_{\max}}$ | T_{opt} | $\eta_{B_{\max}}$ | $\eta_{E_{\max}}$ | T_{opt} |
| 10-40° | 0.283 | 0.238 | 0.088 | 0.170 | 0.137 | 0.068 |
| 30-60° | 0.211 | 0.167 | 0.088 | 0.148 | 0.110 | 0.073 |
| 50-80° | 0.117 | 0.089 | 0.056 | 0.093 | 0.065 | 0.048 |

Figure 5.6a. Partial backscatter coefficients and optimum thresholds for the 0.125 μm hole and 0.125 μm step structures.

| 25 kV Incident Beam Energy | | | | | | |
|----------------------------|------------------------|-------------------|-----------|------------------------|-------------------|-----------|
| 0.25 μm hole | | | | | | |
| Angle Range | 0.2 μm fwhm | | | 0.5 μm fwhm | | |
| | $\eta_{B_{\min}}$ | $\eta_{E_{\min}}$ | T_{opt} | $\eta_{B_{\min}}$ | $\eta_{E_{\min}}$ | T_{opt} |
| 10-40° | 0.031 | 0.026 | 0.065 | 0.116 | 0.096 | 0.130 |
| 30-60° | 0.038 | 0.030 | 0.081 | 0.151 | 0.121 | 0.160 |
| 50-80° | 0.028 | 0.022 | 0.059 | 0.113 | 0.089 | 0.120 |
| 0.25 μm step | | | | | | |
| Angle Range | 0.2 μm fwhm | | | 0.5 μm fwhm | | |
| | $\eta_{B_{\max}}$ | $\eta_{E_{\max}}$ | T_{opt} | $\eta_{B_{\max}}$ | $\eta_{E_{\max}}$ | T_{opt} |
| 10-40° | 0.296 | 0.237 | 0.089 | 0.176 | 0.137 | 0.068 |
| 30-60° | 0.242 | 0.190 | 0.094 | 0.159 | 0.118 | 0.075 |
| 50-80° | 0.152 | 0.118 | 0.064 | 0.106 | 0.077 | 0.052 |

Figure 5.6b. Partial backscatter coefficients and optimum thresholds for the 0.25 μm hole and 0.25 μm step structures.

| 10 kV Incident Beam Energy | | | | | | |
|-----------------------------|-------------------------|---------------------|-------------|-------------------------|---------------------|-------------|
| 0.2 μm beam fwhm | | | | | | |
| Angle Range | 0.25 μm hole | | | 0.25 μm step | | |
| | $\eta_{B_{\min}}$ | $\eta_{E_{\min}}^*$ | T_{opt}^* | $\eta_{B_{\max}}$ | $\eta_{E_{\max}}^*$ | T_{opt}^* |
| 10-40° | 0.041 | 0.013 | 0.028 | 0.200 | 0.062 | 0.032 |
| 30-60° | 0.053 | 0.016 | 0.037 | 0.255 | 0.080 | 0.042 |

* normalized to 25 kV incident beam energy

Figure 5.6c. Partial backscatter coefficients and optimum thresholds for the 0.25 μm hole and 0.25 μm step structures at 10 kV.

| 25 kV Incident Beam Energy | | | | | |
|----------------------------|------------------------|--|---------------------------------|-------|---------------------------------|
| 0.125 μm hole | | | | | |
| Angle | 0.1 μm fwhm | | 0.25 μm fwhm | | |
| | Range | $\frac{SNR_{opt}}{(I_B/\Delta f)^{1/2}} *$ | $(I_B/\Delta f)$ for $SNR=7$ | Range | $(I_B/\Delta f)$ for $SNR=7$ |
| | 10-40° | 14.27 | 0.241 | 5.81 | 1.450 |
| | 30-60° | 17.02 | 0.169 | 7.12 | 0.967 |
| | 50-80° | 14.93 | 0.220 | 6.26 | 1.252 |
| 0.125 μm step | | | | | |
| Angle | 0.1 μm fwhm | | 0.25 μm fwhm | | |
| | Range | $\frac{SNR_{opt}}{(I_B/\Delta f)^{1/2}}$ | $(I_B/\Delta f)$ for $SNR=7$ | Range | $(I_B/\Delta f)$ for $SNR=7$ |
| | 10-40° | 16.78 | 0.174 | 10.39 | 0.454 |
| | 30-60° | 10.84 | 0.417 | 6.47 | 1.170 |
| | 50-80° | 6.35 | 1.220 | 3.89 | 3.240 |

* I_B is in nA, Δf is in Mhz

Figure 5.7a. Optimum SNRs and required $I_B/\Delta f$ ratios for a SNR of 7. 0.125 μm hole and 0.125 μm step structures.

optimum threshold locations. Also listed are the $I_B/\Delta f$ values required for a SNR of 7. Results for the 0.25 μm structures at 25 kV and 10 kV are shown in Figures 5.7b and 5.7c, respectively. Results for bulk gold and silicon at 25 and 10 kV are shown in Figure 5.7d for comparison purposes.

The results of Figure 5.7 are left in terms of $(I_B/\Delta f)^{1/2}$ so that one can calculate SNRs for I_B given Δf and vice versa. As can be seen, the optimum threshold position with respect to the bulk gold and silicon signal levels changes with beam size, beam voltage, defect type, and defect size. Thus, the information in Figure 5.7 can be used to correctly set the threshold position for a variety of minimum detectable defect sizes over a range of beam sizes. Note that the effect of using a lower beam voltage is to increase the $I_B/\Delta f$ requirements, especially for the step structures at low take off angle collection. This is because at the lower voltage of 10 kV, most electrons incident near the center of the 0.25 μm step see only gold and; therefore, the maximum signal level at the middle of the structure is not very different than the signal from bulk gold.

As was discussed earlier, the threshold level can be increased from T_{opt} for detecting opaque defects and decreased for detecting clear defects. This is because a typical mask will contain very few defect locations relative to the number of inspection locations. Thus, the SNR requirement for detecting all the defects is less than that for false alarm free detection. As can be seen from equations 5.9a and 5.9b, the SNR for the maximum and minimum signal levels have a linear dependence on the threshold location. The SNR values at T_{opt} listed in this chapter should be thought of as limiting values which can be increased by appropriate setting of the threshold, depending on the expected defect distribution on the x-ray mask.

Figures 5.7a-c show a principal reason the 30-60 degrees angle range is favored for mask inspection. For detecting defects smaller than the incident beam size, the 30-60 degrees range gives more balanced SNR characteristics for the step and hole structures. In other words, the required $I_B/\Delta f$ for inspection is limited by the poorest quality signal and the required $I_B/\Delta f$ is less for the 30-60 degrees angle range. Also, an annular diode detector collecting backscattered

| 25 kV Incident Beam Energy | | | | | |
|----------------------------|------------------------|--|-------------------------------|--|-------------------------------|
| 0.25 μm hole | | | | | |
| Angle | 0.2 μm fwhm | | 0.5 μm fwhm | | |
| | Range | $\frac{SNR_{opt}}{(I_B/\Delta f)^{1/2}} *$ | $(I_B/\Delta f)$ for SNR=7 | $\frac{SNR_{opt}}{(I_B/\Delta f)^{1/2}}$ | $(I_B/\Delta f)$ for SNR=7 |
| | 10-40° | 13.51 | 0.269 | 5.23 | 1.790 |
| | 30-60° | 16.55 | 0.179 | 6.79 | 1.060 |
| | 50-80° | 14.35 | 0.238 | 5.87 | 1.420 |
| 0.25 μm step | | | | | |
| Angle | 0.2 μm fwhm | | 0.5 μm fwhm | | |
| | Range | $\frac{SNR_{opt}}{(I_B/\Delta f)^{1/2}} *$ | $(I_B/\Delta f)$ for SNR=7 | $\frac{SNR_{opt}}{(I_B/\Delta f)^{1/2}}$ | $(I_B/\Delta f)$ for SNR=7 |
| | 10-40° | 17.04 | 0.169 | 10.47 | 0.447 |
| | 30-60° | 12.52 | 0.313 | 7.21 | 0.943 |
| | 50-80° | 8.98 | 0.608 | 5.23 | 1.790 |

* I_B is in nA, Δf is in Mhz

Figure 5.7b. Optimum SNRs and required $I_B/\Delta f$ ratios for a SNR of 7. 0.25 μm hole and 0.25 μm step structures.

| 10 kV Incident Beam Energy | | | | |
|-----------------------------|--|---------------------------------|--|---------------------------------|
| 0.2 μm beam fwhm | | | | |
| Angle | 0.25 μm hole | | 0.25 μm step | |
| | $\frac{SNR_{opt}}{(I_B/\Delta f)^{1/2}} *$ | $(I_B/\Delta f)$ for $SNR=7$ | $\frac{SNR_{opt}}{(I_B/\Delta f)^{1/2}}$ | $(I_B/\Delta f)$ for $SNR=7$ |
| 10-40° | 11.81 | 0.351 | 10.92 | 0.411 |
| 30-60° | 15.03 | 0.217 | 11.86 | 0.348 |

* I_B is in nA, Δf is in Mhz

Figure 5.7c. Optimum SNRs and required $I_B/\Delta f$ ratios for a SNR of 7. 0.25 μm hole and 0.25 μm step structures at 10 kV.

| Bulk Gold on Silicon | | | | | | |
|----------------------|-------------|---|---------------------------------|-----------|--|---------------------------------|
| Angle Range | 25 kV | | | 10 kV | | |
| | T_{opt}^* | $\frac{SNR_{opt}}{(I_B/\Delta f)^{1/2}}^{**}$ | $(I_B/\Delta f)$ for $SNR=7$ | T_{opt} | $\frac{SNR_{opt}}{(I_B/\Delta f)^{1/2}}$ | $(I_B/\Delta f)$ for $SNR=7$ |
| 10-40° | 0.074 | 12.31 | 0.323 | 0.033 | 10.80 | 0.421 |
| 30-60° | 0.100 | 14.27 | 0.241 | 0.044 | 12.97 | 0.291 |
| 00-90° | 0.194 | 19.87 | 0.124 | 0.084 | 18.33 | 0.146 |

* normalized to 25 kV incident beam energy

** I_B is in nA, Δf is in Mhz

Figure 5.7d. Optimum SNRs and required $I_B/\Delta f$ ratios for a SNR of 7. Bulk gold on silicon at 25 and 10 kV.

electrons in the 30-60 degrees range has less surface area than one collecting electrons in the 10-40 degrees range.

It is instructive to see at what bandwidth, shot noise will become the fundamental limitation to the speed of mask inspection. Consider a new electron-beam system being developed by the Electron Beam Corporation [79]. It has been reported that its thermal field emitter gun can put $0.4 \mu\text{A}$ in a $0.125 \mu\text{m}$ spot and $2.4 \mu\text{A}$ in a $0.5 \mu\text{m}$ spot. Using these currents and the $I_B/\Delta f$ requirements for the $0.125 \mu\text{m}$ structures gives a conservative shot noise bandwidth limitation of over 600 Mhz. Using the reported beam currents and the $I_B/\Delta f$ requirements for the $0.25 \mu\text{m}$ defects at 25 kV gives limiting bandwidths of 1.3 and 2.3 Ghz for the 0.2 and $0.5 \mu\text{m}$ beam sizes, respectively. Clearly, shot noise will not be a fundamental limitation for inspection of x-ray masks with a machine of this type.

Consider an IBM EL-3 variable shaped beam electron-beam system [80]. An EL-3 modified to produce a $0.5 \times 0.5 \mu\text{m}$ rectangular shaped spot has about 25 nA of beam current at 25 kV. Using the results for a $0.5 \mu\text{m}$ beam and $0.25 \mu\text{m}$ structures gives a limiting bandwidth of 23.6 Mhz. This is still well above the bandwidth of most currently available solid-state detectors. Thus, it can be seen that with the beam currents available in electron-beam systems, shot noise will not be a fundamental limitation unless the beam size is significantly greater ($> 2x$) than the minimum defect size. However, as can be seen from analysis of Figures 5.6 and 5.7, shot noise can be a problem if the thresholds for detecting clear and opaque defects are not set correctly, especially when the beam is larger than the defect.

5.3.3. A SNR Comparison of Gold and Chrome Masking Material

Although this research is primarily concerned with x-ray mask inspection, it is interesting to explore the SNR characteristics of the backscattered electron signal from a typical optical lithography mask. Typical optical masks will consist of a thin layer ($0.08 \mu\text{m}$) of chrome on SiO_2 . For simulation purposes, the backscattered electron signal characteristics from chrome on silicon were calculated using the Monte Carlo program. Figure 5.8 lists the SNR information

| Bulk Chrome, Thin Chrome, Thin Gold on Silicon | | | | | |
|---|--------------------------|--|---------------------|-----------|--|
| Material | Beam Voltage (kV) | $\frac{SNR_i}{(I_B/\Delta f)^{1/2}} *$ | $\eta_E^{*\dagger}$ | T_{opt} | $\frac{SNR_{opt}}{(I_B/\Delta f)^{1/2}} *$ |
| Bulk Cr | 25 | 19.24 | 0.098 | 0.070 | 5.65 |
| 0.08 μm Cr | 25 | 14.62 | 0.054 | 0.052 | 0.64 |
| 0.08 μm Cr | 10 | 17.25 | 0.034 | 0.029 | 2.90 |
| 0.08 μm Au | 25 | 19.95 | 0.139 | 0.080 | 8.54 |
| 0.08 μm Au | 10 | 25.52 | 0.084 | 0.044 | 12.25 |

* 30-60° angle collection range

† all results normalized to 25 kV incident beam energy

Figure 5.8. Signal to noise characteristics of chrome and gold on silicon.

for thick chrome at 25 kV and 0.08 μm chrome on silicon at 25 and 10 kV. As can be seen, the thin chrome requires a large $I_B/\Delta f$ for adequate SNR. The situation is improved somewhat if the beam energy is lowered. Using the beam currents available from the electron-beam machines discussed in the previous section, calculations for a SNR of 7 show that the EBC machine is shot noise limited, for thin chrome at 25 kV, at about 20 Mhz and the EL-3 machine is shot noise limited at about 200 Khz. Remember that these bandwidths are fundamental limitations and that system noise will likely reduce the actual inspection bandwidth.

Figure 5.8 also shows the SNR results for 0.08 μm gold on silicon at 25 and 10 kV. Note the large increase in SNR at the optimum threshold level. Essentially, these results show that at higher beam voltages, it will be difficult to inspect optical photomasks using an electron-beam system. However, if the beam voltage is lowered to around 10 kV, the fundamental shot noise limitations become less severe. However, as the beam voltage is lowered, the amount of current in a beam of a given size is reduced [14]. If optical masks are fabricated out of a thin gold or other high atomic number layer [4], there would not be any fundamental shot noise limitations to inspecting optical masks with an electron-beam system. Similar results could be obtained if a gold on silicon copy of the mask was fabricated using optical lithography.

5.4. Relationship of ΔSNR to SNR

The ΔSNR was introduced in Chapter 3 as a means of quantitatively evaluating the noise quality of the backscattered electron signal. After the discussion of SNR requirements in this chapter, it is worthwhile to see how the ΔSNR actually relates to the SNR for various structures. Figures 5.9a and 5.9b list the ΔSNR , SNR with the threshold set at the middle of the two signal levels, and SNR with the threshold set at T_{opt} for the 0.25 μm step and hole. The three angle ranges are used and the beam sizes are 0.2 and 0.5 μm . The ΔSNR accurately tracks the calculated middle threshold SNR over all angle ranges, beam sizes, and defect types. This is important since it verifies that the ΔSNR correctly predicts limiting behavior of the noise characteristics of the signal. As shown in Figure 5.9, the SNR of the high signal is always lower

| 0.25 μm Hole | | | | |
|-----------------------------|--------------------|---|---|---|
| 0.2 μm beam fwhm | | | | |
| Angle Range | ΔSNR | $\frac{\text{SNR}_{opt}}{(I_B/\Delta f)^{1/2}} *$ | $\frac{\text{SNR}_{Au-Middle-T}}{(I_B/\Delta f)^{1/2}}$ | $\frac{\text{SNR}_{Si-Middle-T}}{(I_B/\Delta f)^{1/2}}$ |
| 10-40° | 0.67 | 13.51 | 9.48 | 23.50 |
| 30-60° | 0.80 | 16.55 | 11.36 | 30.64 |
| 50-80° | 0.69 | 14.35 | 9.75 | 27.27 |
| 0.5 μm beam fwhm | | | | |
| 10-40° | 0.33 | 5.23 | 4.65 | 6.00 |
| 30-60° | 0.42 | 6.79 | 5.90 | 7.96 |
| 50-80° | 0.36 | 5.87 | 4.15 | 6.98 |

* I_B is in nA, Δf is in Mhz

Figure 5.9a. A comparison of the ΔSNR with the SNR at the optimum threshold and with the SNR at the middle threshold. 0.25 μm hole structure.

| 0.25 μm Step | | | | |
|-----------------------------|--------------------|---|---|---|
| 0.2 μm beam fwhm | | | | |
| Angle Range | ΔSNR | $\frac{\text{SNR}_{opt}}{(I_B/\Delta f)^{1/2}} *$ | $\frac{\text{SNR}_{Au-Middle-T}}{(I_B/\Delta f)^{1/2}}$ | $\frac{\text{SNR}_{Si-Middle-T}}{(I_B/\Delta f)^{1/2}}$ |
| 10-40° | 0.82 | 17.04 | 11.53 | 32.59 |
| 30-60° | 0.64 | 12.52 | 9.09 | 20.10 |
| 50-80° | 0.48 | 8.98 | 6.77 | 13.34 |
| 0.5 μm beam fwhm | | | | |
| 10-40° | 0.53 | 10.47 | 7.71 | 16.33 |
| 30-60° | 0.39 | 7.21 | 5.76 | 9.73 |
| 50-80° | 0.29 | 5.23 | 4.31 | 6.55 |

* I_B is in nA, Δf is in Mhz

Figure 5.9b. A comparison of the ΔSNR with the SNR at the optimum threshold and with the SNR at the middle threshold. 0.25 μm step structure.

than the SNR of the low signal. It is this limiting high signal level's SNR which the Δ SNR tracks.

Generally, the Δ SNR also tracks, in a relative manner, the SNR at the T_{opt} level. However, since the Δ SNR uses the maximum signal level to estimate the noise in the signal, there are differences between the Δ SNR and SNR if the low signal level is relatively high. This is the case for the 30-60 degrees angle range and 0.5 μ m beam size. The Δ SNR is slightly higher for the hole; but, the optimum threshold SNR is slightly higher for the step. This is because the low signal level's shot noise has more of an effect than the high signal level's shot noise when the threshold is set to T_{opt} . It can be concluded; however, that the Δ SNR is still a good figure of merit in estimating the noise quality of backscattered electron signal.

5.5. Summary

In this chapter, we examined the various backscattered electron detectors which can be used in an electron-beam system. From a practical point of view, the diode detector would seem to be the best choice over the scintillator-photomultiplier and channel plate detectors.

The effects of shot noise, the fundamental limitation to reliable high speed mask inspection using an electron-beam system, were studied on the backscattered electron signal for a variety of structures. It was shown that the difference in signal levels between gold and silicon along with the placement of the comparator threshold level were critical in determining the SNR quality of a backscattered electron signal. The SNR characteristics of shot noise limited signals were investigated for 0.125 μ m, 0.25 μ m, and bulk structures. All results were left in terms of $(I_B/\Delta f)^{1/2}$ so that they could be applied to a variety of electron-beam systems. The optimum threshold was introduced as the threshold location at which the SNR for both the high and low signal levels are the same.

For beam sizes smaller than the structure fwhm, the placement of the threshold is not as critical as it is for larger beam sizes in which the signal level difference is reduced. Analysis shows that the shot noise will not be a fundamental problem until the beam size is over twice

the defect size. The shot noise limited SNR depends on the $(I_B/\Delta f)^{1/2}$ value and tables showing the shot noise SNR characteristics of the backscattered electron signals from various structures were presented to aid in the design of an electron-beam inspection system.

It was also shown that thin ($0.08 \mu\text{m}$) chrome structures, such as those found on optical lithography masks, will be difficult to inspect at high electron-beam voltages because of poor SNR quality. The situation can be improved somewhat by increasing the chrome thickness or by lowering the beam energy. Using gold instead of chrome as the masking material also greatly improves the SNR.

Finally, the ΔSNR parameter introduced in Chapter 3 was shown to track the actual shot noise limited SNR fairly well and is therefore a valuable figure of merit for backscattered electron signal quality.

CHAPTER 6

6. MASK INSPECTION USING AN ELECTRON-BEAM SYSTEM

6.1. Introduction

The previous chapters have been concerned with the simulation and analysis of the back-scattered electron signal used to detect the presence or absence of masking material. The goal of this chapter is to see how the backscattered electron signal from the mask or mask copy can be compared to design data in order to detect defects. The design data is derived from the computer aided design (CAD) data and specifies what patterns should be present on the mask.

In this chapter, an overview of optical and electron-beam inspection systems will be presented. The question of whether to inspect the mask or a copy of the mask will also be discussed. An inspection scheme using a vector scan electron-beam lithography system will be proposed. Finally, using the results of the previous chapters, various electron-beam scanning techniques will be discussed.

6.2. Optical and Electron-Beam Inspection

6.2.1. Optical Inspection Techniques

Automatic inspection techniques have been used on optical lithography masks and reticles since the middle 1970's. Early methods [81-83] involved scanning two neighboring chip patterns with two laser beams. The two signals, each generated by the transmitted laser light through the mask, are compared and any deviations are recorded as defects. Surface defects, which can easily be removed unlike actual mask defects, can be distinguished by sensing non-specularly scattered light in coincidence with the normal defect detection signal [81-83]. These early systems identified the location of defects and an operator was required to manually characterize each of the detected defects. Systems were also designed which used two microscope

objectives to detect transmitted light through the mask. These light signals were then detected using video sensors, such as photodiode arrays, correlated, and then compared [84]. The minimum detectable defect size for these first systems was reported to be in the 2-5 μm range [81,83] with a complete inspection time, including manual characterization, for a 4 inch by 4 inch mask being about 1 hour [83].

The chip to chip comparison technique outlined above is limited in its resolution limit to 1-2 μm , does not allow the inspection of single die reticles, does not allow complete automatic characterization of defects, neglects defects caused by lithographic exposure errors, and is incapable of detecting lost or missing patterns which can occur when a pattern is transferred from a reticle to a master mask [85,86]. New optical techniques have been developed which allow the inspection to take place by a comparison of the pattern image with CAD data [85-90]. Typically, the image is acquired by detecting transmitted light through a microscope objective. The light is then amplified using photodiodes [88] or video pick-up tubes [85] and the resulting signal is digitized. Recent image acquisition schemes have allowed the images from resist patterns on wafers to be detected and digitized [89-90]. The resulting digitized signal is then compared with a database prepared from the original CAD data describing the mask.

The inspection of the mask, wafer, or reticle is not done all at once. Only a small portion, 512 \times 512 pixels for example, is inspected at a given time and the mask and design images are correlated to eliminate registration errors [88]. Image processing techniques are then used to identify and characterize the defects [85,88-90]. Minimum detectable defect sizes are usually reported as between 0.5 and 1.0 μm for 90 percent detection reliability. The minimum feature sizes of the patterns to be inspected are usually between 1.25 and 1.5 μm . The actual inspection time for these systems depends upon the amount of image processing required, the complexity of the patterns, and the size of the mask. For example, the Contrex system [89,91] specifications state that it can inspect a 7.6 \times 7.6 mm die in one hour at a defect detection resolution of 0.5 μm . The inspection pixel size for this resolution is 0.15 μm . The Cambridge system [90,92] reports a typical inspection time of 10 minutes for a 10 mm \times 10 mm die with a

defect resolution of $0.8 \mu\text{m}$. Both the Contrex and Cambridge systems can inspect resist images on wafers. The KLA system [88,93] is reported to be able to inspect a $10 \text{ mm} \times 10 \text{ mm}$ pattern with $0.9 \mu\text{m}$ defect detection resolution in 6 minutes. The pixel size used for this resolution is $0.5 \mu\text{m}$. All of these systems use image processing to characterize the defects and also to correct for registration errors. Note that these times listed here do not include the time to convert from CAD data to inspection data. Also, the amount of time required to inspect will depend on the pattern complexity. The approximate costs for these advanced optical inspection systems runs from 700,000 (KLA) to 850,000 (Contrex) dollars. In a later section, we will examine the time required by an electron-beam system to scan x-ray mask patterns of similar sizes.

6.2.2. Electron-Beam Inspection Techniques

There have been only several reports of electron-beam systems being modified to perform the mask inspection function [1-4]. It is worthwhile to examine the techniques outlined in these papers.

The method of Goto et al [1] uses a scanning electron microscope and a feature extraction (image processing) algorithm to inspect a mask for defects. Essentially, a portion of the mask is scanned with the SEM and the image is digitized. A window of pixels slightly smaller than the minimum linewidth of the pattern is used to extract the defects using a pattern recognition algorithm. A defective pattern in a window has several parallel contour lines while a normal pattern has none. It is assumed that a defect has a complicated fine structure which can be electronically detected while normal structures are smoother and have specified directions [1].

There are several disadvantages to this technique. As presented in the article, a defect's type (presence or absence of masking material) and location on the chip are not recorded. However, there are more fundamental problems. The main problem lies in the assumption that defects usually have complicated fine structures and that they are smaller than the minimum linewidth. This neglects any defects which might consist of missing lines or spaces, shifted

patterns, patterns too large or too small, and defects larger than the minimum linewidth (although it is possible that the edges of a large defect would be detected). As far as inspection speed is concerned, the time it takes to inspect the digitized mask pattern data is reasonable (a 2 inch square mask with 9×10^{10} pixels is estimated to take 2 hours to inspect for $0.3 \mu\text{m}$ defects). However, no indication is given to the significant amount of time it takes to collect and process the mask pattern data into the digitized form needed for inspection. Although not mentioned, parallel processing would enable windows to be inspected while other windows were being scanned in the SEM. Advantages of this technique are that registration is not required and a CAD data set is not needed.

The mask inspection method proposed by Wada and others [2] uses an electron-beam system and software comparison of CAD data to mask pattern data. Registration to the mask is performed and measured pattern data for the inspection field is detected, digitized, and stored in a memory matrix. This data is then compared to the design data matrix in the control computer. To allow for registration error, a dead region is set up around pattern shapes. Any defects detected in this region are not recorded.

The major limitation of this method is that the inspection is not done in real time. The defect inspection is done after the pattern data is gathered. Memory requirements are also substantial. Recall that the $2.5 \text{ cm} \times 2.5 \text{ cm}$ mask described in Chapter 5 contained over 10^{11} beam locations. Therefore, only portions of the mask could be inspected at a given time. The electron-beam system would then be idle while the control computer is involved with the comparison of the image data to design data. Note that another requirement is that design data be converted into bit map format. To do this efficiently, another pattern generator would be required to convert the compressed shapes of the design data into the bit map. It has been reported that the mask inspection system described in [2] is being modified to perform the inspection by a real time comparison of design data to the backscattered electron signal [94] although this work has not appeared in the literature to date.

Migitaka and others [3] have reported a more recent automated mask inspection system. However, their paper deals with a system which is designed to automatically measure pattern width, pattern position, and chip position. It was reported that the system was being modified to detect pattern defects on the mask.

Simpson and Davis [4] have reported a real-time mask inspection system which utilizes the IBM EL-3 variable shaped electron-beam system. Their technique, similar to the one which will be discussed for use on a vector scan electron-beam system later in this chapter, involves scanning over the positive areas of a mask (where masking material is present). Therefore, the backscattered electron signal should always remain high. A low signal during this scan indicates a clear defect. A similar technique is used to scan the negative areas of the mask. In this case, a defect is detected when the signal goes high. A dead zone is put around all shapes to allow for registration error. Inspection is performed by breaking the pattern data into subfields and then registering to each subfield before inspecting. The detection scan is performed as quickly as possible and detected defects are then checked in another scan to eliminate false alarms caused by low SNR. Different thresholds are used for clear and opaque defects. The advantage of this technique is that the backscattered electron signal does not have to be compared with a stream of specially processed design data. The comparison is taken care of by scanning the electron-beam over the positive and negative regions of the mask using data sets similar to the data used to write the mask. One disadvantage of this technique is that if the system used to write the mask is used to inspect it as well, any systematic machine problems (such as rotation or offset) will not be detected.

6.3. Inspect Mask or a Copy of the Mask?

An important question which must be considered is whether to inspect the actual mask itself or a copy of the mask made using its associated lithography tool. The mask copy can be fabricated with material parameters which allow for the optimum detection of defects. For example, we have seen that a typical chrome on SiO_2 optical mask will be very difficult to

inspect using an electron-beam system because of noise limitations. However, a copy of the mask could be fabricated out of about $0.20\ \mu\text{m}$ of gold on silicon and be perfectly suitable for electron-beam inspection at 25 kV. Also, by inspecting a copy of the mask, the effects of the resist and the lithographic process bias are included. Thus, only defects reproduced by the lithography system for which the mask is used are detected. This is important in x-ray lithography in which some particles will have very little influence on the x-rays transmitted through the mask. Moreover, the copy is not as fragile as the actual mask, especially for the thin membrane x-ray mask, and the mask is not subject to additional defects introduced by the inspection process (such as someone putting his or her thumb through the mask membrane).

Obviously, some false defects will be introduced by the fabrication of the mask copy; but, these can be overcome fairly easily, especially if a step-and-repeat mask is being inspected. In that case, the mask pattern can be exposed in several locations on a wafer. One pattern can be completely inspected and then the other patterns can be inspected only in the defect location areas in order to eliminate the random defects introduced during the fabrication of the mask copy. Inspection of a mask copy has been mentioned as an attractive option by several authors of papers dealing with optical mask inspection [87,89,94]. It has also been suggested that for optical mask inspection with electron-beams that the optical masks be fabricated with gold, instead of chrome, as the masking material [4].

6.4. Demonstrating Mask Inspection Using a Vector Scan Electron-Beam System

The vector scan electron-beam system [7] used in fabricating the test patterns of Chapter 2 and in the experimental backscattered electron signal studies of Chapter 3 was used in an experimental demonstration of an x-ray mask inspection system [6]. This is important since this same electron-beam system was designed to write the actual x-ray mask.

The inspection technique consists of comparing the backscattered electron signal from the copy of the mask with the design data stored in the memory of the electron-beam system control computer. This is accomplished in real time by first registering to the alignment marks

contained in the pattern to be inspected and then scanning the electron-beam over all areas where there is gold. During this scan over gold, the backscattered electron signal should always be high. If the signal goes low, a clear defect (i.e. a hole) in the gold has been detected. A similar method is used to detect opaque defects (gold in designed clear areas). This technique is similar to the method discussed by Simpson and Davis [4]. For the gold on silicon patterns fabricated for this study, the positive scan detects clear defects in the gold while the negative scan detects opaque defects. The dead zone, formed by reducing the size of the rectangles in the inspection pattern, is needed to allow for registration error and is illustrated in Figure 6.1. In this study each rectangle was reduced $0.25 \mu\text{m}$ per side.

The system used for demonstrating the proposed mask inspection technique is shown in Figure 6.2. The control computer instructs the pattern generator to deflect the electron-beam over the positive or negative zone of a portion ($128 \mu\text{m} \times 128 \mu\text{m}$ subfield) of the test pattern. The x,y position signals are amplified and along with the beam blanking signal are input to the storage tube. At the same time, the backscattered electron signal is inverted and sent to the video input of the storage tube. Thus, for a positive scan over gold, holes in the gold will appear as bright images on the storage tube. The next step is then to switch the video input of the storage tube to the background bias and rewrite the design image so that the designed pattern is stored at a reduced intensity. The net result as seen on the TV monitor shows bright defects on a low intensity image of the designed pattern. Thus, the approximate size and location of the defects are known.

Detection of sub-micron defects using this method is illustrated in Figures 6.3 and 6.4. Figure 6.3a shows the inspection (design) pattern with reduced size rectangles. The design pattern was an array of $0.5 \mu\text{m}$ gold squares surrounded by gold. Figure 6.3b shows the effect of misregistration during an inspection scan. The bright bands around the outer portions of the rectangles as well as the many pseudo-defects in the central area are due to poor registration in both the x and y directions. However, an actual clear defect can easily be seen. Figure 6.3c shows the actual defect detected after proper registration. For this study, registration was

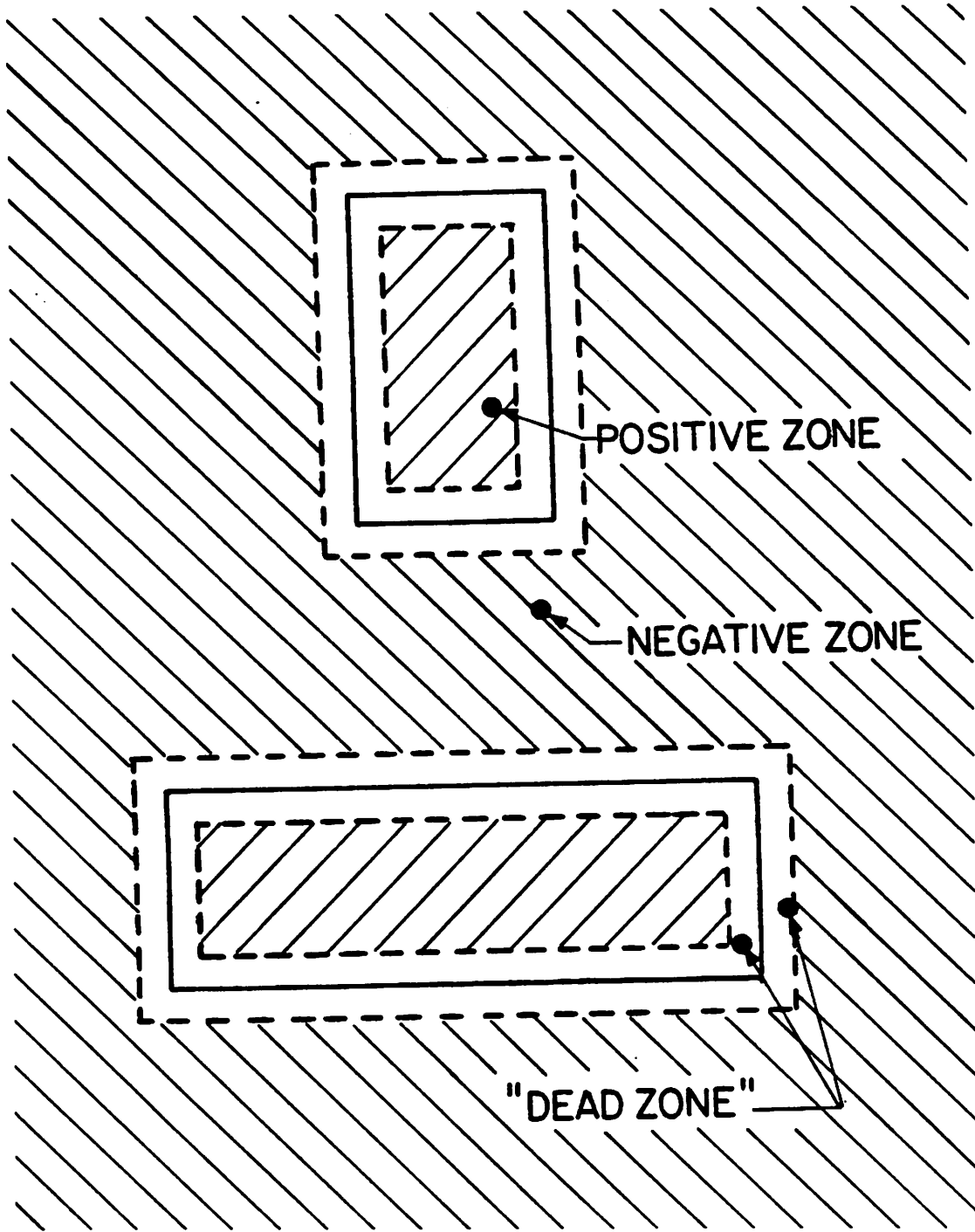


Figure 6.1. An illustration of the dead zone as well as the positive and negative scan regions for the proposed mask inspection system.

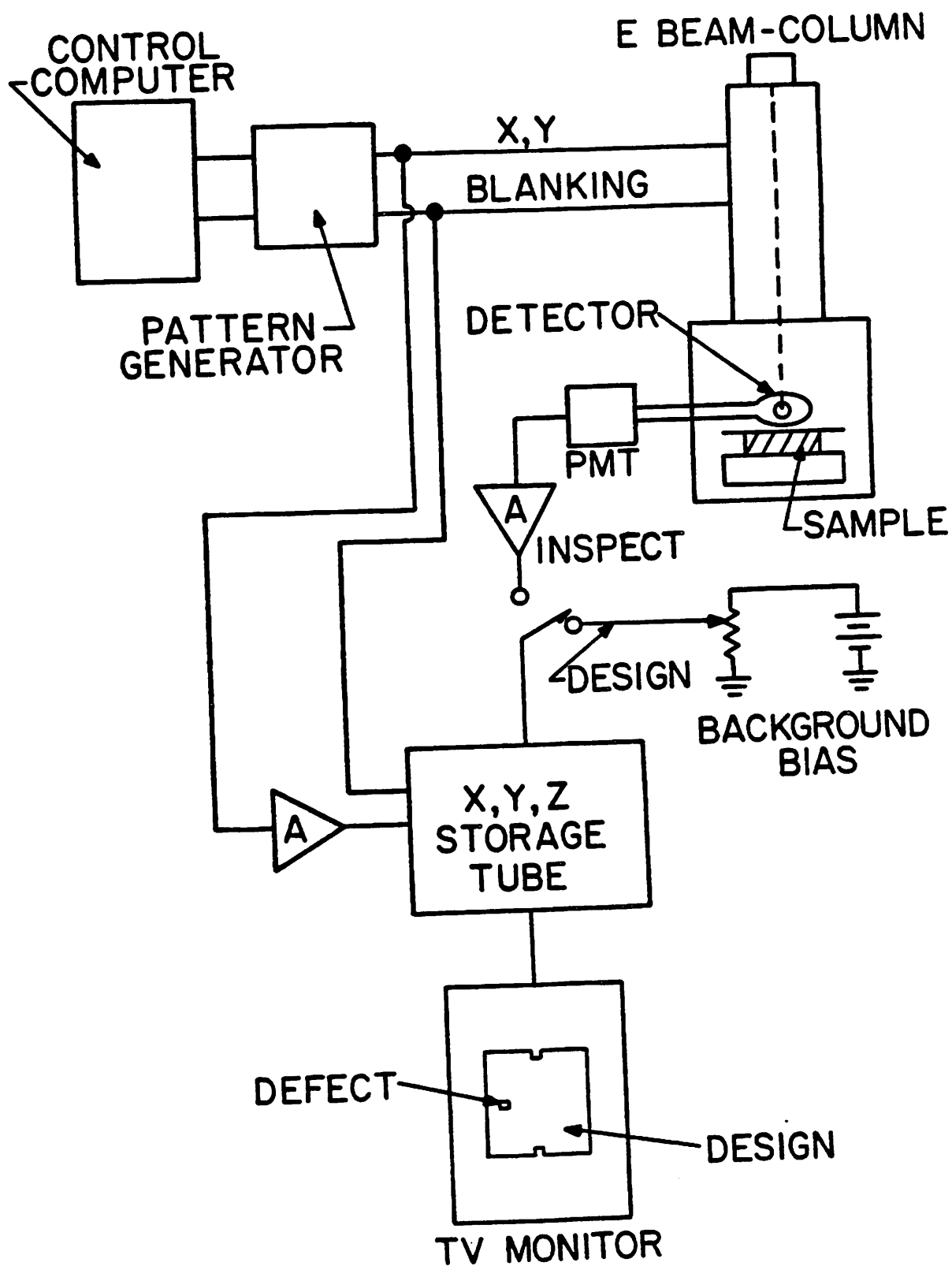


Figure 6.2. The system used to demonstrate a mask inspection algorithm using a vector scan electron-beam system.

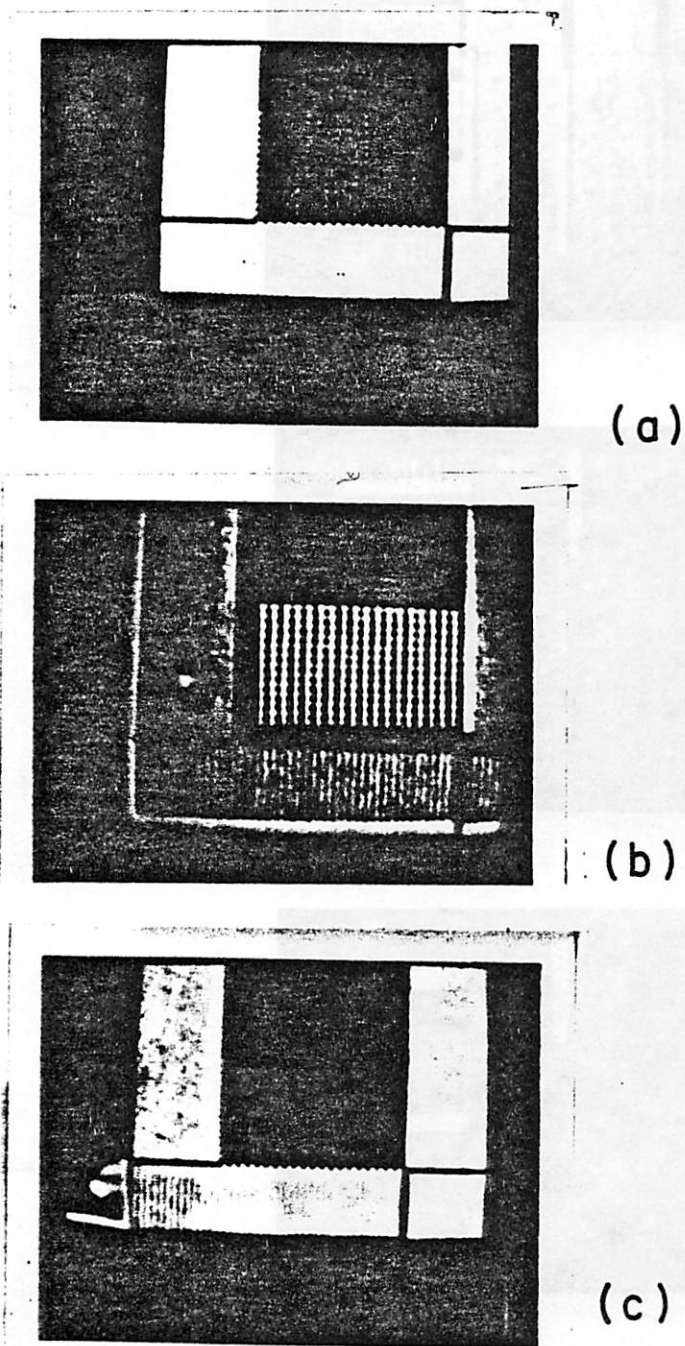


Figure 6.3. Isolation of a submicron defect (a) designed pattern with reduced sized rectangles (b) effects of misregistration on inspection (c) proper registration and isolated submicron defect.

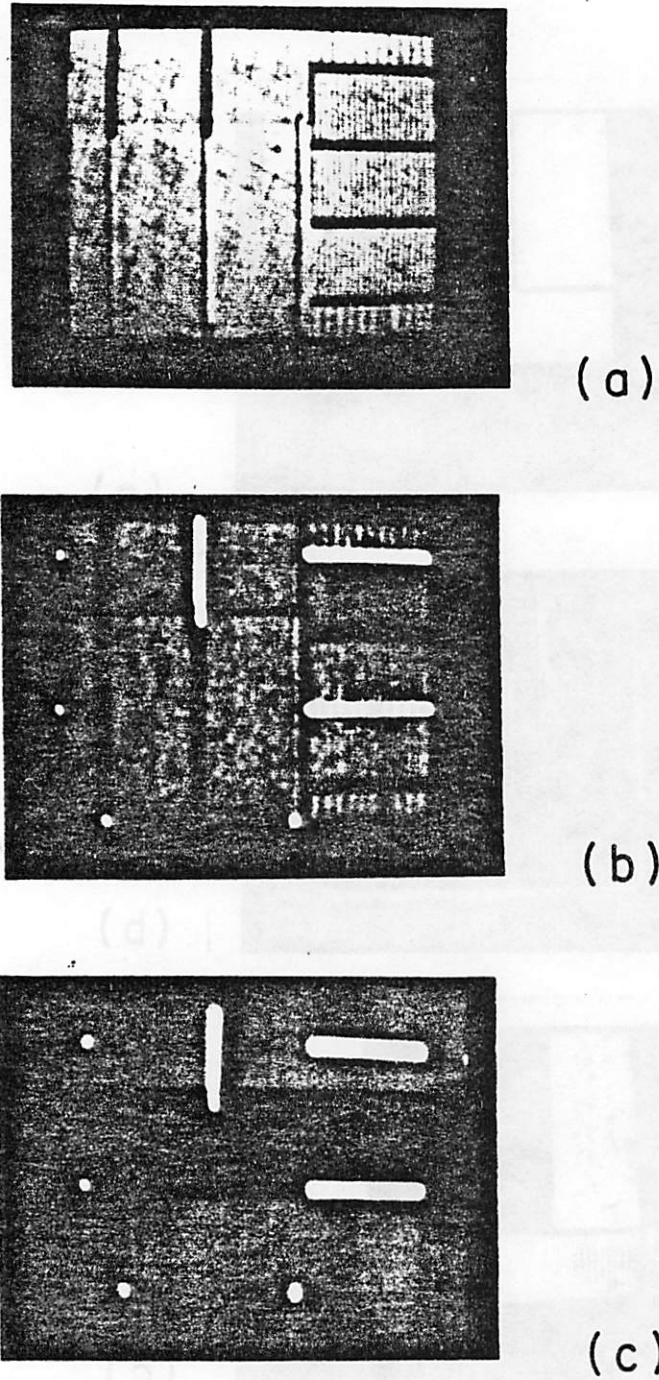


Figure 6.4. Use of programmed defects (a) designed pattern (b) detected defects overlaid on design pattern (c) isolated programmed defects.

performed manually. This irregularly shaped defect was $0.5 \mu\text{m}$ at its smallest and $0.9 \mu\text{m}$ at its largest dimension.

Figure 6.4 illustrates the use of programmed defects. Figure 6.4a shows the designed pattern of $0.75 \mu\text{m} \times 15 \mu\text{m}$ and $0.75 \mu\text{m} \times 0.75 \mu\text{m}$ indentations. The actual fabricated pattern's feature sizes were reduced to $0.5 \mu\text{m}$ because of process bias. Figure 6.4b shows 7 programmed clear defects detected over a background of the actual designed pattern. Figure 6.4c shows just the detected programmed defects. Note the linewidth of the line defect was $0.5 \mu\text{m}$ while the square programmed defects were $0.5 \mu\text{m} \times 0.5 \mu\text{m}$. Because of the $0.25 \mu\text{m}$ dead zone around the inspection rectangles, the $0.5 \mu\text{m} \times 0.5 \mu\text{m}$ clear defects were detected by scanning over only a $0.25 \mu\text{m} \times 0.5 \mu\text{m}$ portion of each defect.

These experiments were carried out using a 15 nA beam current and a scan frequency of 100 kHz . The rather slow scan speed was due to bandwidth limitations in the amplifiers used to amplify the x,y position signal of the electron beam. Using wide band amplifiers specifically designed for this purpose, automatic registration, and a fast diode detector, it should be possible to scan at TV rates. The storage tube is used for display purposes only. In an actual system, the defect location and type would be stored in the memory of the control computer. A block diagram of the mask inspection system is shown in Figure 6.5.

6.5. A Mask Inspection System Using a Vector Scan Electron-Beam System

The work of the previous section demonstrated that a vector scan electron-beam system could be modified to perform the mask inspection function. In this section, a mask inspection system will be proposed for a Gaussian beam shape vector scan electron-beam system. The use of raster scan and variable spot size electron-beam lithography systems will also be investigated.

The complete outline of the mask inspection system is shown in Figure 6.6 The system is similar to that proposed by Simpson and Davis [4] except that it is applied to a vector scan electron-beam system. The first step in using this system to inspect a mask is to take the original design data set and etch the pattern shapes to allow for an inspection dead zone. The

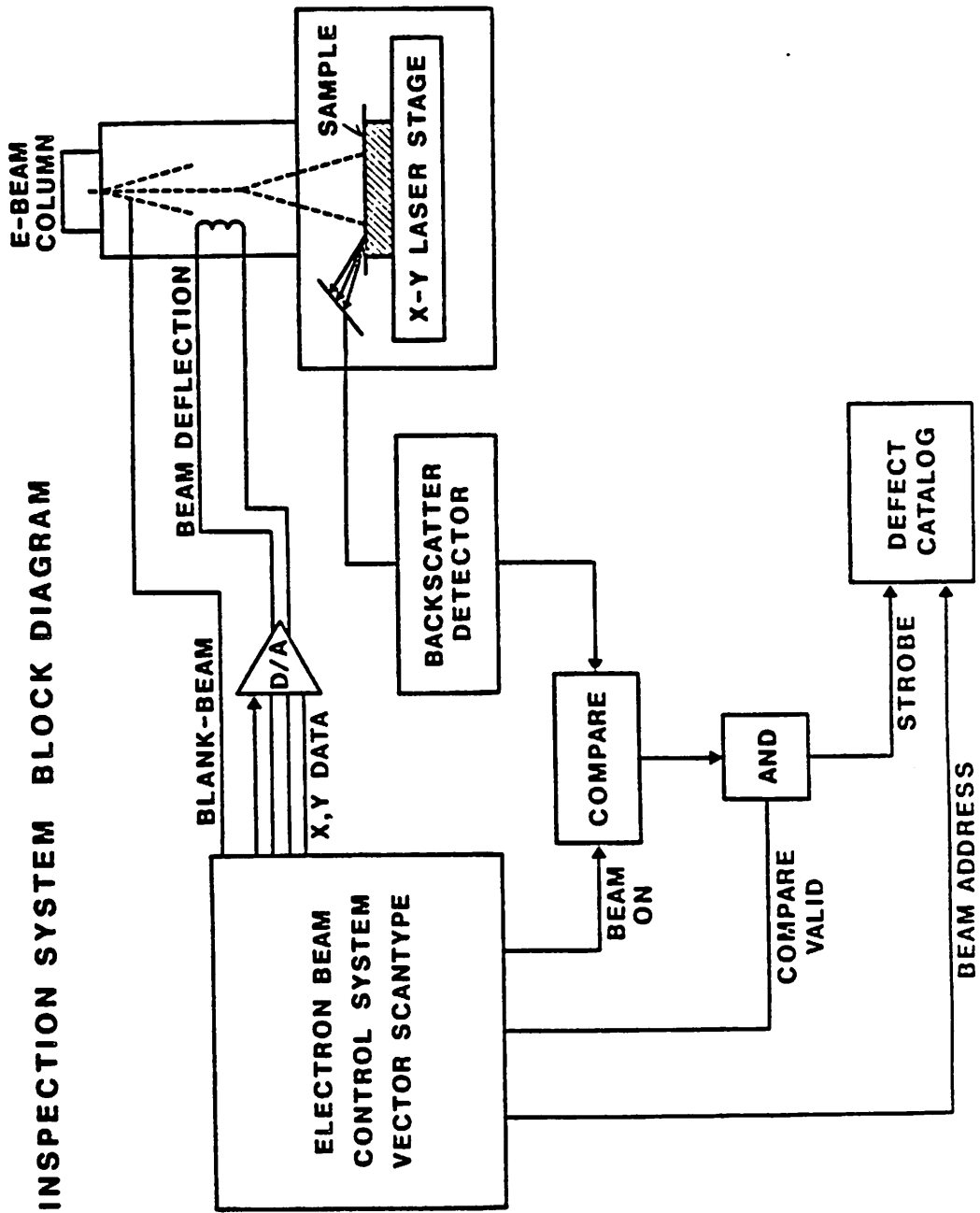
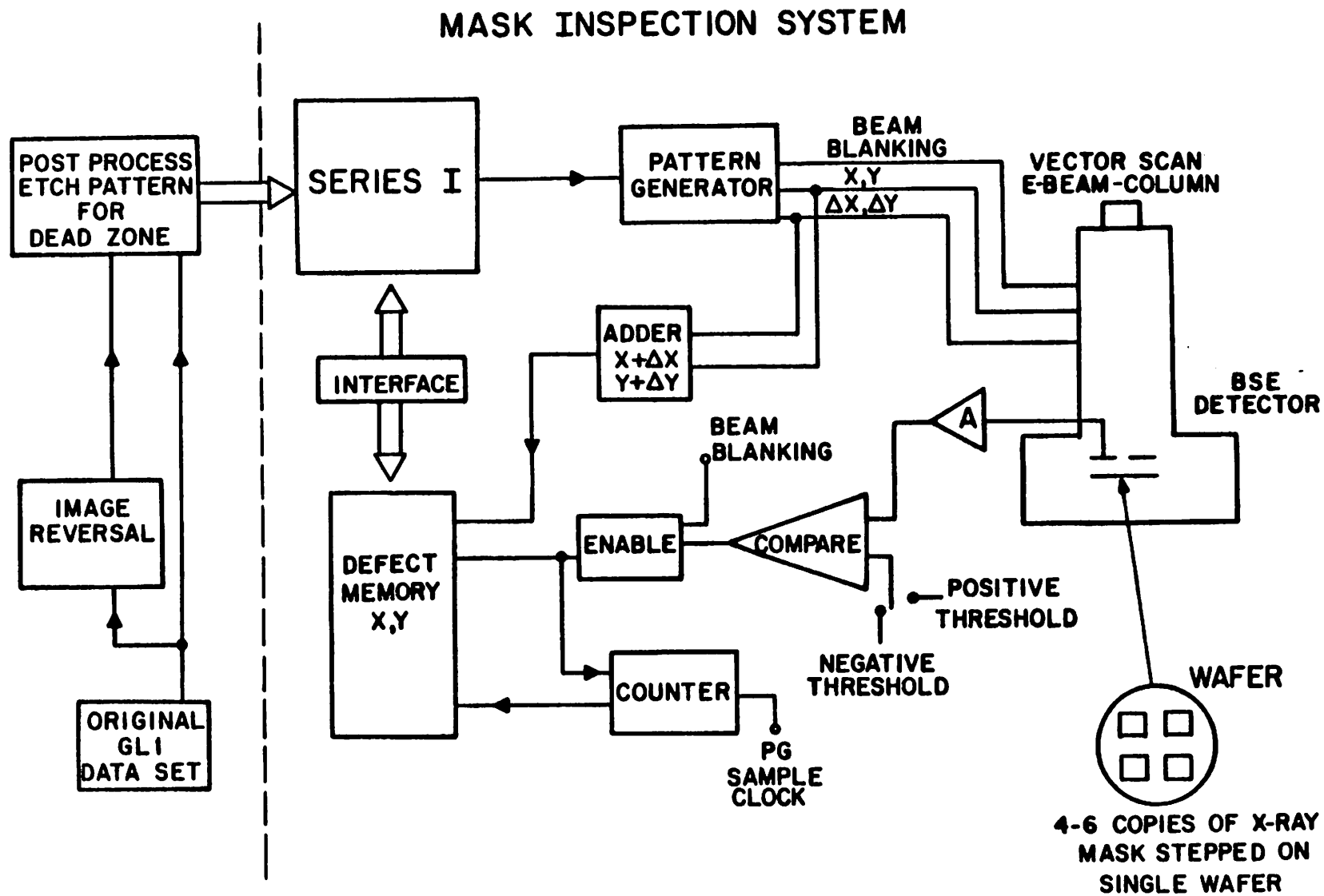


Figure 6.5. A general outline of an electron-beam mask inspection system.

Figure 6.6. A more detailed diagram of the proposed mask inspection system.



negative of the design data set is obtained using proprietary IBM software and the resulting negative pattern is etched to create a dead zone. The two data sets are then post-processed into the format required by the electron-beam system. The pattern data post-processing is relatively straightforward since proximity correction is not required. Also, note that very little additional software is required to prepare these data sets since they are of the same type as those which are used for resist exposure. The inspection data sets are then downloaded to the IBM Series I control computer.

The actual mask inspection process is conceptually very simple. The x-ray mask copy (hereafter referred to as the wafer) is loaded into the system and the inspection system electron-beam deflection field is matched to the pattern to be inspected. This is performed by calibrating the inspection field to the pattern field [96]. In most electron-beam systems, the movement of the table is monitored by an x,y laser interferometer. Any movement of the table produces a signal which is amplified and then sent back to the beam deflection circuitry to keep the electron-beam positioned in the proper location, independent of small table position variations. Thus, it is important that the interferometer and deflection systems be matched very accurately. The amount of beam deflection amplifier gain required for a given inspection field size must also be calibrated [47]. Any rotation of the wafer with respect to the x,y axis of the stage must also be compensated for. This is done by a process known as wafer mapping [97] in which four marks near the outside of the wafer are used to match the chip locations on the wafer with the actual stage movement. Depending on the minimum detectable defect size, detector amplifier settings, beam current, and beam voltage, the comparator thresholds discussed in Chapter's 4 and 5 are then set. One threshold is for detecting clear defects (scan over gold) and the other is for detecting opaque defects (scan over silicon). After these initial calibrations are complete, the first field can be inspected.

A registration [98] is first performed to overlay the inspection pattern to the wafer patterns. This can either be done globally by aligning to registration marks at the corners of the chip or by aligning to smaller portions of the field using subfield registration [4].

The positive portion of the pattern is then scanned with the electron-beam and the amplified backscattered electron signal is compared to the clear defect threshold level. The scanning of the beam is controlled by the pattern generator [99] which reads in the inspection data set and deflects the beam over the specified locations. If the signal drops below the threshold while the beam blanking signal is high, a defect has been detected and the x,y location is stored in memory. Note that a high beam blanking signal indicates that the beam is scanning over a pattern and not moving from one shape to another. After scanning the positive portion of the field, another registration can be performed and the negative field can be inspected for opaque defects. Upon completion of the inspection for a field, the defect locations, if any, are transferred to the control computer and the stage is moved so that the next field can be inspected.

Once an entire copy of the mask has been inspected completely, the other copies of the mask on the wafer are inspected only in the area of the defects to eliminate false defects introduced by the fabrication of the mask copy. Since most masks will only have a few defects, the defects can be categorized by an image processing scan, such as the one in reference [1], over the defect locations.

This type of inspection technique can easily be applied to the other types of electron-beam systems since it takes full advantages of the capabilities inherent in any electron-beam machine. These capabilities include automatic registration, field calibration, precise table movement, and pattern scanning. The inspection capability is added to the electron-beam machine by making peripheral changes to the system. The lithography capabilities of the system are not changed. For example, consider a raster scan electron-beam system [100-102] in which the beam and, sometimes, table move so that the chip area is scanned in a raster manner. The electron-beam is simply blanked on in areas where exposure is desired. Thus, it can be seen that the raster scan data is in a bit map format with one bit signifying beam on and the other signifying beam off. The inspection method outlined above can be easily incorporated into a raster scan system. The original design data shapes can be etched to allow for an inspection dead zone and a

corresponding negative inspection data set can also be created. An alternative is to analyze the position of the beam by comparing its location to the designed data in bit map form. The bit map data will specify what type of inspection is to be performed (clear or opaque defect detection) and when the beam is in a dead zone (disable inspection). The presence of the dead zone can be detected by real time electronic analysis of the pattern data surrounding the location of the beam [2]. The rest of the inspection system is similar to that proposed for a vector scan system.

As far as variable shaped electron-beam systems are concerned, Simpson and Davis [4] have demonstrated that a technique similar to the one above for a vector scan system can be incorporated into an IBM EL-3 electron-beam tool.

The advantages of the proposed inspection system are that it is conceptually easy to implement on existing electron-beam systems and that it takes advantage of the capabilities already present in the electron-beam systems. Major changes to the electron-beam system are not required to enable it to be used for real time inspection. Also, the cost of adding this relatively simple inspection capability to an existing electron-beam system will be far lower than the cost of a stand alone inspection system (if one existed which could detect $0.25 \mu\text{m}$ or smaller defects). The main disadvantage of this technique is that accurate overlay of the inspection field to the wafer is required since the beam must scan the inside and outside of the pattern shapes. If the overlay error is about the same or greater than the dead zone width, many false defects will be recorded. Thus, this technique is limited by the registration and overlay capabilities of the electron-beam tool and; therefore, will not allow the inspection of masks for defects smaller than the overlay specifications of the tool. Also, if the same system which writes the mask is used to inspect it as well, any systematic errors caused by problems with the electron-beam system will most likely not be detected. However, problems such as these are usually apparent as soon as the resist is developed. Moreover, all electron-beam systems are periodically checked for registration, overlay, and stitching accuracy at which time system errors are usually detected. In a production environment, it may not be desirable to tie up an electron-

beam lithography system for mask inspection. However, in a research and development environment, this will not be as much of a problem. Finally, this inspection technique requires that additional offline processing of the defect data be performed to categorize the defects.

It is possible that defect characterization and the problems due to overlay error could be alleviated by using a more complicated image processing or pattern recognition scheme [1,88-90] as is used in some optical inspection systems. This would require that the pattern data be put into a different format (such as a bit map) for comparison to design data. Parallel processing would also be needed so that one area could be scanned by the electron-beam while the pattern to design comparison was being done on another area. Basically, this type of inspection method uses very few of the advantages inherent in an electron-beam lithography system since it uses image processing techniques to replace the need for the electron-beam system's extensive overlay and calibration electronics. Also, the development costs of such a complicated inspection system would be much higher than the simpler system outlined above. Thus, this more complicated image processing approach is not a good match to an electron-beam lithography system and would be better suited for use in a stand alone inspection system. If a stand alone high resolution mask inspection system is required for a production environment (in which the electron-beam systems are being used for lithography 100 percent of the time), it is reasonable to suggest that an electron-beam front end be put onto one of the optical image processing mask inspection systems [88-90]. A complicated electron-beam system would not be required since the beam would only have to scan in a raster fashion and the advanced image processing electronics could be used to alleviate registration error.

At this point in time, x-ray lithography is still in the experimental stage and there are few electron-beam systems which can write an x-ray mask, let alone inspect it. Thus, in this research and development atmosphere, it seems wise to develop a mask inspection system which is capable of high resolution defect detection and which uses the capabilities present in the electron-beam system to align the inspection pattern to the wafer. Once this simple and relatively inexpensive mask inspection system is functioning, the complicated task of building a

more advanced stand alone mask inspection system can be undertaken, if needed.

6.6. Mask Inspection Experiments

Mask inspection test electronics were designed and built to determine the difficulties in using an electron-beam system for mask inspection. The circuit diagram is shown in Figure 6.7. The circuit consists simply of two comparators with variable thresholds along with the associated gating to compare the digitized backscattered electron signal to a beam blanking signal. The beam blanking indicates when the electron-beam is turned on and scanning over a pattern. For example, suppose we are interested in scanning for opaque defects. Thus, the beam will be scanning over silicon and the backscattered electron signal should always be low. Therefore, the top comparator in the circuit of Figure 6.7 will be used so a low signal normally disables the comparing AND gate. If an opaque defect is encountered, then the comparator output will go high and the AND gate output will go high if the blanking signal is also high. This defect is then counted and defect signal sent to the output stage of the electronics where it can be observed on a CRT display. These electronics, along with an IBM vector scan electron-beam system and the diode detector used in the experiments of Chapter 3, were used in the studies which follow.

Test patterns, as described in Chapter 2, were fabricated by first fabricating gold on silicon registration marks and then manually or automatically registering to those marks before exposing the desired test patterns. After exposure, the process outlined in Chapter 2 was used to fabricate the gold on silicon test patterns. The inspection was carried out by registering to the marks and scanning over the shrunken positive and negative images of the test patterns. Defects were observed by connecting the output of the defect inspection electronics to a CRT display.

It is worthwhile to discuss the manner in which the vector scan system scans the beam over patterns as it will help explain some of the results which follow. Figure 6.8 illustrates the type of fill pattern used to expose the shapes. The beam starts in the lower left corner and

MASK INSPECTION TEST ELECTRONICS

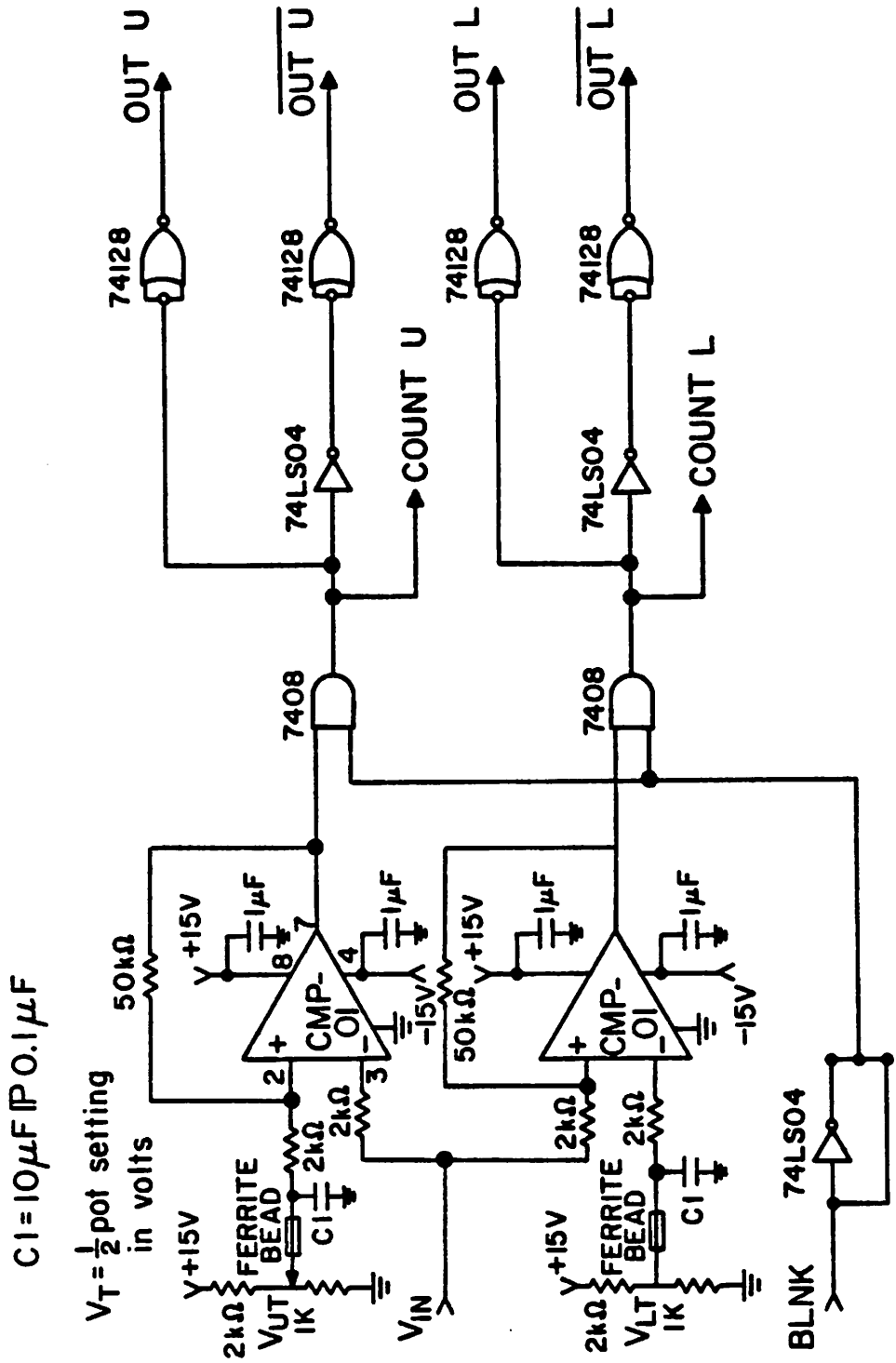


Figure 6.7. The mask inspection test electronics.

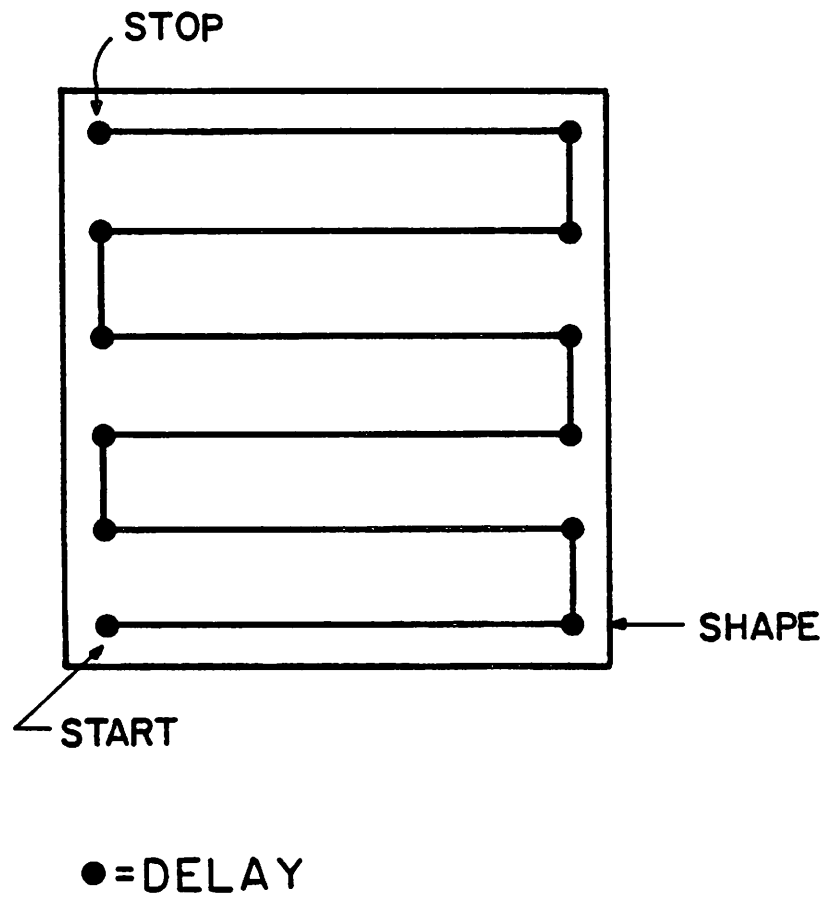


Figure 6.8. The manner in which the vector scan electron-beam machine scans a shape. The delays are required by the pattern generator electronics.

scans upward in a serpentine manner to the top of the shape. The solid dots indicate areas in the shape where the beam is blanked off during a delay period required by the vector scan pattern generator electronics [103]. Shapes are scanned in a vector scan fashion within subfields comprised of 512×512 beam locations and the subfields are scanned in a raster fashion [78].

The first problem encountered in using the test inspection electronics was due to the above mentioned delays while scanning a shape and limited frequency response of the diode detector (which was not optimized for Mhz scanning bandwidths). At first, while scanning a shape, the beam was blanked on and off along with the blanking signal. However, the diode's response time, as shown in Figure 6.9a, is on the order of 2-3 μsec . The problem can easily be seen: If the beam is scanning over a gold pattern, the signal will be high while the beam is on. However, if the beam is blanked off while scanning a shape and then blanked on again, the beam blanking signal will be high; but, the signal to the comparator input will be low for several μsec because of the diode's response time. Therefore, false defects will be detected until the diode signal crosses the comparator threshold. This problem will also occur at the beginning of a scan over a shape and when the beam is scanning the negative patterns. A simple programmable digital delay network, Figure 6.10, was constructed to shift the blanking signal in time to correspond to the delayed diode signal (Figure 6.9b) [103]. Also, the beam was disconnected from the blanking signal and left on during the entire scan. The blanking signal was used only to indicate to the electronics when the beam is scanning over a pattern. The delay circuitry is needed when the beam jumps from one gold pattern, over silicon, to another gold pattern. A higher bandwidth detector, currently being fabricated, will eliminate much of this problem.

It was found that it was not possible to align simply to the registration marks and overlay the inspection pattern (with a $0.125 \mu\text{m}$ per side etch) with the pattern on the wafer. The inspection pattern would be overlaid correctly in some areas and incorrectly in others, leading to false defect detection. If the stage was moved to compensate for the mismatch in overlay in one area, new overlay errors would be produced in other areas. Therefore, it was decided to

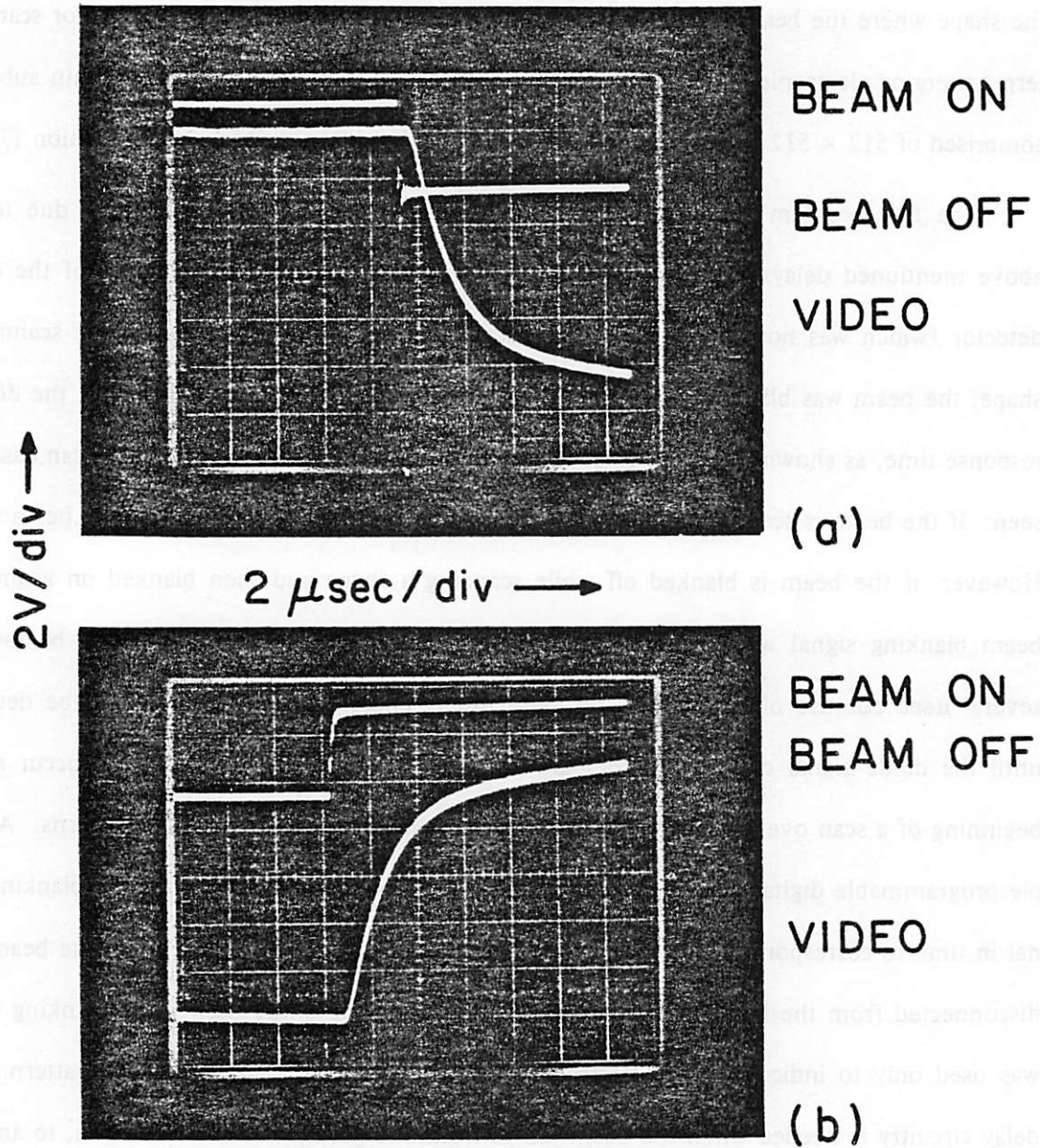


Figure 6.9a. An example of the delay inherent in the signal from the diode detector (a) scan over gold and blank beam off (b) scan over gold and blank beam on. Scan bandwidth is 33.3 KHz.

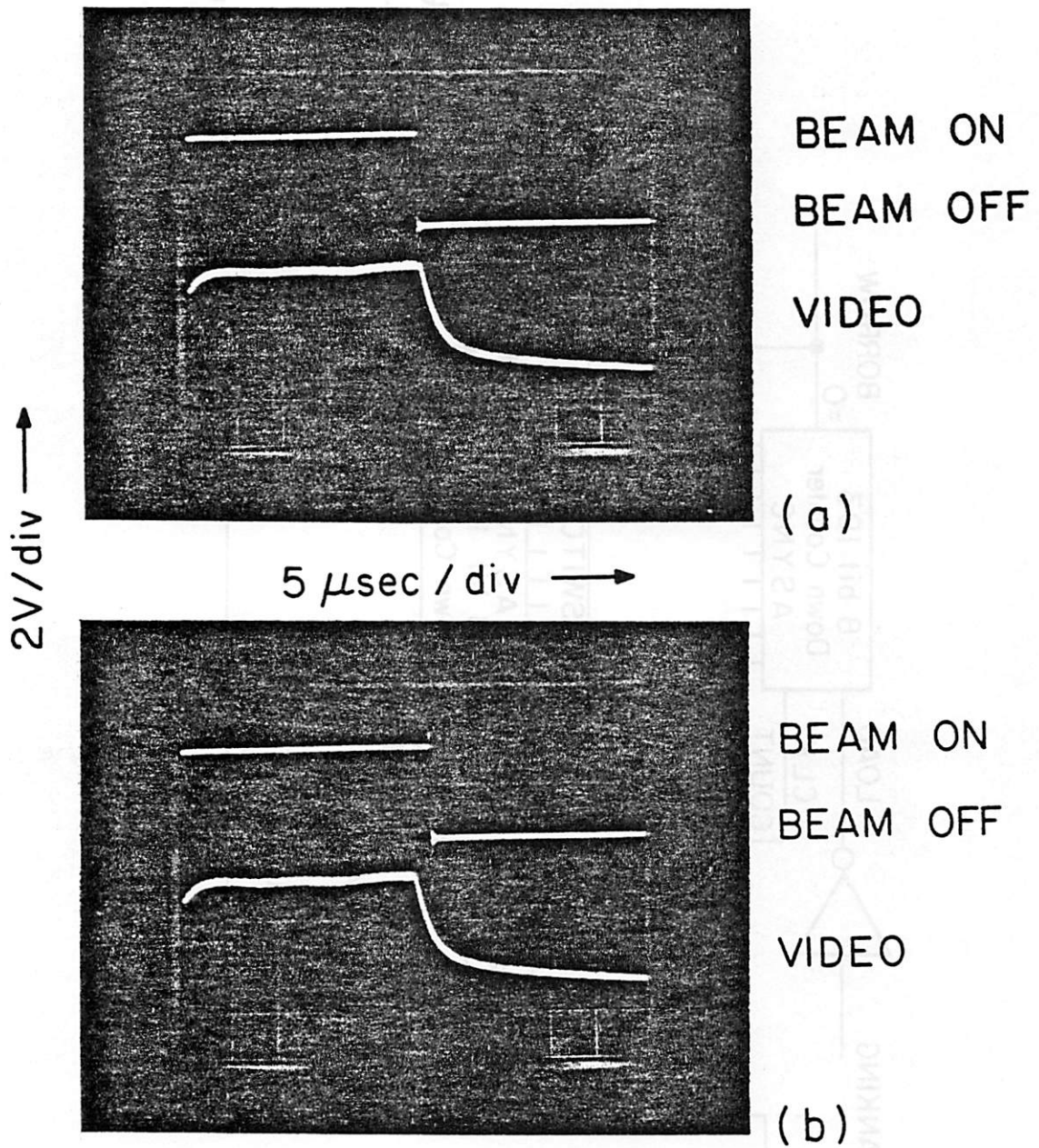


Figure 6.9b. Using the programmed delay to correlate the blanking and detector signal (a) no programmed delay (b) a programmed delay of 2.3 μ sec.

investigate the effects of overlay error on the proposed mask inspection algorithm.

Figure 6.11a shows the blanking signal and the backscattered electron signal from a $1.8 \mu\text{m}$ square inspection shape overlaid on a $2.1 \mu\text{m}$ per side gold square. The overlay was good enough so that the defect inspection electronics did not indicate a defect. The inspection field size was 1 mm , indicating a beam location separation of $0.0625 \mu\text{m}$. The beam off delays inherent in the scanning of a shape can be seen every $28 \mu\text{sec}$ ($28 \text{ beam locations} \times 1.0 \mu\text{sec}/\text{beam location}$). The beam was kept on during the entire scan. The effects of moving the stage $1.0 \mu\text{m}$ in the y direction can be seen in Figure 6.11b. Note how the signal is low while the beam is scanning over the silicon and gradually rises as the beam begins to scan over the gold. It can be seen from the scope tracing that the signal is back to high level after approximately $16 \text{ beam locations}$ ($1.0 \mu\text{m}$). The gradual fall off in signal is predicted by the effects of the beam scanning near and past the edge of the gold shape as discussed in Chapter 4. Recall that the detector was placed so that backscattered electrons in the $35\text{-}62.5$ degrees range were picked up. The signal is not smooth due to curvature in the pattern being inspected. For some scans near the edge, the beam scanned partly on gold and partly on silicon.

Effects of misregistration in the x direction can be seen in Figure 6.11c. Since the beam scans in the serpentine fashion shown in Figure 6.8, a false defect signal is generated on every horizontal scan when the beam is located over silicon.

In order to determine that the electron-beam and inspection electronics were capable of correctly imaging the test patterns, the electron-beam was scanned over the entire test chip and the output of the test electronics, indicating opaque defects, was recorded on the CRT. Thus, we would expect to be able to image the test patterns using the electron-beam and electronics as a digital SEM. A camera was held against the CRT screen while the electron-beam was scanning and the digital SEM images are shown in Figure 6.12. The dark areas (except for the long horizontal cracks caused by camera movement) are the gold patterns on silicon and the light area is silicon. Even at a 10 Mhz scan rate ($0.1 \mu\text{sec}/\text{beam location}$), the detector was able to isolate $1.2 \mu\text{m}$ alignment marks. This is to be expected since the $1.2 \mu\text{m}$ marks are about 19

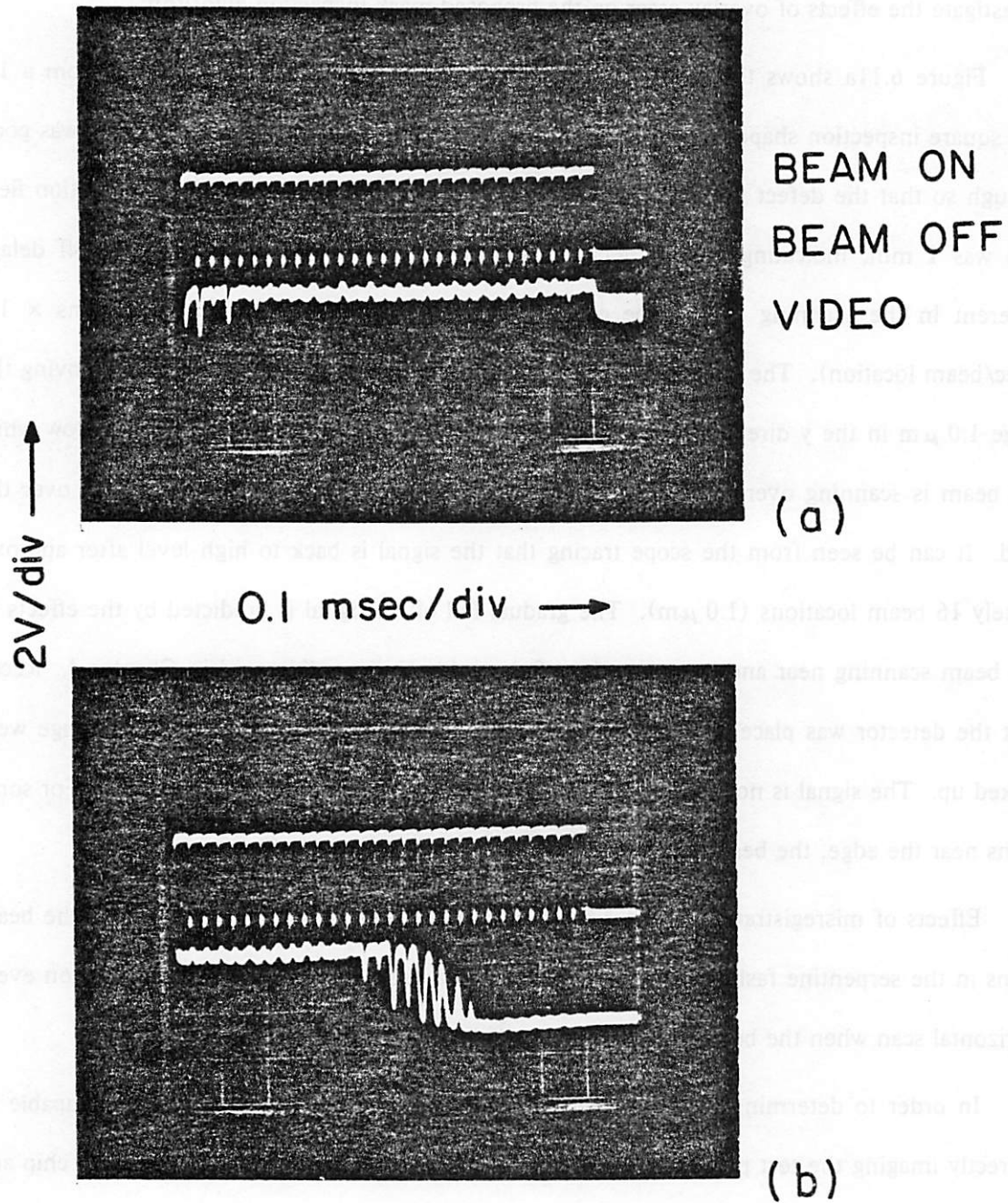
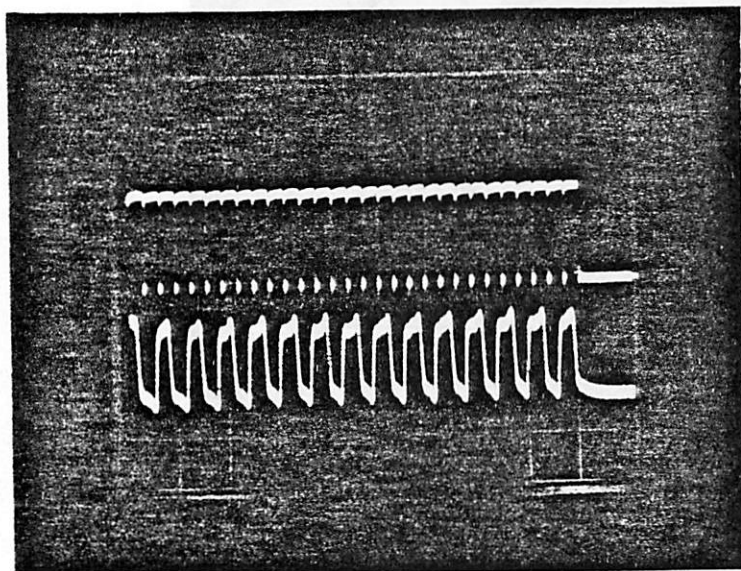
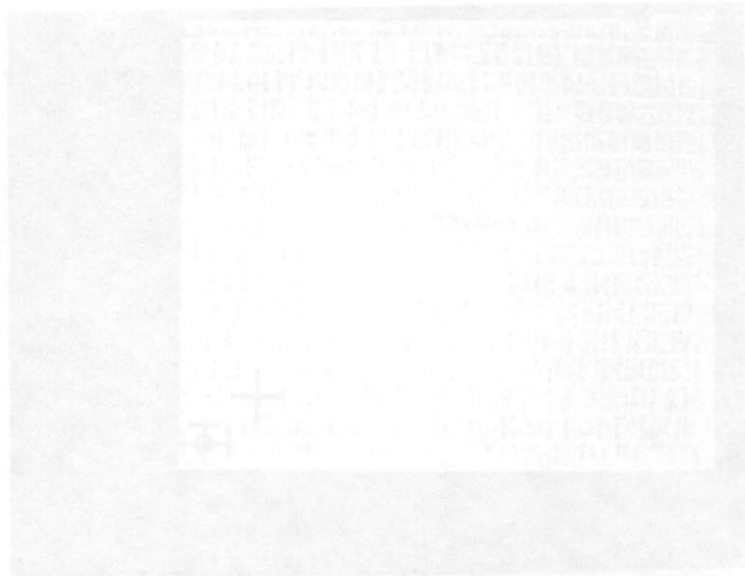


Figure 6.11. The effects of poor registration (a) scanning over a $1.8 \mu\text{m}$ square with no defects detected (b) scan after moving the table $1.0 \mu\text{m}$ in the y direction (c) scan after moving the table $1.0 \mu\text{m}$ in the x direction.



(c)



(d)

Figure 6.11. (cont.)

Figure 6.11. Using the mask inspection test electronics as a direct SEM test a 1 MIP test pattern scan over the test patterns (b) a 10 MIP full field scan over adjacent test patterns. Long horizontal cracks are due to camera tube.

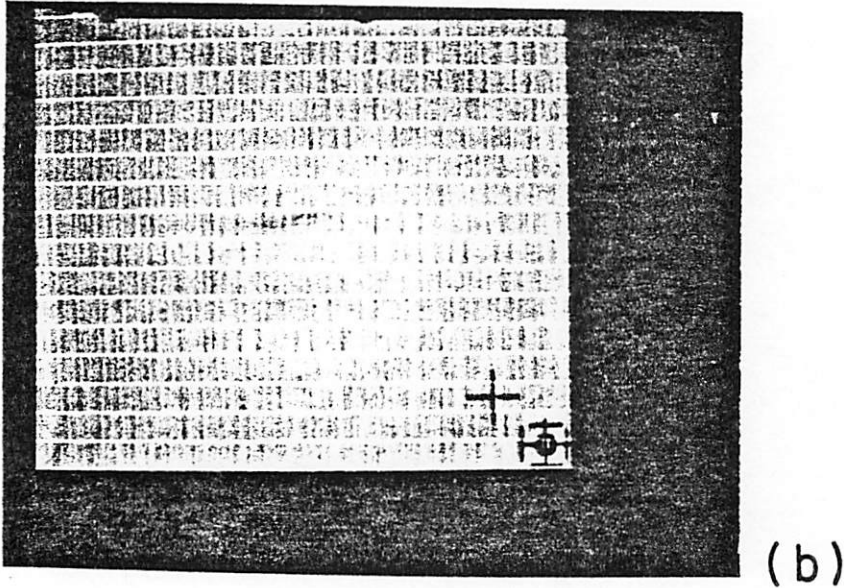
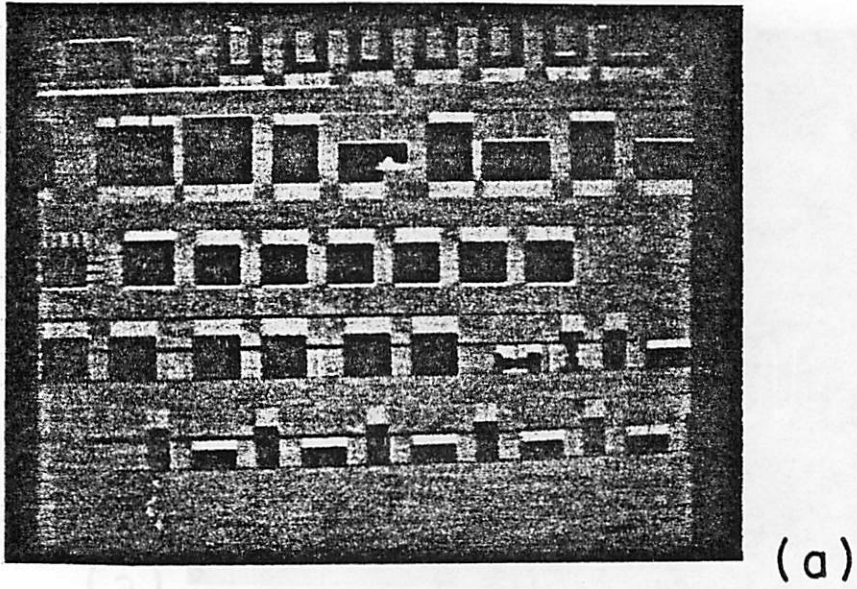


Figure 6.12. Using the mask inspection test electronics as a digital SEM (a) a 1 Mhz full field scan over the test patterns (b) a 10 Mhz full field scan over alignment marks. Long horizontal cracks are due to camera motion.

beam locations wide, giving a signal with a bandwidth of about 500 Khz - well within the limitations of the diode detector.

The most important result of this experimental study was to emphasize that the overlay of the inspection pattern to the wafer pattern is critical. The proposed mask inspection algorithm requires precise overlay of the wafer patterns or else many false defects will be recorded. Since an accurate overlay study has not been performed on the vector scan system used in the experiments, it has not been possible to determine the cause of the overlay errors. In the future, after an overlay study as done, it will be possible to determine the resolution of the inspection method. It may be desirable to overlay the inspection pattern by registering to the wafer pattern itself and not to the separately fabricated registration marks. The amount of offset, rotation, and trapezoidal error in the pattern can then be measured. If registration to the pattern is found to be inadequate, then subfield registration [4] will be required. The size of the subfield will be determined by the overlay capabilities of the electron-beam system.

We have also seen that the type of false defect signal will depend on the type of overlay error as well as the manner in which the beam scans over the shapes. The response time of the diode detector is also important in that the gating blanking signal must be delayed in order to have a proper comparison with the backscattered electron signal. It would also appear that it is best to keep the beam on during the entire inspection and only use the blanking signal as a means to indicate when the beam is scanning a pattern.

6.7. Software and Hardware Requirements

6.7.1. Software Requirements

The proposed inspection method utilizes much of the software built into the electron-beam system. However, some peripheral software is required. Some type of control program is needed to enter inspection instructions and execute the inspection. This would include identifying the names of the inspection data sets and the locations of the corresponding patterns on

the wafer. The location of registration areas and the times to perform automatic registration must also be known to the system. Moreover, pauses and interrupts for data transfer between the defect electronics and control computer are needed. There also has to be a method of transferring the defect locations from memory to the control computer. Once the defect locations are in the control computer, the defect data should be categorized and a data set for the re-inspection of the defect areas be created. Software similar to that needed for mask inspection is already incorporated into most electron-beam operating systems. Therefore, much of the required inspection software can be written by modifying existing routines.

Positive and negative inspection patterns, derived from the original CAD data, are also required. Software already exists to transfer CAD designs to electron-beam format and it is not difficult to adapt this software to reduce or expand the sizes of the shapes. The problem of inverting an image is not new and programs exist which can perform this function [104].

6.7.2. Hardware Requirements

It will be assumed in this section that an electron-beam system with automatic registration capabilities already exists. Additional hardware requirements for mask inspection include a fast (5-10 Mhz) backscattered electron detector and amplifier along with the comparison electronics. As we have seen, the required comparison electronics are rather simple and present no real problem to construct. Once a defect is detected, electronics are needed to transfer the x,y location of the electron-beam to a memory array. This involves taking the address in the pattern generator and transferring it to memory. An interface is also needed between the memory and the control computer. Due to possible diode frequency limitations, a delay system for the blanking signal may also be required. It should be noted that the hardware requirements for the proposed mask inspection system are very straightforward and should not be difficult to design and fabricate.

As mentioned previously, the overlay of the inspection pattern to the wafer pattern is important. Thus, the causes and magnitude of the overlay error in the inspecting electron-

beam system must be known. Since there is no image processing of the defect data, the electron-beam system cannot be used to inspect a pattern with better overlay than when it writes the pattern. In other words, if a system has a specified $0.25\ \mu\text{m}$ overlay accuracy, many false defects will result if only a $0.125\ \mu\text{m}$ wide dead zone is used around the inspection patterns. However, if the electron-beam system has such poor overlay capabilities, then it also will not be able to write masks with minimum feature sizes below about $1.0\ \mu\text{m}$.

The effects of scanning with a miscalibrated inspection field are illustrated in Figure 6.13. The inspection pattern suffers from offset as well as trapezoidal distortions [96]. Thus, the rectangular inspection patterns are offset and slanted resulting in false defect detection. Even with an image processing mask inspection technique, in which an entire subfield would be scanned in a raster fashion, the shapes would not be interpreted as being rectangular. Since an electron-beam system already can compensate for offset, rotation, and trapezoidal distortions [96], it would seem wise to do this with existing hardware if possible. Any inspection system should report how much field correction was required before the actual inspection could take place. This would indicate whether the wafer patterns are distorted.

Good temperature control inside the electron-beam chamber is also required since the laser interferometer output is extremely temperature dependent. There is also the compression and expansion of the silicon wafer with temperature to contend with. Small temperature variations could cause apparent shifts of the wafer position on the stage, resulting in a misregistered inspection field and many false defects. A stable temperature environment is also required for writing masks and it is reasonable to expect that the electron-beam column will be kept at a constant temperature.

6.8. Inspection Scanning Techniques

Recall that a $2.5\ \text{cm} \times 2.5\ \text{cm}$ area written with a $1.0\ \text{mm}$ field size is made up of about 1.678×10^{11} beam locations (or pixels) spaced $0.0625\ \mu\text{m}$ apart. It would take 4.66 hours to scan each beam location at a 10 Mhz scan rate ($0.1\ \mu\text{sec}/\text{pixel}$). This does not include

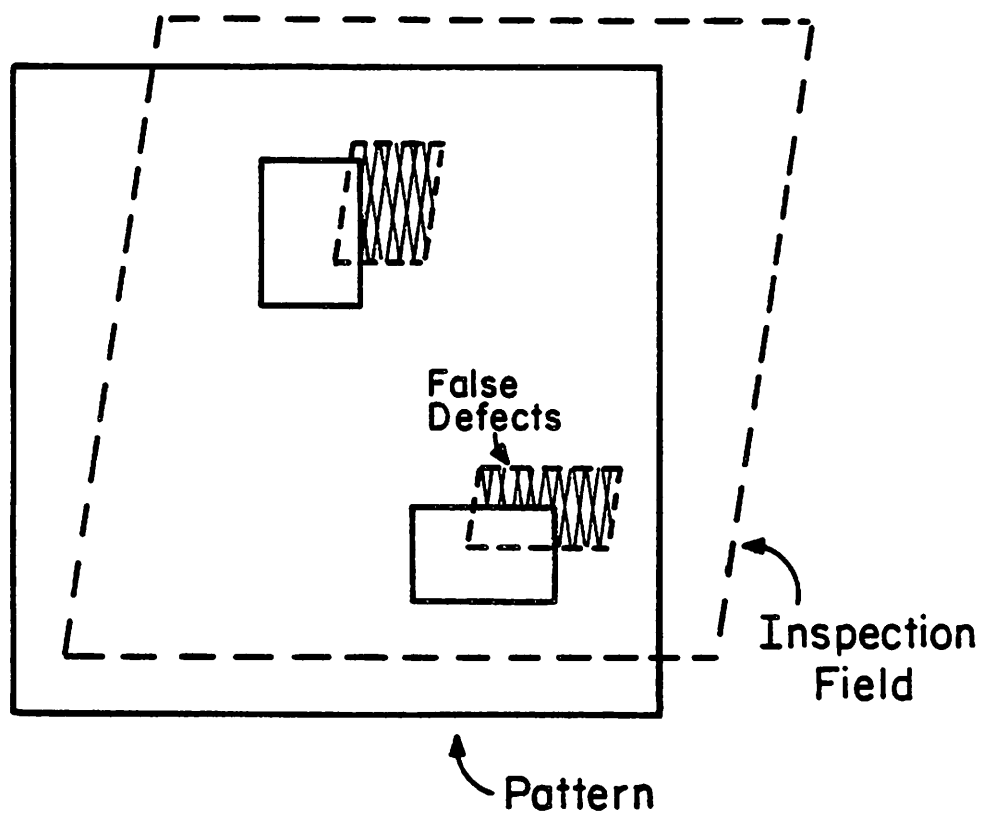


Figure 6.13. The effects of scanning with a poorly calibrated inspection field.

overhead times such as registration, load and unload, and pattern generator delays. At 5 Mhz, the time increases to 9.32 hours and at 1 Mhz, it would take 46.6 hours for inspection. However, these times can be reduced by a factor of 4 by skipping every other beam location in x and y and by another factor of 4 by stepping between every fourth beam location. The required SNR of the signal for false alarm free detection drops from about 6.8 for inspecting every beam location to 6.4 for every fourth beam location.

The electron-beam remains on as the beam is deflected from one beam location to the next. The effect of inspecting every fourth pixel, for example, would be that it would take $1/(\text{scan rate})$ seconds for the beam to travel from one beam location to the next. Assuming that the scan rate is 10 Mhz, a $0.25 \mu\text{m}$ defect, four beam locations wide, would give a back-scattered electron signal with a bandwidth of approximately 10 Mhz. Thus, the detector and associated electronics would have to have at least that bandwidth to detect $0.25 \mu\text{m}$ defects reliably. If it was required that $0.125 \mu\text{m}$ defects be detected using this scan scheme, a detector bandwidth of 20 Mhz would be required even though the electron-beam is scanning at a 10 Mhz rate.

The effects of scanning by skipping beam locations can now clearly be seen. A substantial reduction in inspection time can be achieved at the expense of increasing the minimum detectable defect size. For example, by inspecting every fourth beam location in x and y, the electron-beam would be assured of passing over all defects of about $0.25 \mu\text{m}$ or greater size. However, smaller defects could lie between the inspection pixels in the y direction (Figure 6.14). A solution to this problem, which would increase the inspection time somewhat, would be to skip beam locations only in x and not in y. Also, the signal from a defect smaller than the distance between inspection beam locations would require detector bandwidths greater than the inspection scanning bandwidth. By skipping beam locations, the $2.5 \text{ cm} \times 2.5 \text{ cm}$ mask pattern could be inspected for $0.25 \mu\text{m}$ defects at a 1 Mhz scan rate in about 3 hours. The required detector bandwidth would only be about 2 Mhz to detect $0.125 \mu\text{m}$ defects. Thus, we see that a large amount of area can be inspected in a reasonable time with very modest

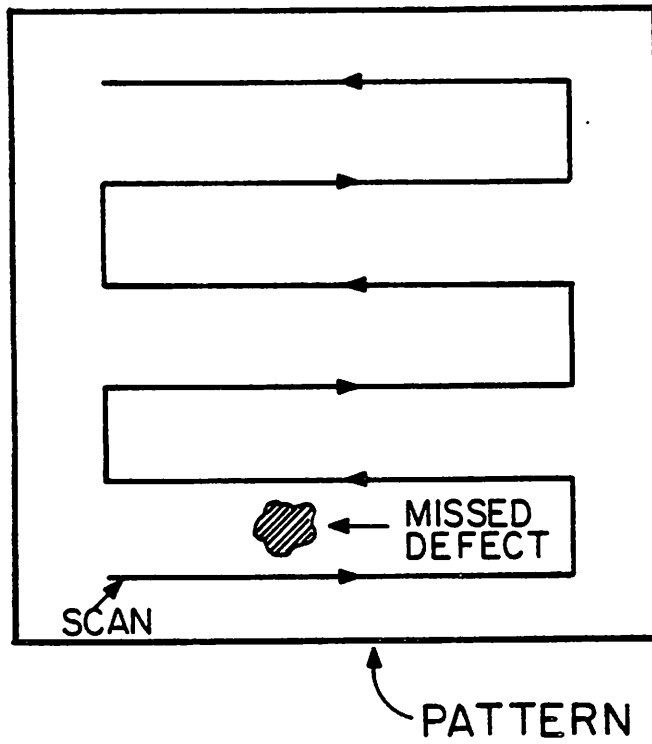


Figure 6.14. An example of how a small defect can be missed if the separation of inspection scan lines is too large.

bandwidth requirements.

The minimum detectable defect size specification will also determine the size of the inspecting electron-beam. We saw in Chapter 5 that signals with adequate SNR were generated from structures which were one-half the size of the inspecting electron-beam. Thus, if the specification on the mask inspection system is to be able to detect $0.25 \mu\text{m}$ defects and also $0.125 \mu\text{m}$ defects if possible, a beam size of about $0.25 \mu\text{m}$ should be used. Keep in mind that the larger the beam size, the more severe the drop in signal will be if the beam begins to scan near the edge of a shape. Also the larger the size of the beam, the more current, and; therefore, the better the SNR at a given bandwidth.

It is possible with certain electron-beam systems that the chosen scanning technique is hindered by poor SNR quality of the signal, generating many false alarms. One method of compensating for poor SNR is the scan, rescan technique reported by Simpson and Davis [4]. It was shown that if the signal is SNR limited, then the scan, rescan technique allows the inspection to take place faster than with a single scan technique. In this scheme, the defect locations stored after a first pass inspection are used to create a data set which instructs the electron-beam to re-inspect the defect locations. Thus, many, if not all, of the false alarms will be detected on the second inspection pass. This second inspection can be done at a slower speed to increase SNR quality. This will have little effect on inspection time since the number of false alarms and/or defects is much smaller than the number of inspection beam locations.

For example, consider a system which has a SNR of 7 for the backscattered electron signal at a 2.5 Mhz bandwidth. However, the system is capable of scanning at a 10 Mhz rate. At the 2.5 Mhz scan rate, the required scan time for the 1 square inch mask would be about 18.6 hours with no false alarms. If a 10 Mhz scan rate was used, the SNR would drop to 3.5 ($P_e = 2.4 \times 10^{-4}$) and the scan time would decrease to 4.7 hours. However, there would be about 4.03×10^7 false alarms requiring an additional 16 seconds of re-inspection time at 2.5 Mhz. To save memory, the false alarms could be re-inspected after the inspection of each 1.0 mm field. Thus, by using a scan, rescan technique, a $4\times$ increase in inspection speed is realized.

Figure 6.15 shows the effects of using a signal with low SNR for inspection of the 2.5 cm \times 2.5 cm mask. It can be seen that the SNR requirement is reduced from approximately 7 to 4 or 5 depending on the scan technique and the number of re-inspection passes. The calculations in the figure assume that the second and third inspection passes are performed at the same inspection speed as the first inspection scan. The need for a third pass could be eliminated by decreasing the scan speed on the second pass to improve the SNR.

The scan, rescan technique can be used to decrease inspection time in another manner. Scanning by skipping beam locations with a corresponding increase in beam size will improve inspection throughput. In this case, the beam may not directly pass over the defects; therefore, the threshold levels must be set to detect small changes in the signal level. The false alarms generated by this technique can be eliminated in a second scan. The use of this technique will be limited by the detector bandwidth, as discussed earlier, and the size of the dead zone around the shapes.

It is interesting to compare the required inspection times for similar patterns using optical and electron-beam techniques. It will be assumed that a high atomic number copy of the mask has been fabricated or that high atomic number masking material, such as tungsten or gold, is used on the mask. Inspecting a copy of an optical mask has been suggested by several groups [87,89]. Consider an 8 mm \times 8 mm inspection field. Using a vector scan electron-beam system and 1 mm field size, it would be possible to inspect for 0.25 μ m defects in about 7 minutes at a very reasonable 2.5 Mhz inspection scan rate (not including overhead times). This can be compared to the Contrex optical system [89,91] which reports an inspection time of 1 hour for a 7.6 mm \times 7.6 mm field and 0.5 μ m defects. Note that the Contrex system inspects copies of the mask fabricated out of photoresist on silicon. This material combination would be extremely difficult to inspect with an electron-beam system because of the poor backscattered electron signal quality of resist on silicon. However, both techniques involve making a copy of the original mask and the electron-beam technique requires the simple additional step of electroplating.

| Scan, Rescan Technique | | | |
|--------------------------------------|----------------------------|----------------------------|----------------------------|
| Scan every pixel * | | | |
| SNR | # of false alarms | | |
| | 1st pass | 2nd pass | 3rd pass |
| 6 | 168 | <1 | <1 |
| 5 | 50340 | <1 | <1 |
| 4 | 5.54×10^6 | 183 | <1 |
| 3 | 2.18×10^8 | 2.84×10^5 | 369 |
| Scan every other pixel (x,y) | | | |
| 6 | 42 | <1 | <1 |
| 5 | 12585 | <1 | <1 |
| 4 | 1.39×10^6 | 46 | <1 |
| 3 | 5.45×10^7 | 7.09×10^4 | 92 |
| Scan every fourth pixel (x,y) | | | |
| 6 | 11 | <1 | <1 |
| 5 | 3147 | <1 | <1 |
| 4 | 3.48×10^5 | 12 | <1 |
| 3 | 1.36×10^7 | 1.77×10^4 | 23 |

* 1.6777×10^{11} total pixels

Figure 6.15. The effect of reduced SNR on the number of false alarms and the use of a scan, rescan technique to eliminate the false alarms. The bandwidth is the same for all passes.

The KLA optical inspection system [88,93] reports the inspection of a 10 mm × 10 mm field for 0.9 μm defects in 6 minutes. A vector scan electron-beam system could scan for 0.5 μm defects over the same area in slightly less than 3 minutes (plus overheads).

It is also important to realize that, unlike the optical inspection techniques, the inspection time for the proposed electron-beam system is relatively independent of pattern complexity. Pattern complexity is not an issue during the inspection process since the electron-beam is already scanning over the entire inspection field. The complexity of these patterns only affects the processing time of the CAD data into inspection data and will have much less of an effect on the actual inspection time.

The proposed inspection method requires a dead zone around the edges of shapes to allow for registration errors. The size of this dead zone will limit, to some extent, the minimum detectable defect size. If the inspection pattern is perfectly overlaid on the wafer pattern, then the dead zone will make it improbable to detect protrusions or indentations smaller than the dead zone width. In a worst case scenario, with the inspection pattern misregistered by an amount equal to the dead zone width, protrusion and indentation defects equal in size to twice the dead zone width could go undetected. However, the registration of the inspection pattern to the wafer pattern should be quite good ($< 0.1 \mu\text{m}$) since the gold on silicon patterns make extremely accurate (high SNR signal) registration marks [19,21]. As stated earlier, the overlay specifications of the electron-beam system is an extremely important parameter which will affect the inspection resolution for the electron-beam inspection system.

Bias, or difference in linewidth between the CAD patterns and the wafer patterns, should also be considered when specifying the size of the dead zone. However, the CAD data represents the required size of the features and any large discrepancies should be categorized as a defects. Therefore, the width of the dead zone should allow for permissible linewidth variations of the wafer patterns.

6.9. Summary

In this chapter, we have discussed the systems aspects of using electron-beam techniques for mask inspection. A review of current optical and electron-beam inspection systems was presented. At present, there are no commercially available inspection systems with reliable defect detection resolution below $0.5 \mu\text{m}$. The question of inspecting the mask or a copy of the mask was addressed and it was concluded that, for x-ray mask inspection, a copy of the mask is preferred. A mask inspection algorithm was demonstrated using a vector scan electron-beam system and a complete mask inspection system was proposed. The inspection consists of scanning over the positive (gold) areas of a wafer and detecting clear defects if the backscattered electron signal goes low. Opaque defects are detected by scanning over the negative (silicon) areas and detecting defects if the signal goes high. Experiments showed that accurate overlay of the inspection pattern to the wafer pattern is required if the proposed algorithm is to be implemented. If accurate overlay over an entire writing field is not easily obtained, it may be required to overlay smaller subfields [4]. The experiments also illustrated that if the detector's response time is too slow, false defects may be detected at the points where the beam begins its scan over the gold. The software and hardware requirements for an electron-beam inspection system were also discussed.

It was observed that the proposed inspection system utilized all of the capabilities inherent in an electron-beam lithography system such as, accurate registration, precise beam positioning, and easy design data manipulation. These capabilities allow the mask inspection to take place in real time with no image processing requirements. Also, the conversion of an existing electron-beam system into a mask inspection system using the proposed algorithm is likely to be much less expensive than implementing a more complicated image processing approach. The proposed system uses the built in electronics of the electron-beam system to compensate for field distortion and overlay errors instead of image processing. The proposed system is intended for a research and development environment in which heavy demands are not made on the electron-beam system for lithography. If a stand alone high resolution inspection system is

required, it seems advantageous to put an electron-beam front end onto an image processing based optical inspection system. A very simple electron-beam system could be used because of the limited scanning requirements.

Some inspection scanning techniques were also discussed. It was shown that the minimum sized detectable defect will influence the manner in which a pattern is scanned. It will be possible to decrease the inspection time by skipping over beam locations used in writing the pattern. A scan, rescan technique [4] was also mentioned as a method to reduce SNR requirements. Finally, it was shown that the proposed inspection system will allow inspection throughput comparable to existing optical techniques at 2-4 times the resolution.

CHAPTER 7

7. CONCLUSION

The design and implementation of a high resolution mask inspection system using an electron-beam probe is a difficult task. Many different areas must be investigated and understood before a reliable high speed inspection system can be built. In this thesis, we have discussed the fundamental aspects of x-ray mask inspection using an electron-beam system. The goal of this research was to gain a complete understanding of the nature of the backscattered electron signal from submicron structures and use this knowledge in the design of a mask inspection system.

A Monte Carlo program has been developed to simulate the backscattered electron signal from the complicated structures encountered in mask inspection. The program is based on the standard continuous slowing down approximation, Bethe energy loss equation, and the screened Rutherford collision cross-section. It was found that the simulated energy signal, the total energy of the electrons striking the detector, gave good agreement with experiment for different submicron structures, collection angle ranges, beam voltages, gold thicknesses, and beam sizes. This excellent agreement with experiment was important since it gave confidence in using the program to investigate the backscattered electron signal properties of interest for mask inspection.

It has been shown that electrons scattered into the middle take-off angle ranges (30-60 degrees from the plane of the target) gave the best overall backscattered electron signal quality for clear and opaque defect structures. Although the 30-60 degrees range is best overall, the signal for submicron step structures can be enhanced by also collecting the lower angle backscattered electrons.

The effect of electron-beam size on the backscattered electron signal characteristics was also described. A Gaussian electron-beam shape was used in the simulations. A quantity, Δ SNR [19], was used as a figure of merit for the noise quality of the signal. Curves of Δ SNR,

signal fwhm, and threshold (DC level) versus beam fwhm were presented for a variety of sub-micron gold on silicon structures over three different angle ranges. The Δ SNR was shown to give a more realistic representation of the degradation in signal noise quality with increasing beam size than the signal contrast. A fall off in Δ SNR was found to begin to occur when the beam size becomes about 0.4 of the structure fwhm. For steps, a 25 percent loss of Δ SNR occurs when the (beam fwhm)/(structure fwhm) ratio is about 1.2. Similar results are seen for holes with a 25 percent reduction in Δ SNR being observed at a ratio of about 1.1.

It was observed that the graph of signal fwhm versus beam fwhm has two distinct regions for various structures. There is a flat region for beam sizes up to about 0.5 of the structure fwhm and a region for larger beam sizes in which the signal fwhm rises steadily with the beam fwhm. For steps, a signal fwhm 50 percent larger than the structure fwhm occurs for a (beam fwhm)/(structure fwhm) ratio of about 1.3-1.4. For holes, a 50 percent increase is seen for a ratio of about 1.1-1.2. It was also found that the thresholds or DC levels of the signals from step and hole structures are different and behave in different manners as the beam size is increased. For steps, the threshold drops towards the silicon signal level as the beam size increases. For holes, the threshold rises toward the gold signal level.

Universal curves for various beam energies showed that to collect 90 percent of the available backscattered electron signal, the scattering material should be about $0.13 R_B$ or $0.33 R_G$ thick. It is desirable to use the Gruen range, R_G since it is easily calculated using a simple analytical expression. The universal relationship of the backscatter coefficients to material thickness normalized to R_G is interesting because the backscatter coefficients are calculated using the Monte Carlo program while R_G is calculated using an empirically derived equation. Similar universal curves were introduced to illustrate the effect of scanning the electron-beam near the edges of shapes. As the beam scans near the shape edges, it is possible that the back-scattered electron signal can fall off. If low take-off angle electrons are collected, an increase in signal is observed. For a 30-60 degrees angle collection range, the signal begins to drop off at about $0.2 R_G$ from the edge while for a 50-80 degrees range, the signal begins to drop off at

about $0.33 R_G$ from the edge. This decrease in signal level is important since it can cause the signal to fall below the comparator threshold used for determining the presence or absence of masking material. Collecting backscattered electrons in the 20-50 degrees range should reduce the drop in signal near a step edge with only a 6 percent loss in signal from bulk materials.

A simple technique of calculating signal levels for two and three dimensional structures was introduced. The method is based on knowing the fraction of the beam which is incident on the structure along with knowledge of the scattering properties of that structure.

The various backscattered electron detectors which can be used in an electron-beam system were examined from a practical point of view. The diode detector seems to be the best choice over the scintillator-photomultiplier and channel plate detectors as far as ease of installation, complexity, and bandwidth are concerned.

The effects of shot noise, the fundamental limitation to reliable high speed mask inspection using an electron-beam system, were studied on the backscattered electron signal for a variety of structures. It was shown that the difference in signal levels between gold and silicon along with the placement of the comparator threshold level were critical in determining the SNR quality of a backscattered electron signal. The SNR characteristics of shot noise limited signals were investigated for $0.125 \mu\text{m}$, $0.25 \mu\text{m}$, and bulk structures. All results were left in terms of $(I_B/\Delta f)^{1/2}$ so that they could be applied to a variety of electron-beam systems. The optimum threshold was introduced as the threshold location at which the SNR for both the high and low signal levels are the same.

For beam sizes smaller than the structure fwhm, the placement of the threshold is not as critical as it is for larger beam sizes in which the signal level difference is reduced. Analysis showed that the shot noise will not be a fundamental problem until the beam size is over twice the defect size. The shot noise limited SNR depends on the $(I_B/\Delta f)^{1/2}$ value and tables listing the shot noise SNR characteristics of the backscattered electron signals from various structures were presented to aid in the design of an electron-beam inspection system.

It was also shown that thin ($0.08\ \mu\text{m}$) chrome structures, such as those found on optical lithography masks, will be difficult to inspect at high electron-beam voltages because of poor SNR quality. The situation can be improved somewhat by increasing the chrome thickness or by lowering the beam energy. Using gold instead of chrome as the masking material also greatly improves the SNR.

The ΔSNR parameter introduced in Chapter 3 was shown to track the actual shot noise limited SNR fairly well and is therefore a valuable figure of merit for backscattered electron signal quality.

The systems aspects of using electron-beam techniques for mask inspection were also discussed. A review of current optical and electron-beam inspection systems was presented. At present, there are no commercially available inspection systems with reliable defect detection resolution below $0.5\ \mu\text{m}$. The question of inspecting the mask or a copy of the mask was addressed and it was concluded that, for x-ray mask inspection, a copy of the mask is preferred. A mask inspection algorithm was demonstrated using a vector scan electron-beam system and a complete mask inspection system was proposed. The inspection consists of scanning over the positive (gold) areas of a wafer and detecting clear defects if the backscattered electron signal goes low. Opaque defects are detected by scanning over the negative (silicon) areas and detecting defects if the signal goes high. Experiments showed that accurate overlay of the inspection pattern to the wafer pattern is required if the proposed algorithm is to be implemented. If accurate overlay over an entire writing field is not easily obtained, it may be required to overlay smaller subfields [4]. The experiments also illustrated that if the detector's response time is too slow, false defects may be detected at the points where the beam begins its scan over the gold. The software and hardware requirements for an electron-beam inspection system were also presented.

It was observed that the proposed inspection system utilized all of the capabilities inherent in an electron-beam lithography system such as accurate registration, precise beam positioning, and easy design data manipulation. These capabilities allow the mask inspection to take place in

real time with no image processing requirements. Also, the conversion of an existing electron-beam system into a mask inspection system using the proposed algorithm is likely to be much less expensive than implementing a more complicated image processing approach. The proposed system uses the built in electronics of the electron-beam system to compensate for field distortion and overlay errors instead of image processing. The proposed system is intended for a research and development environment in which heavy demands are not made on the electron-beam system for lithography. If a stand alone high resolution inspection system is required, it seems advantageous to put an electron-beam front end onto an image processing based optical inspection system. A very simple electron-beam system could be used because of the limited scanning requirements.

Some inspection scanning techniques were also discussed. It was shown that the minimum sized detectable defect will influence the manner in which a pattern is scanned. It will be possible to decrease the inspection time by skipping over beam locations used in writing the pattern. A scan, rescan technique [4] was also mentioned as a method to reduce SNR requirements. Finally, it was shown that the proposed inspection system will allow inspection throughput comparable to existing optical techniques at 2-4 times the resolution.

There are several areas in which further work is needed. It would be interesting to extend the Monte Carlo program to simulate three dimensional structures to follow up on the simple analytical techniques discussed in Chapter 4. Also, a study of more complicated defect structures, besides steps and holes, could be performed with the program in its present form. In this research, we have mainly looked at the backscattered electron signal. It would be worthwhile to extend the simulation so that the secondary electron signal could be simulated as well. The signal and SNR characteristics of the backscattered and secondary electron signals could then be compared for the inspection of low atomic number material combinations, such as resist on silicon.

Overlay studies should be performed and the proposed mask inspection algorithm should be implemented on the vector scan electron-beam system. Also, the possibilities of putting an

electron-beam front end onto an optical image processing inspection system should be explored more completely. It is also important to develop techniques which will allow for the repair of the x-ray masks after the defects have been detected.

Mask inspection is one of the few areas remaining in the electron-beam system field which has not been fully explored. It is hoped that this work will be of use to others interested in the development of high resolution mask and wafer inspection systems.

APPENDIX A

THE MONTE CARLO SIMULATION PROGRAM

A.1. Introduction

The Monte Carlo computer program described in this work uses the standard continuous slowing down approximation with the screened Rutherford collision cross-section and Bethe energy loss equation. Parts of the code are based on a Monte Carlo program written by Lin [19] in a study of the backscattered electron alignment signal from resist covered silicon steps. The new program, described in this work, has been used to calculate and analyze the backscattered electron signal from structures encountered during x-ray mask inspection. The simulated target structures are two dimensional in that they extend to infinity in both directions on the y axis. The program is written in standard Fortran 77 and consists of about 3900 lines of code. In this appendix, we will briefly describe the operation of the program and list an input and output example.

A.2. Program Operation

The structure to be simulated is specified by a piecewise approximation as shown in Figure A.1. XO, XP, XQ, etc. are the variables used in the program to specify the structure. The entire region is broken up into 17 zones, numbered in the figure. Zones 8, 9, and 10 comprise the top layer while zones 11-17 make up the bottom layer. Zones 1-7 are considered to be vacuum. Planes 1-13 separate the zones from the vacuum and also the top layer from the bottom layer. The top layer structure has a constant thickness of ZT.

A sample input file is shown in Figure A.2. The resulting target structure, incident beam position, and trajectories of the firsts 25 electrons are shown in Figure A.3. The input file is for the most part self explanatory, with a few exceptions. To simulate a PMMA top layer, it is necessary to enter a value of 0.0 for the atomic weight of the top layer element. It does not matter what values are given to the atomic number and density of the top layer in this case. Note that all units of distance are in cm. The thickness of the top layer must be entered as a

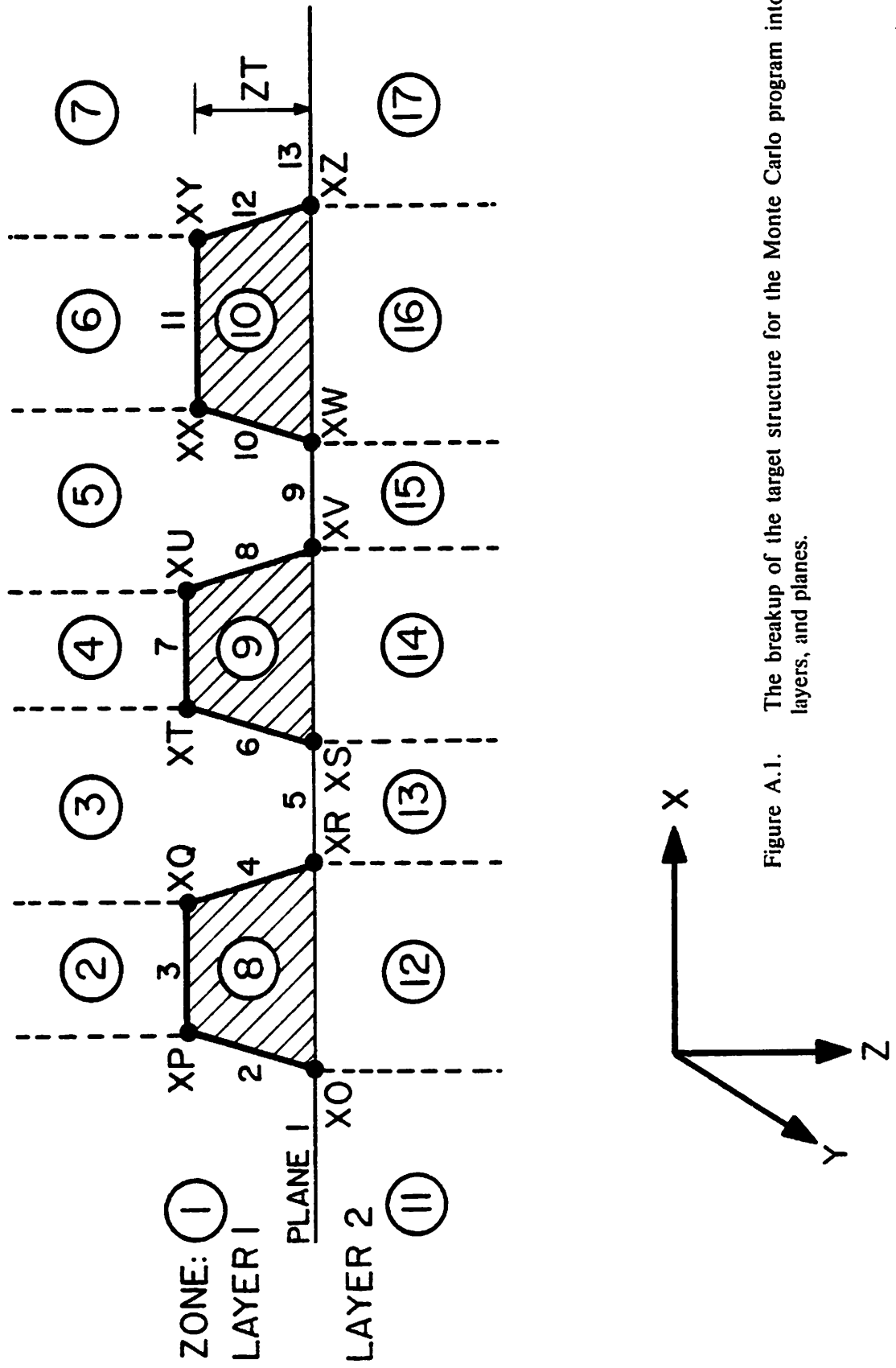


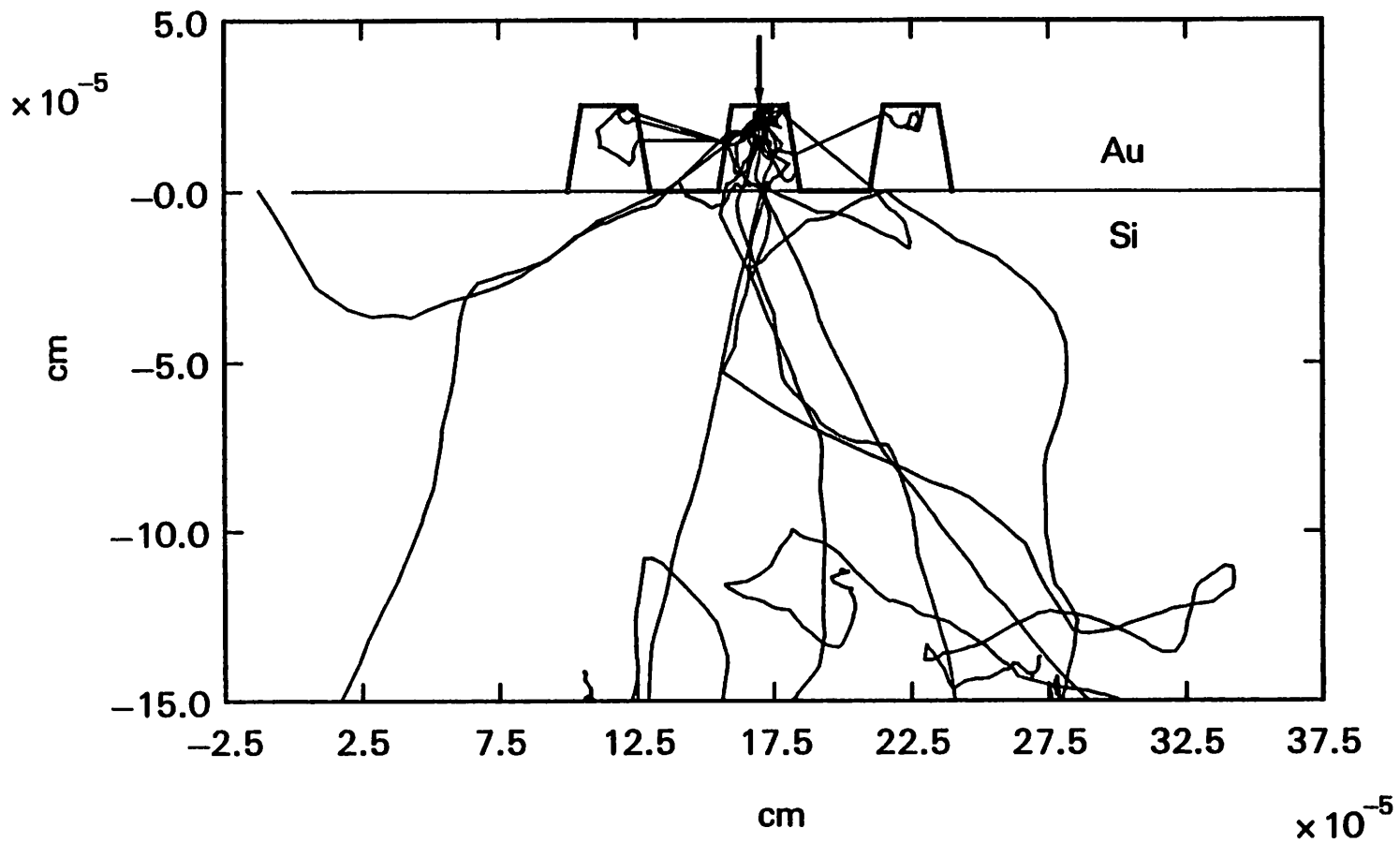
Figure A.1. The breakup of the target structure for the Monte Carlo program into zones, layers, and planes.

```

196.967000      ATOMIC WEIGHT, TOP LAYER
79.             ATOMIC NUMBER, TOP LAYER
19.30000       DENSITY (G/CM**3), TOP LAYER
28.0860000    ATOMIC WEIGHT, BOTTOM LAYER
14.           ATOMIC NUMBER, BOTTOM LAYER
2.330000      DENSITY (G/CM**3), BOTTOM LAYER
001.000E-4    PIECEWISE FIT TO TARGET (CM) -- XO
001.050E-4    ----- XP
001.250E-4    ----- XQ
001.300E-4    ----- XR
001.550E-4    ----- XS
001.600E-4    ----- XT
001.800E-4    ----- XU
001.850E-4    ----- XV
002.100E-4    ----- XW
002.150E-4    ----- XX
002.350E-4    ----- XY
002.400E-4    ----- XZ
-00.250E-4    THICKNESS OF TOP LAYER (CM)
25000.0000    INCIDENT BEAM ENERGY (EV)
00100         NUMBER OF TRAJECTORIES
00850.0000    ENERGY AT WHICH CALCULATIONS STOP (EV)
001.700E-4    X POSITION OF INCIDENT E-BEAM (CM)
010.000E-4    Z POSITION AT WHICH CALCULATIONS STOP (CM)
00.16754756D+8 INITIAL RANDOM NUMBER
0            1 = PRINT POINTS FOR EACH TRAJECTORY  0 = NO PRINT
-00.000E-4    XMIN (CM)
004.000E-4    XMAX (CM)
-02.500E-4    ZMIN (CM)
000.750E-4    ZLAR (CM)

```

Figure A.2. An example of an input file to the Monte Carlo program.



SIMULATION OF 25 ELECTRON TRAJECTORIES

Au on a Si substrate

Au thickness = 0.25 μm , beam energy = 25 kV

Figure A.3. The target structure, incident beam position, and first 25 electron trajectories for the input file shown in Figure A.2.

negative number. Also, it would be wise to keep the numbers in the column fields shown in Figure A.2. Some computer systems may be upset if the numbers are placed outside the specified format fields. This restriction could be eliminated by replacing the specified formats in the input subroutine with general '*' formats. The minimum energy for calculations is necessary since at low values of electron energy, the argument in the logarithm of the Bethe equation becomes less than one causing the electron to gain energy. For gold, this minimum energy is about 750 eV while for silicon it is about 200 eV [37].

Routine MAIN executes the simulation of the electron trajectories. The program is extremely modular in nature and contains many subroutines. It is fully realized that some of the subroutines are repetitive and could be combined into one. It is also realized that there may be slightly more efficient ways of writing the program code; however, this program has one big advantage over more efficient programs which one could write: it works. However, care was taken to eliminate repetitive calculations as much as possible and the search and energy loss routines are written so that the most likely event is checked for and executed first.

An electron's trajectory is simulated in the following manner. The last position of the electron is known along with the number of the zone in which it is located. Subroutine NXTXYZ is called and in turn calculates the ΔX , ΔY , and ΔZ values for the previous two steps in the trajectory. Subroutines STEPL, DIRETN, and XYZ are then called to calculate the step length for the next part of the trajectory, the direction of scatter, and the new location of the electron. This assumes that the electron stays in the same zone which it began scattering in. A SRCH subroutine is then called, depending on what zone the electron was in at the beginning of this scattering event, to determine where the new location (or next scattering location) is located. The most likely locations (zones) are checked first. The appropriate ENLS subroutines are called to calculate the energy loss of the electron as it travels from the old location to the new location. These subroutines calculate the energy lost during the step length, the crossing of zone boundaries, and the tabulation of the backscattered electron data. Again, the most likely events are checked for first.

The SRCH and ENLS subroutines assume that an electron can, in one step length, travel completely through one of the bottom layer zones. For example, an electron could travel from zone 11 to zone 13; but, could not travel from zone 8, through zone 9, and into zone 10 in one step length. A variable step length is used so that it is possible for an electron to travel up to 5 times its calculated mean free path [19,39]. The assumption of scattering into surrounding zones limits the minimum size of complicated structures to about $0.1 \mu\text{m}$ at 25 kV. This is primarily due to the larger step length of an electron in silicon.

The resulting output file after the program has been run with the input file shown in Figure A.2 is shown in Figure A.4. Again, most of the output file is self explanatory. The energy distribution of electrons shows the number of backscattered electrons, in histogram form, with energies ranging from 0 to ENIN (input energy) in ENIN/40 steps. Directly below is the corresponding energy histogram which lists the amount of electron energy deposited in each bin of the histogram.

The theta angle distribution is in a similar format and lists the number and total energy of electrons backscattered into the 90-0 degrees take-off angle range. The histogram size is 2.5 degrees and starts with electrons backscattered into a take-off angle range of 90-87.5 degrees as measured from the plane of the substrate.

The phi angle distribution lists the number and then total energy of the electrons backscattered into the 0-360 degrees azimuthal angle range. The histogram size is 5 degrees and it starts with electrons backscattered into the 0-5 degrees azimuthal angle range. Looking down at the target, this range starts to the right of the δ -function electron-beam and goes counterclockwise.

Finally, the separation into different theta and phi regions is left over from Lin's Monte Carlo program [19]. Again, the number and energy of the electrons scattered into the specified regions are listed. PHI1 is 0-90 degrees in the azimuthal range, PHI2 is 90-180 degrees, etc.

As can be seen, quite a bit of information is generated by the program for one δ -function electron-beam. This is why, for the results presented in this thesis, programs were written to

| | | | | | | | | | | | | | |
|----------------|---|---|---|----------------|---|---|---|----------------|---|---|---|----------|---|
| 0 | 2 | 0 | 0 | 1 | 1 | 1 | 2 | 0 | 2 | 4 | 1 | 0 | 2 |
| 0 | 5 | 4 | 1 | 3 | 3 | 5 | 1 | 3 | 3 | 1 | 4 | 4 | 5 |
| 0 | 1 | 0 | 0 | 0 | | | | | | | | | |
| 0.00000000E+00 | | | | 0.31196352E+05 | | | | 0.00000000E+00 | | | | 0.000000 | |
| 0.13160574E+05 | | | | 0.12791312E+05 | | | | 0.14990824E+05 | | | | 0.438490 | |
| 0.00000000E+00 | | | | 0.30837238E+05 | | | | 0.78628562E+05 | | | | 0.239389 | |
| 0.00000000E+00 | | | | 0.38376578E+05 | | | | 0.69956187E+05 | | | | 0.339816 | |
| 0.00000000E+00 | | | | 0.10929044E+06 | | | | 0.81217812E+05 | | | | 0.237203 | |
| 0.62777613E+05 | | | | 0.70192125E+05 | | | | 0.82934250E+05 | | | | 0.225056 | |
| 0.64445633E+05 | | | | 0.51430988E+05 | | | | 0.22963520E+05 | | | | 0.858295 | |
| 0.90944875E+05 | | | | 0.10141187E+06 | | | | 0.24468758E+05 | | | | 0.000000 | |
| 0.00000000E+00 | | | | 0.20130895E+05 | | | | 0.00000000E+00 | | | | 0.000000 | |
| 0.00000000E+00 | | | | | | | | | | | | | |

THE PHI-ANGLE DISTRIBUTION (5 DEG PER DIVISION)

| | | | | | | | | | | | | | |
|----------------|---|---|---|----------------|---|---|---|----------------|---|---|---|----------|---|
| 1 | 0 | 1 | 0 | 0 | 1 | 1 | 0 | 0 | 1 | 1 | 0 | 0 | 0 |
| 0 | 0 | 0 | 0 | 1 | 2 | 0 | 0 | 1 | 2 | 0 | 1 | 0 | 2 |
| 2 | 2 | 0 | 2 | 1 | 2 | 1 | 0 | 0 | 2 | 1 | 1 | 0 | 0 |
| 0 | 1 | 0 | 1 | 0 | 2 | 2 | 1 | 2 | 2 | 0 | 1 | 0 | 1 |
| 0 | 0 | 1 | 2 | 2 | 3 | 2 | 2 | 0 | | | | | |
| 0.13160574E+05 | | | | 0.00000000E+00 | | | | 0.19174238E+05 | | | | 0.000000 | |
| 0.00000000E+00 | | | | 0.15896980E+05 | | | | 0.20073020E+05 | | | | 0.000000 | |
| 0.00000000E+00 | | | | 0.23065512E+05 | | | | 0.13713160E+05 | | | | 0.000000 | |
| 0.00000000E+00 | | | | 0.00000000E+00 | | | | 0.00000000E+00 | | | | 0.458247 | |
| 0.00000000E+00 | | | | 0.00000000E+00 | | | | 0.00000000E+00 | | | | 0.000000 | |
| 0.24174086E+05 | | | | 0.31966387E+05 | | | | 0.00000000E+00 | | | | 0.000000 | |
| 0.23244297E+05 | | | | 0.33019602E+05 | | | | 0.00000000E+00 | | | | 0.157880 | |
| 0.00000000E+00 | | | | 0.43806566E+05 | | | | 0.22875340E+05 | | | | 0.783772 | |
| 0.28336758E+05 | | | | 0.44806020E+05 | | | | 0.00000000E+00 | | | | 0.370190 | |
| 0.21159504E+05 | | | | 0.35174687E+05 | | | | 0.18740172E+05 | | | | 0.000000 | |
| 0.00000000E+00 | | | | 0.43700453E+05 | | | | 0.22366801E+05 | | | | 0.200873 | |
| 0.00000000E+00 | | | | 0.00000000E+00 | | | | 0.17950609E+05 | | | | 0.000000 | |
| 0.00000000E+00 | | | | 0.23522719E+05 | | | | 0.00000000E+00 | | | | 0.182398 | |
| 0.00000000E+00 | | | | 0.46615254E+05 | | | | 0.45726340E+05 | | | | 0.226955 | |
| 0.43212734E+05 | | | | 0.24376691E+05 | | | | 0.00000000E+00 | | | | 0.496883 | |
| 0.00000000E+00 | | | | 0.20455805E+05 | | | | 0.57740090E+05 | | | | 0.183608 | |
| 0.00000000E+00 | | | | 0.00000000E+00 | | | | 0.22504172E+05 | | | | 0.488601 | |
| 0.43474977E+05 | | | | 0.59060715E+05 | | | | 0.46683902E+05 | | | | 0.459722 | |
| 0.00000000E+00 | | | | | | | | | | | | | |

THE TOTAL NUMBER OF ABSORBED ELECTRONS IS 34

THE TOTAL ENERGY ABSORBED IN SUBSTRATE IS 1194022.000000 EV

| | |
|--|----|
| THE BACKSCATTERED ELECTRONS COMING OUT FROM PLANE 1 | 6 |
| THE BACKSCATTERED ELECTRONS COMING OUT FROM PLANE 2 | 0 |
| THE BACKSCATTERED ELECTRONS COMING OUT FROM PLANE 3 | 3 |
| THE BACKSCATTERED ELECTRONS COMING OUT FROM PLANE 4 | 0 |
| THE BACKSCATTERED ELECTRONS COMING OUT FROM PLANE 5 | 2 |
| THE BACKSCATTERED ELECTRONS COMING OUT FROM PLANE 6 | 10 |
| THE BACKSCATTERED ELECTRONS COMING OUT FROM PLANE 7 | 29 |
| THE BACKSCATTERED ELECTRONS COMING OUT FROM PLANE 8 | 8 |
| THE BACKSCATTERED ELECTRONS COMING OUT FROM PLANE 9 | 0 |
| THE BACKSCATTERED ELECTRONS COMING OUT FROM PLANE 10 | 0 |
| THE BACKSCATTERED ELECTRONS COMING OUT FROM PLANE 11 | 2 |
| THE BACKSCATTERED ELECTRONS COMING OUT FROM PLANE 12 | 1 |
| THE BACKSCATTERED ELECTRONS COMING OUT FROM PLANE 13 | 5 |

SEPARATION INTO DIFFERENT THETA AND PHI REGIONS
 THE ROWS ARE 0-30, 30-60, AND 60-90 DEG
 AND THE COLUMNS ARE PHI1, PHI2, PHI3 AND PHI4.

| | | | | |
|----------------|---|----------------|----------------|----------|
| 4 | 4 | 8 | 6 | |
| 7 | 6 | 10 | 7 | |
| 6 | 0 | 4 | 4 | |
| 0.88986875E+05 | | 0.85613375E+05 | 0.15845856E+06 | 0.128567 |

Figure A.4. (cont.)

| | | | |
|----------------|----------------|----------------|----------|
| 0.15120631E+06 | 0.10939431E+06 | 0.20636294E+06 | 0.127988 |
| 0.11302831E+06 | 0.00000000E+00 | 0.67416187E+05 | 0.689483 |

THE RANDOM NUMBER FOR NEXT RUN IS 0.866674200D+07

TOTAL BACKSCATTER COEFFICIENT = 0.65999997E+00

Figure A.4. (cont.)

automatically read in the output files describing the signal from a target and selectively pick out the desired information. In this manner, it was possible to effectively utilize the program to perform a variety of simulation studies.

REFERENCES

- [1] Y. Goto, Y. Furukawa, and T Inagaki, "Inspection for defects of a mask containing one-to submicrometer patterns using a scanning electron microscope and feature extraction method", *J. Vac. Sci. Technol.* 15 (3), 953 (1978).
- [2] Y. Wada, Y. Hisamoto, K. Mizukami, and M. Migitaka, "Studies on an electron-beam mask-defect inspection system", *J. Vac. Sci. Technol.* 19 (1), 36 (1981).
- [3] M. Migitaka, K. Mizukami, Y. Hisamoto, and Y. Wada, "An automated VLSI-mask inspection system", *J. Vac. Sci. Technol.* 20 (1), 26 (1982).
- [4] R. A. Simpson and D. E. Davis, "Detecting submicron pattern defects on optical photomasks using an enhanced EL-3 e-beam lithography tool", *SPIE 334*, Santa Clara, (1982).
- [5] W. D. Grobman, "Mask inspection using electron-beam systems", *IBM Technical Disclosure Bulletin* 22 (12), (1980).
- [6] M.G. Rosenfield, R. Viswanathan, A.D. Wilson, P. Vettiger, and A.R. Neureuther, "X-ray mask inspection using a vector scan electron-beam system", *Proceedings of Microcircuit Engineering*, 179 (1982).
- [7] R. Viswanathan, A.D. Wilson, J.M. Lafuente, H.R. Voelker, and A. Kern, "Electron beam pattern writer for x-ray masks", *SPIE 448*, Brookhaven, (1983).
- [8] R.E. Acosta, J.M. Warlaumont, and R. Viswanathan, "Masks for storage ring x-ray lithography", *J. Vac. Sci. Technol.*, to be published Dec. (1983).
- [9] R.E. Acosta, "Silicon mask technology", *SPIE 448*, Brookhaven, (1983).
- [10] W.A. Johnson, "Boron nitride mask technology", *SPIE 448*, Brookhaven, (1983).
- [11] See the proceedings of *SPIE 333*, Santa Clara, (1982).
- [12] K. Suzuki, Y. Lida, T. Torikai, and J. Matsui, "X-ray masks with high aspect ratio submicron patterns fabricated using plasma-CVD SiN_x spacer and membrane", *Proceedings of the 10th International Conference on Electron and Ion Beam Science and Technology*,

edited by R. Bakish (Electrochemical Society, Pennington NJ, 1982), 333.

- [13] O.C. Wells, *Scanning Electron Microscopy*, (McGraw Hill, New York, 1974).
- [14] J.I. Goldstein, D.E. Newbury, J.W. Colby, H. Yakowitz, E. Lifshin, and J.R. Coleman, *Practical Scanning Electron Microscopy*, edited by J.I. Goldstein and H. Yakowitz (Plenum Press, New York, 1975).
- [15] V.N.E. Robinson and E.P. George, "Electron scattering in the SEM", *SEM/1978* 1, 859 (1978).
- [16] V.N.E. Robinson, "Backscattered electron imaging", *SEM/1975 (Part 1)*, 61 (1975).
- [17] O.C. Wells, R.J. Savoy, and P.J. Bailey, "Backscattered electron imaging in the scanning electron microscope -- measurement of surface layer mass-thickness", *Proceedings of the Asilomar Conference on Electron Beam Interactions with Solids*, (April, 1982).
- [18] V.N.E. Robinson, "Imaging with backscattered electrons in a scanning electron microscope", *Scanning* 3 (1), 15 (1980).
- [19] Y.C. Lin, "Alignment signals from electrons scattering near an edge for electron beam microfabrication", Ph.D. Dissertation, Department of Electrical Engineering and Computer Sciences, University of California, Berkeley (1981).
- [20] D. Stephani and E. Froschle, "High precision automatic alignment procedure for vector scan e-beam lithography", *J. Vac. Sci. Technol.* 15 (3), 906 (1978).
- [21] D.E. Davis, "Registration mark detection for electron-beam lithography - EL1 system", *IBM J. Res. Develop.* 24 (5), 545 (1980).
- [22] J.I. Goldstein, D.E. Newbury, P. Echlin, D.C. Joy, C. Fiori, and E. Lifshin, *Scanning Electron Microscopy and X-Ray Microanalysis*, (Plenum Press, New York, 1981). Also, see reference 14.
- [23] For an excellent review of the Monte Carlo method, see, D.F. Kyser, "Monte Carlo calculations for electron microscopy, microanalysis, and microlithography", *SEM/1981*, 47 (1981).

- [24] G. Fontaine, *Microanalysis and Scanning Electron Microscopy*, edited by F. Maurice, L. Meny, and R. Tixier (Les Editions de Physique, Orsay, France, 1978).
- [25] W.D Grobman and A.J. Speth, "An exposure wedge for electron beam lithography development control and for the determination of resist development and proximity effect parameters", *Proceedings of the 8th International Conference on Electron and Ion Beam Science and Technology*, edited by R. Bakish (Electrochemical Society, Princeton NJ, 1978), 276.
- [26] M.G. Rosenfield, A.R. Neureuther, and C.H. Ting, "The use of bias in electron beam lithography for improved profile quality and linewidth control", *J. Vac. Sci. Technol.* 19 (4), 1242 (1981).
- [27] See *J. Vac. Sci. Technol.* 19 (4), pp. 1304-1332 (1981).
- [28] M. Hatzakis, "Multilayer resist systems for lithography", *Solid State Technol.* 24 (8), 74 (1981).
- [29] C. Dix and P. Hendy, "A double PMMA resist structure for submicron lithography using a single developer", *Proceedings of the 10th International Conference on Electron and Ion Beam Science and Technology*, edited by R. Bakish (Electrochemical Society, Pennington NJ, 1982), 204.
- [30] With J.R. Paraszczak of IBM T.J. Watson Research Center, Yorktown Heights, NY 10598.
- [31] I. Adesida, "Electron energy dissipation in layered media", Ph.D. Dissertation, Department of Electrical Engineering and Computer Sciences, University of California, Berkeley (1979).
- [32] D. Stephani, "Monte Carlo calculations of backscattered electrons at registration marks", *J. Vac. Sci. Technol.* 16 (6), 1739 (1979).

- [33] Y. Kato, T. Takigawa, M. Yoshimi, and K. Kawabuchi, "Mark detection in high voltage electron beam lithography", *Proceedings of Microcircuit Engineering*, 28 (1982).
- [34] G.G. Hembree, S.W. Jensen, and J.F. Marchiando, *Microbeam Analysis-1981*, edited by R.H. Geiss (San Francisco Press, San Francisco, 1981), 123.
- [35] E.P. George and V.N.E. Robinson, "The dependence of SEM contrast upon electron penetration", *SEM/1976 (Part 1)*, 17 (1976).
- [36] See *Use of Monte Carlo Calculations in Electron Probe Microanalysis and Scanning Electron Microscopy*, edited by K.F.J. Heinrich, D.E. Newbury, and H. Yakowitz, National Bureau of Standards, Special Publ. 460 (1976).
- [37] D.F. Kyser and K. Murata, "Monte Carlo simulation of electron beam scattering and energy loss in thin films on thick substrates", *Proceedings of the 6th International Conference on Electron and Ion Beam Science and Technology*, edited by R. Bakish, (Electrochemical Society, Princeton NJ, 1974) 205.
- [38] K. Murata, E. Nomura, K. Nagami, T. Kato, and H. Nakata, "Experimental and theoretical study of cross-sectional profiles of resist patterns in electron-beam lithography", *J. Vac. Sci. Tech.* 16 (6), 1734 (1979).
- [39] K. Murata, "Monte Carlo simulation of electron scattering in resist film/substrate targets", *Proceedings of the Asilomar Conference on Electron Beam Interactions with Solids*, (April, 1982).
- [40] R.J. Hawryluk, A.M. Hawryluk, and H.I. Smith, "Energy dissipation in a thin polymer film by electron beam scattering", *J. Appl. Phys.* 45 (6), 2551, (1974).
- [41] Y.C. Lin and A.R. Neureuther, "Alignment signals from resist-coated marks for direct wafer writing", *IEEE Trans. Electron Devices* ED-28 (11), 1397 (1981).
- [42] H. Niedrig, "Electron backscattering from thin films", *J. Appl. Phys.* 53 (4), R15 (1982).

- [43] T.E. Everhart and P.H. Hoff, "Determination of kilovolt electron energy dissipation vs penetration distance in solid materials", *J. Appl. Phys.* 42 (13), 5837 (1971).
- [44] J.S. Greeneich and T. Van Duzer, "An approximate formula for electron energy versus path length", *IEEE Trans. on Electron Devices*, (1973).
- [45] M. Parikh and D.F. Kyser, "Energy deposition functions in electron resist films on substrates", *J. Appl. Phys.* 50 (2), 1104 (1979).
- [46] R.J. Hawryluk, "Energy dissipation by electron beam scattering in thin polymer films", Ph.D Dissertation, Massachusetts Institute of Technology (1974). Also published as Technical Report 511, Lincoln Laboratory (1974).
- [46a] E.D. Wolf, P.J. Coane, and F.S. Ozdemir, "Composition and detection of alignment marks for electron-beam lithography", *J. Vac. Sci. Technol.* 12 (6), 1266 (1975).
- [47] A.D. Wilson, T.W. Studwell, G. Folchi, A. Kern, and H. Voelker, "A comparison of pattern stitching by subfield registration and laser interferometer servo control", *Proceedings of the 8th International Conference on Electron and Ion Beam Science and Technology*, edited by R. Bakish, (Electrochemical Society, Princeton NJ, 1978) 198.
- [48] Dieter Kern, IBM T.J. Watson Research Center, Yorktown Heights, NY 10598, private communication.
- [49] D.F. Kyser and R. Pyle, "Computer simulation of electron-beam resist profiles", *IBM J. Res. Develop.* 24 (4), 426 (1980).
- [50] R.D. Moore, G.A. Caccoma, H.C. Pfeiffer, E.V. Weber, and O.C. Woodard, "EL-3: a high throughput, high resolution e-beam lithography tool", *J. Vac. Sci. Technol.* 19 (4), 950 (1981).
- [51] B.P. Piwczyk and A.E. Williams, "High throughput variable shaped electron beam lithography", *Solid State Technol.* 26 (9), 127 (1983).

- [52] M.G. Rosenfield, "Simulation of developed resist profiles for electron-beam lithography", M.S. Report, Department of Electrical Engineering and Computer Sciences, University of California, Berkeley (1981).
- [53] M.G. Rosenfield, A.R. Neureuther, and R. Viswanathan, "Simulation of backscattered electron signals for x-ray mask inspection" J. Vac. Sci. Technol., to be published Dec. (1983).
- [54] S.W. Jensen and D. Swyt, "Sub-micrometer length metrology: problems, techniques, and solutions", SEM/1980 (Part 1), 393 (1980).
- [55] D.A. Gedeke, J.B. Ayers, and P.B. DeNee, "A solid state backscattered electron detector capable of operating at T.V. scan rates", SEM/1978, 581 (1978).
- [56] A. Rose, Advan. Electron. 1, 131 (1948): also A. Rose, *Vision: Human and Electronics* (Plenum, NY, 1973).
- [57] Y.C. Lin and T.E. Everhart, "Study on voltage contrast in SEM", J. Vac. Sci. Technol. 16 (6), 1856 (1979).
- [58] O.C. Wells, "Note on signal-to-noise ratio (SNR) in the scanning electron microscope", SEM/1978 (Part 1), 299 (1978).
- [59] G.F. Knoll, *Radiation Detection and Measurement*, (Wiley, NY, 1979).
- [60] N.R. Comins and J.T. Thirlwall, "Quantitative studies and theoretical analysis of the performance of the scintillation electron-detector", J. Microscopy, 24 (2), 119 (1981).
- [61] T.E. Everhart and R.F.M. Thornley, "Wide-band detector for micro-microampere low energy electron currents", J. Sci. Instr. 37, 246 (1960).
- [62] J.B. Pawley, "Performance of SEM scintillation materials", SEM/1974, 27 (1974).
- [63] W. Baumann and L. Reimer, "Comparison of the noise of different electron detection systems using a scintillator-photomultiplier combination", Scanning 4 (3), 141 (1981).

- [64] B. Volbert and L. Reimer, "Advantages of two opposite Everhart-Thornley detectors in SEM", SEM/1980 (Part 4), 1 (1980).
- [65] L. Reimer, W. Popper, and W. Brocker, "Experiments with a small solid angle detector for bse", SEM/1978 (Part 1), 705 (1978).
- [66] M.E. Taylor, "An improved light pipe for the scanning electron microscope", Rev. Sci. Instr. 43 (12), 1846 (1972).
- [67] K. Schur, R. Blaschke, and G. Pfefferkorn, "Improved conditions for back-scattered electron SEM micrographs on polished sections using a modified scintillator detector", SEM/1974, 1003 (1974).
- [68] Y. Furukawa, N. Nakayama, Y. Goto, S. Igaki, and T. Inagaki, "Auto-registration technique for an electron beam exposure system using a new sheet structured detector for back-scattered electrons", *Proceedings of the 8th International Conference on Electron and Ion Beam Science and Technology*, edited by R. Bakish, (Electrochemical Society, Princeton NJ, 1978) 63.
- [69] W. Baumann, A. Niemiets, L. Reimer, and B. Volbert, "Preparation of P-47 scintillators for STEM", J. Microscopy 122 (2), 181 (1981).
- [70] B. Volbert and L. Reimer, "Preparation of P-47 scintillators", Scanning 2 (2), 107 (1979).
- [71] S.H. Moll, F. Healey, B. Sullivan, and W. Johnson, "A high efficiency, nondirectional backscattered electron detection mode for SEM", SEM/1978 (Part 1), 303 (1978).
- [72] C.B. Norris, Jr., "Optimum design of electron beam-semiconductor linear low pass amplifiers-part I: bandwidth and rise time", IEEE Trans. on Electron Devices ED-20 (4), 447 (1973).
- [73] C.B. Norris, Jr., "Optimum design of electron beam-semiconductor linear low pass amplifiers-part II: output capabilities", IEEE Trans. on Electron Devices ED-20 (4), 827 (1973).

- [74] P.S.D. Lin and R.P. Becker, "Detection of backscattered electrons with high resolution", SEM/1975 (Part 1), 61 (1975).
- [75] M.J. Penberth and B.A. Wallman, "Low profile electron collector system", J. Vac. Sci. Technol. 16 (6), 1719 (1979).
- [76] Phillips Scanning Electron Microscope SEM 505, "Multi-function detector system", Specification sheet (1982).
- [77] A.B. Carlson, *Communication Systems, 2nd edition*, (McGraw Hill, NY, 1975).
- [78] W.D. Grobman, H.E. Luhn, T.P. Donahue, A.J. Speth, A.D. Wilson, M. Hatzakis, and T.H.P. Chang, "1 μ m mosfet VLSI technology: part VI - electron-beam lithography", IEEE Trans. Electron Devices ED-26 (4), 360 (1979).
- [79] W.R. Livesay, J.S. Greeneich, J.E. Wolfe, and R.J. Felker, "A process-compatible electron beam direct write system", Solid State Technol. 26 (9), 137 (1983).
- [80] R.D. Moore, "EL systems: high throughput electron beam lithography tools", Solid State Technol. 26 (9), 127 (1983).
- [81] J.H. Bruning, M. Feldman, T.S. Kinsel, E.K. Sittig, and R.L. Townsend, "An automated mask inspection system-AMIS", IEEE Trans. Electron Devices ED-22 (7), 487 (1975).
- [82] R.A. Kaplan, "A microprocessor-controlled mask inspection and repair system", Solid State Technol. April, 74 (1976).
- [83] J.D. Knox, P.V. Goedertier, D. Fairbanks, and F. Caprari, "Inspecting IC masks with a differential laser scanning inspection system", Solid State Technol. May, 48 (1977).
- [84] K. Levy, "Automated equipment for 100% inspection of photomasks", Solid State Technol. May, 60 (1978).
- [85] B. Tsujiyama, K. Saito, and K. Kurihara, "A highly reliable mask inspection system", IEEE Trans. Electron Devices ED-27 (7), 1284 (1980).

- [86] Y. Suzuki and T. Yamazaki, "An automatic reticle inspection technique for wafer steppers", *Proceedings of Kodak Microelectronics Seminar - Interface 1982*, (1982).
- [87] R. Van Asselt and G. Brooks, "Technique for inspecting photomasks with pellicles attached", *Proceedings of Kodak Microelectronics Seminar - Interface 1982*, (1982).
- [88] H. Yang, "An automatic mask and reticle inspection system", SPIE 334, Santa Clara, (1982).
- [89] H. Liff, R. Brauner, P. Esrig, and J. Fee, "Automatic inspection for in-aligner reticle qualification", SPIE, Santa Clara, (1983).
- [90] I.A. Cruttwell, "A fully automated pattern inspection system for reticles and masks", SPIE, Santa Clara, (1983).
- [91] Contrex *Wafer VisionTM* 2000 System Specifications (1983).
- [92] Cambridge Instruments *ChipcheckTM* Specifications (1983).
- [93] KLA Automatic Reticle Inspection System, *KLARISTM*, Specifications (1982).
- [94] Y. Hisamoto, Hitachi Corporation, private communication.
- [95] J.H. Bruning, Bell Laboratories, Murray Hill, NJ 07974, private communication.
- [96] R. Viswanathan, T.H.P. Chang, and D. Coffey, "Distortion correction in scanning electron beam systems", *Proceedings of the 8th International Conference on Electron and Ion Beam Science and Technology*, edited by R. Bakish, (Electrochemical Society, Princeton NJ, 1978) 44.
- [97] J.M. Lafuente, IBM T.J. Watson Research Center, Yorktown Heights, NY 10598, private communication, to be published.
- [98] A.D. Wilson, T.H.P. Chang, and A. Kern, "Experimental scanning electron-beam automatic registration system", *J. Vac. Sci. Technol.* 12 (6), 1240 (1975).
- [99] A.M. Patlach, P.R. Jaskar, and T.W. Studwell, "Electron-beam lithographic pattern generation system", *J. Vac. Sci. Technol.* 15 (3), 874 (1978).

- [100] J.A. Doherty, "Recent advances in electron beam systems for mask making", Solid State Technol. May, 83 (1979).
- [101] J.A. Reynolds, "An overview of e-beam mask making", Solid State Technol. August, 87 (1979).
- [102] J.C. Eidson and R.K. Scudder, "A high speed electron beam lithography system", J. Vac. Sci. Technol. 19 (4), 932 (1981).
- [103] R.A. Flavin, IBM T.J. Watson Research Center, Yorktown Heights, NY 10598, private communication.
- [104] IBM vector scan electron-beam system design data post-processor.